Source process and physical mechanism of global large deep-focus earthquakes

A Dissertation Presented

by

Yu Chen

to

The Graduate School

in Partial Fulfillment of the

Requirements

for the Degree of

Doctor of Philosophy

in

Geosciences

Stony Brook University

Aug 2015

Stony Brook University

The Graduate School

Yu Chen

We, the dissertation committee for the above candidate for the

Doctor of Philosophy degree, hereby recommend

acceptance of this dissertation.

Lianxing Wen – Dissertation Advisor
Professor, Department of Geosciences

William Holt - Chairperson of Defense
Professor, Department of Geosciences

Donald J. Weidner
Distinguished Professor, Department of Geosciences

Baosheng Li
Research Professor, Department of Geosciences

Chen Ji
Associate Professor, Department of Earth Science,
University of California, Santa Barbara

This dissertation is accepted by the Graduate School

Charles Taber
Dean of the Graduate School

Abstract of the Dissertation

Source process and physical mechanism of global large deep-focus earthquakes

by

Yu Chen

Doctor of Philosophy

in

Geosciences

Stony Brook University

2015

We develop a multiple source inversion method that treats a large earthquake as a combination of double couple sub-events, and resolves spatio-temporal distribution and focal mechanisms of the sub-events, based on waveform modeling of P, pP, SH and sSH wave data. We study source processes of 26 large deep-focus earthquakes with Mw > 7.0 and depth > 400 km from 1994 to 2013. They are classified into three categories based on spatial distribution and focal mechanisms of the inferred sub-events: 1) category one, with non-planar distribution of the sub-events and focal mechanisms inconsistent with a single fault plane, represented by the 1994 Bolivia earthquake and the 2013 Okhotsk earthquake; 2) category two, with planar distribution but focal mechanisms inconsistent with the plane, including eighteen earthquakes; and 3) category three, with planar distribution and focal mechanisms consistent with the plane, including six earthquakes. We discuss possible physical mechanisms for earthquakes in each category in the context of plane rupture, transformational faulting and shear thermal instability. The weak initiation sub-events are studied for 6 of those earthquakes, with at least one-order smaller seismic moment. These initiation sub-events exhibit great variability of focal mechanisms as the major sub-events, and the stress drops of the sub-events can be fit in the range between 2.5 MPa and 70 MPa, however, the initiation sub-events and the major sub-events do not seem fundamentally distinguishable, implying that the earthquakes are a combination of sub-events with various magnitudes. We suggest that the inferred source processes of all the analyzed earthquakes can be best interpreted by a cascading failure of shear thermal instabilities in pre-existing weak zones, with the perturbation of stress generated by a shear instability triggering another and the orientations of the pre-existing weak zones control the focal mechanisms of pre-existing weak zones. The proposed mechanism can also explain the observed great variability of focal mechanisms and super-shear rupture of deep-focus earthquakes in the previous studies.

Table of Contents

List of Figures

(Az=64°) vs CHTO (Az=250°); (2) FUNA (az=151°) vs GRFO (az=335°); (3) POHA (az=111°) vs AAK (az=290°). Seismic records are labeled with station name along with azimuth (Az) and epicentral distance (Δ). Energy pulses are marked in accordance with those in Fig. 3-1a. For display purpose, the polarities of some records have been flipped.

Fig. 3-2. (a) Comparison of observed P (black) and pP (red) displacement seismograms as a function of azimuth. The black and red lines indicate the ending time of P and pP data, respectively. (b) Overlays of P (black) and pP (red) displacements observed at five stations: KBL, HKT, CCM, WCI and SSPA. Seismic records are labeled with station name along with azimuth (Az) and epicentral distance (Δ). The black and red lines mark the maximal of the second and fourth groups of energy labeled in Fig. 2-2a. For display purpose, the polarities of some records have been flipped.

Fig. 3-3. Selected seismograms (black traces) comparing with synthetics (red traces) predicted based on the inverted six sub-event model (Table 2-1) in four quadrants for, P phase (vertical displacement), pP phase (vertical displacement), SH phase (tangential displacement) and sSH phase (tangential displacement). Seismic records are labeled with station name along with azimuth (Az), epicentral distance (Δ), and the maximum amplitude (Amp) of the data. The unit of the amplitude is 10^{-6} m. The whole waveform fitting of all used stations is shown in Fig. S2-1.

Fig. 3-4. (a) Locations of sub-events (red points), aftershocks (purple triangles) and background seismicity (green triangle), along with slab depth contours (black traces, labeled with slab depth). Black beach ball describes GCMT focal mechanism of the mainshock. Red beach balls represent inverted focal mechanisms of the sub-events, labeled with sub-event depth and the occurring sequence number as defined in Fig. 2-2a. Sub-events are connected by blue arrows following the sequence of their occurring times. Green ellipses represent the 95% confidence levels of the relocated fore/aftershocks. Sub-events, aftershocks and background seismicity are labeled with depth, depth uncertainty and sequence number in Tables 2-1, 2-2. Slab depth contours are from the USGS Slab 1.0 model (Hayes et al., 2012). (b) Three dimensional spatial distribution and focal mechanisms of inverted sub-events (red beach balls) labeled with sequence of their occurring times, along with the focal planes (gray planes) in the GCMT solution. Purple and green spheres represent the fore/aftershocks in (a).

Fig. 3-5. (a) Measured difference in absolute arrival time (circles and squares) of the P phases (with respect to their mean) between the mainshock and one aftershock 201305241456, plotted centered at the location of each station, along with the great circle paths (green traces) from the mainshock (star) to the stations (labeled with station name in Fig. 3-5b). (b) Same as Fig. 3-5a, except that travel time residuals between the two events are corrected using the best-fitting relative location (Table 3-1).

Fig. 3-6. (a) Three dimensional spatial distribution of focal mechanisms of the best-fitting model (red beach balls) and the inverted model of compelling the sub-events on the GCMT sub-horizontal plane (blue beach balls) labeled with sequence of their occuring time, along with the focal planes (gray planes) in the GCMT solution. (b) Selected seismograms (black traces) comparing with synthetics (red traces) predicted by the best-fitting source model (Table 1, red beach balls in Fig. 3-6a) and synthetics (blue traces) predicted by the best-fitting source model (Table S3-1, blue beach balls in Fig. 3-6a) on the GCMT sub-horizontal plane. Arrows point to the misfits of the blue traces. The waveform fitting of all used stations is shown in Fig. S3-2.

Fig. 3-7. (a) Three dimensional spatial distribution of focal mechanisms of the best-fitting model (red beach balls) and the inverted model of compelling the sub-events on the sub-horizontal plane (blue beach balls) based on the constaints of P wave only, labeled with sequence of their occuring time, along with the focal planes (gray planes) in the GCMT solution. (b) Selected seismograms (black traces) comparing with synthetics (red traces) predicted by the best-fitting source model (Table 2-1, red beach balls in Fig. 3-7a) and synthetics (blue traces) predicted by the best-fitting source model (Table S3-2, blue beach balls in Fig. 3-7a) on the GCMT sub-horizontal plane based on P wave data only. Arrows point to the misfits of the blue traces. The waveform fitting of all used stations is shown in Fig. S3-3.

Fig. 3-8. (a) Three dimensional spatial distribution of focal mechanisms of the best-fitting model (red beach balls) and the inverted model compelling the sub-events on the GCMT sub-vertical plane (blue beach balls), labeled with sequence of their occuring time, along with the focal planes (gray planes) in the GCMT solution. (b) Selected seismograms (black traces) comparing with synthetics (red traces) predicted by the best-fitting source model (Table 2-1, red beach balls in Fig. 3-8a) and synthetics (blue traces) predicted by the best-fitting source model (Table S3-3, blue beach balls in Fig. 3-8a) on the GCMT sub-vertical plane. The waveform fitting of all used stations is shown in Fig. S3-4.

Fig. 3-9. (a) Three dimensional spatial distribution of focal mechanisms of the best-fitting model (red beach balls) and the inverted model compelling the sub-events on the plane that best connects the best-fitting model (blue beach balls), labeled with sequence of their occuring time, along with the focal planes (gray planes) in the GCMT solution. (b) Selected seismograms (black traces) comparing with synthetics (red traces) predicted by the best-fitting source model (Table 2-1, red beach balls in Fig. 3-9a) and synthetics (blue traces) predicted by the best-fitting source model (Table S3-4, blue beach balls in Fig. 3-9a) on a plane that best connects the inferred sub-events in Table 2-1. The waveform fitting of all used stations is shown in Fig. S3-5.

Fig. 3-10. (a) Synthetics (red traces) of pP waves attenuated by $t^* = 1.45$ based on the PREM model and synthetics (blue traces) of pP waves attenuated by $t^* = 2.61$ (1.8 times of PREM values) predicted by the best-fitting source model (Table 2-1). The red and blue lines mark the peaks of sub-events 2 and 4. (b) The misfits (RMS) of amplitudes between the data and synthetics predicted based on the best fitting model by varing t^* of pP phase from 0.5 to 2.0 times of the PREM values.

Fig. 3-11. (a) Location and focal mechanisms (red beach balls) of the mainshock and a near-by aftershock. The depth contours labeled with slab depth are from the USGS Slab

1.0 model. (b) Observed vertical P (black traces) and pP (red traces) displacement seismograms of the aftershock as a function of azimuth.

Fig. 3-12. (a) Three dimensional spatial distribution of focal mechanisms of the best-fitting model (red beach balls) and the inverted model compelling sub-event 4 to 90 km south to the initiation of the earthquake (blue beach balls), labeled with sequence of their occuring time, along with the focal planes (gray planes) in the GCMT solution. (b) Selected seismograms (black traces) comparing with synthetics (red traces) predicted by the best-fitting source model (Table 2-1, red beach balls in Fig. 3-12a) and synthetics (blue traces) predicted by the best-fitting source model (Table S3-5, blue beach balls in Fig. 3-12a) by compeling sub-event 4 to 90 km south to the initiation of the earthquake. Arrows point to the misfits of the blue traces. The waveform fitting of all used stations is shown in Fig. S3-6.

Fig. 3-13. A two-plane rupture model (green planes) that could accommodate the locations and focal mechanisms of the inferred sub-events (red beach balls labeled with sequence of their occurring times). Two GCMT fault planes are presented as blue planes.

Fig. 4-1. Distribution of the global large deep-focus earthquakes (Mw > 7 and depth > 400 km) from 1994 to 2012, and their GCMT focal mechanisms, labeled with event numbers in Table S3-0. The earthquakes labeled with green, blue and red represent the earthquakes in categories one to three as classified in Section 3.5. The events labeled with red numbers are the example events presented in the main text. Three earthquakes with black beach balls are not studied (see text for the reasons).

Fig. 4-2. (a) Comparison of observed P (black traces) and pP (red traces) displacement seismograms as a function of azimuth. The black and red lines indicate the peak times of the sub-events for P and pP, respectively. (b) Overlays of P and pP displacements observed at five example stations: COR, RAR, SPA, SUR and PAB. The black and red lines mark the maximal of the first, second, fourth and fifth sub-events labeled in (a). For the display purpose, the polarities of some records have been flipped.

Fig. 4-3. (a) Locations of the best-fitting sub-events (red points), the best planar model (blue points, the inferred sub-events compelled to the sub-horizontal plane), and the initiated location (black star) of the 1994 Bolivia earthquake (E2), along with slab depth contours (black traces, labeled with slab depths). Black beach ball describes GCMT solution of the event. Red and blue beach balls represent inferred focal mechanisms of the sub-events of the best-fitting model and the best planar model, labeled with the sub-event peak times/moment magnitudes/depths. (b) Three-dimensional spatial distribution and focal mechanisms of inferred sub-events of the best-fitting model (red beach balls) and the best planar model (blue beach balls) labeled with their occurring sequence. (c) Selected observed seismograms in Fig. S3-2 (black traces) comparing with synthetics (red traces) predicted by the best-fitting source model and synthetics (blue traces) predicted by the best planar model. The red and blue lines label the peak times of the sub-events predicted by the best-fitting model and the best planar model.

initiation sub-events of the best-fitting model in Fig. S1. Amps represent the maximum amplitudes of the whole seismograms.

Fig. 5-3. Similar as Fig. 5-2, except for event E8. (c) Selected waveform comparisons in Fig. S5-2.

Fig. 5-4. Relationships between seismic moment and source duration of the best-fitting initiation and major sub-events of the earthquakes. Circles, inverted triangles, triangles, squares, stars and crosses represent the initiation sub-events (red) and the major sub-events (black) of earthquakes E2, E8, E14, E16, E20 and E23, respectively.

List of Tables

Acknowledgements

The six-year stay in Stony Brook University is a precious treasure in my life. It is my pleasure to thank all the faculty, staff and students in Geosciences Department for building a wonderful research environment and making this dissertation possible.

I would like to express my deepest gratitude to my dissertation advisor: Lianxing Wen. He has been inspiring and encouraging me to pursue a career in geophysics study, providing a thoughtful guidance and been very supportive in every way during my study. I could not have wished a better advisor. In the same vein, I want to thank Chen Ji, who has supervised me when I was developing my multiple source inversion method and writing my first paper. Without his support, this dissertation would not be possible. I am grateful to the other members of my dissertation committee, William Holt, Donald J. Weidner and Baosheng Li, for spending time to read my dissertation and discuss the dissertation with me. I benefit from the discussion and assistances from my lab colleagues, Yi Wang, Hui Long and the visiting scholars. I would like to thank the students in Geosciences department, especially Michael Thorpe for their help to improve the dissertation.

In the end, I would like to thank my family. Their love and unmoved faith in me is the source of my energy and confidence, and have walked me through all the difficult times.

Chapter 1 General Introduction

1.1. What are deep earthquakes?

Deep earthquakes were first discovered in the 1920s through determining S-P differential time (Wadati, 1928), and defined as the earthquakes occurring deeper than 60 km (Wadati, 1929). Deep earthquakes were then classified into two groups, intermediate-focus (60 - 350 km) and deep-focus (350 - 700 km) earthquakes (the allocated depths may vary in different literature), based on the global bimodal distribution of earthquake focal depths (Fig. 1-1a). The earthquake rate decreases exponentially between 60 and 300 km, increases beneath 450 km, reaches a maximum at ~600 km, and ceases abruptly at ~700 km.

Intermediate-focus earthquakes are usually associated with the plate boundaries and active volcanism (red dots in Fig. 1-1b). Most of the intermediate-focus earthquakes are distributed along mid-ocean ridges and subduction zones, whereas deep-focus earthquakes are more concentrated in subduction zones (blue dots in Fig. 1-1b). About two third of deep-focus seismicity occurs within the Tonga-Kermadec Slab, while most of the other classes of earthquakes are located within Java, Philippine, Mariana, Japan, Kuril, Central American and South American Slabs. The slabs listed above are currently active. A small portion of deep-focus earthquakes may be linked to ancient slabs (e.g. the earthquakes beneath Spain-Morocco region).

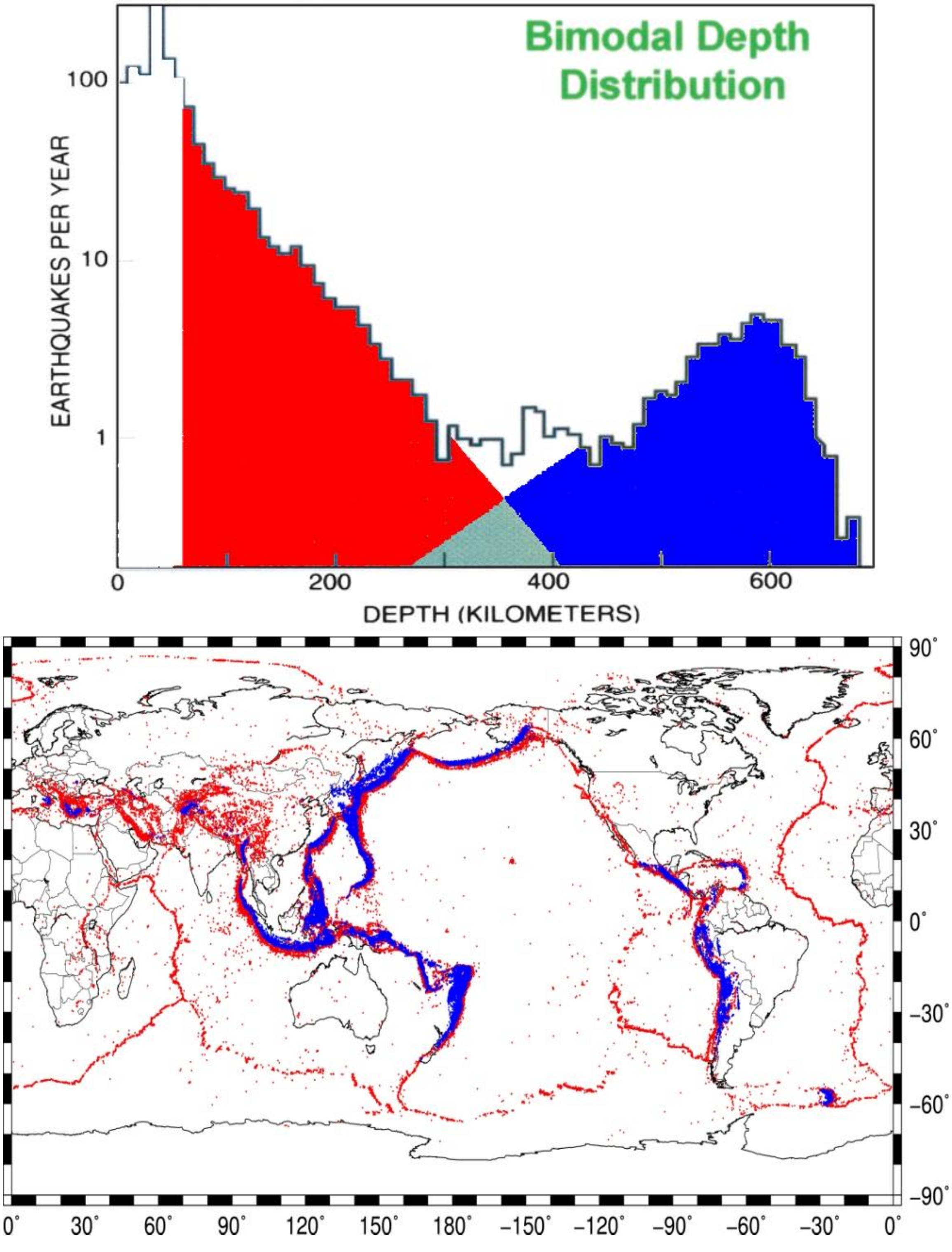

Fig. 1-1. (a) Depth distribution of deep earthquake occurrence (figure modified from Green, 2007). (b) Geographic distribution of intermediate- (red dots) and deep-focus (blue dots) earthquakes (ISC EHB database from 1994 to 2008).

1.2. Physical mechanisms proposed for deep earthquakes

Earthquakes below 60 km are unexpected, where the pressure would strongly inhibit brittle failure and the temperature would result in ductile deformation (Scholz, 2002). It suggests that deep earthquakes cannot be explained by the same mechanism as shallow earthquakes. However, double couple radiation patterns from deep earthquakes exhibit that deep earthquakes are in fact not fundamentally different from shallow earthquakes.

The origin of deep earthquakes remains enigmatic. A wide variety of physical models have been invoked to explain the unexpected occurrence of deep earthquakes. We summarize the models as three major categories, dehydration embrittlement (Jung et al., 2004; Meade and Jeanloz, 1991; Raleigh and Paterson, 1965), transformational faulting (Green and Burnley, 1989; Green and Houston, 1995; Kirby, 1987), and shear thermal instability (Hobbs and Ord, 1988b; Karato et al., 2001; Kelemen and Hirth, 2007; Ogawa, 1987). These mechanisms may cause or trigger deep earthquakes. A combination of different physical mechanisms is also proposed to explain deep-focus earthquakes (Green, 2007; Meng et al., 2014; Zhan et al., 2014a).

Laboratory experiments and detailed calculations of the pressures and temperatures in subduction zones indicate that, deep earthquakes may be triggered by embrittlement accompanying dehydration of serpentine when it reaches critical conditions, in the hydrated part of the lithosphere that sinks into the upper mantle (Meade and Jeanloz, 1991; Raleigh and Paterson, 1965). Raleigh and Paterson (1965) performed high-temperature and high-pressure experiments on the Cabramurra serpentinite and observed a brittle type of failure at 600 and 650°C, where ductility might normally be expected (Fig. 1-2). Meade and Jeanloz (1991) detected acoustic emission during dehydration of serpentinite in experiments for pressures up to 9 GPa (Meade and Jeanloz, 1991). The recent experimental observation further suggested that dehydration embrittlement is a viable mechanism to nucleate intermediate-focus earthquakes independent of depth, not restricted to conditions where the total volume change of reaction is positive or negative (Jung et al., 2004). Seismological observations of double seismic zones of intermediate-focus earthquakes are potentially explained as the result of dehydration include antigorite and chlorite in hydrous peridotite (Brudzinski et al., 2007; Peacock, 2001). However, it is unclear if the water content below the 400 km depth can support this mechanism (Green et al., 2010).

Transformational faulting mechanism hypothesizes that a meta-stable olivine wedge can exist in cold slabs, and the phase transformation can lead to catastrophic earthquake failure (Green and Houston, 1995; Kirby et al., 1996). Numerical simulations show that the olivine to spinel transformation should be kinetically hindered in old and cold slabs descending into the transition zone (Fig. 1-3a), and seismological evidences also suggests that the meta-stable wedges may exist in some specific slabs (Iidaka and Suetsugu, 1992; Wiens et al., 1993). Laboratory deformation experiments show that under meta-stable conditions, some minerals partially transform to a high-pressure denser phase by localization of transformation and strain into thin shear zones (Kirby et al., 1996). Anti-crack theory is further proposed that, the meta-stable olivine transforms to the spinel structure and filled in the lens-like cracks under the compressive stress (Fig. 1-3c), analog to the crack open by tensile stress in shallow depth (Fig. 1-3b). During rapid anti-cracks grow, sufficient heat is released by the exothermic reaction to raise the local temperature and causes the reaction rate to increase; and the positive feedback between reaction rate and temperature incites a thermal runaway that causes the fault to grow catastrophically (Fig. 1-3d) (Green and Burnley, 1989; Green and Houston, 1995).

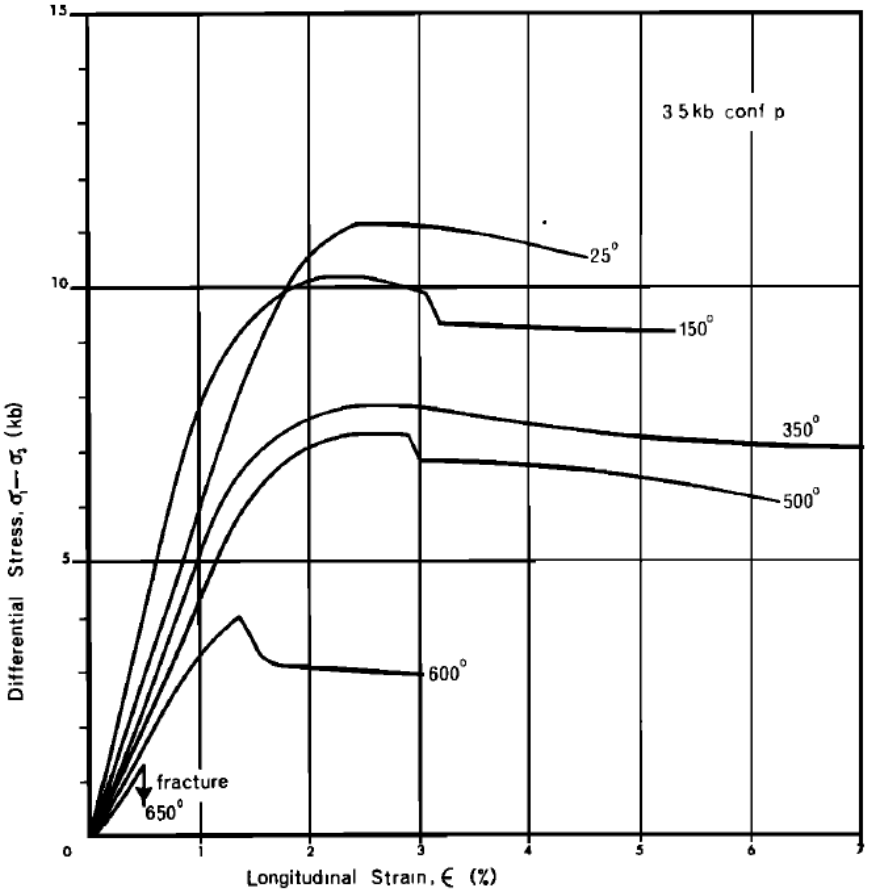

Fig. 1-2. Stress-strain curves at various temperature and 3.5 kbar confining pressure for Cabramurra serpentinite (Raleigh and Paterson, 1965).

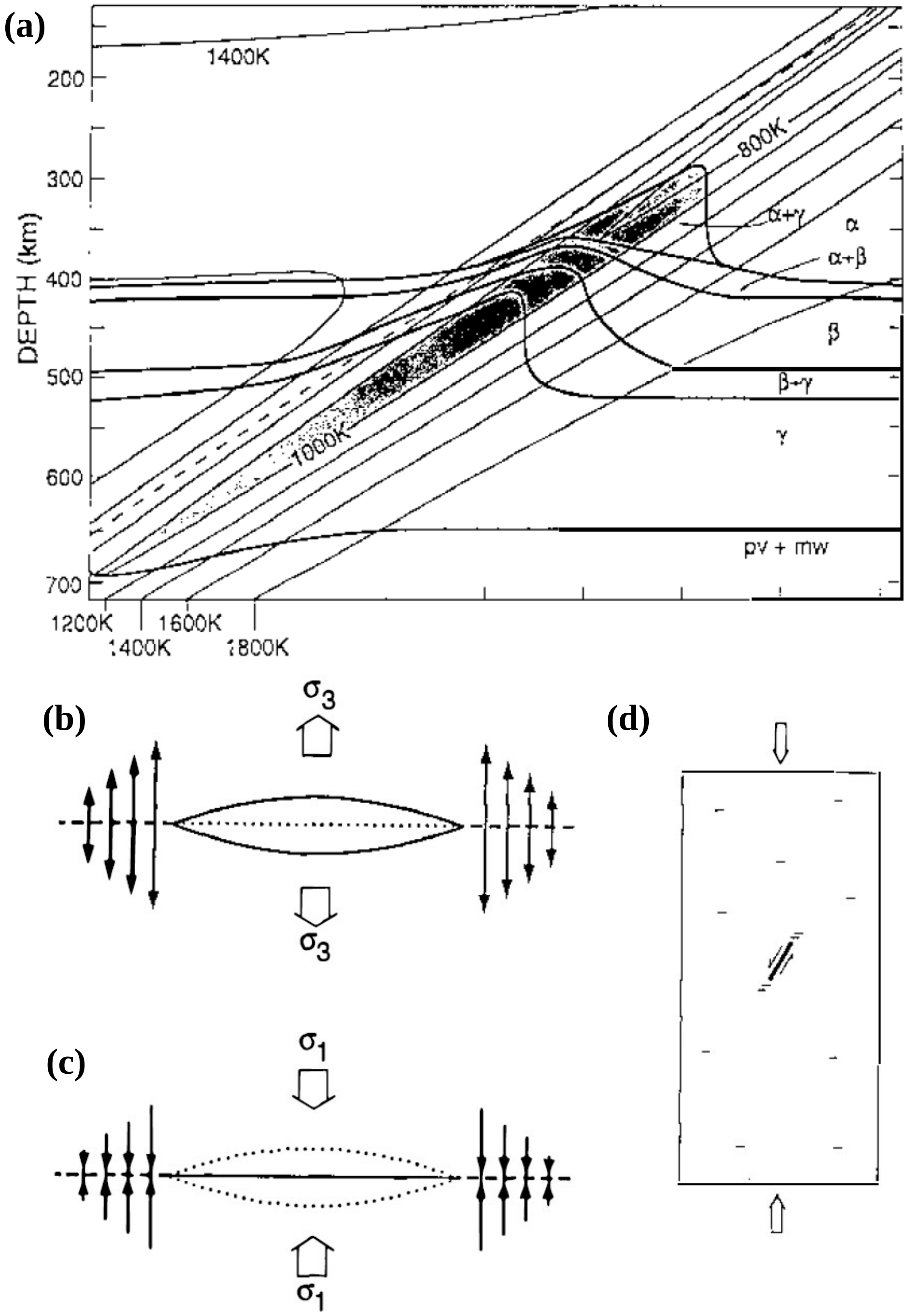

Fig. 1-3. (a) Thermal model of cold subducting slab showing isotherms and phase relations for mantle olivine. Stipple region within the 1000 K isotherm represents a wedge containing meta-stable olivine that is potentially present due to thermal inhibition of reactions. (b) A small planar flaw in a solid (dotted line) is pulled open by a remote tensile stress, yielding a lens-shape void with tensile stress concentration at its tip. (c) A small lenticular void (dotted) in a solid is pushed close by a remote compressive stress, yielding a compressive stress concentration at its tip. Growth of a denser phase with the geometry produces a similar stress pattern. (d) Transformation-triggered faulting with “process zone” of anti-cracks. (Green and Houston, 1995)

Shear thermal instability suggests that rapid deformation can be achieved when a stress or temperature perturbation promotes a positive feedback between shear heating and temperature-dependent rheology (Fig. 1-4) (Hobbs and Ord, 1988b; Kelemen and Hirth, 2007; Ogawa, 1987). Shear thermal instability can occur in a viscous medium with a uniform rheological property, which depends strongly on the stress in the slabs, but does not depend on the detail of the creep law (Ogawa, 1987). The instability may also occur in a pre-existing zone of different rheological properties with a lower threshold of strain rate (Ogawa, 1987). The pre-existing weak zone is known to exist within the subducted slab, due to either past faulting before subduction (Jiao et al., 2000; Silver et al., 1995) or existence of preexisting fine-grained shear zones (Kelemen and Hirth, 2007). Kelemen and Hirth (2007) further suggested that a quasi-periodic series of a fine-grained, viscous olivine shear zone in a course-grained elastic half space, can produce a quasi-periodic series of shear instabilities, with initial temperatures from 600-800˚C (coinciding with the environment of intermediate-focus earthquakes). Such feedback within a system is naturally influenced by perturbation of stress.

In this study, we are going to concentrate on deep-focus earthquakes. Therefore, we will focus on the discussion of transformational faulting and shear thermal instability in the following sections.

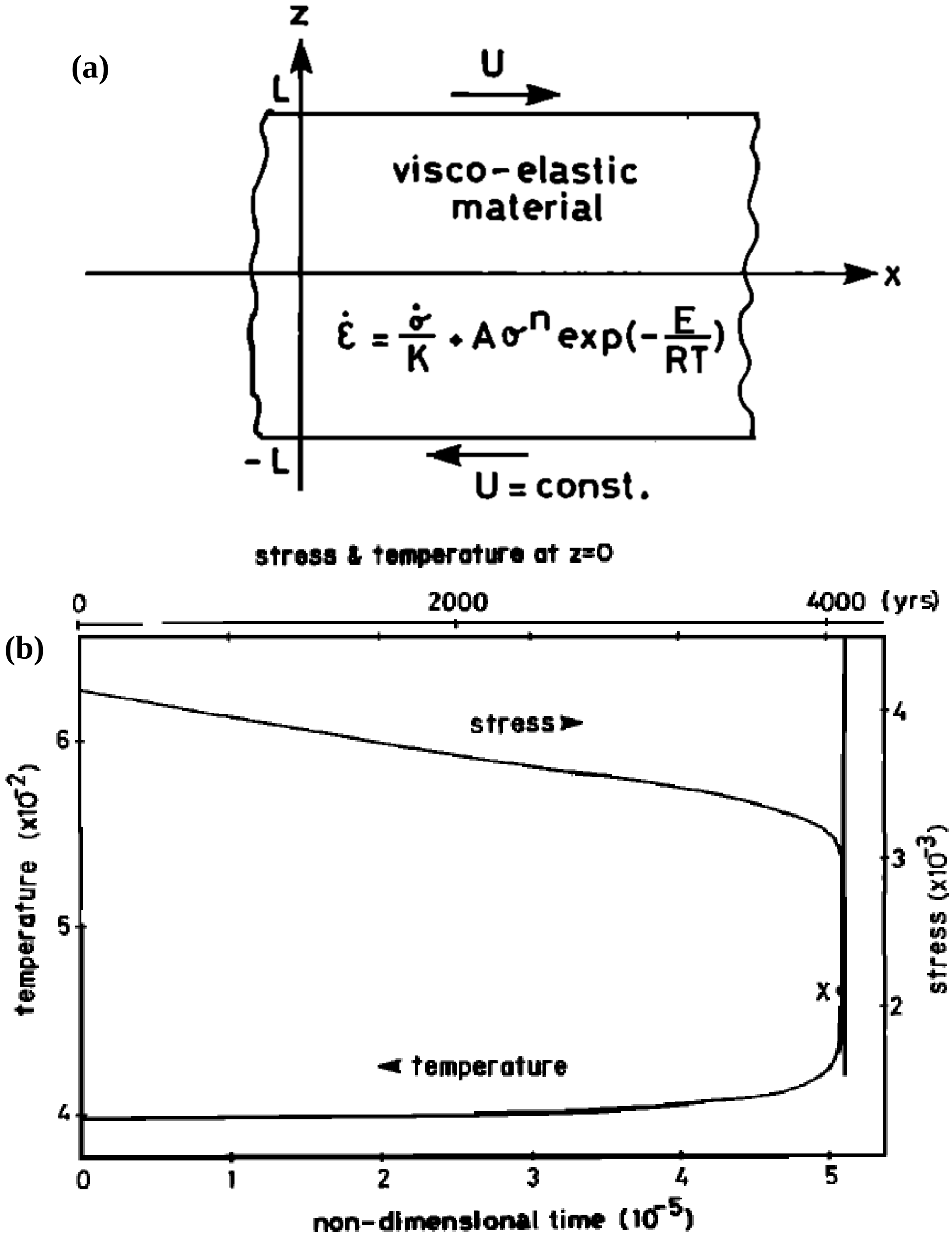

Fig. 1-4. (a) Illustration of shear instability model. (b) Changes in the stress and the temperature when shear instability occurs.

1.3. Seismological studies

Since the transition zone was first discovered, it is natural to relate deep-focus earthquake to phase transformation at the depth range of ~350 km to ~700 km. An isotropic implosive component has long been sought as a manifestation of the volumetric change associated with phase transformation in the slab (e.g. Frohlich, 2006). However, systematical analysis of deep-focus earthquakes shows that no significant isotropic component exists. A sudden implosive phase change can thus be ruled out as the primary physical mechanism for deep earthquakes (Kawakatsu, 1991).

CLVD (Compensated linear vector dipole) has also been investigated for deep earthquakes. CLVD component can be interpreted in three ways, including volume preserving phase transformation, fluid filled tensile cracks, and the sum of suitable double couple (Frohlich, 2006). Significant CLVD components were observed for intermediate- and deep-focus earthquakes (Kuge and Kawakatsu, 1993), and the CLVD components are explained by source irregularities (i.e. summation of double couples) (Kuge and Kawakatsu, 1990; Kuge and Kawakatsu, 1992; Kuge and Lay, 1994).

Whether deep earthquakes fault in new-generated fault or pre-existing weak zone provides additional constraint on the physical mechanisms. Jiao et al. (2000) studied the statistical distribution of fault plane orientations in Tonga subduction zone by using fault plane solutions, and found that an asymmetric fault system persists in the slab down to 450 km, which is consistent with those of outer rise earthquakes in the oceanic plate prior to subduction. They suggested that the intermediate-focus earthquakes (defined above as 450 km) are caused by the reactivation of pre-existing fault zones created in the oceanic plate down to this depth, while deep-focus events may be owing to new-generated faulting or pre-existing weak zones, probably suggesting a change of mechanism or loss of slab integrity. Rupture directivity was also analyzed to determine fault plane orientations of deep earthquakes occurring in the Tonga-Kermadec subduction zone (Myhill and Warren, 2012; Warren et al., 2007; Warren et al., 2008). Intermediate-focus (100 km – 300 km) earthquakes prefer sub-horizontal fault plane, consistent with a downdip compressional stress, suggesting a new-generated fault system. However, both sub-horizontal and sub-vertical fault planes are detected for deep-focus earthquakes, corresponding to a complex rupture system with either a reactivated or newly generated fault system (Warren et al., 2007).

Rupture velocity is an important source parameter, which is mostly from 0.2 to 1.2 times of the S wave velocity in the source region (e.g., Frohlich, 2006). Previous studies also suggested that rupture velocity depend on slab temperature. Earthquakes within a warmer slab may be related to a lower rupture propagating velocity (Tibi et al., 2003a; Wiens, 2001). Super-shear rupture was also reported for an Mw 6.7 aftershock of the Okhotsk earthquake (Zhan et al., 2014b).

Aftershock distributions are also utilized to determine the fault geometry and extension (Tibi et al., 2001; Wiens, 1998; Wiens et al., 1994). An extensive aftershock sequence was observed after the 1994 Mw 7.7 Tonga deep-focus earthquake. Most of the well located aftershocks were concentrated along a steeply dipping plane consistent with sub-vertical fault plane of focal mechanism of the main-shock and three large aftershocks. The aftershocks define a 50 x 65 km fault plane extending across the entire width of the meta-stable olivine wedge, probably excluding the physical mechanism of transformational faulting (Wiens et al., 1994).

Studies of source processes of large deep-focus earthquakes provided significant insights on deep-focus earthquake mechanisms. A number of large deep earthquakes, especially the 1994 Mw 8.2 Bolivia and 2013 Mw 8.3 Okhotsk deep earthquakes, have also been studied by multiple source inversion (Chen et al., 2014; Silver et al., 1995; Zhan et al., 2014a) and finite fault inversion (Antolik et al., 1996, 1999; Estabrook, 1999; Wei et al., 2013; Ye et al., 2013). The source processes of these two largest ever-recorded deep earthquakes provided particularly important insights on the physical mechanisms. Both the Bolivia earthquake (Silver et al., 1995; Zhan et al., 2014a) and the Okhotsk earthquake (Wei et al., 2013; Ye et al., 2013) were determined to have a large source region that totally cut out of the assumed meta-stable olivine zone, seemingly excluding the transformation faulting as a possible mechanism. The source parameters of the Bolivia earthquake suggest a high stress drop and a low seismic efficiency. The amount of non-radiated energy was sufficient to have melted a layer as thick as 31 centimeters. (Kanamori et al., 1998).

1.4. Objectives

The past studies have provided important constraints on the physics of deep-focus earthquakes. However, several issues remain to be resolved. 1. Do deep-focus earthquakes rupture in a fault plane? 2. Do deep-focus earthquakes behave the same between hot and cold subducted slabs? 3. How do deep earthquakes initiate? 4. Is there a unified mechanism to explain all the seismic results?

In this study, we develop a multiple source inversion method based on modeling direct and near-surface reflected waveforms presented in Chapter 2. We investigate the source process of the 24 May 2013 Mw 8.3 Okhotsk earthquake as an example in Chapter 3. We further study the major sub-events of 26 global large deep-focus earthquakes with Mw > 7.0 and depth > 400 km, and suggest cascading failure of shear instability in pre-existing weak zones in Chapter 4. We study source process and stress drop of the weak initiation sub-events of 7 earthquakes in Chapter 5.

Chapter 2 Methodology

2.1. Multiple source inversion method

We apply a multiple point source inversion procedure to infer the source processes based on waveform fitting of direct phases P/SH and near-surface reflected phases pP/sSH (Chen et al., 2014). The method treats a large earthquake as a combination of multiple double couple point sources (sub-events) separated in space and time, and resolves the spatio-temporal separation and focal mechanism of each sub-event by modeling the seismic data. Each sub-event is represented by nine parameters: seismic moment, seismic duration (the width of the source time function represented by a half sine function), strike, dip and slip for focal mechanism, *dt* for time separation of origin time from the initiation time, and *de*, *dn* and *dz* for distance separations from the initiation point in east-, north- and vertical-direction, respectively. Seismic Green's functions are computed by the Generalized Ray Theory method (Helmberg, 1968), based on the velocity and attenuation structures of PREM (Preliminary Reference Earth Model, downloaded from IRIS EMC-PREM) (Dziewonski and Anderson, 1981). The seismic response of each sub-event is obtained by convolving the Green's function with source time function (Ji et al., 2002).

The number of sub-events (N) relies on manual inspection. Typically, one needs to visually examine the move-outs of energy packets in the seismic waveforms to determine an initial guess of the sub-event number, locations and depths. The 9×N (N, number of sub-events) model parameters are searched by the simulated heat annealing algorithm for the best-fitting solution that generate the least root-mean-square residual (L2 norm) between the seismic data and synthetic waveforms (Chen et al., 2014). In Chapter 5, we define the objective function as L2 norm plus correlative function for pP waves to better capture the arrival times of the initiation sub-events, because the amplitudes of the pP synthetics cannot match the data quite well in some specific azimuths.

We align broadband P phases by the first arrival onsets, which can be clearly identified and picked in the high-pass filtered data above 1Hz. SH, pP and sSH phases are aligned iteratively in the inversion process: we first pick them based on IASP91 model (Kennett and Engdahl, 1991) and perform a preliminary inversion with P wave heavily weighted over other phases. The alignments of pP, S and sS phases are adjusted based on the best match between synthetics and the data during the inversions, until no further adjustment observed from the previous inversion. The final inversion weights each phase equally.

2.2. Importance for depth constraint by including the near-surface reflected waves

Most of previous studies inverted the source process using P waves only, which would have poor resolution in determining depth distribution of the seismic energy release during the earthquake, as the inferred depth of energy release trade-offs with the inferred occurring time of the energy release (Fig. 2-1). Combining pP wave with P wave data into the seismic inversion would place a tight constraint on the depth of seismic energy release, as pP waves take off from the opposite hemisphere of the source from the P waves (Fig. 2-1a).

We illustrate the necessity of combining P and pP waves to resolve the depth of propagating seismic energy release, using the following synthetic examples of a source consisting of two sub-events. We generate synthetics of sub-event 1 and a delayed sub-event 2 (black stars in Fig. 2-1b) at a group of hypothetical stations at different azimuths. We also generate synthetics for another sub-event 2 (red star in Fig. 2-1b) with a greater source depth and a delayed occurring time. These two sub-event 2s produce synthetics that exhibit only slight time offsets for P waves at various epicenter distances (Fig. 2-1c). These travel time differences are not resolvable in the real data inversion. However, the deeper sub-event 2 (red star in Fig. 2-1b) generates travel time delays of pP wave up to 3 s (red traces in Fig. 2-1d) in comparison with the shallower sub-event 2 (black star in Fig. 2-1b), since the deeper source has a longer path for pP wave. The above example indicates that combining direct waves and near-surface reflected waves is critical for resolving source distribution in depth.

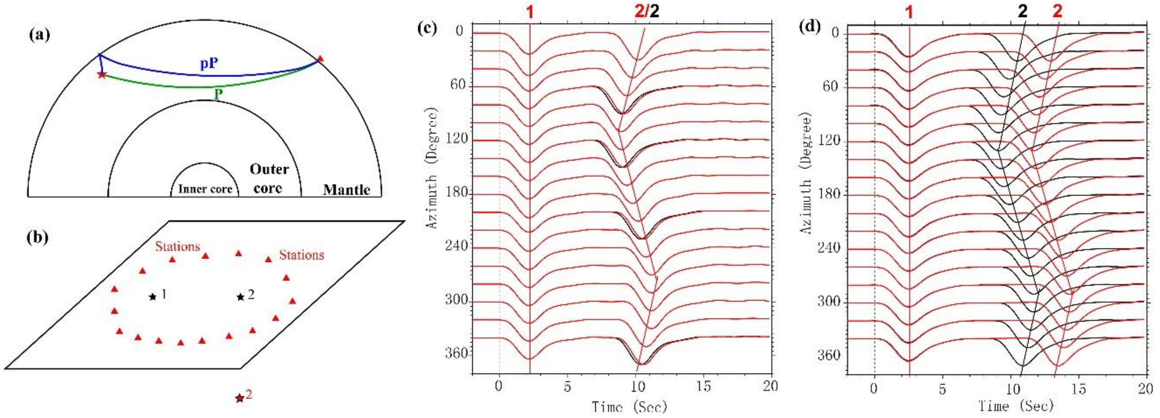

Fig. 2-1 (a) Ray paths for P (green path) and pP (blue path) waves from earthquake source (star) to a seismic station (triangle). (b) Sub-event 1 (black star), sub-event 2s (red and black star) and stations (red triangles) used for synthetics calculations (sub-event 2 in red is located 20 km deeper, but with a 1.5 s later occurring time than sub-event 2 in black). (c) P synthetics generated using a source that consists of sub-event 1 and sub-event 2 in black in (b) (black traces) and a source that consists of sub-event 1 and sub-event 2 in red in (b) (red traces). The pulses of two sub-events are labeled accordingly with their numbers. (d) Same as (c), except for pP synthetics.

2.3. Resolution tests

2.3.1. Resolvability of sub-events

We perform a model resolution test with a synthetic earthquake. We use our expected source model of the 2013 Mw 8.3 Okhotsk earthquake (Table 2-1) and the station distribution (Figs. 2-2a, 2-2b) for the 2013 Mw 8.3 Okhotsk earthquake. Noise is added to the synthetics, taken from the observed noise before the earthquake and normalized to 5% maximum amplitude of the synthetic waveforms similar to the noise level in the seismic data. The inverted model is presented in Table 2-2 and the waveform fitting is showed in Fig. S2-1. In the test, the starting parameters are estimated based on the directivity analysis as in Chapter 3, and their searching ranges are as follow: strike, dip and slip are within ±30°, *dt* within ±3 s, and *de*, *dn*, *dz* within ±30 km from the test model. The bounds for source duration and moment are 50% deviated from the test model.

The inversion results show that the inversion procedure can recover the focal mechanisms and locations of sub-events 1-4 (Tables 2-1, 2-2). The uncertainty is ±2° for each focal parameter, ±0.5 s for *dt* and ±4 km for location. The procedure also recovers the total moment to be 3.53×10^{28} dyn-cm, 5% lower than 3.71×10^{28} dyn-cm of the test model. The obtained moments for the individual sub-event trade-off each other because the energy of those sub-events overlaps in time at most of the stations. Our inversion results further indicate that the focal mechanism of the first initiation sub-event (sub-event 0) has a larger error, as its energy is at least one-order of magnitude smaller than the others.

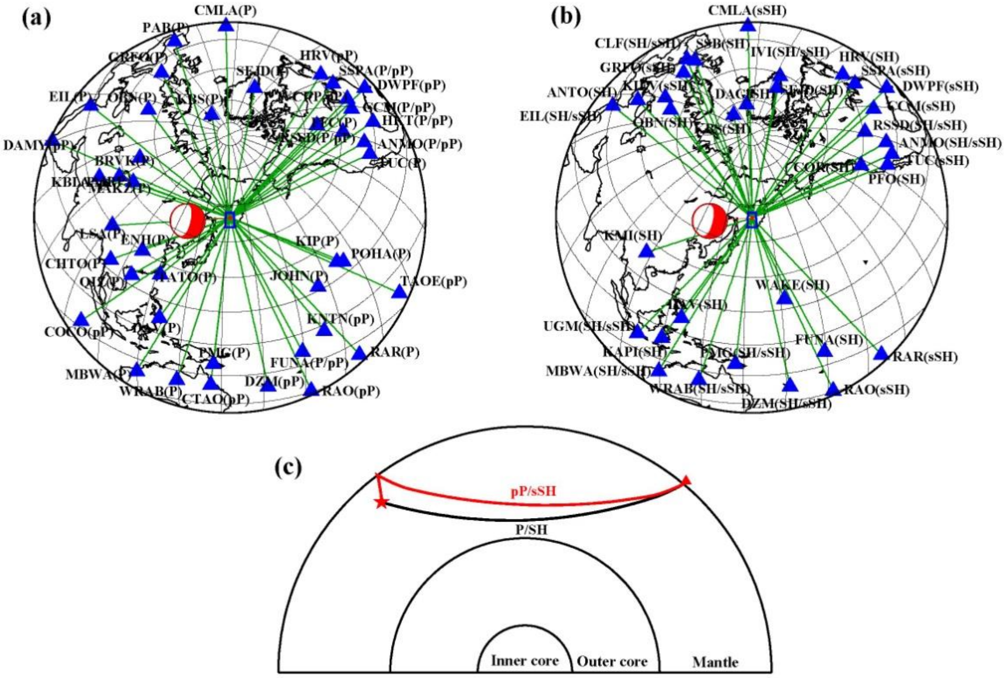

Fig. 2-2 and pP waves and (b) SH and sSH waves. Blue triangles represent seismic stations, labeled with station name and seismic phase used. Red rectangle is the studied area with the seismic result presented in Fig. 3-4. Red beach balls describe GCMT focal mechanism of the mainshock (c) Ray. (a, b) Location of the 24 May 2013 earthquake (red dots) and seismic coverage of (a) P paths for direct phases P/SH (black path) and near-surface reflected phases pP/sSH (red path) from earthquake source (star) to a seismic station (triangle) at an epicentral distance of 80˚.

Table 2-1. Source parameters of inverted six sub-events of 24 May 2013 Earthquake

Sub-event	dt (s)	dn (km)	de (km)	dz (km)	duration (s)	moment (dyn-cm)	strike (°)	dip (°)	slip (°)
0	0	0	0	0	3	3.0E+26	8.9	87.7	278.0
1a	1.7	4.3	4.6	1.1	12.0	6.8E+27	13.7	85.2	278.1
1b	7.8	-6.2	8.5	0.1	12.0	6.6E+27	23.3	86.6	263.6
2	12.0	-44.9	15.7	16.7	9.0	7.4E+27	4.0	76.3	282.3
3	16.2	-21.8	10.1	4.2	11.8	8.2E+27	17.6	85.4	256.4
4	22.5	-57.8	15.4	35.4	12.0	7.9E+27	-5.7	69.5	272.4

Table 2-2. Source parameters of the inversion of the synthetic model (Table 2-1)

Sub-event	dt (s)	dn (km)	de (km)	dz (km)	duration (s)	moment (dyn-cm)	strike (°)	dip (°)	slip (°)
0	0	0	0	0	2.8	2.1E+26	-2.1	88.1	283.8
1a	1.8	4.3	1.7	1.4	12.0	6.5E+27	13.2	86.0	278.5
1b	8.0	-5.4	6.1	-0.4	11.2	5.9E+27	23.2	84.8	263.0
2	11.9	-44.6	16.9	15.9	8.9	7.4E+27	4.6	77.4	283.0
3	16.1	-20.0	8.9	4.9	12.0	8.0E+27	17.5	85.0	254.4
4	22.7	-58.0	19.1	37.2	11.3	7.3E+27	-6.5	69.6	272.3

2.3.2. Effectiveness of the iterative procedure of picking pP, SH and sSH arrival times

We perform a test on the effectiveness of the iterative procedure of picking arrival time of pP, SH and sSH phases under the situation of large initial match of phase arrival time, variation of waveform shape due to large attenuation variation, interference of an additional phase generated by possible multi-path effects of wave propagation due to complex seismic structures, and noise. We test on the synthetics for the best-fitting model of E19 as an example (Table 2-3). To simulate the effects of lateral change of velocity structure and attenuation, for the synthetics of the best-fitting model, we shift pP, S and sS waves randomly within 5 s, convolve the effect of attenuation for attenuation values perturbed randomly with 0.5 – 2 times of PREM values, superimpose an additional phase with a 50% amplitude of the initial synthetics 2 s after the arrival time of the main phase for 3 pP (SCZ, RPN, PAF) and 2 sSH (MIDW, SCZ) waveforms, and add random noise with 10% of the amplitude of the initial synthetics (black dash traces in Fig. S2-2). We apply the same procedure of multiple source inversion on the altered synthetics and iteratively picking of pP, SH and sSH waves during inversions. The arrival time of each seismogram is not further adjusted after five iterative inversions. The inverted model produces synthetic seismograms (black traces in Fig. S2-2) that align well with the original unaltered synthetics (red traces in Fig. S2-2), indicating the effectiveness of the iterative procedure in aligning the pP, SH and sSH phases.

Table 2-3. Source parameters of inferred sub-events of E19 in Chapter 4

Sub-event	dt (s)	dn (km)	de (km)	dz (km)	duration (s)	Mw	strike (°)	dip (°)	slip (°)
1	2.9	2.9	9.8	-2.8	3.4	7.0	46.1	71.6	261.9
2	6.0	12.1	12.8	-5.0	3.6	6.8	50.7	78.8	257.8
3	7.6	19.9	20.7	-28.8	5.8	6.9	78.1	59.9	200.4

2.3.3. Improved constraint on the focal mechanisms of sub-events by combining pP, SH and sSH phases

In the teleseismic distances, P waves take off in the lower hemisphere of the source region. Incorporating pP, SH and sSH observations would also improve the resolution of the focal mechanism inversion of the sub-events. We show such improvement in an example using the synthetics of the best-fitting model of E19 in Chapter 4 (Table 2-3) in the presence of noise, and waveform distortion. We invert focal parameters for the cases of using 1) P waves only, 2) P and pP waves, 3) P + pP + SH waves and 4) P, pP, SH and sSH waves. The uncertainties of focal parameter estimate are 10°, 6°, 5° and 5°, for cases from 1 to 4 respectively, indicating the improvement of the focal mechanism solution when constraints from additional phases are added.

2.3.4. Little trade-off between sub-event focal mechanism and location

We test trade-offs between sub-event focal mechanism and location using the synthetics of the best-fitting model of E19 in Chapter 4 (Table 2-3). We compel the first sub-event away (moving north) from its best-fitting location and invert the other parameters. When the distance of sub-event 1 is moved away from its best-fitting location by 5 km, the misfit of the synthetic data and synthetics of the testing source model becomes unacceptable (> 0.25%) (Fig. 2-3), and the waveform misfits appear around stations in the azimuths of 0° and 180° (Fig. S2-3). Within this maximum allowable difference of location (5 km), the difference of the inverted focal parameters and the best fitting model is ±1° (Table 2-3). We thus conclude that trade-offs are minor between focal mechanism and location of the sub-events in our inversions.

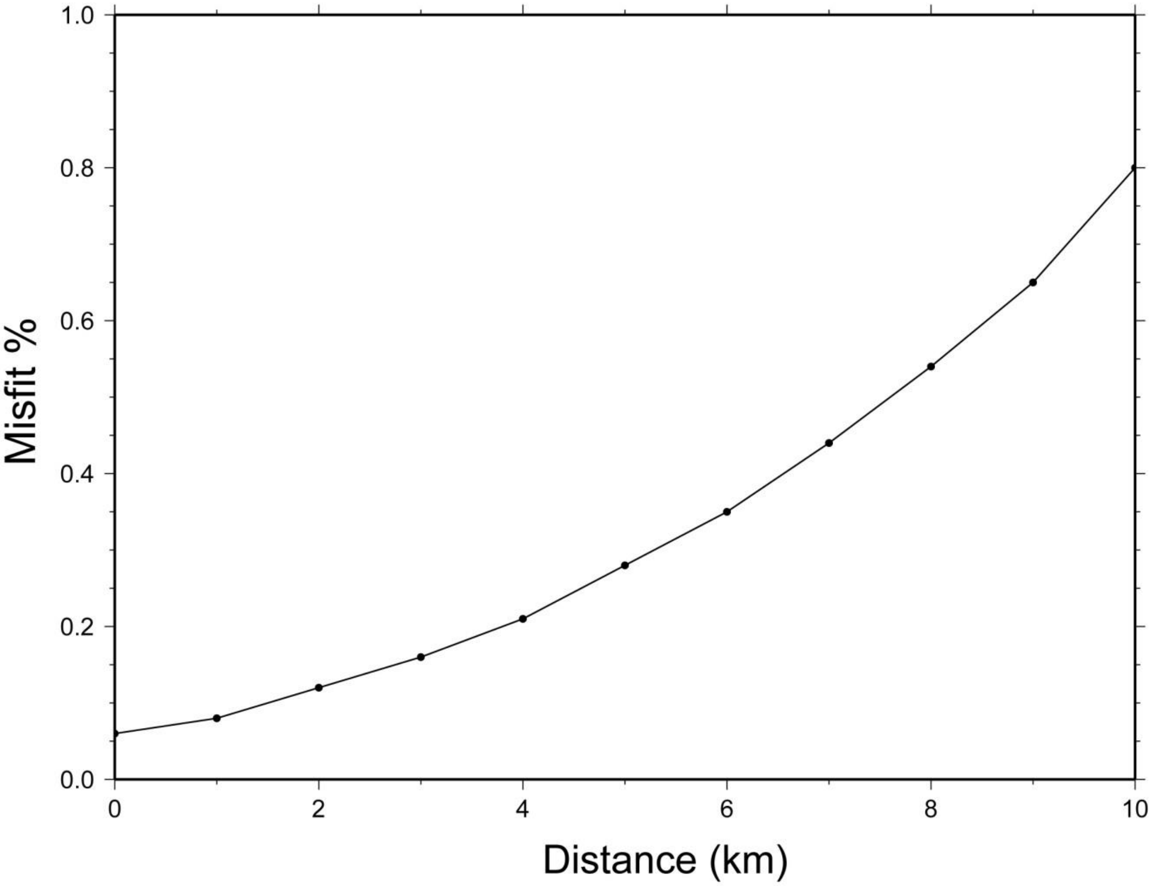

Fig. 2-3. The misfits (RMS) of amplitudes between the synthetics predicted by the best-fitting model, and the synthetics predicted by the inferred model with sub-event 1 moved 0 – 10 km away from it best-fitting location.

2.3.6. Effects of high frequency content

In this study, we use the data band-passed between 0.01 and 4 Hz. Data in such frequency band would allow excellent reading of P wave onsets. However, we should point out our model features are mainly constrained by the seismic energy in the lower frequency band. Take E20 in Chapter 4 as example, the event has the largest high-frequency energy among others and the seismograms look ‘noisy’ at the second portion of the seismogram which cannot be modeled well (Fig. S4-19), as we mention in E20 of the SI. But such high frequency energy did not affect the inversion results. We show the comparisons of the data and the synthetics of the best-fitting model, low-passed filtered to 0.5 Hz. Note that the energy associated with all the sub-events is clearly visible in the lower frequency data and synthetics (Fig. S2-4). We conclude that the high-frequency energy of the seismic data did not produce artifacts in our inversion results.

Chapter 3 A Cascading failure of the 2013 Great Okhotsk earthquake

3.1. Abstract

On May 24 2013, the largest ever-recorded deep earthquake occurred beneath Sea of Okhotsk. A multiple source inversion procedure is applied to constrain source process of this earthquake, based on waveform modeling of both direct P and SH waves and near-surface reflected pP and sSH waves. Our results indicate that the earthquake consists of six major sub-events separated in space and time, encompassing a horizontal dimension of ~60 km along ~N160°E and a downward depth extension of ~35 km. The geographic distribution and focal mechanisms of the inferred sub-events and fore/aftershock locations do not fit into plane rupture. We suggest that the earthquake can be best explained by a cascading failure of shear instability within pre-existing weak zones in the region, with the perturbation of stress generated by a shear instability triggering another.

3.2. Introduction

The occurrence of deep-focus earthquakes remains enigmatic, because the pressure in the upper mantle would strongly inhibit brittle failure and the temperature would result in ductile deformation (Scholz, 2002). Three physical mechanisms have been put forward, including dehydration embrittlement (Jung et al., 2004; Meade and Jeanloz, 1991), shear thermal instability (Green, 2007; Hobbs and Ord, 1988a; Kanamori et al., 1998; Kelemen and Hirth, 2007; Meade and Jeanloz, 1989; Ogawa, 1987) and transformational faulting (Green and Houston, 1995; Kirby, 1987; Kirby et al., 1996; Wiens et al., 1993).

Studies of the source processes and aftershock distributions of major deep earthquakes provided important constraints on the deep earthquake mechanisms. For example, seismic studies of the 1994 Mw 8.2 Bolivia earthquake, the largest deep earthquake before the occurrence of 2013 Mw 8.3 Okhotsk earthquake, suggested a large near-horizontal fault plane with its lateral extension exceeding the width of the metastable olivine (Antolik et al., 1996; Silver et al., 1995; Zhan et al., 2014a). The study of seismic efficiency of that earthquake also proposed possible melting during the earthquake (Kanamori et al., 1998). The aftershock sequence of the 1994 Mw 7.6 Tonga deep earthquake suggested rupture propagating in a direction normal to the expected metastable olivine wedge and over a distance too large to fit within the expected dimensions of the wedge (Wiens et al., 1994). On the other hand, some studies have suggested seismological evidence for the existence of metastable olivine wedge (Wiens et al., 1993). And, the observations of a broad peak in seismicity between 300 and 530 km (Estabrook, 2004) and major deep-focus earthquake moment releasing in the slab core (Antolik et al., 1999) suggested that the transformational faulting may play an important role in cold slab.

The 24 May 2013 deep earthquake occurred beneath Sea of Okhotsk, with a moment magnitude of $M_W = 8.3$ in the Global Centroid Moment Tensor (GCMT) solution and a hypocenter depth of 598 km reported by the United States Geological Survey (USGS). The earthquake is also reported to have a near-horizontal rupture with a great dimension (Wei et al., 2013; Zhan et al., 2014a), low stress drop and a heterogeneous rupture with pre-existing weak zone (Ye et al., 2013). However, only direct P wave observations have been used in these studies to constrain the rupture process of this earthquake. In this study, we constrain the source process of this earthquake based on waveform modeling of direct P and SH waves and near-surface reflected pP and sSH waves. Using all these types of seismic waves allows the source process of this earthquake better constrained, especially the depth extent of seismic energy propagation. In fact, our results would show that the earthquake rupture does not fit into a single plane. We present seismic data in section 3.3, directivity analysis of seismic waves in section 3.4, multiple source inversion in section 3.5, fore/aftershocks relocation in section 3.6, model resolution tests in section 3.7 and our preferred physical mechanism in section 3.8.

3.3. Seismic data

The earthquake is well recorded by the Global Seismographic Network (GSN). A total of 33 broadband compressional wave (P), 17 near-surface reflected compressional wave (pP), 24 transversally polarized shear wave (SH) and 19 near-surface reflected transversally polarized shear wave (sSH) observations recorded at tele-seismic distances between 30° and 90° are selected (Figs. 2-2a, 2-2b, and ray paths in Fig. 2-2c). The selected data constitute good azimuthal coverage. As we will show, the combination of direct P and SH waves with the near-surface reflected pP and sSH waves (Fig. 2-2c) places tight constraints on the depth extent of seismic energy propagation. The displacement seismograms are deconvolved with their respective instrument responses and bandpass filtered between 0.01 and 4 Hz.

We align broadband P phases by the first arrival onsets, which can be clearly identified and picked in the data high-pass filtered above 1 Hz. pP, S and sS phases are aligned iteratively in the inversion process: we first pick them based on IASP91 model

(Kennett and Engdahl, 1991) and perform a preliminary inversion with P wave heavily weighted over other phases. The alignments of pP, SH and sSH phases are adjusted based on the best match between synthetics and data during the inversions.

3.4. Seismic source directivity

The propagation of seismic energy can be inferred from the seismic data, with the lateral direction and distance from the observed azimuthal waveform variation of P waves (Fig. 3-1), and the vertical extension and distance from jointly modeling the P and pP waves (Fig. 3-2). Using a plane wave approximation, the duration of the P or pP wave pulse observed at a station can be represented as:

$$T(Az,\Delta) = T_r - \delta L \cdot \cos(\theta - Az) \cdot P(\,\Delta) - \delta H \cdot \sqrt{\frac{1}{v^2} - p^2(\Delta)} \qquad \text{(3-1)}$$

where, Az and Δ represent the azimuth and epicenter distance relative to the station, v the P-wave velocity in the source region, T_r rupture duration. δL and δH the horizontal and depth offsets of the rupture, θ the horizontal direction of the rupture, and p the horizontal slowness of P or pP wave.

The earthquake begins with a small amplitude phase with a duration of about 5 s, followed by strong moment release lasting 30 s. The observed P wave waveforms exhibit a strong azimuthal variation with four groups of major energy pulses during the strong moment release, discernible with different move-outs (time windows labeled 1 to 4, Fig. 3-1a). The azimuthal variation of the P wave data indicates that the seismic energy propagates along ~N160°E (the azimuth with the shortest duration of the P wave waveforms, Fig. 3-1a). The directivity can also be clearly seen from data pairs at different azimuths. We select three pairs of P wave data observed at similar epicentral distances but at opposite direction from the source (Fig. 3-1b). The first pair of P observations are from stations COR and CHTO roughly normal to the N160°E direction; both observations exhibit similar arrival times for all major pulses (top pair, Fig. 3-1b). The second pair are from stations FUNA and GRFO roughly parallel to N160°E. The arrival time differences of each group of energy almost reach the maximum in these opposite azimuths (middle pair, Fig. 3-1b). The third pair are from stations POHA and AAK oblique to the N160°E direction but roughly perpendicular to the strikes of GCMT nodal planes (13° or 191°). Each of the major groups of energy arrives earlier at station POHA (bottom pair, Fig. 3-1b). The azimuthal variations of the P wave data clearly indicate a lateral propagation of seismic energy along an azimuth of ~160°. It is also clear that the third group of energy exhibits a smaller move-out with respect to those of the second and fourth groups of energy, indicating that the third group of energy propagates backward to the opposite direction (Fig. 3-1a).

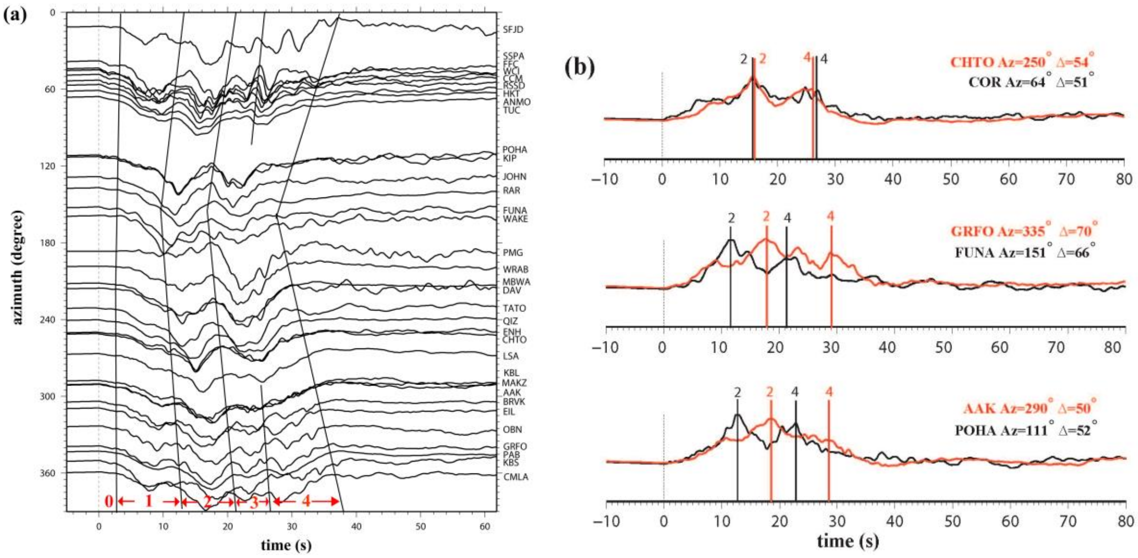

Fig. 3-1. (a) Observed vertical P displacement seismograms as a function of azimuth. Black lines divide the seismograms into four major energy pulses (labeled 1-4) and an initiation phase (labeled 0). Seismograms are aligned along the arrival onsets (t = 0 s), hand-picked from their high-frequency counterparts. (b) Overlays of P displacement seismograms observed at three station pairs in roughly opposite azimuths: (1) COR (Az=64°) vs CHTO (Az=250°); (2) FUNA (az=151°) vs GRFO (az=335°); (3) POHA (az=111°) vs AAK (az=290°). Seismic records are labeled with station name along with azimuth (Az) and epicentral distance (Δ). Energy pulses are marked in accordance with those in Fig. 3-1a. For display purpose, the polarities of some records have been flipped.

The pP waveforms exhibit similar azimuthal variation as the P waveforms (Fig. 3-2a), corroborating the inferred lateral propagation direction of various groups of energy based on the observed P waveforms. However, major groups of energy are delayed in pP waveforms than in P waveforms, and the duration of pP waveforms is about 7-8 s longer (Fig. 3-2a). We show five example pairs of P and pP seismograms observed at stations KBL, HKT, CCM, WCI and SSPA, to further illustrate this feature (Fig. 3-2b). Two reference times are marked in Fig. 3-2b, corresponding to the peaks of the second and fourth energy pulses in Fig. 3-1a. The second and fourth pulses exhibit 3-4 s and 7-8 s delays in pP waveforms than in P waveforms, respectively. The positive delays of different groups of energy observed in the pP waveforms than in P waveforms indicate the propagating of energy goes deeper, as a deeper source would make seismic energy arrive later in pP than in P. A 3-4 s delay of the second pulse and a 7-8 s delay of the fourth pulse in pP waveforms correspond to that the sources of the second and fourth pulses are about 15 - 20 km and 35 - 40 km deeper than the earthquake initiation point, respectively.

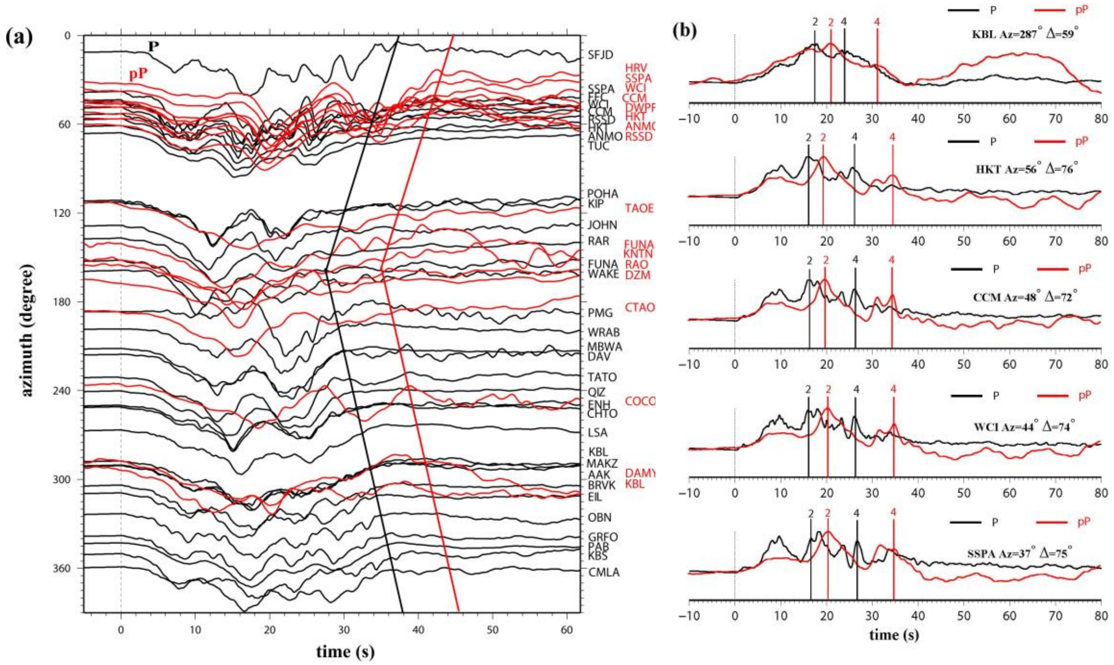

Fig. 3-2. (a) Comparison of observed P (black) and pP (red) displacement seismograms as a function of azimuth. The black and red lines indicate the ending time of P and pP data, respectively. (b) Overlays of P (black) and pP (red) displacements observed at five stations: KBL, HKT, CCM, WCI and SSPA. Seismic records are labeled with station name along with azimuth (Az) and epicentral distance (Δ). The black and red lines mark the maximal of the second and fourth groups of energy labeled in Fig. 3-1a. For display purpose, the polarities of some records have been flipped.

3.5. Multiple source inversion

Because the multiple source inversion is non-linear, we adopt a two-step inversion procedure. We first perform the inversion with four sub-events that correspond to groups of major energy in the observed seismograms. We then refine the data fitting with a six sub-event inversion and narrow down the search parameter ranges based on the four sub-event inversion results. In the first four sub-event inversion, the search focal parameters are ±30° from the CMT vertical plane (13°/79°/270°). The searching ranges for other parameters are ± 3 s for *dt*, ± 30 km for *dx*, *dy*, *dz*, and ± 50% for source durations and moments. In the second step of six-event inversion, we add sub-event 0 for the weak initiation onset and split sub-event 1 into two for better fitting directivity of the first main pulse (Fig. 3-1a). The search ranges for the parameters of the six sub-events are ±30° for focal parameters, ±2 s for *dt*, ±20 km for *dx*, *dy*, *dz*, and ± 50% for source durations and moments.

The inversion results in excellent waveform fitting between synthetics and seismic data for P, pP, SH and sSH waves (Figs. 3-3, S3-1). The inverted best-fitting six sub-events are showed in Table 2-1 and Fig. 3-4. The inverted source region has a horizontal extension of 64 km and a depth extension of 35 km. Sub-events 2-4 propagate downward along an azimuth of 155°-165°, while sub-events 1a and 1b exhibit bilateral propagation to northeast and southwest, respectively (Fig. 3-4). Sub-event 2 has a duration of 9 s and a peak moment rate at 16.5 s (origin time of the sub-event from the initiation plus half duration of the sub-event). And it is located about 45 km S160°E and 17 km down from the epicenter. Sub-event 3 has a duration of 12 s and a peak moment rate at 22 s, and it is located between sub-events 1 and 3, 24 km S155°E and 4 km deeper from the epicenter. Sub-event 4 is 58 km S165°E and 35 km deeper from the epicenter, with a duration of 12 s and a peak moment rate at 28.5 s. The focal parameters of sub-events 1-4 deviate about 20° from the GCMT solution. The focal mechanism of sub-event 0 is not well resolved, due to its moment release being at least one-order of magnitude smaller than other sub-events. The summation of the focal mechanisms of the inferred sub-events yields an overall focal mechanism of 10/80/270 (strike/dip/slip), similar to that reported for the mainshock in the GCMT solution (13/79/270). The predicted total moment is $3.7\text{x}10^{28}$ dyn·cm, slightly lower than $4.1\text{x}10^{28}$ dyn·cm in the GCMT solution.

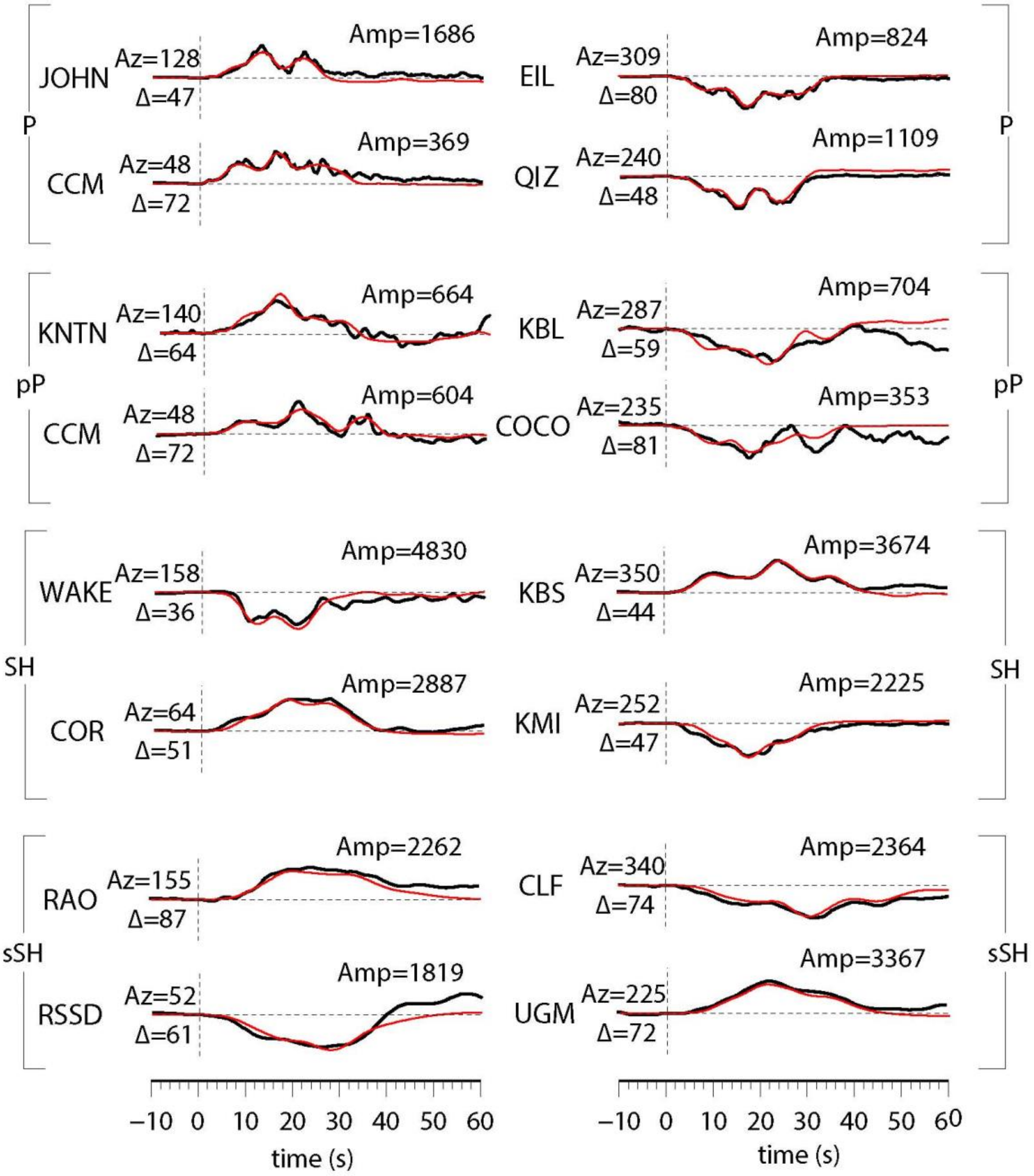

Fig. 3-3. Selected seismograms (black traces) comparing with synthetics (red traces) predicted based on the inverted six sub-event model (Table 2-1) in four quadrants for, P phase (vertical displacement), pP phase (vertical displacement), SH phase (tangential displacement) and sSH phase (tangential displacement). Seismic records are labeled with station name along with azimuth (Az), epicentral distance (Δ), and the maximum amplitude (Amp) of the data. The unit of the amplitude is 10^{-6} m. The whole waveform fitting of all used stations is shown in Fig. S3-1.

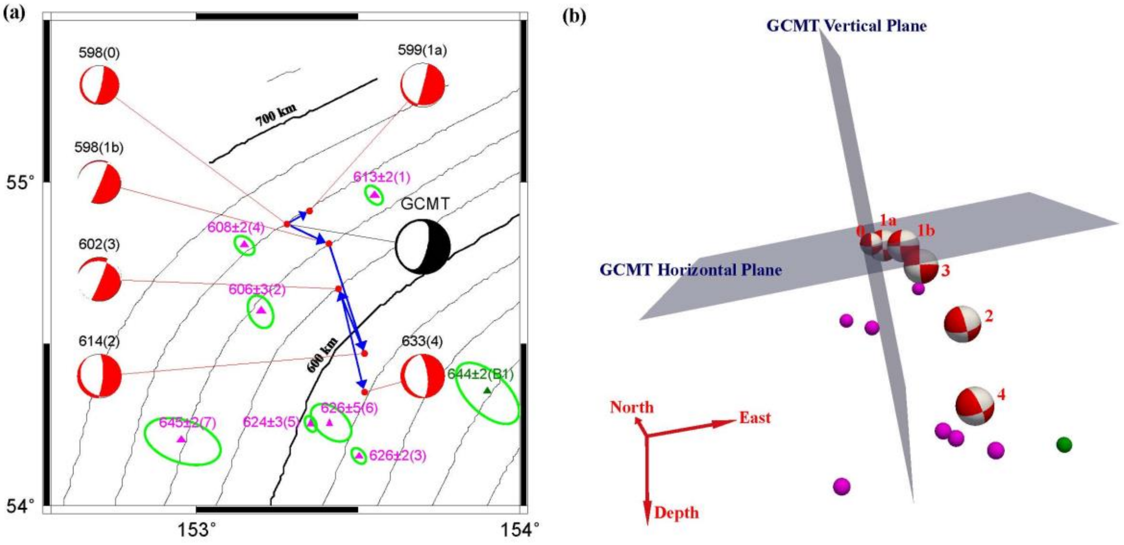

Fig. 3-4. (a) Locations of sub-events (red points), aftershocks (purple triangles) and background seismicity (green triangle), along with slab depth contours (black traces, labeled with slab depth). Black beach ball describes GCMT focal mechanism of the mainshock. Red beach balls represent inverted focal mechanisms of the sub-events, labeled with sub-event depth and the occurring sequence number as defined in Fig. 3-1a. Sub-events are connected by blue arrows following the sequence of their occurring times. Green ellipses represent the 95% confidence levels of the relocated fore/aftershocks. Sub-events, aftershocks and background seismicity are labeled with depth, depth uncertainty and sequence number in Tables 2-1, 2-2. Slab depth contours are from the USGS Slab 1.0 model (Hayes et al., 2012). (b) Three dimensional spatial distribution and focal mechanisms of inverted sub-events (red beach balls) labeled with sequence of their occurring times, along with the focal planes (gray planes) in the GCMT solution. Purple and green spheres represent the fore/aftershocks in (a).

3.6. Relationship with aftershocks and background seismicity

We use a relocation method (Wen, 2006) to determine the locations of the aftershocks and background seismicity relative to the mainshock. The method uses the arrival time difference of a particular seismic phase between a waveform doublet, defined as a pair of seismic events occurring at different times but in close location. Because the events occur very close in location, the relative travel times are sensitive primarily to the relative change of event location.

We use the differential travel times of P and pP waves recorded at the GSN stations at the distance ranges less than 45˚ for relocation. The seismic stations constitute good azimuthal coverage between 220° and 60°, but only one station PET is available in other azimuths. A weight is assigned to keep balance with the azimuthal coverage. We are also able to pick pP phase for events 1, 7 and B1. The depths of these events are relocated using P and pP travel times with respect to those of the mainshock. Each of the aftershock relocations has at least eight station pairs with four-quadrant coverage.

The M_W 8.3 mainshock is used as the master event, with its location fixed to that reported in the USGS catalog. The search region for the relative locations of the aftershocks is 3˚ (latitude) × 3˚ (longitude) × 200 km (depth) centered in the mainshock location. The search grid intervals are 0.05˚ in latitude, 0.05˚ in latitude and 2 km in depth. The best-fitting location and origin time significantly reduce the root-mean-square (RMS) travel time residual (Figs. 3-5a, 3-5b).

We relocate eight fore/aftershocks with M_W>4.0 based on the Preliminary Determination of Epicenters (PDE) Bulletin by USGS (Table 3-1 and Fig. 3-5). The aftershock locations further support the inference that the May 24, 2013 Okhotsk earthquake is not a rupture on a single fault plane. The scattered aftershocks do not fall into the same region of the sub-events or fit into a possible plane. Neither is the one only small earthquake occurring in the region before the mainshock (Fig. 3-4).

Table 3-1. Locations of aftershocks and background seismicity.

					Before relocation			After relocation		
ID	Date	Time	Mb	No.	Lon (°E)	Lat (°N)	Depth (km)	Lon (°E)	Lat (°N)	Depth (km)
1	5/24/2013	07:32:04	4.3	9	153.56	54.95	602	153.55	54.95	613*
2	5/24/2013	12:35:00	4.1	8	153.17	54.53	606	153.20	54.60	606
3	5/24/2013	14:33:24	4.1	8	153.50	54.11	625	153.50	54.15	626
4	5/26/2013	12:40:59	4.1	8	153.14	54.81	599	153.15	54.80	608
5	5/28/2013	08:58:39	4.4	15	153.40	54.24	627	153.35	54.25	624
6	6/5/2013	23:29:44	4.0	8	153.35	54.27	621	153.40	54.25	626
7	6/11/2013	10:56:38	4.8	15	152.99	54.14	642	152.95	54.20	645*
B1	5/24/2000	15:42:57	4.4	18	153.42	54.55	572	153.90	54.35	644*

Note: ID is sequence number of aftershocks and background seismicity. No. is the number of stations used in relocation. The depth with * is relocated using pP phase.

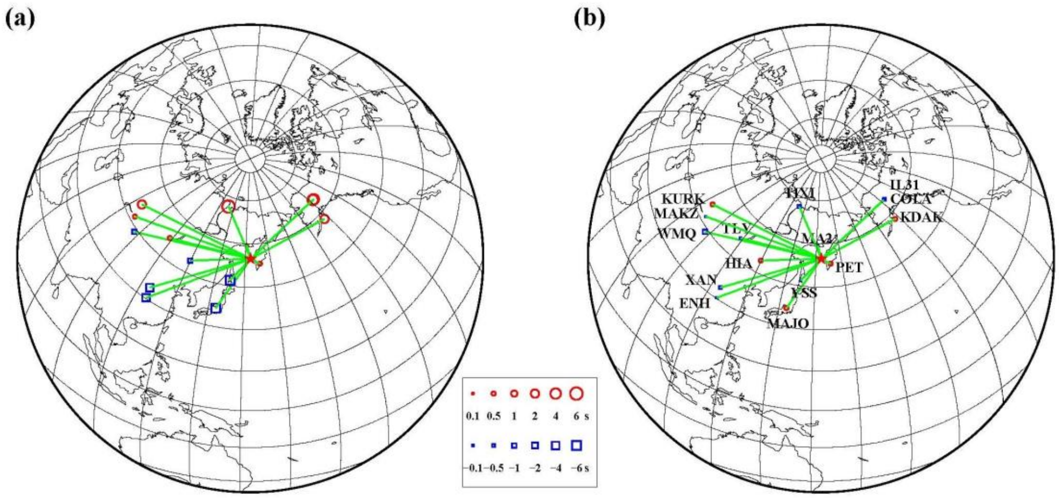

Fig. 3-5. (a) Measured difference in absolute arrival time (circles and squares) of the P phases (with respect to their mean) between the mainshock and one aftershock 201305241456, plotted centered at the location of each station, along with the great circle paths (green traces) from the mainshock (star) to the stations (labeled with station name in Fig. 3-5b). (b) Same as Fig. 3-5a, except that travel time residuals between the two events are corrected using the best-fitting relative location (Table 3-1).

3.7. Resolution tests

3.7.1. Single-plane Rupture Model Test

The spatial distribution of the inverted sub-events indicates that the energy release of this event does not follow a particular plane of rupture. We perform further inversion tests to check if the fitting of seismic data can be compromised with rupture along a particular plane. We perform tests for possible plane rupture of the earthquake for three possible planes: the CMT sub-horizontal plane, the CMT sub-vertical plane and a plane that best connects the inferred sub-event locations (Table 2-1) from the multiple-source inversion.

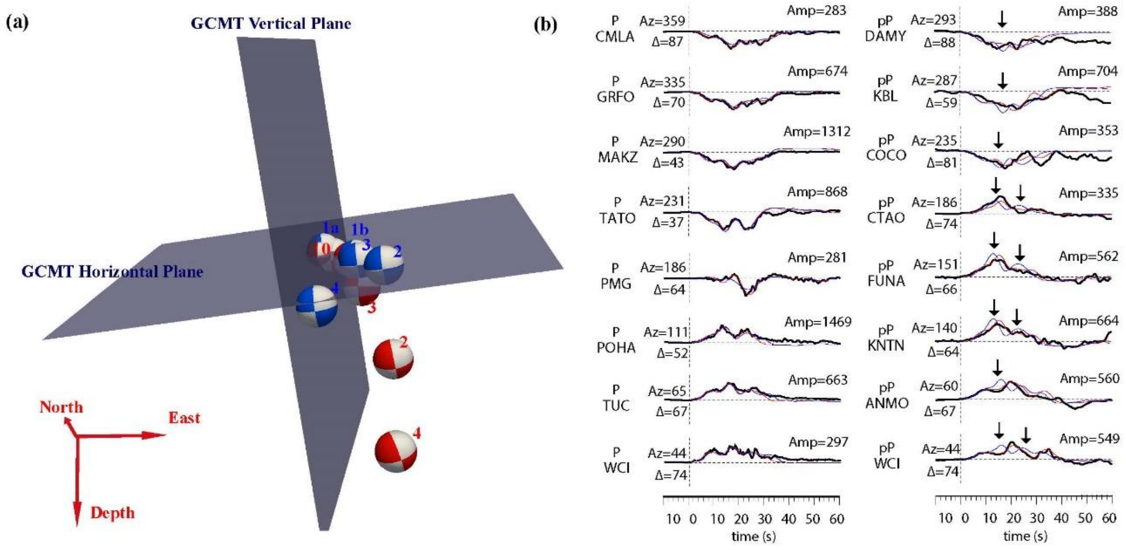

Fig. 3-6. (a) Three dimensional spatial distribution of focal mechanisms of the best-fitting model (red beach balls) and the inverted model of compelling the sub-events on the GCMT sub-horizontal plane (blue beach balls) labeled with sequence of their occuring time, along with the focal planes (gray planes) in the GCMT solution. (b) Selected seismograms (black traces) comparing with synthetics (red traces) predicted by the best-fitting source model (Table 2-1, red beach balls in Fig. 3-6a) and synthetics (blue traces) predicted by the best-fitting source model (Table S3-1, blue beach balls in Fig. 3-6a) on the GCMT sub-horizontal plane. Arrows point to the misfits of the blue traces. The waveform fitting of all used stations is shown in Fig. S3-2.

Our first test is to adopt the CMT sub-horizontal focal plane. The locations and focal mechanisms of sub-events are inverted in a plane with a strike of 191.0˚ and a dip of 11.2˚, corresponding to the CMT sub-horizontal plane (Fig. 3-6a, Table S3-1). The most notable misfits are time differences of major groups of energy between synthetics and the data in P, pP and sS phases marked with black arrows in Figs. 3-6b and S3-2. In the direction of inferred lateral rupture propagation, the sub-horizontal plane rupture would require the rupture to be up-going, rather than down-going as required from the comparison of P and pP data (Fig. 3-2). It should be pointed out that it is crucial to combine both P and pP observations in the inversion of source process. The direct teleseismic P or SH observations have poor resolution in resolving the depth of the propagating energy, as the depth has strong trade-offs with origin time.

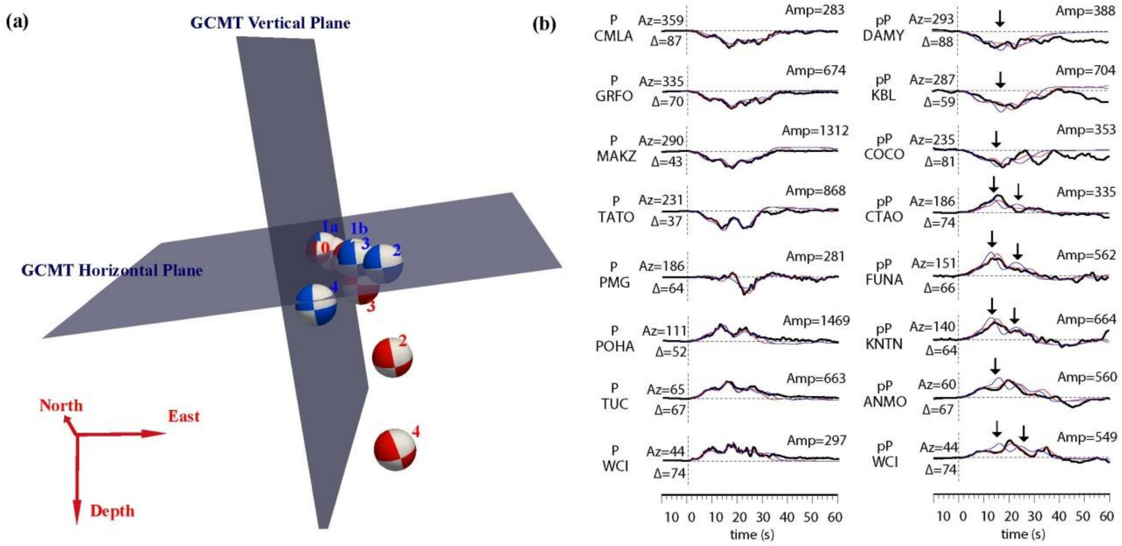

Fig. 3-7. (a) Three dimensional spatial distribution of focal mechanisms of the best-fitting model (red beach balls) and the inverted model of compelling the sub-events on the sub-horizontal plane (blue beach balls) based on the constaints of P wave only, labeled with sequence of their occuring time, along with the focal planes (gray planes) in the GCMT solution. (b) Selected seismograms (black traces) comparing with synthetics (red traces) predicted by the best-fitting source model (Table 2-1, red beach balls in Fig. 3-7a) and synthetics (blue traces) predicted by the best-fitting source model (Table S3-2, blue beach balls in Fig. 3-7a) on the GCMT sub-horizontal plane based on P wave data only. Arrows point to the misfits of the blue traces. The waveform fitting of all used stations is shown in Fig. S3-3.

We perform the same test, but using the P waves only. In this inversion, sub-events 1-3 propagate up-going along southeast and sub-event 4 propagates to south/southwest in horizontal direction (Fig. 3-7a, Table S3-2). The inverted model predicts P synthetics that fit the data equally well as the best fitting model in the main text (Figs. 3-7b, S3-3a). However, the pP waveforms predicted by this model misfit the data at all the stations, with all groups of energy arriving much earlier in synthetics than in the data (Figs. 3-7b, S3-3b). Same is also true for sS waveforms at stations RAR, RAO, UGM, EIL, KIEV and GRFO (Fig. S3-3d). This is due to the fact that the sub-events are prescribed to move shallower on the CMT sub-horizontal plane.

The second test is to confine the seismic energy on the CMT vertical plane. The synthetics of such inversion results (Table S3-3 and Fig. 3-8a) cannot match the observations in both arrival times and radiation patterns of major energy groups. The mismatches are due to the fact that the assumed vertical plane of rupture prescribes the seismic source to move in a way that the predicted energy associated with the second and fourth pulses would not fit the azimuthal dependence of their arrival times and amplitudes in the P and pP observations. The seismic source for the second and fourth pulses are required to move east and deeper, while the CMT vertical inversion places the energy north and shallower resulting in the synthetic misfits to the observations. The most obvious misfits are revealed at stations around 90˚ and 270˚. The major groups of energy arrive earlier in the observed P waveforms than in the synthetics at stations POHA, KIP, JOHN and RAR, and later at stations ENH, CHTO, LSA, KBL, MAKZ, AAK and BRVK (Figs. 3-8b, S3-4a). The mismatch of arrival times is also evident in the S waveforms at stations PFO, COR and WAKE, and the sS waveforms at stations EIL, KIEV, and GRFO (Fig. S3-4c). The misfits of radiation pattern are evident in P waveform at station PMG (Fig. S3-4d) and in sS waveforms at stations ANMO and TUC (Figs. 3-8b, S3-4).

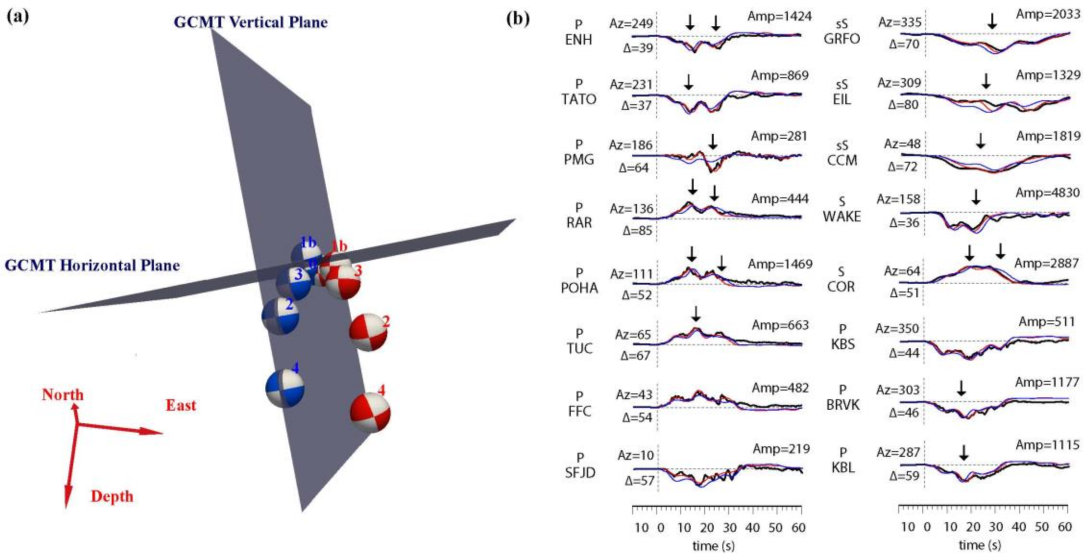

Fig. 3-8. (a) Three dimensional spatial distribution of focal mechanisms of the best-fitting model (red beach balls) and the inverted model compelling the sub-events on the GCMT sub-vertical plane (blue beach balls), labeled with sequence of their occuring time, along with the focal planes (gray planes) in the GCMT solution. (b) Selected seismograms (black traces) comparing with synthetics (red traces) predicted by the best-fitting source model (Table 2-1, red beach balls in Fig. 3-8a) and synthetics (blue traces) predicted by the best-fitting source model (Table S3-3, blue beach balls in Fig. 3-8a) on the GCMT sub-vertical plane. The waveform fitting of all used stations is shown in Fig. S3-4.

Our third test is to adopt a plane that best fits the spatial distribution of the sub-events from the multiple-source inversion. The plane has a strike of 350° and a dip of 65°. While the predicted arrival times of major groups of the energy fit the observations reasonably well, the predicted amplitudes do not fit the data (Table S3-4, Fig. 3-9a). This is due to the fact that such a plane would prescribe focal mechanisms that would not fit the azimuthal variations of seismic amplitudes in the data (Figs. 3-9b, S3-5). These inversion tests indicate that the fitting of the seismic data cannot be compromised with rupture on a plane.

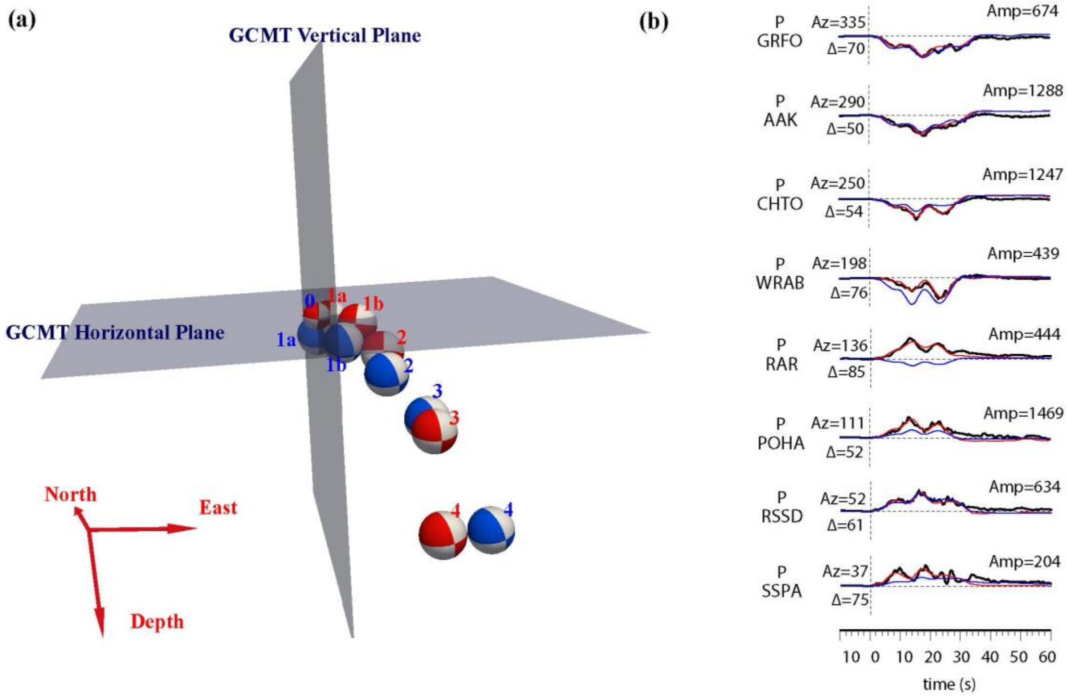

Fig. 3-9. (a) Three dimensional spatial distribution of focal mechanisms of the best-fitting model (red beach balls) and the inverted model compelling the sub-events on the plane that best connects the best-fitting model (blue beach balls), labeled with sequence of their occuring time, along with the focal planes (gray planes) in the GCMT solution. (b) Selected seismograms (black traces) comparing with synthetics (red traces) predicted by the best-fitting source model (Table 2-1, red beach balls in Fig. 3-9a) and synthetics (blue traces) predicted by the best-fitting source model (Table S3-4, blue beach balls in Fig. 3-9a) on a plane that best connects the inferred sub-events in Table 2-1. The waveform fitting of all used stations is shown in Fig. S3-5.

3.7.2. Effects of Attenuation

Earth's attenuation would result in broadening of wave shapes and apparent "delay" of the peaks of seismic energy (Fig. 3-10a). However, the different durations observed between pP and P waveforms (Fig. 3-2a) are not caused by the effect of attenuation. We test various attenuation models by changing path-integrated attenuation t* value from 0.5 to 2 times of PREM values for pP synthetics. The misfits do not vary much with t* values ranging from 0.6 to 1.7 times of PREM values (Fig. 3-10b). When t* reaches 1.8 times of PREM values, misfits start to increase rapidly (Fig. 3-10b). With this attenuation structure, the apparent “delay” of the peaks of individual pulses of pP waves is at most 1.5 s (Fig. 3-10a), which is significantly smaller than 7-8 s observed in the P and pP data (Fig. 3-2). More importantly, the predicted time differences between the peaks of different sub-event energy, which are used to infer the depth separations between the sub-events, differ at most by 0.2 s between different attenuation models. (Fig. 3-10a). Therefore, the depth extension among sub-events 1-4 is little affected by attenuation. We conclude that the observed time difference between P and pP wave energy is caused by the depth extension of seismic source.

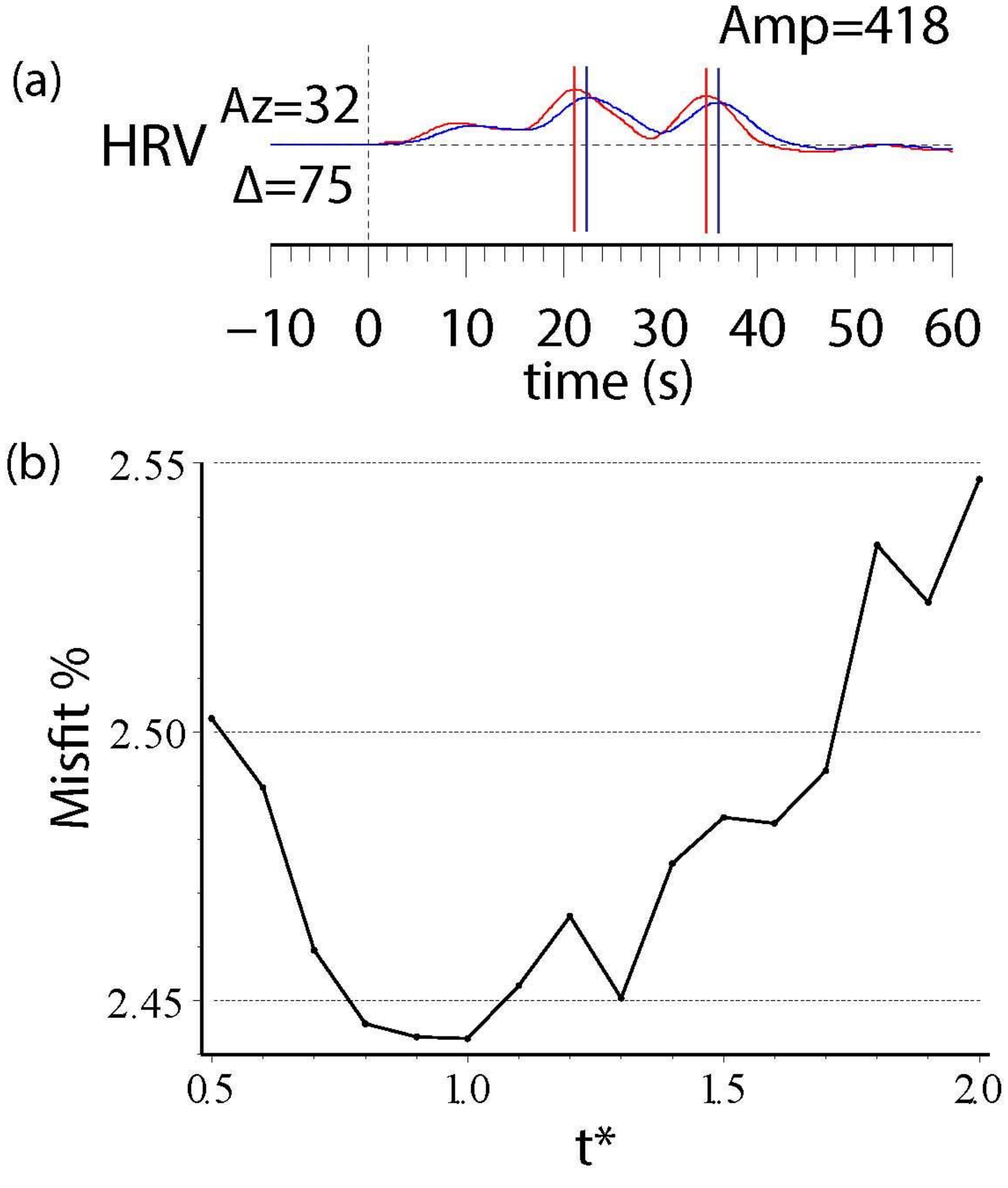

Fig. 3-10. (a) Synthetics (red traces) of pP waves attenuated by t* = 1.45 based on the PREM model and synthetics (blue traces) of pP waves attenuated by t* = 2.61 (1.8 times of PREM values) predicted by the best-fitting source model (Table 2-1). The red and blue lines mark the peaks of sub-events 2 and 4. (b) The misfits (RMS) of amplitudes between the data and synthetics predicted based on the best fitting model by varing t* of pP phase from 0.5 to 2.0 times of the PREM values.

3.7.3. Three dimensional effect of slab structure

It is well known that a sharp structure of a subducted slab may have profound effects on wave propagation (Chen et al., 2007). In some specific slab geometry, the sharp feature of the slab structure may exhibit multi-path effects, producing an additional pulse at some azimuths. The extent of such effects would likely vary from slab to slab. However, if such effect exists, the additional pulse in the propagational effects could be mistaken as a sub-event or contaminate our results during the inversion. For the seismic data used in the present study, the three-dimensional (3D) propagational effects due to the slab structure are minor. This is demonstrated in a near-by aftershock data recorded at these stations (Fig. 3-11a). The P waves of the aftershock exhibit a simple pulse with a duration of 2 s in four quadrants (Fig. 3-11b). No obvious additional pulses are observed within the range of time separation between the inverted sub-events for the mainshock (Fig. 3-11b). Same waveform characteristics are observed for the pP waves as well, although their main phases exhibit a longer duration, which may be due to either stronger attenuation or down-dip rupture directivity. We thus conclude that the 3D slab effect is minor in our data and does not affect our inversion result of the Okhotsk earthquake.

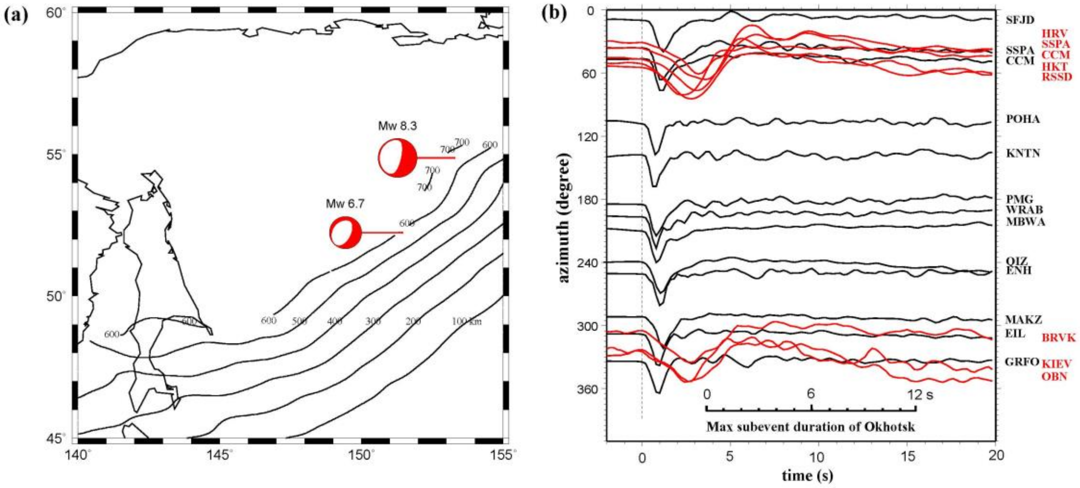

Fig. 3-11. (a) Location and focal mechanisms (red beach balls) of the mainshock and a near-by aftershock. The depth contours labeled with slab depth are from the USGS Slab 1.0 model. (b) Observed vertical P (black traces) and pP (red traces) displacement seismograms of the aftershock as a function of azimuth.

3.7.4. Horizontal Extension of the Energy Propagation

The spatial distribution of the source process in this study represents the centroid location of each sub-event. Therefore, the horizontal extension of 64 km in this study is roughly consistent with the previous study (Ye et al., 2013), and smaller than 100 km reported by the others (Wei et al., 2013; Zhan et al., 2014a). The discrepancy arises from the fact that different types of data used between the studies. The result of the previous study is inferred from waveform fitting of P wave data only, while our result is obtained based on waveform fitting of both P and S wave data. While a lateral extent larger than 100 km would still produce reasonably good fit to the P wave data, it would generate an S wave energy move-out different from the observed data. We present an example of synthetic test to illustrate the effect, by compelling the parameter ‘dn’ of sub-event 4 to be larger than 90 km south to the earthquake initiation point (Fig. 3-12a, Table S3-5).

While the observed P waveforms can still be reasonably fit by the model (Figs. 3-12b, S3-6a), significant misfits are apparent in S waves at stations SFJD, IVI, CLF, KBS and DAG (Figs. 3-12b, S3-6c). The seismic energy generated by sub-event 4 exhibits a very different move-out from the data (Figs. 3-12b, S3-6c). And some misfits are exhibited in pP and sS as well (Figs. S3-6b, S3-6d).

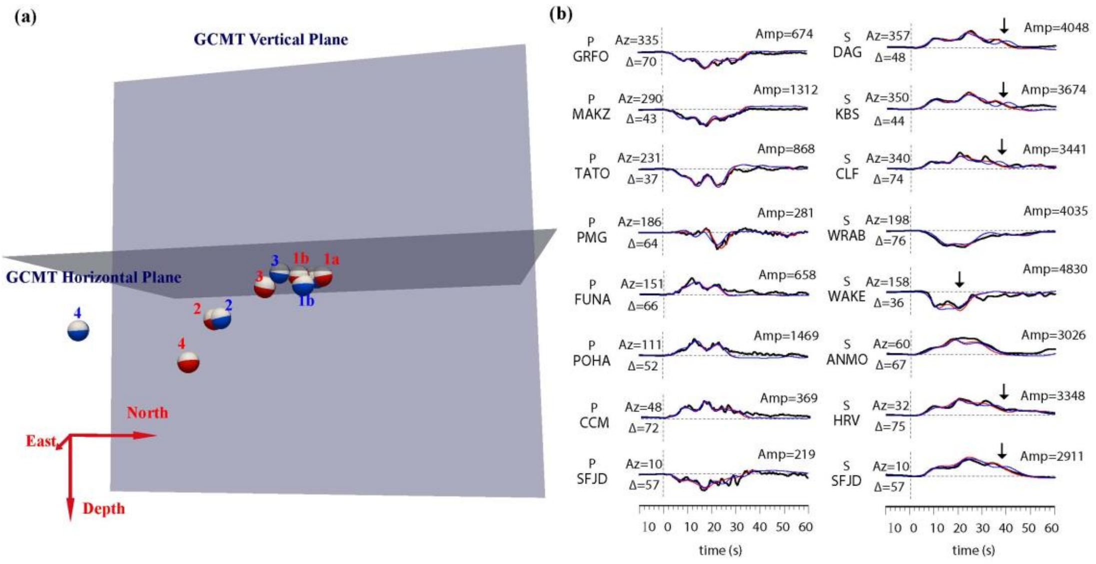

Fig. 3-12. (a) Three dimensional spatial distribution of focal mechanisms of the best-fitting model (red beach balls) and the inverted model compelling sub-event 4 to 90 km south to the initiation of the earthquake (blue beach balls), labeled with sequence of their occuring time, along with the focal planes (gray planes) in the GCMT solution. (b) Selected seismograms (black traces) comparing with synthetics (red traces) predicted by the best-fitting source model (Table 2-1, red beach balls in Fig. 3-12a) and synthetics (blue traces) predicted by the best-fitting source model (Table S3-5, blue beach balls in Fig. 3-12a) by compeling sub-event 4 to 90 km south to the initiation of the earthquake. Arrows point to the misfits of the blue traces. The waveform fitting of all used stations is shown in Fig. S3-6.

3.8. Possible interpretations

The inferred source process does not prefer phase transformational faulting. The transformational faulting events would occur in the interface of the meta-stable olivine-spinel wedge, so the orientation of the wedge would follow the sub-event locations as in Fig. 3-4a. It is unlikely that the meta-stable wedge would possess that kind of geometry.

It is interesting to note that the inferred sub-events could be classified into two groups with similar focal mechanisms, with sub-events 0, 1a, 1b, 3 forming one and sub-events 2 and 4 the other. The spatio-temporal distribution of the sub-events could be explained with rupture on two planes approximately orthogonal to each other with one sub-horizontal plane hosting the rupture of sub-events 0, 1a, 1b and 3 and one sub-vertical plane hosting the rupture of sub-events 2 and 4 (Fig. 3-13). In this scenario, the earthquake is initiated on the sub-horizontal plane with a rupture velocity of 2 km/s and a lateral dimension of 27 km. At 12 seconds during the sub-horizontal rupture, a downward rupture is triggered on a near sub-vertical plane 24 km southeast of the sub-horizontal rupture, with a rupture velocity of 2 km/s. It is also interesting to note that such rupture process would resemble that of the April 11 2012 great earthquake in the Indian ocean (Meng et al., 2012; Yue et al., 2012), and may represent reactivation at depth of such a pre-existing type of fault system observed in oceanic lithosphere before subduction. However, none of the aftershock locations fits into these two possible rupture planes (Fig. 3-4a), making this two-plane rupture explanation unlikely.

The source process and fore/aftershocks distribution indicates that the earthquake is a combination of smaller earthquakes occurring in close space and time. The close proximity and timing of the sub-events suggest a cascading failure of the region during this earthquake, with some triggering mechanisms between the sub-events. The likely triggering forces are the static or dynamic stress generated by the preceding sub-event(s) (Hill, 2008; Tibi et al., 2003b).

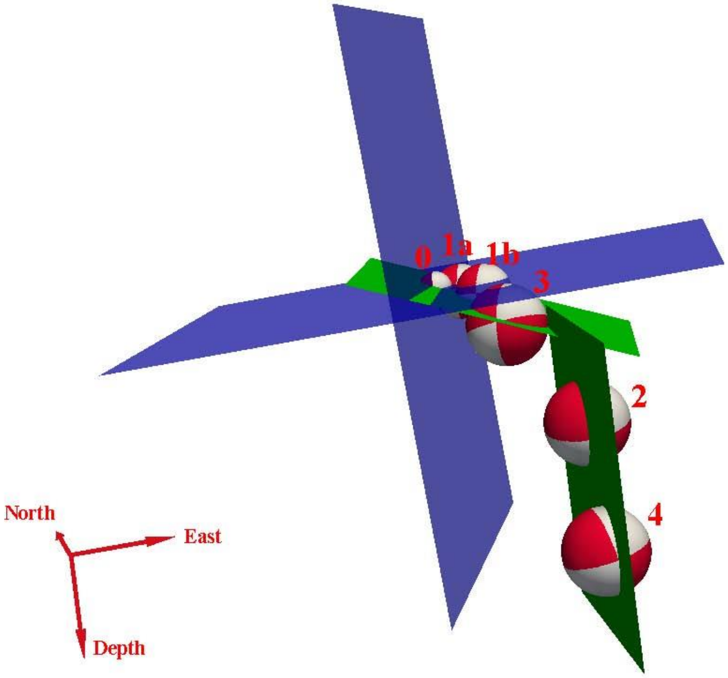

Fig. 3-13. A two-plane rupture model (green planes) that could accommodate the locations and focal mechanisms of the inferred sub-events (red beach balls labeled with sequence of their occurring times). Two GCMT fault planes are presented as blue planes.

The inferred source process of the Okhotsk earthquake is more consistent with a cascading failure of shear thermal instabilities in the region. Shear thermal instability is a failure due to positive feedback between viscous heating and temperature-dependent rheology (Hobbs and Ord, 1988b; Kelemen and Hirth, 2007). Such feedback system is naturally influenced by perturbation of stress, providing a mechanism for a cascading failure in a region. While a pre-existing zone of weak rheology is not a requirement for shear thermal instability to occur, it would prescribe the instability to occur along its orientation. Such weak zones are known to exist within the subducted slab, due to either past faulting before subduction (Silver et al., 1995) or existence of pre-existing fine-grained shear zones (Kelemen and Hirth, 2007). The focal mechanisms of the sub-events thus could reflect the orientations of the pre-existing weak zones. In short, the Okhotsk earthquake can be best explained by a cascading series of failures in a region of pre-existing weak zones, with the perturbation of stress generated by a shear instability triggering another and the orientations of the pre-existing weak zones controlling the focal mechanisms of these instabilities.

3.9. Conclusion

We investigate the source process of the 24 May 2013 Mw 8.3 Okhotsk deep earthquake based on waveform modeling of P, pP, SH and sSH wave data. The seismic source directivity analyses and multiple-source inversion results suggest that the earthquake can be modeled by six sub-events, with a horizontal extension of 64 km and a depth extension of 35 km. The model resolutions are ±2° for each focal parameter, ±0.5 s for dt and ±4 km for location. Synthetics tests further indicate that the seismic data cannot be explained by rupture on a single plane. The spatial distribution of the fore/aftershocks also does not fit into a plane or two planes with the inferred sub-events. These results suggest that the earthquake is a combination of smaller earthquakes close in time and space. We suggest that the earthquake can be best explained by a cascading failure of shear instability within pre-existing weak zones in the region, with the perturbation of stress generated by a shear instability triggering another.

Chapter 4 Source process and physical mechanism of the major sub-events of global large deep-focus earthquakes

4.1. Abstract

We apply a multiple source inversion method to systematically study the source processes of 25 large deep-focus (depth > 400 km) earthquakes with Mw > 7.0 from 1994 to 2012, based on waveform modeling of P, pP, SH and sSH wave data. The earthquakes are classified into three categories based on spatial distributions and focal mechanisms of the inferred sub-events: 1) category one, with non-planar distribution and variable focal mechanisms of sub-events, represented by the 1994 Mw 8.2 Bolivia earthquake and the 2013 Mw 8.3 Okhotsk earthquake; 2) category two, with planar distribution but focal mechanisms inconsistent with the plane, including eighteen earthquakes; and 3) category three, with planar distribution and focal mechanisms consistent with the plane, including six earthquakes. We discuss possible physical mechanisms for earthquakes in each category in the context of plane rupture, transformational faulting and shear thermal instability. We suggest that the inferred source processes of large deep-focus earthquakes can be best interpreted by cascading failure of shear thermal instabilities in pre-existing weak zones, with the perturbation of stress generated by a shear instability triggering another and focal mechanisms of the sub-events controlled by orientations of the pre-existing weak zones. The proposed mechanism can also explain the observed great variability of focal mechanisms, the presence of large values of CLVD (Compensated Linear Vector Dipole) and the super-shear rupture of deep-focus earthquakes in the previous studies. In addition, our studies suggest existence of relationships of seismic

moment ~ (source duration)^3 and moment ~ (source dimension)^3 in large deep-focus earthquakes.

4.2. Introduction

Physics of deep-focus earthquakes remains enigmatic, since deep-focus earthquakes occur at the depth below 400 km where the pressure would strongly inhibit brittle failure and the temperature would result in ductile deformation (Scholz, 2002). Various models have been proposed to explain the unexpected occurrence of deep-focus earthquakes, including dehydration embrittlement, transformational faulting and shear thermal instability. Dehydration embrittlement suggests that deep earthquakes may be triggered by embrittlement accompanying dehydration of hydrous minerals (such as serpentine) (Jung et al., 2004; Meade and Jeanloz, 1991), although it is unclear if the water content below the 400 km depth can support this mechanism. Transformational faulting mechanism hypothesizes that a meta-stable olivine wedge exists in the mantle transition zone and the phase transformation can lead to catastrophic earthquake failure (Green, 2007; Green and Burnley, 1989; Green and Houston, 1995; Kirby, 1987; Wiens et al., 1993) And, shear thermal instability suggests that rapid deformation can be achieved (especially, in pre-existing rheological weak zones), when a stress or temperature perturbation promotes a positive feedback between shear heating and temperature-dependent rheology (Hobbs and Ord, 1988b; Karato et al., 2001; Kelemen and Hirth, 2007; Ogawa, 1987).

Studies of source processes of large deep-focus earthquakes provided important constraints on deep-focus earthquake mechanisms. During the past 20 years, various methods have been applied to study source processes of deep-focus earthquakes. Rupture directivity is analyzed to determine fault plane orientations of deep-focus earthquakes occurring in the Tonga-Kermadec subduction zone (Warren et al., 2007). Both sub-horizontal and sub-vertical fault planes are detected, corresponding to a complex rupture system with either a reactivated or new generated fault system (Warren et al., 2007). Super-shear rupture was also reported for an Mw 6.7 aftershock of the Okhotsk earthquake (Zhan et al., 2014b). A number of large deep earthquakes, especially the 1994 Mw 8.2 Bolivia and 2013 Mw 8.3 Okhotsk deep earthquakes, have also been studied by multiple source inversion (Chen et al., 2014; Silver et al., 1995; Zhan et al., 2014a) and finite fault inversion (Antolik et al., 1996, 1999; Estabrook, 1999; Wei et al., 2013; Ye et al., 2013). The source processes of these two largest ever-recorded deep earthquakes provided particularly important insights on the physical mechanisms of deep earthquakes. Both the Bolivia earthquake (Silver et al., 1995; Zhan et al., 2014a) and the Okhotsk earthquake (Wei et al., 2013; Ye et al., 2013) were determined to have a large source region that totally cuts out of the assumed meta-stable olivine zone, seemingly excluding the transformation faulting as a possible mechanism. In a recent study, we showed that the Okhotsk earthquake consists of six sub-events that cannot spatially be fit into plane rupture and have variable focal mechanisms; we further suggested that the source process can be best explained by a cascading failure of shear thermal instabilities distributed at different depths, with one shear instability triggering another (Chen et al., 2014).

Though the past studies have provided important constraints on deep earthquake physics, several issues remain to be resolved. 1. Do deep-focus earthquakes rupture in a single fault plane? 2. Do deep-focus earthquakes behave the same between hot and cold subducted slabs? 3. Is there a unified mechanism to explain all the seismic results? In this study, we perform a systematical study of source processes of the global large deep-focus earthquakes with a moment magnitude greater than 7 and depth larger than 400 km, based on waveform modeling of direct P and SH waves and near-surface reflected pP and sSH waves through multiple source inversion. Combining the direct and near-surface reflected phases places a tight constraint on the depth distribution of the seismic energy release during these earthquakes (Chen et al., 2014). The multiple source inversion also makes no *a prior* assumption on the focal mechanism of the sub-events in waveform modeling. In the following sections, we present event information and seismic data in section 4.3, multiple source inversion method in section 4.4, multiple source inversion results in section 4.5, a unified physical mechanism of shear thermal instability for explaining the seismic results in section 4.6, and implications to the observed focal mechanism variation of deep earthquakes and super-shear rupture in section 4.7.

4.3. Seismic data

We search the events with Mw > 7.0 and depth > 400 km from 1994 to 2012. There are a total of 28 earthquakes matching the criterion (Fig. 4-1 and Table S4-0). The studied events are well recorded by the Global Seismographic Network (GSN). The data consist of broadband compressional waves (P), near-surface reflected compressional waves (pP), transversally polarized shear waves (SH) and near-surface reflected transversally polarized shear waves (sSH) recorded at tele-seismic distances between 30° and 90°. The selected data constitute good azimuthal coverage for all the events (Figs. S4-1a – S4-25a). As we will mention later, the combination of direct P and SH waves with the near-surface reflected pP and sSH waves places a tight constraint on depth extent of seismic source. The displacement seismograms are deconvolved with their respective instrument responses and bandpass filtered between 0.01 and 4 Hz. Our source models are constrained mostly by the seismic energy in a lower frequency band, but the use of the high-frequency data provides better arrival time reading of the P wave onsets while producing little artifacts in the inversions (supplementary information).

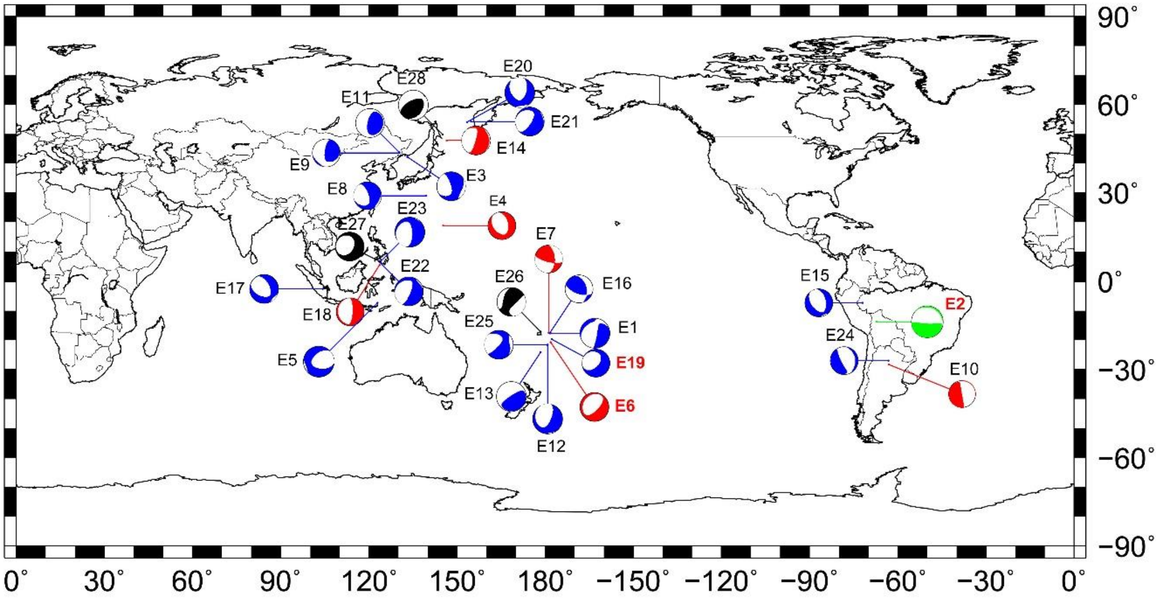

Fig. 4-1. Distribution of the global large deep-focus earthquakes (Mw > 7 and depth > 400 km) from 1994 to 2012, and their GCMT focal mechanisms, labeled with event numbers in Table S4-0. The earthquakes labeled with green, blue and red represent the earthquakes in categories one to three as classified in Section 4.5. The events labeled with red numbers are the example events presented in the main text. Three earthquakes with black beach balls are not studied (see text for the reasons).

4.4. Source processes of global large deep-focus earthquakes

We apply our multiple source inversion procedure to study the source processes of 28 deep-focus earthquakes. The observed waveforms of 25 of those earthquakes can be modeled reasonably well, using one to eight sub-events (green, blue, and red beach balls in Fig. 4-1). Three earthquakes (E26, E27 and E28, black beach ball in Fig. 4-1) are excluded in the present study. The seismic waves of event E27 are mixed with that of event E24 which occurred 24 minutes earlier, while E26 and E28 generated too complex waveform to be modeled by our method.

We align broadband P phases by the first arrival onsets, which can be clearly identified and picked in the high-pass filtered data above 1Hz. SH, pP and sSH phases are aligned iteratively in the inversion process: we first pick them based on IASP91 model (Kennett and Engdahl, 1991) and perform a preliminary inversion with P wave heavily weighted over other phases. The alignments of pP, SH and sSH phases are adjusted based on the best match between synthetics and the data during the inversions, until no further adjustment is observed from the previous inversion. The final inversion weights each phase equally. Synthetics tests indicate that such procedure of phase alignment is effective even in the presence of noise, large initial misalignment and waveform distortions due to attenuation or multi-path effects (supplementary information).

For each event, we also test whether the seismic data can be compromised with rupture in a single fault plane. We test three planar models: the two GCMT (Global Centroid Moment Tensor) fault planes and the plane that best geographically connects the inverted best-fitting sub-events in the multiple source inversion. Obviously, the best-fitting sub-event models of the multiple source inversion would always fit the data better than any planar models, but we test if the better data fitting is significant. We define that the earthquake can be modeled by a single fault plane if the misfit difference between the best planar model and the best-fitting sub-event model is less than 5%, a threshold above which better waveform fitting can be visually noticeable at stations around the nodal planes. The synthetics (blue traces) of the best planar models are presented in Figs. S4-1

– S4-25, along with the synthetics (red traces) predicted by the best-fitting sub-event models.

The inversion results of the 26 earthquakes can be divided into three categories based on the focal mechanisms and spatial distributions of the inferred sub-events: 1) category one, with non-planar spatial distribution and variable focal mechanisms of the sub-events, represented by the Bolivia earthquake (E2, green beach ball in Fig. 4-1) and the 2013 Mw 8.3 Okhotsk deep earthquake (Chen et al., 2014), 2) category two, with planar distribution but focal mechanisms of the sub-events inconsistent with the best-fitting plane, including eighteen earthquakes (blue beach balls in Fig. 4-1), and 3) category three, with planar distribution and focal mechanisms of sub-events consistent with the plane, including six earthquakes (red beach balls in Fig. 4-1). Earthquakes in categories one and two have greater moment magnitudes, longer source durations and larger source regions. We discuss the main features of the source process in each of the three categories, using an earthquake in each category as example. The detailed results of all the earthquakes are presented in the supplementary information with descriptions, tables of the best-fitting sub-event models (Tables S4-1 – S4-25) and the waveform fitting comparisons between the synthetics predicted by the best-fitting sub-event models (red traces) and the best planar models (blue traces) (Figs. S4-1 – S4-25). So are the results of our previous study of the 2013 Mw 8.3 Okhotsk earthquake (Chen et al., 2014), in Table S4-26 and Fig. S4-26.

4.4.1. Category 1: Non-planar spatial distribution of sub-events (Bolivia and Okhotsk)

The two largest ever recorded 2013 Okhotsk earthquake (Chen et al., 2014) and 1994 Bolivia earthquake exhibit large depth extensions of the sub-events. The sub-events of these two earthquakes are not distributed in a plane and exhibit variable focal mechanisms. We have reported the results related to the Okhotsk earthquake in our previous study (Chen et al., 2014). The Okhotsk earthquake consists of six sub-events with a horizontal extension of 64 km and a vertical extension of 35 km (Fig. S4-26). The geographic distribution and focal mechanisms of the inferred sub-events and fore/aftershocks locations do not fit into plane rupture (Chen et al., 2014). We focus on discussing the results of the Bolivia earthquake here.

The Bolivia earthquake has been well studied (Antolik et al., 1996; Goes and Ritsema, 1995; Silver et al., 1995; Zhan et al., 2014a). All the previous studies have suggested that the Bolivia earthquake ruptured on the GCMT sub-horizontal plane (Silver et al., 1995; Zhan et al., 2014a). Seismic data used in those studies included mostly P waves, with exceptions of Goes and Ritsema (1995) where both P and pP waves were used at the stations around the azimuth of 310˚, and Antolik et al (1996) where three pP observations were used. In this study, we revisit the issue by joint inversion of the P and pP waves recorded globally. We find that the seismic P and pP waves of the Bolivia earthquake exhibit a vertical extension during the earthquake, inconsistent with rupture on the GCMT sub-horizontal plane (Fig. 4-2).

The earthquake begins with an ~10 s weak initiation phase, followed by strong moment release lasting ~35 s. As the present study deals with major source process of deep-focus earthquake, the initiation phase is ignored and ignorance of such phase does not affect the seismic results presented here (supplementary information). The observed P waveforms exhibit strong azimuthal variations with five major seismic pulses during the strong moment release, discernible with different move-outs (peak times labeled 1 to 5 in black, Fig. 4-2a). The pP waveforms exhibit similar azimuthal variation as the P waveforms (peak times label with 1 to 5 in red, Fig. 4-2a). However, pulses of sub-events 4 and 5 are delayed in pP waveforms than in P waveforms, and the duration of pP waveforms is about 7-8 s longer (Fig. 4-2a). We show five example pairs of P and pP seismograms observed at stations TAM, SUR, SPA, RAR and COR, to further illustrate this feature (Fig. 4-2b). The first two pulses present almost the same arrival times in P and pP waveforms, corresponding to the same source depths. The fourth and fifth pulses exhibit 3-4 s and 7-8 s delays in pP waveforms than in P waveforms, corresponding to event sources that are 15-20 km and 35-40 km deeper than the earthquake initiation point.

In the inversion, we adopt two sub-events 3a and 3b to better fit the observed waveform features in the time window labeled between 3 and 4 in Fig. 4-2. The Bolivia earthquake can be modeled by 6 sub-events (Figs. 4-3, Table S4-2), with a total duration of 44 s. The source has a horizontal extension of 44 km and a vertical extension of 38 km. The inverted fault plane orientations of the sub-events are less than 10° different from the GCMT solution (Table S4-2). In comparison, the source of the Okhotsk earthquake has a duration of 28.5 s, a horizontal extension of 64 km and a vertical extension of 35 km (Chen et al., 2014). The sub-event durations of both earthquakes are about 10 s. We perform the planar tests for the Bolivia earthquake by compelling the sub-events on three planar rupture models. The sub-horizontal plane is determined to be the best planar model. However, the sub-horizontal plane model predicts synthetics arrival times that match the data in the early part of the seismograms (associated with sub-events 1, 2 3a and 3b), but not in the later portion of the seismograms (associated with the last two sub-events) (Fig. 4-3c). For example, in comparison with the observations (black traces), the last sub-event in the best planar model (synthetics in blue traces) predicts later P waves at stations TAM and HRV, but earlier pP waves at stations PAB, RAR and COR (Fig. 4-3c). Synthetics waveform amplitudes of the model also misfit the early portion of the seismograms associated with the first sub-event (e.g., the P wave at station RAR, Fig. 4-3c). The GCMT sub-vertical plane model generates late P and pP arrival times around the azimuth of 0° and early arrival times around the azimuth of 180°. And, while the plane that best connects the spatial distribution of the inferred sub-events (with a strike of 281° and a dip of 45°) can predict correct arrival times for most of the sub-events except at the time window that is associated with sub-event 3a and 3b, it generates synthetics that do not fit the azimuthal variation of seismic amplitudes in the data. These modeling results suggest that the Bolivia earthquake, like the Okhotsk earthquake, is a combination of sub-events that are distributed at different depths and out of a plane, and have variable focal mechanisms.

Although the horizontal distribution of the sub-events in our study is quite similar to those previous studies using P waves (e.g., Silver, et al., 1995, Zhan et al., 2014a), our results indicate that the sub-events 4 and 5 are 18 and 39 km deeper, and the spatial distribution of the sub-events is inconsistent with rupture on the GCMT sub-horizontal plane. This difference in the seismic results lies on that only the P waves were used in those studies (Silver et al., 1995; Zhan et al., 2014a), and P waves alone do not have source depth resolution (Fig. 2-1). We discuss the discrepancies between our results and those of the two previous studies using P and pP wave observations below. In the study of Antolik et al. (1996), they used three pP wave observations and only tested two plane models from the GCMT solution. Their best fitting plane model (the GCMT sub-horizontal plane) predicted earlier pP wave than the data recorded at station ALE (Figure 4 in Antolik et al., 1996), which implies inaccuracy in the inferred source depths. In the study of Goes and Ritsema (1995), they concluded that similar durations were observed between the stacked P and pP waveforms around the azimuth of 310°. However, we should note that the first sub-event is weak in the azimuth range between 310˚ and 70˚ (Fig. 4-2a), which would mislead the comparison of the durations of P and pP waves. At other azimuths, the observed pP waveforms clearly exhibit longer durations than P waveforms (Fig. 4-2).

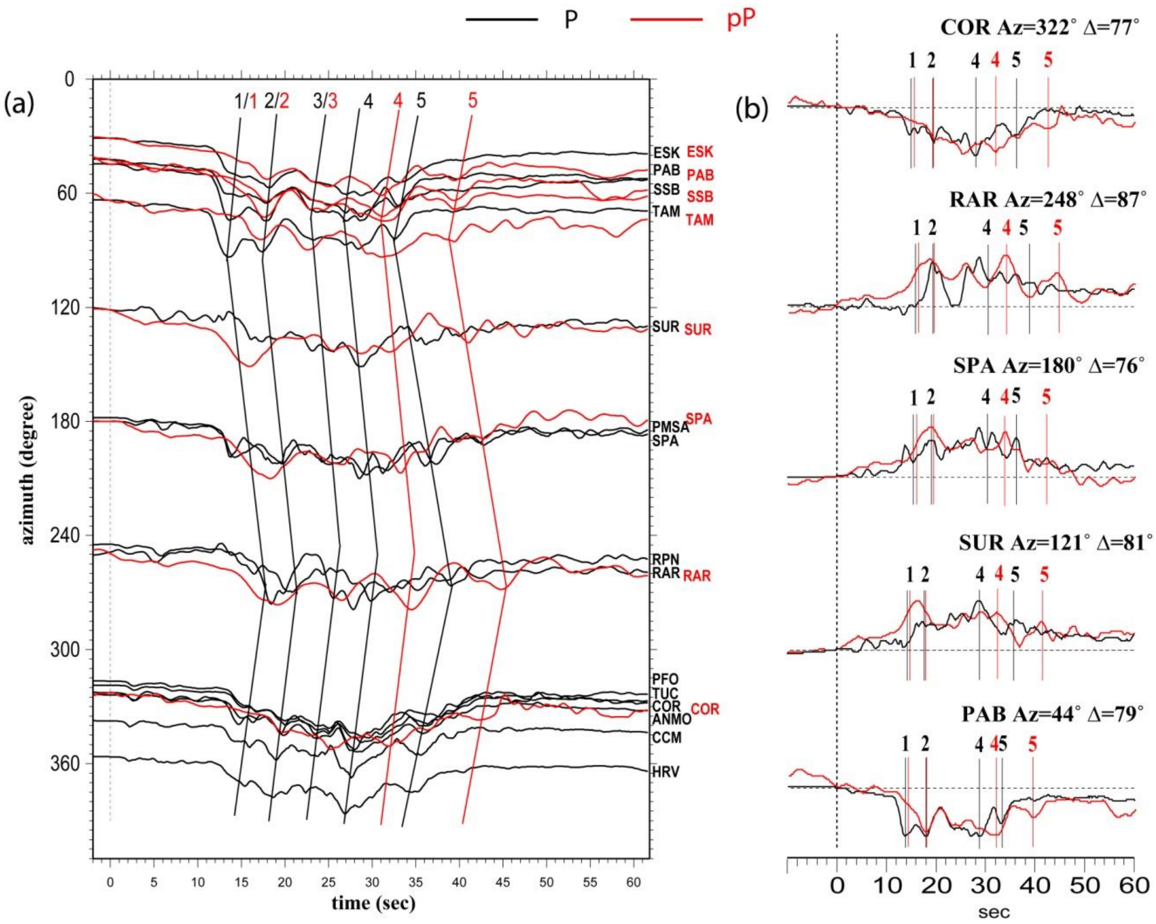

Fig. 4-2. (a) Comparison of observed P (black traces) and pP (red traces) displacement seismograms as a function of azimuth. The black and red lines indicate the peak times of the sub-events for P and pP, respectively. (b) Overlays of P and pP displacements observed at five example stations: COR, RAR, SPA, SUR and PAB. The black and red lines mark the maximal of the first, second, fourth and fifth sub-events labeled in (a). For the display purpose, the polarities of some records have been flipped.

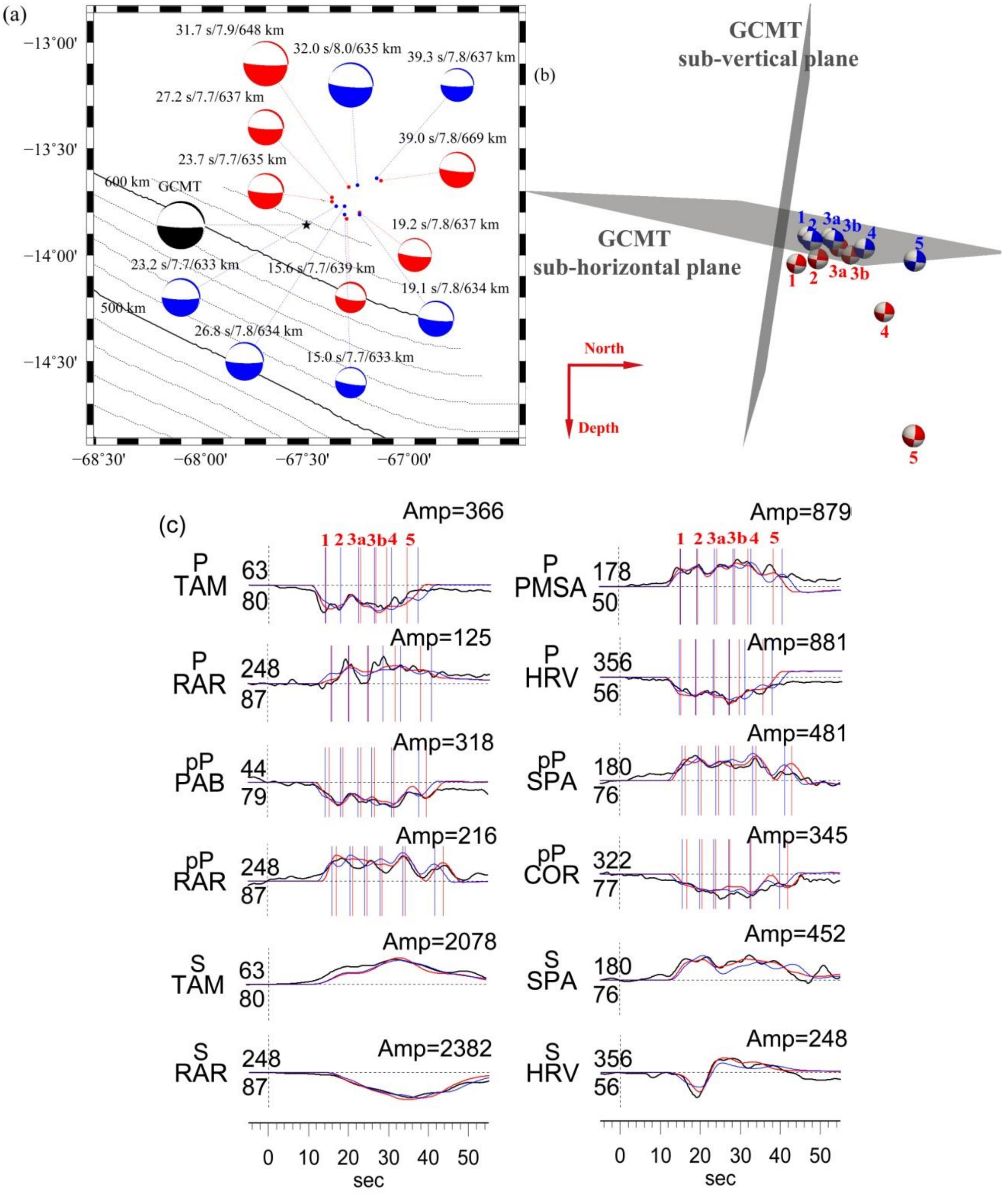

Fig. 4-3 (a) Locations of the best-fitting sub-events (red points), the best planar model (blue points, the inferred sub-events compelled to the sub-horizontal plane), and the initiated location (black star) of the 1994 Bolivia earthquake (E2), along with slab depth contours (black traces, labeled with slab depths). Black beach ball describes GCMT solution of the event. Red and blue beach balls represent inferred focal mechanisms of the sub-events of the best-fitting model and the best planar model, labeled with the sub-event peak times/moment magnitudes/depths. (b) Three-dimensional spatial distribution and focal mechanisms of inferred sub-events of the best-fitting model (red beach balls) and the best planar model (blue beach balls) labeled with their occurring sequence. (c) Selected observed seismograms in Fig. S4-2 (black traces) comparing with synthetics (red traces) predicted by the best-fitting source model and synthetics (blue traces) predicted by the best planar model. The red and blue lines label the peak times of the sub-events predicted by the best-fitting model and the best planar model.

4.4.2. Category 2: Planar spatial distribution of sub-events, but with focal mechanisms inconsistent with the plane (18 events)

The geographic distribution of the inferred sub-events of category two earthquakes (E1, E3, E5, E8, E9, E11, E12, E13, E15, E16, E17, E19, E20, E21, E22, E23, E24 and E25) can fit into a plane, but the focal mechanisms of the sub-events are inconsistent with the plane orientations. Most of the fault plane orientations of the sub-events deviate less than 20° from the fault plane orientations of the GCMT solutions, but some up to 50° (e.g., E1, Table S4-1). Synthetics of the best planar model exhibit large amplitude misfits to the seismic data (and even different polarities) at some stations (Fig. 4-4c). The hypocenter depths of this group of earthquakes range from 425 to 675 km, their moment magnitudes between 7.0 and 7.9, total source durations from 8 to 26 s, and the maximum distances among the sub-events between 15 and 70 km. The typical sub-event durations of these earthquakes are between 2 and 8 s.

We present the results of event E19 beneath Tonga region as example. This event consists of three sub-events, with inverted focal mechanisms (strike/dip/rake) of 46/71/262, 51/79/258 and 78/60/200 (Fig. 4-4a, Table S4-19). The best-fitting sub-events of the earthquake are distributed around the GCMT sub-vertical fault plane (Fig. 4-4, Table S4-19). The first two sub-events are roughly consistent with 49/76/252 of the GCMT solution, but the third one is ~30° different from the GCMT sub-vertical fault plane. We compare the best-fitting sub-event model (red traces) and the best planar model (blue traces) that compels the sub-events distributed on the GCMT sub-vertical plane (Figs. 4-4, S4-19). The blue traces can fit the early part of the data (corresponding to the prediction of the first two sub-events) at most of the stations, but significantly misfit the later portion of the data that corresponds to the pulse associated with the third inferred sub-event. The azimuthal distribution of the later portion of the seismograms would require a source that has a quite different radiation pattern from the early sub-events and from the GCMT solution (Fig. 4-4c).

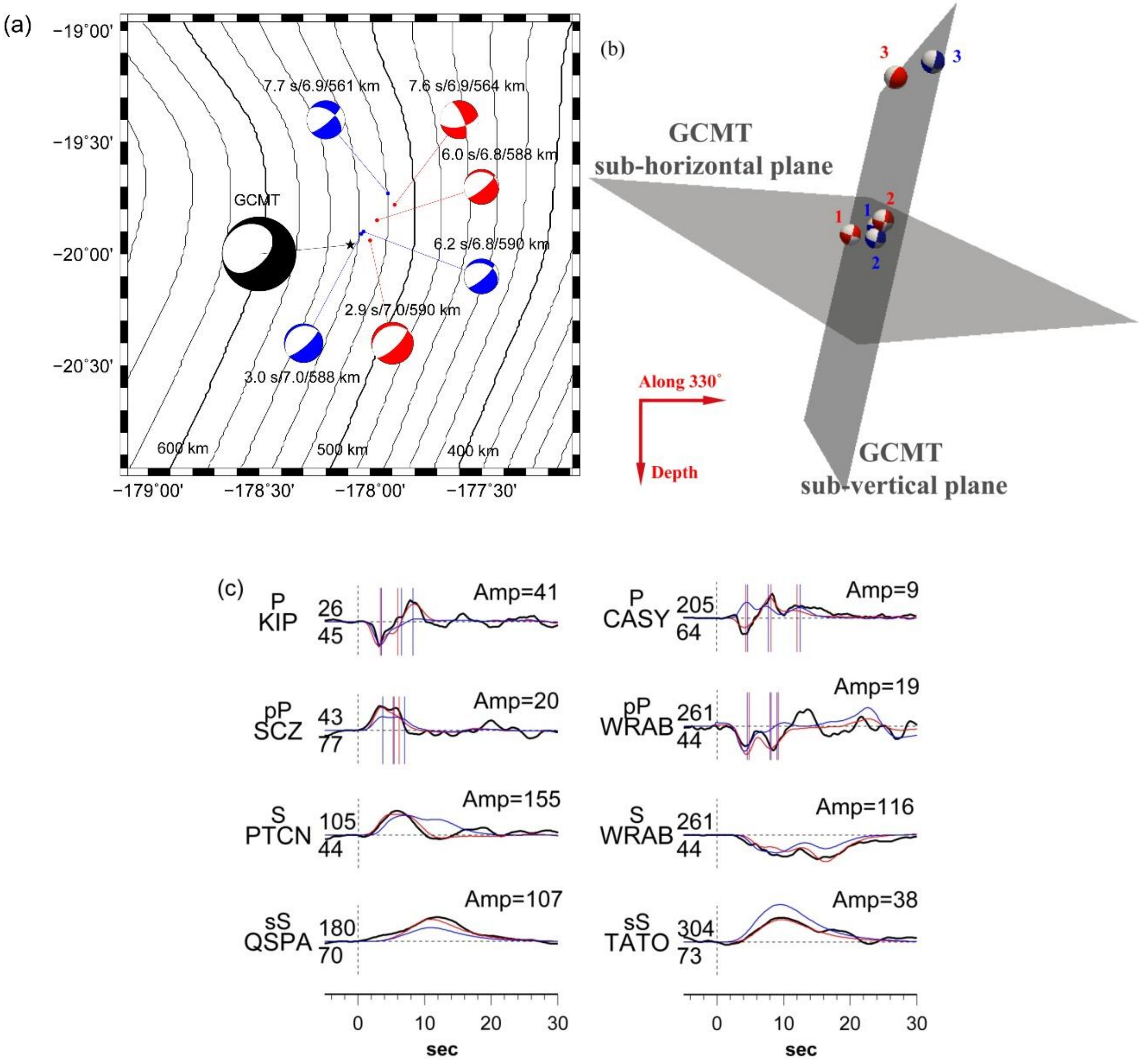

Fig. 4-4. Similar as Fig. 4-3, except for event E19, with the best planar model being the GCMT sub-vertical plane. (c) Selected comparisons between data (black traces) and synthetics based on the best-fitting sub-event model (red traces) and the best planar model (blue traces) in Fig. S4-19.

4.4.3 Category 3: Planar spatial distribution and focal mechanisms of sub-events consistent with the plane (6 events)

The spatial distribution of the inferred sub-events of the category three earthquakes (E4, E6, E7, E10, E14, and E18) fits into one plane and the focal mechanisms of the inferred sub-events are consistent with the best-fitting plane. Naturally, synthetics of the best planar model can fit the data as well as that of the best-fitting sub-event model. The hypocenter depths of this group of earthquakes range from 495 km to 610 km, and their moment magnitudes between 7.0 and 7.4. The extent of the lateral distribution of these events varies from 7 to 25 km, and the total durations of the earthquakes in this category from 4 to 14 s. The typical sub-event durations of these earthquakes are between 2 and 4 s.

We present the results of event E6 beneath Tonga region as example. The earthquake can be modeled by four sub-events with a horizontal extension of 25 km (Table S4-6, Fig. 4-5a). The first three sub-events are distributed on both the GCMT fault planes (along the interface of the two planes) with focal mechanisms consistent with the GCMT solution (Fig. 4-5b). The fourth sub-event is weak and its location is not well constrained. In the test of planar models, both GCMT fault planes could model the data reasonably well, with the sub-vertical plane slightly better (Figs. 4-5c, S4-6). Previous studies also reached different conclusions on the best-fitting plane, between the sub-vertical plane (Warren et al., 2007) and the sub-horizontal plane (Antolik et al., 1999).

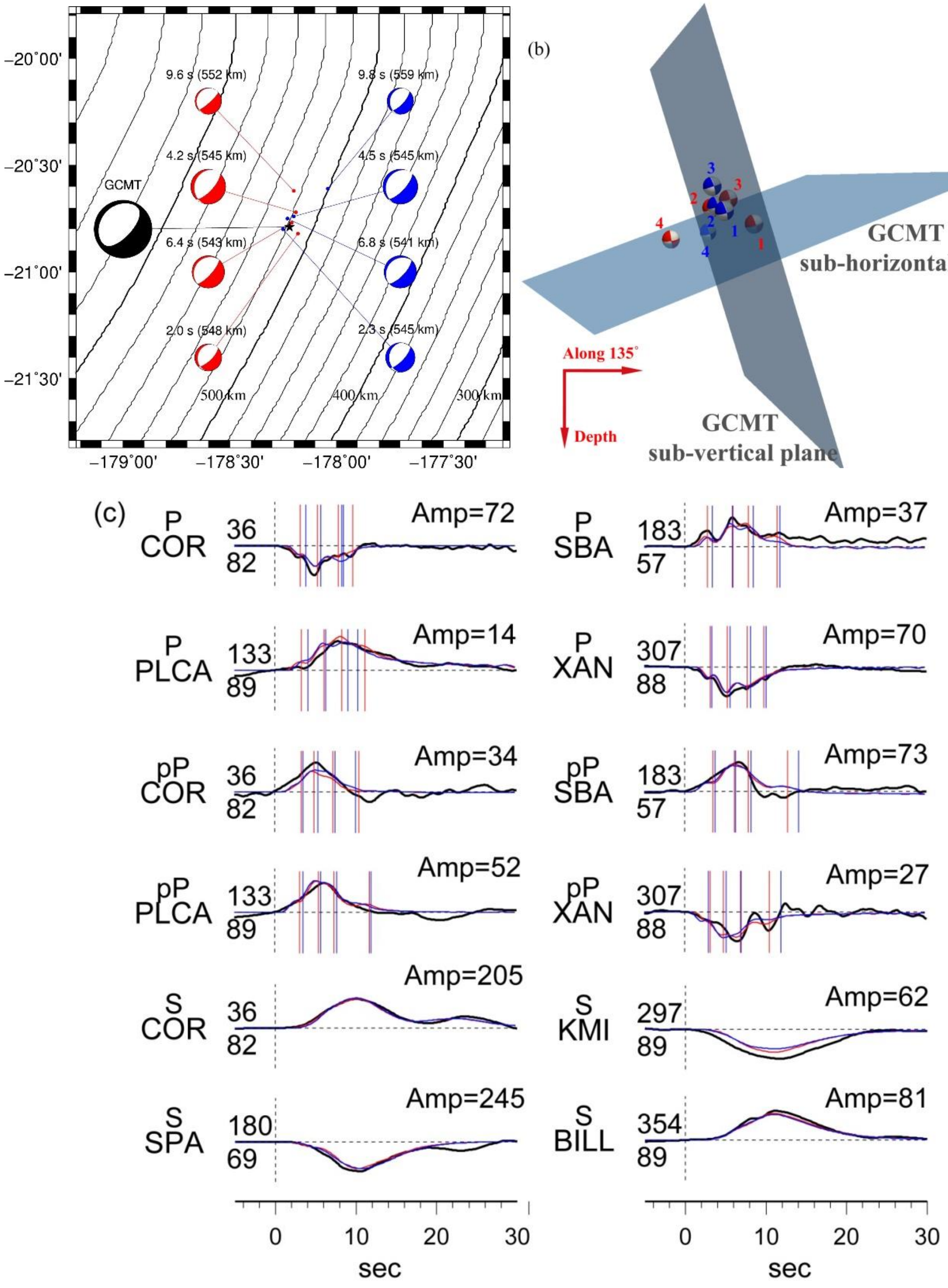

Fig. 4-5. Similar as Fig. 4-3, except for event E6, with the best planar model being the GCMT sub-vertical plane. (c) Selected comparisons between data (black traces) and synthetics based on the best-fitting sub-event model (red traces) and the best planar model (blue traces) in Fig. S4-6.

4.5. Physical mechanism of deep-focus earthquakes

4.5.1. Possible physical mechanisms for earthquakes in each category

The 2013 Okhotsk earthquake and the 1994 Bolivia earthquake in category one consist of sub-events with non-planar distribution. Our previous study indicated that the geographic distribution and focal mechanisms of the inferred sub-events of the Okhotsk earthquake and its fore/aftershocks locations do not fit into plane rupture (Chen et al., 2014). The source geometry of the event does not prefer phase transformational faulting, since it is not consistent with the meta-stable olivine wedge (Chen et al., 2014; Meng et al., 2014). Previous studies suggested that the Bolivia earthquake ruptured on the GCMT sub-horizontal plane and the inferred lateral dimension of the Bolivia event was larger than the hypothesized meta-stable olivine wedge, making the phase transformation faulting unlikely for the event (Silver et al., 1995). Our seismic results are inconsistent with a plane rupture, either on the GCMT sub-horizontal plane or on the plane that best connects the sub-event locations. The spatial distribution of the sub-events of the Bolivia earthquake is inconsistent with the likely slab geometry in the region (Fig. 4-3a) and the lateral extent of the source distribution of the event is estimated to be 50 km (maximum separation distance between the sub-events plus the rupture length of sub-events with 10 s duration and half of local shear wave velocity), exceeding the 10-20 km thick meta-stable olivine wedge estimated based on theoretical estimation of the temperature condition within South American slabs (Silver et al., 1995). The best-fitting sub-event model can be best explained by a cascading failure of shear instabilities with focal mechanisms similar as the GCMT solution.

Eighteen earthquakes in category two consist of sub-events with planar (the GCMT fault planes) distribution, but with focal mechanisms inconsistent with the plane. Those earthquakes cannot be interpreted as rupture in a fault plane. Spatial distributions of the sub-events of some of these earthquakes are also inconsistent with the geometry of the assumed meta-stable olivine wedge. For example, the spatial distribution of the inferred sub-events of E8 has a horizontal extension of ~50 km with an ~10˚ dip to the east, while the slab geometry is ~70˚ dip to the west (Fig. S4-8); and the spatial distribution of the inferred sub-events of E15 possess a horizontal dimension of ~70 km along ~N340˚W and a vertical extension of ~40 km with ~80˚ dipping to the east, while the slab geometry ~60˚ dips to the west along approximately the north direction. We suggest that the source processes of the earthquakes in this category cannot be explained by transformational faulting, similar to the inference based on the aftershock distribution of the 1994 Tonga earthquake (E1), which suggested the aftershock distribution totally cut out of the possible meta-stable olivine wedge (McGuire et al., 1997; Wiens et al., 1994). We suggest that the source processes of this category of earthquakes can also be best explained by a cascading failure of shear instability, same as category one. It is just that the shear thermal instabilities during this category of the earthquakes are aligned approximately along a plane, while those of the 2013 Okhotsk and 1994 Bolivia earthquakes are not.

Six earthquakes in category three (Tables S4-0, S4-4, S4-6, S4-7, S4-10, S4-14 and S4-18) consist of sub-events with planar distribution and focal mechanisms consistent with the plane. These events have relatively smaller magnitudes, source geometry and fewer sub-events. The inferred source processes of these earthquakes can be interpreted in many ways: rupture in a fault plane, transformational faulting or cascading failure in close space and time (as for the earthquakes in the first and second categories). It is interesting to note that the source processes still exhibit complex spatial and temporal relationship: two earthquakes (E4, E7) exhibit unilateral propagations (Tables S4-4, S4-7), two earthquakes (E10, E18) bilateral source processes (Tables S4-10, S4-18), one earthquake (E14) exhibit a backward propagation (Table S4-14) and one earthquake (E6) exhibits a backward-and-forward source process (Fig. 4-5a, Table S4-6).

4.5.2 Cascading failure of shear thermal instabilities as a unified physical mechanism for large deep-focus earthquakes.

While multiple mechanisms exist to explain the inferred source processes of some groups of deep-focus earthquakes, the seismic results of all large deep-focus earthquakes can be explained by a unified physical mechanism of cascading failure of shear thermal instabilities occurring within pre-existing weak zones. Shear thermal instability is a failure due to positive feedback between viscous heating and temperature dependent rheology (Kelemen and Hirth, 2007). Such feedback system is naturally influenced by perturbation of stress. An earthquake would generate static or dynamic stress change in the region, may trigger a cascading failure of shear instability in close space and time (Hill, 2008; Tibi et al., 2003b). Shear thermal instability can occur in a viscous medium with a uniform rheological property (Ogawa, 1987) or a pre-existing zone of different rheological properties (Kelemen and Hirth, 2007) which is known to exist within the subducted slab, due to either past faulting before subduction (Silver et al., 1995) or existence of preexisting fine-grained shear zones (Kelemen and Hirth, 2007). The focal mechanism of a shear instability that occurs in a uniform viscous medium would be controlled by the state of the medium before failure and the triggering force, while the focal mechanism of a shear instability that occurs in a medium with pre-existing weak zones would be controlled by the orientations of the pre-existing weak zones, as the pre-existing weak zones would prescribe the instability to occur in the weak zones. We suggest that the inferred source processes of these earthquakes are consistent with shear thermal instabilities in the pre-existing weak zones for the following reasons: 1) focal mechanism changes during the many large deep-focus earthquakes (the 2013 Okhotsk earthquake in category one and the earthquakes in category two). We argue that the triggering force for a single large earthquake unlikely trigger instabilities with various principle stress axes in a homogeneous viscous medium, but may do so in the pre-existing weak zones with various orientations; 2) it appears that the focal mechanisms of the sub-events are related to the locations of the sub-events, regardless of their hosting large-events. For example, the inferred sub-events of E9 beneath the Kuril-Izu-Bonin subducted slab exhibit two types of focal mechanisms, with one type (the second sub-event) similar to the focal mechanisms of the inferred sub-events of E11 (Fig. 4-6e). The second sub-event of E9 is 10 km south of E11 and 5 km to the north of the first sub-event of E9. There appears existent of location control of focal mechanism between south and north regions of the source region of E9. Location control of focal mechanism of the sub-events regardless of the hosting large earthquakes favors shear thermal instabilities in the medium with pre-existing weak zones over those in a homogeneous medium. In short, the inferred results of our studied events can be best explained by a cascading of shear thermal instabilities in pre-existing weak zones, with the perturbation of stress generated by a shear instability triggering another and the orientations of the pre-existing weak zones controlling the focal mechanisms of these instabilities.

In the context of shear instability in pre-existing weak zones as the physical mechanism of deep-focus earthquakes, we suggest that caution is needed to relate the focal mechanism of deep-focus earthquakes to the stress state in the subducted slabs. The observed great variability of focal mechanisms of small and large deep-focus earthquakes may just reflect existence of pre-existing weak zones with various orientations and may not necessarily be related to the ambient stress in the region of the earthquake sources.

4.6. Discussion

Evaluating the uniqueness of our multiple-CMT solutions is difficult, given the non-linear nature of our inversion approach, and we cannot exclude the possibility that other solutions exist that may fit that data equally well. In addition, we have chosen point sources to explain various energy packets, which may have been resulted from finite rupture. However, it is nonetheless useful to provide a set of solutions computed in a uniform way that fit the main features seen in the direct and depth phases for a large number of deep earthquakes. Base on the seismic result, we suggest that our results can be explained by a unified mechanism of cascading failure of shear thermal instabilities in pre-existing weak zones.

The mechanism of cascading failure of shear thermal instabilities can also explain previously noted features of some deep earthquakes: including great variability of focal mechanism in small distances, large CLVD (Compensated Linear Vector Dipole) component of the inferred moment tensor, and super-shear rupture. It also provides new insights as well.

Previous studies suggested that focal mechanisms of deep-focus earthquakes exhibit great variability in different slabs or in one slab (e.g. Frohlich, 2006; Myhill, 2013). Yu and Wen (2012) also reported that the focal mechanisms of the deep-focus earthquakes can vary significantly within a small distance. It is further noted in this study that focal mechanism also varies significantly during the occurrence of most large earthquakes, as manifested in the source processes of the events in categories one and two. In addition, focal mechanism also varies significantly between large earthquakes in a small distance. We illustrate this feature with the results of earthquake pairs that occurred in a close distance but with complex sub-event focal mechanisms (Fig. 4-6). We determine the relative location of the initiation points of these earthquake pairs based on differential onset times and a master relocation program (Wen, 2006). E25 is 20 km west to and 20 km deeper than E12 in the Tonga-Kermadec subducted slab (Fig. 4-6f). E12 occurred within normal faults, while E25 is dominated by strike-slip faulting (Tables S4-12, S4-25). E23 is 15 km west to and 20 km shallow than E22 in Sumatra-Java-Philippine subducted slab (Fig. 4-6b). The two earthquakes occurred with slightly different focal mechanisms (Tables S4-23, S4-22). Cascading failure of shear thermal instabilities in pre-existing weak zones would explain these observed features well. In the context of this mechanism, the strong variability of the observed focal mechanism reflects complex orientations of the pre-existing weak zones.

The great variability of focal mechanisms during large deep earthquakes can also be the reason of the existence of CLVD component in the GCMT moment tensor solutions of these earthquakes. Kuge and Kawakatsu (1990) reported that the CLVD component of a deep earthquake can be interpreted by the summation of two different double couple sub-events. Later studies further suggested that the CLVD components of shallow and deep earthquakes can be explained by source irregularities (Kuge and Kawakatsu, 1990; Kuge and Kawakatsu, 1992, 1993; Kuge and Lay, 1994). We compare the GCMT CLVDs and the CLVDs in the summed solution over the inferred focal mechanisms of the sub-events (Fig. 4-7a). CLVDs are similarly present in the summed solution for the events with large GCMT CLVDS, although CLVDs from the summed solutions are general smaller. The differences possibly lie on the different ways to represent the earthquake source and different frequency contents of the data used between the studies. Such comparison suggests that GCMT CLVDs may just reflect the variability of focal mechanisms during a large deep-focus earthquake.

Previous studies also suggested that source behavior and physical mechanisms may depend on slab temperature (Wiens, 2001; Wiens and Gilbert, 1996; Wiens and McGuire, 1995; Zhan et al., 2014a). Earthquakes within a warmer slab may be related to a lower rupture propagating velocity and some earthquakes may experience super-shear rupture. However, we find that the source propagating velocities are not correlative with slab temperature with super-shear rupture pervasive during many large earthquakes (Tables S4-1 – S4-26). For each inferred sub-event, we define its source propagating velocity as the ratio between distance separation of the sub-event from the earthquake initiation point, and the time difference between the peak time of the inferred sub-event and the earthquake initiation time. The source propagating velocities are mostly from 0.2 to 1.2 times of the S wave velocity in the source region, consistent with the previous studies (e.g., Frohlich, 2006). The inferred propagating velocity higher than S wave velocity corroborates well with the finding of super-shear rupture in a deep earthquake (Zhan et al., 2014b). Our results further indicate that high propagating velocity is widespread during the occurrence of large deep-focus earthquakes and occurs in various subduction zones. Propagation velocity is also heterogeneous during an earthquake and between the earthquakes in a particular region (Fig. 4-6). For example, beneath the South American subduction where slabs are warm, the 1994 Bolivia earthquake has propagating velocities of 0.9 – 1.6 km/s (Fig. 4-6a, Table S4-2), while event E15 occurring in the similar region in 2003 has propagating velocities from 1.8 to 5.6 km/s (Fig. 4-6a, Table S4-15). Beneath the Tonga-Kermadec subduction where slabs are cold, event E6 has propagating velocities between 1.1 and 3.0 km/s (Fig. 4-6c, Table S4-6), but event E19 has propagating velocities varying from 3.1 to 5.4 km/s (Fig. 4-6c, Table S4-19). We argue that this observed variability of propagating velocity of the sub-events and super-shear rupture do not require additional physical mechanisms for deep earthquakes, as the static or dynamic stress generated by the preceding sub-event(s) could trigger sub-events with various time delays (starting from 0 s by static stress triggering). In fact, some of the high source propagating velocity is not consistent with super-shear rupture when focal mechanism variation is considered. For example, the third sub-event of E19 has a source propagating velocity of 5.4 km/s, higher than S wave velocity (Table S4-19). However, its fault plane orientation is ~30° different from those of the first and second sub-events (Fig. 4-4, Table S4-19), making it unlikely a super-shear rupture on a fault plane.

We investigate the relationships of seismic moment with source duration and source dimension for these deep earthquakes (Figs. 4-7b and 4-7c). We define seismic moment (M) as the summed moments of the sub-events, source duration as peak time of the last sub-event from the initiation time plus its half duration, and source dimension as maximum distance separation among the sub-events. Source durations increase with seismic moments, roughly described by a relationship of M ~ duration^3 (Fig. 4-7b). The relationship is consistent with that of the previous studies (Figure 6.3 in Frohlich, 2006). Source dimensions and seismic moments can also be roughly described by a relationship of M ~ dimension^3 (Fig. 4-7c).

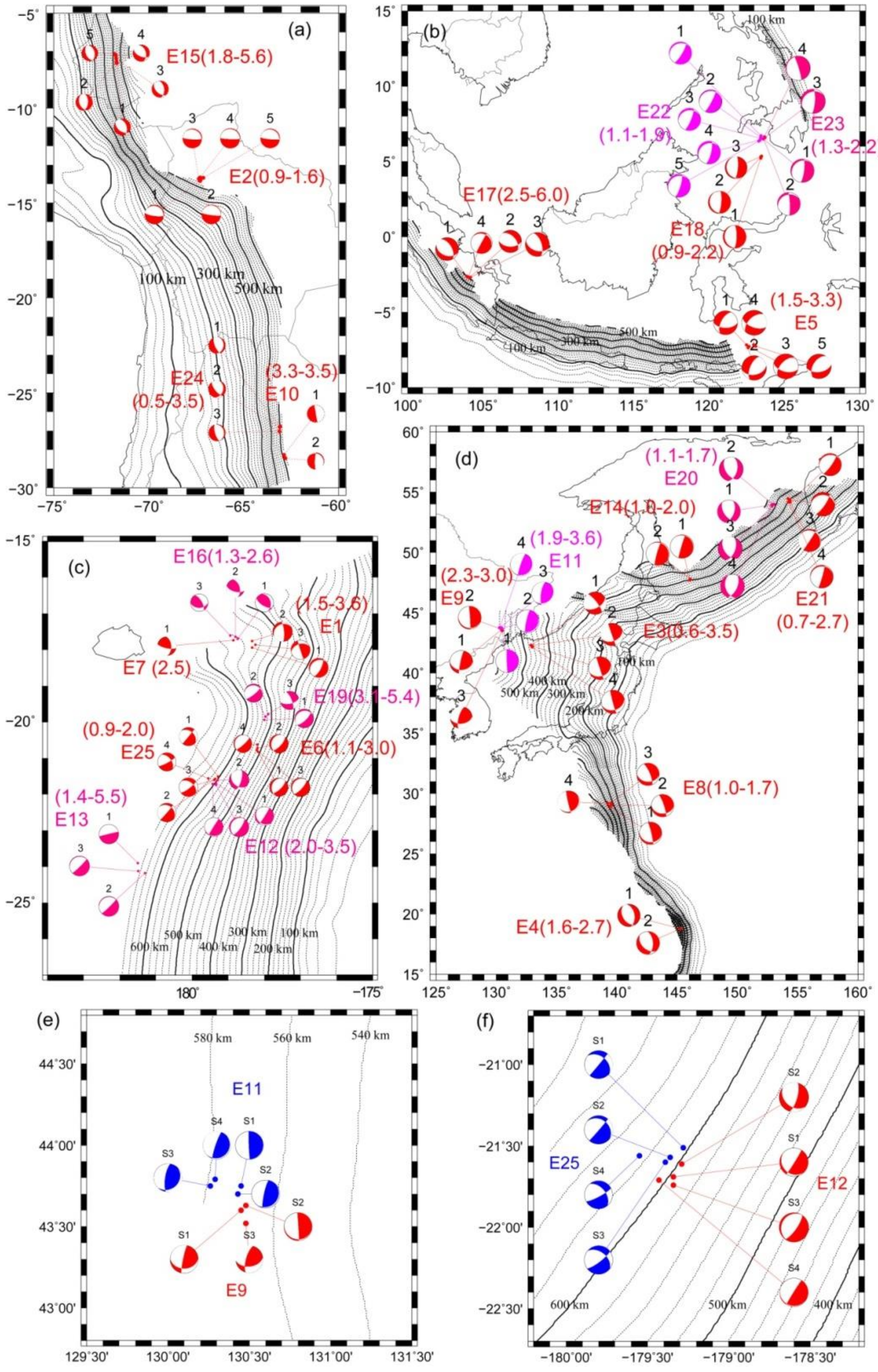

Fig. 4-6. Locations (points) and focal mechanisms (beach balls) of the inferred sub-events of the 25 deep earthquakes (labeled with event IDs as in Table S4-0 and inferred source propagating velocity ranges in parentheses) in four subducted slabs and two doublet-event areas, including (a) South American, (b) Sumatra-Java-Philippine, (c) Tonga-Kermadec, (d) Kuril-Izu-Bonin, (e) E9 and E11, and (f) E12 and E25, along with slab depth contours (black traces, labeled with slab depth). Sub-events are color coded with their hosting large earthquakes and labeled by the occurring sequence in the earthquake.

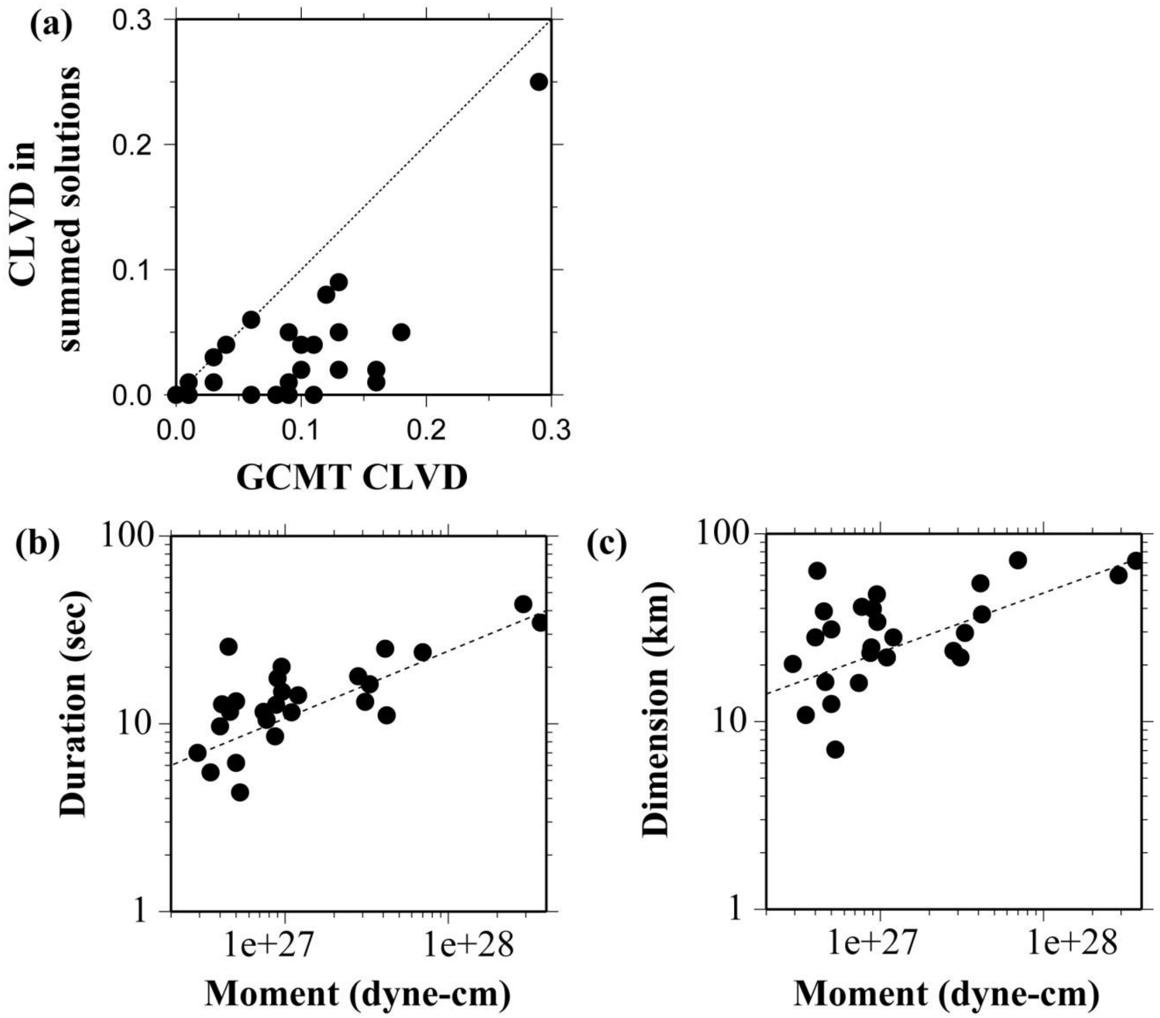

Fig. 4-7. (a) Comparison between GCMT CLVDs and CLVDs in the summed solution of the inferred focal mechanisms of the sub-events. (b-c) Relationships between seismic moment and (b) source duration and (c) source dimension. Circles represent the analyzed earthquakes (E1 – E25) and the Okhotsk earthquake (Table S4-0).

4.7. Conclusion

We apply a multiple source inversion method to study the source processes of 25 deep-focus earthquakes from 1994 to 2012, with Mw > 7.0 and depth > 400 km, based on waveform modeling of P, SH, pP and sSH waves. The multiple source inversion method treats a large earthquake as a combination of smaller sub-events in space and time, and resolves the spatio-temporal separation and focal mechanism of each sub-event, based on waveform modeling of seismic data. We show two aspects of the scientific approach are of particular importance in resolving the source process of a large deep earthquake: 1) combining the direct and near-surface reflected phases as seismic constraints, which is needed to resolve the depth distribution of the sub-events during a large earthquake, and 2) adopting the multiple source inversion, which makes no *a prior* assumption on the focal mechanism of the sub-events in waveform modeling and is capable of resolving the focal mechanism change during the earthquake.

All the studied deep-focus earthquakes can be modeled using one to eight sub-events. We classify these earthquakes into three categories based on the focal mechanisms and spatial distributions of the inferred sub-events: 1) category one, with non-planar spatial distribution and variable focal mechanisms of sub-events, represented by the Bolivia earthquake and the 2013 Mw 8.3 Okhotsk deep earthquake, 2) category two, with planar distribution but fault mechanisms of the sub-events inconsistent with the best-fitting plane, including eighteen earthquakes, and 3) category three, with planar distribution and focal mechanisms of sub-events consistent with the plane, including six earthquakes.

We discuss possible physical mechanisms for earthquakes in each category, including transformational faulting, shear instability in a homogeneous medium and shear instability in pre-existing weak zone. We suggest that the inferred results of all the studied events can be best explained by a cascading failure of shear thermal instabilities in pre-existing weak zones, with the perturbation of stress generated by a shear instability triggering another and the orientations of the pre-existing weak zones controlling the focal mechanisms of these instabilities. The proposed mechanism can also explain the observed great variability of focal mechanisms, large values of CLVD component and super-shear rupture of deep-focus earthquakes in the previous studies. We further suggest that caution is needed to relate the focal mechanism of deep-focus earthquakes to the stress state in the subducted slabs, as the observed great variability of focal mechanisms of small and large deep-focus earthquakes may just reflect existence of pre-existing weak zones with various orientations and may not necessarily be related to the ambient stress in the region of the earthquake sources. The relationships between seismic moment and source duration and dimension in large deep earthquakes can be roughly described as seismic moment ~ (source duration)^3 and moment ~ (source dimension)^3.

Chapter 5 Source process and physical mechanism of the initiated sub-events of global large deep-focus earthquakes

5.1. Abstract

We systematically study source process of 26 large deep-focus earthquakes with Mw > 7.0 and depth > 400 km, and classify them into three categories based on the presence of the initiation phases: 1) category one, with the weak initiation phases clear observed in most of the azimuths and their spatial distribution and focal mechanisms can be inferred (six earthquakes); 2) category two, with the weak initiation phases observable in some azimuths, but the azimuth range is not broad enough to infer reliable focal mechanisms and distribution of the phases (seven earthquakes); and 3) category three, without observable weak initiation phases. We model the source processes of the 6 earthquakes with clear weak initiation phases, with direct waves and near-surface reflected waves. The initiation sub-events exhibit complex source processes with variable fault plane orientations, as the major sub-events observed in our previous studies. The result suggests a relationship of M ~ (source dimension)^3. The stress drops of the initiation sub-events are not fundamentally different from those of the major sub-events. The stress drops of all the sub-events are variable between 2.5 MPa and 70 MPa (assume half shear wave velocity of the depth to be rupture velocity in bilateral faulting). We suggest that these deep-focus earthquakes are cascading failure of sub-events with different magnitudes. The initiation process is different from the shallow earthquakes, indicating that shear instability may be the potential physical mechanisms of these earthquakes.

5.2. Introduction

Occurrence of deep-focus earthquakes is unexpected under the temperature and pressure below the depth of 400 km (Scholz, 2002). Various models have been proposed to explain the occurrence of deep-focus earthquakes. Currently, two mechanisms are widely accepted, including transformational faulting (Green and Burnley, 1989; Green and Houston, 1995; Kirby, 1987; Wiens et al., 1993) and shear thermal instability (Hobbs and Ord, 1988b; Karato et al., 2001; Kelemen and Hirth, 2007; Ogawa, 1987). Shear instability accompanying transformational faulting is also proposed for deep-focus earthquakes (Green, 2007). Seismological studies provide important constraints on deep-focus earthquakes. The depth distribution of deep-focus earthquakes is consistent with the depth of olivine phase transformation in the mantle transition zone, naturally suggesting transformational faulting as a candidate (Estabrook, 2004). The possible existence of meta-stable olivine wedge in cold slabs is also supportive to transformational faulting (Iidaka and Suetsugu, 1992). However, the source geometry of the large deep-focus earthquakes are proposed to be inconsistent with the geometry of the meta-stable olivine wedge (Chen and Wen, 2015; Chen et al., 2014; Meng et al., 2014; Silver et al., 1995; Wiens et al., 1994), excluding transformation faulting as the mechanism. The low seismicity efficiency and high stress drop suggested that shear instability is the mechanisms of the 1994 Bolivia earthquake. In addition, the recent studies also suggested that different mechanisms may evolve in large deep-focus earthquakes simultaneously (Meng et al., 2014; Zhan et al., 2014a).

Previous studies mostly focus on the major energy release of deep-focus earthquakes, the initiation phases with one-order magnitude smaller were only reported during the 1994 Mw 8.2 Bolivia earthquake (Silver et al., 1995; Zhan et al., 2014a). Systematical investigation of the weak initiation phases potentially provides new insights on the mechanisms of global large deep-focus earthquakes. Comparison of the initiation phases and the major energy packets is helpful to understand the nucleation of deep-focus earthquakes. Previous studies of shallow earthquakes suggested that, many large subduction zone earthquakes begin with a "whimper" and grows rapidly into a devastating megathrust event (Chu et al., 2011). The size and mechanism of the beginning of an earthquake have direct relevance to the physics of earthquake nucleation (Ellsworth and Beroza, 1995). It is also useful to compare the initiation phases of deep-focus earthquake with those of shallow earthquakes.

The main objective of this study is to systematically investigate the size, focal mechanism and relative stress drop of global large deep-focus earthquakes. In the following sections, we present seismic data and observed weak initiation phases in section 5.3, spatio-temporal distribution and focal mechanisms of the initiation phases of the studied earthquakes in section 5.4, stress drops of the sub-events in section 5.5, and discussion and conclusion in section 5.6.

5.3. Seismic data and observed initiation phases

We re-visit 26 earthquakes with Mw > 7.0 and depth > 400 km from 1994 to 2013 (Fig. 1a and Table S0), whose major energy releases are studied in our previous studies (Chen and Wen, 2015; Chen et al., 2014). In this study, we further examine the weak initiation phases at the beginning of some analyzed earthquakes, whose moments are usually one-order smaller than those of the major energy packets.

The 26 events are classified into three categories based on the presence of the observed initiation phases and if their focal mechanisms are inferable: 1) category one, with clear weak initiation phases in most of the azimuth ranges (Fig. 5-1b), whose spatial distribution and focal mechanisms can be inferred (six earthquakes, blue beach balls in Fig. 5-1a); 2) category two, with the weak initiation phases observable in some azimuths (Fig. 5-1c) but the azimuth range is not broad enough to infer a reliable focal mechanisms and distribution of the initiation sub-events (seven earthquakes, green beach balls in Fig. 5-1a); and 3) category three, without observable weak initiation phases (thirteen earthquakes, red beach balls in Fig. 5-1a). The earthquakes have quite impulsive onsets (Fig. 5-1d). In the following sections, we study the properties of the weak initiation phases of the earthquakes in category one.

The studied events are well recorded by the Global Seismographic Network (GSN) (Figs. S5-1a – S5-6a). The data consist of broadband compressional waves (P), near-surface reflected compressional waves (pP), and transversally polarized shear waves (SH) recorded at teleseismic distances between 30° and 90°. The displacement seismograms are deconvolved with their respective instrument responses and bandpass filtered between 0.01 and 4 Hz. We selected the data with high signal-to-noise ratio (SNR) between the weak initiation phases and the data before the phase arrivals. The adopted P and SH wave data are with a good SNR > 5. The near-surface reflected waves are noisy, perhaps due to the coda of the direct waves. We used pP with a SNR > 2 (mostly > 3). Although SNR > 2 is somewhat low, we use correlation coefficients to capture the major features of the pP waves, since arrival times of the near-surface reflected wave are critical to determine the depths of the sub-events (Chen and Wen, 2015).

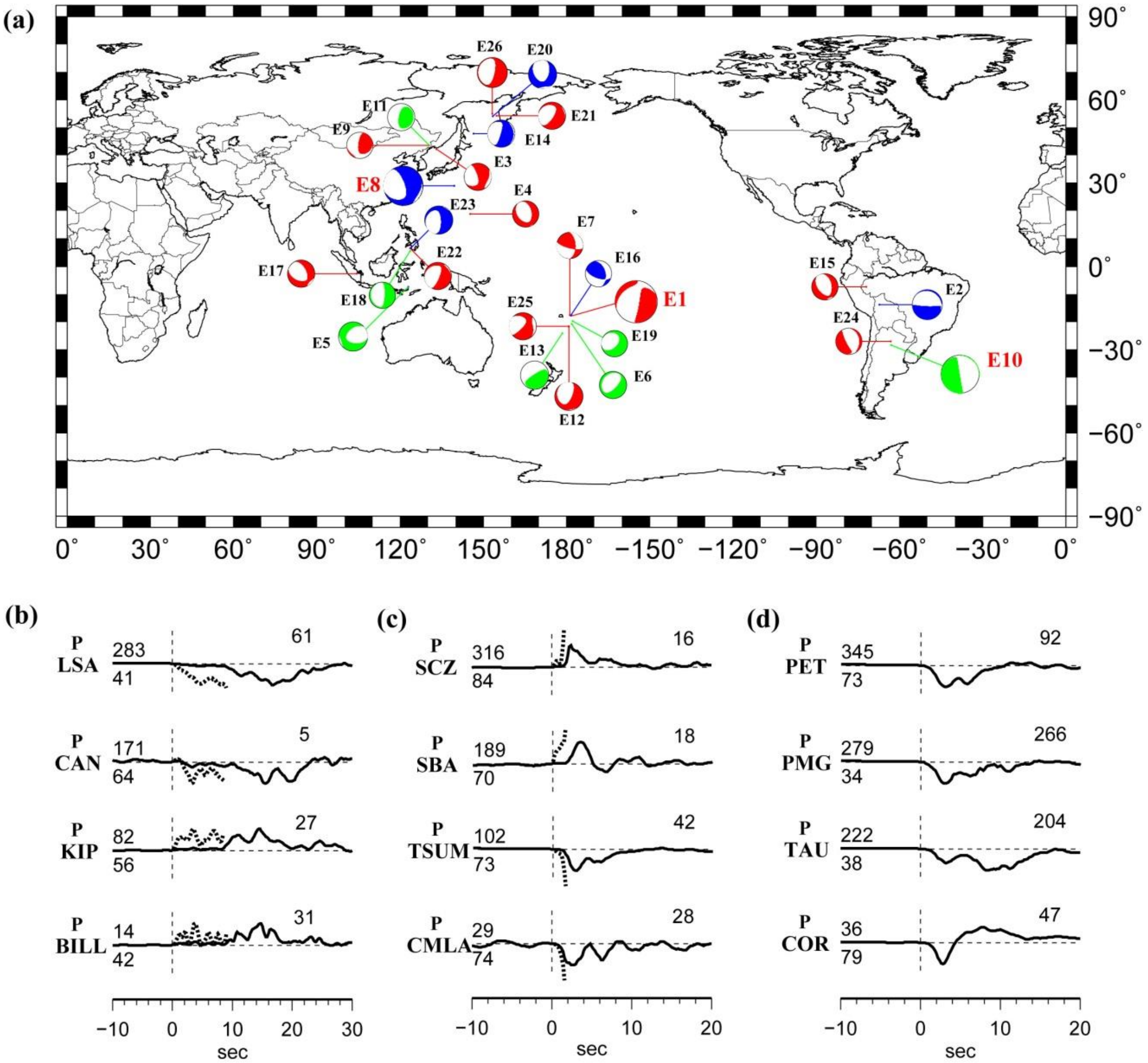

Fig. 5-1. (a) Distribution of the global large deep-focus earthquakes (Mw > 7 and depth > 400 km) from 1994 to 2013, and their GCMT focal mechanisms, labeled with event numbers in Table S4-0. The earthquakes labeled with blue, green and red represent the earthquakes in categories one to three. The events labeled with red numbers are the example events whose seismograms presented in (b), (c) and (d). (b), (c) and (d) Selected observed seismograms normalized by the maximum amplitudes of the seismograms (black traces) comparing with those normalized by the maximum amplitudes of the initiation phases (dash traces), for the earthquakes E8, E10 and E1, respectively.

5.4. Multiple source inversion

We apply a multiple point source inversion procedure to infer the source processes based on waveform fitting of direct and near-surface reflected waves (Chen et al., 2014). The method treats a large earthquake as a combination of multiple double couple point sources (sub-events) separated in space and time, and resolves the spatio-temporal separation and focal mechanism of each sub-event by modeling the seismic data. Seismic Green's functions are computed by the Generalized Ray Theory method (Helmberg, 1968), based on the velocity and attenuation structures of PREM (Preliminary Reference Earth Model, downloaded from IRIS EMC-PREM) (Dziewonski and Anderson, 1981). The seismic response of each sub-event is obtained by convolving the Green's function with source time function (half sine function) (Ji et al., 2002). The model parameters are searched by the simulated heat annealing algorithm for the best-fitting solution. We obtained the least misfit (root-mean-square) between the seismic data and the synthetics data for P, SH and sSH phases, while we apply both L2 norm and correlation coefficient for the pP phases to better resolve the arrival times of each sub-events, since the imperfect fitting of the weak initiation amplitudes.

Broadband P waves are aligned by the first-arrival onsets, which can be clearly identified and picked in the data high-pass filtered above 1 Hz. SH and pP phases are aligned iteratively in the inversion process: we first pick them based on PREM model (Dziewonski and Anderson, 1981) and perform a preliminary inversion with P wave heavily weighted over other phases. The alignments of pP and SH phases are adjusted based on the best match between synthetics and the data during the inversions, until no further adjustment observed from the previous inversion (Chen and Wen, 2015).

4, 5, 3, 2, 2 and 2 weak initiation sub-events are modeled before the major energy releases of the earthquakes E2, E8, E14, E16, E20 and E23, respectively (Table S5-1 – S5-6). We inferred the source processes of the initiation sub-events (green beach balls in Figs. S1b – S6b), and the major sub-events (red beach balls in Figs. S1b – S6b). The sub-events can be modeled by double couple point sources reasonably well. No significance of non-double-couple components has been found. The best fitting sub-event models of the earthquakes are presented in supplementary information (Table S5-1 – S5-6, Figs. S5-1b – S5-6b).

The inversion results show source processes with varying focal mechanisms and complex spatio-temporal distribution during these earthquakes (Table S5-1 – S5-6, Figs. S1b – S6b). The focal mechanisms of most the sub-events deviates within 30º from the GCMT solution. The sub-events propagate in variable directions, sometimes with backward and forward propagation. The 1994 Mw 8.2 Bolivia earthquake (E2) can be modeled by four initiation and five major sub-events distinguishable in the whole source process (Fig. 5-2b). The previous studies suggested that the earthquake begins with ~10s initiation with weak sub-events, followed by strong moment release lasting ~35 s (Chen and Wen, 2015; Silver et al., 1995; Zhan et al., 2014a). Our preferred source process exhibits a horizontal extension of 44 km and a vertical extension of 38 km, with non-planar distribution of the sub-event and their focal mechanism inconsistent with a single fault plane (Chen and Wen, 2015). The source process indicates an overall propagation to the northeast but with variable directions for each sub-event (Table S5-1). Sub-event I1 is close to the initiation point, and sub-events I2, I3 and I4 are to the east of sub-event I1. Sub-events S1 and S2 are close to sub-event I4, but sub-event S3 is to the northwest of sub-events S1 and S2. Sub-events S4 and S5 are to the further northeast. The focal mechanisms of all the sub-events are variable within 10° from the GCMT solution. The initiation sub-events have moments in the order of 10^{26} dyne·cm, while the major sub-events have those in the order of 10^{27} dyne·cm.

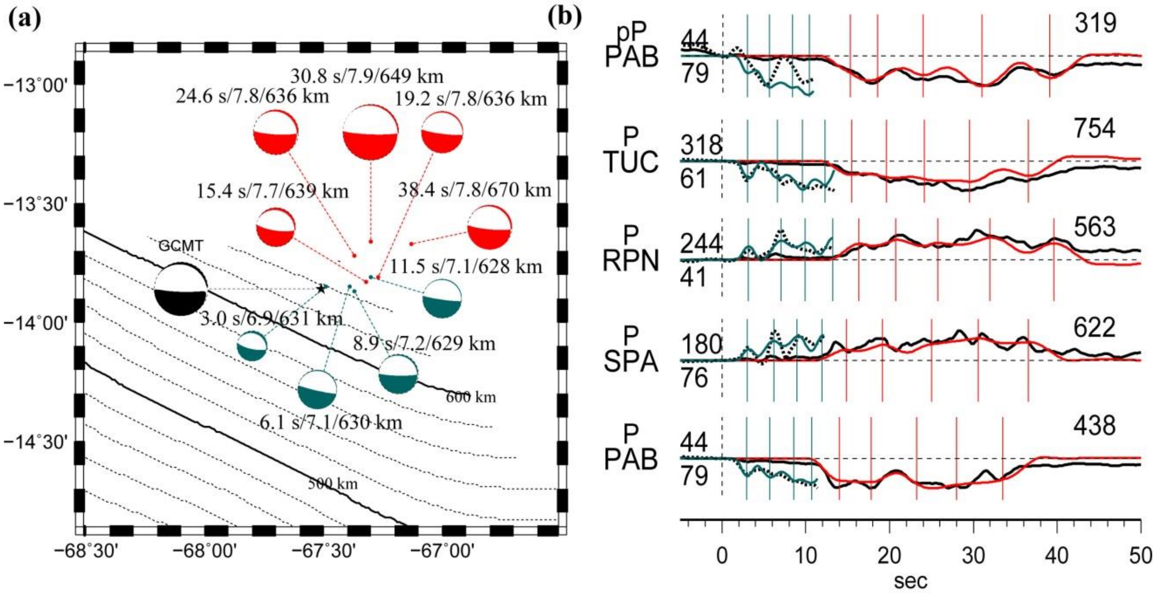

Fig. 5-2 (a) Locations of the major sub-events (red points) and the initiation sub-events (green points) of the best fitting model, and the initiated location (black star) of the 1994 Bolivia earthquake (E2), along with slab depth contours (black traces, labeled with slab depths). Black beach ball describes GCMT solution of the event. Red and green beach balls represent inferred focal mechanisms of the major sub-events and the initiation sub-events of the best-fitting model, labeled with the sub-event peak time/moment magnitude/depth. (b) Selected observed seismograms normalized by the maximum amplitudes of the major sub-events and the initiation sub-events in Fig. S5-1 (black traces) comparing with synthetics (red traces) predicted by the inferred major sub-events and synthetics (green traces) predicted by the inferred initiation sub-events. The red and green lines label the peak times of the sub-events predicted by the major sub-events and the initiation sub-events of the best-fitting model in Fig. S1. Amps represent the maximum amplitudes of the whole seismograms.

Another example is the 20 Aug 1998 Mw 7.0 earthquake beneath Bonin Islands region (Table S4-0). The earthquake has a duration of 29 s, relatively longer than those of the other deep-focus earthquakes with similar moment magnitudes (Chen and Wen, submitted). The earthquake has a complex spatio-temporal distribution of the sub-events. Sub-event I1 is close to the initiation point; sub-event I2 is ~5 km to the northeast of the initiation point; sub-events I3, I4 and I5 propagate back and sub-event I5 is close to the initiation point and sub-event I1. It is interesting to note that sub-events I1 and I5 may be close to each other within 3 km, but with different focal mechanisms. Sub-events S1, S2, S3 and S4 distribute around the initiation point in various directions. The focal mechanisms of all the sub-events deviate within 15° from the GCMT solution. The initiation sub-events have moments in the order of 10^{24} dyne·cm, while the major sub-events with moments in the order of 10^{25} dyne·cm.

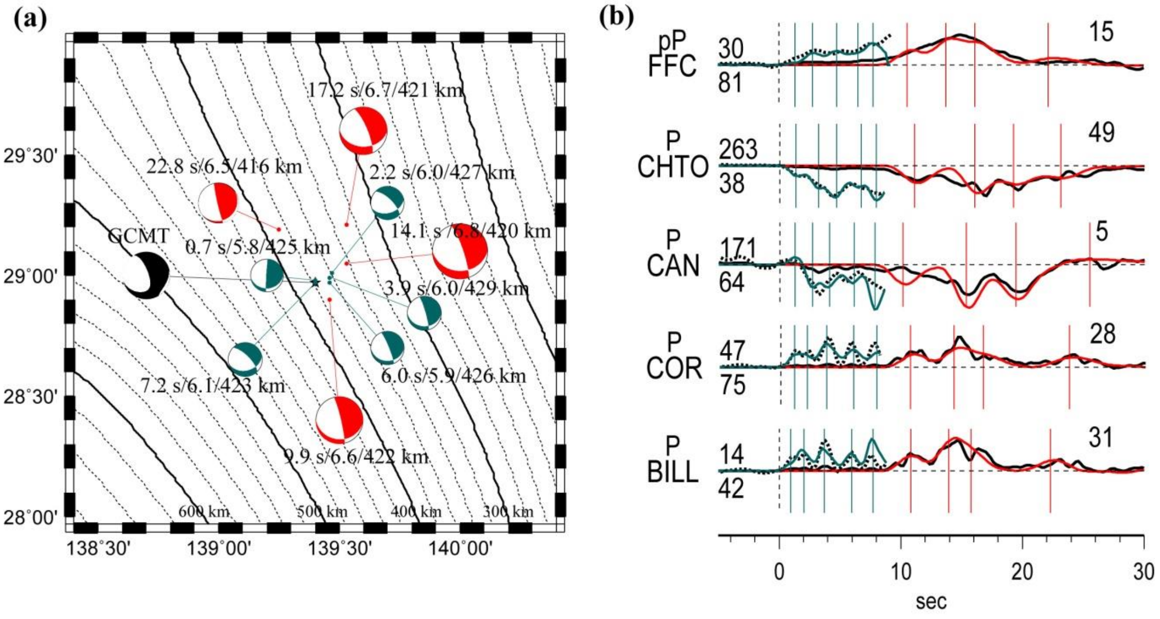

Fig. 5-3. Similar as Fig. 5-2, except for event E8. (c) Selected waveform comparisons in Fig. S5-2.

5.5. Moment-duration relationship and static stress drops

Stress drop is a fundamental scaling parameter of the earthquakes, relating to the dynamic characteristics of rupture, slip, velocity and acceleration (Scholz, 2002). It is of great importance to estimate the relative stress drops, in order to understand the difference between the initiation and the major process of large deep-focus earthquakes.

If we assume that each sub-event faults in a circular patch, we adopt a relationship $M_0=(16/7)\cdot\Delta\sigma\cdot a^3$ (Eshelby, 1957). M_0 is seismic moment, $\Delta\sigma$ is stress drop, and a is the radius of a circular patch. Previous studies suggested that the average rupture velocity for deep earthquake is about 0.6 times shear wave velocity (Frohlich, 2006; Vallee, 2013). We adopt a decelerating model for a circular fault (Boatwright, 1980). The radius a is equal to $v \cdot t \cdot \left(\frac{v-1}{v}\right)^{\frac{1}{2}}$, where v is the rupture velocity roughly equal to 3 km/s at the depth, and t is the duration of the sub-event.

We plot a figure with moment-dimension relationship (Fig. 5-4). The moments are the summed inferred seismic moments of the sub-events, and the dimensions are the inferred radii of the sub-events. It is evident that source dimensions increase with seismic moments, described by a relationship of M ~ dimension^3, consistent with previous studies (e.g., Frohlich, 2006), indicating that stress drop is approximately constant and independent of the sub-event magnitude.

We find that the stress drops of the sub-events are variable within the range between 2.5 MPa and 70 MPa. No fundamental difference of the stress drops are observed between the initiation and the major sub-events. The stress drops of the sub-events of the Bolivia earthquake (circles in Fig. 5-4) are roughly consistent with the stress drop of 15 MPa (dash line in Fig. 5-4). We also observe that the initiation sub-events of the Bolivia earthquake have similar dimensions and moments as the major sub-events of the other earthquakes (Fig. 5-4). The stress drops of the initiation sub-events of earthquake E8 (red inverted triangles in Fig. 5-4) are much lower than those of the major sub-events (black inverted triangles in Fig. 5-4), while the stress drops of the initiation sub-events of earthquake E16 (red squares in Fig. 5-4) are much higher than those of the major sub-events (black squares in Fig. 5-4).

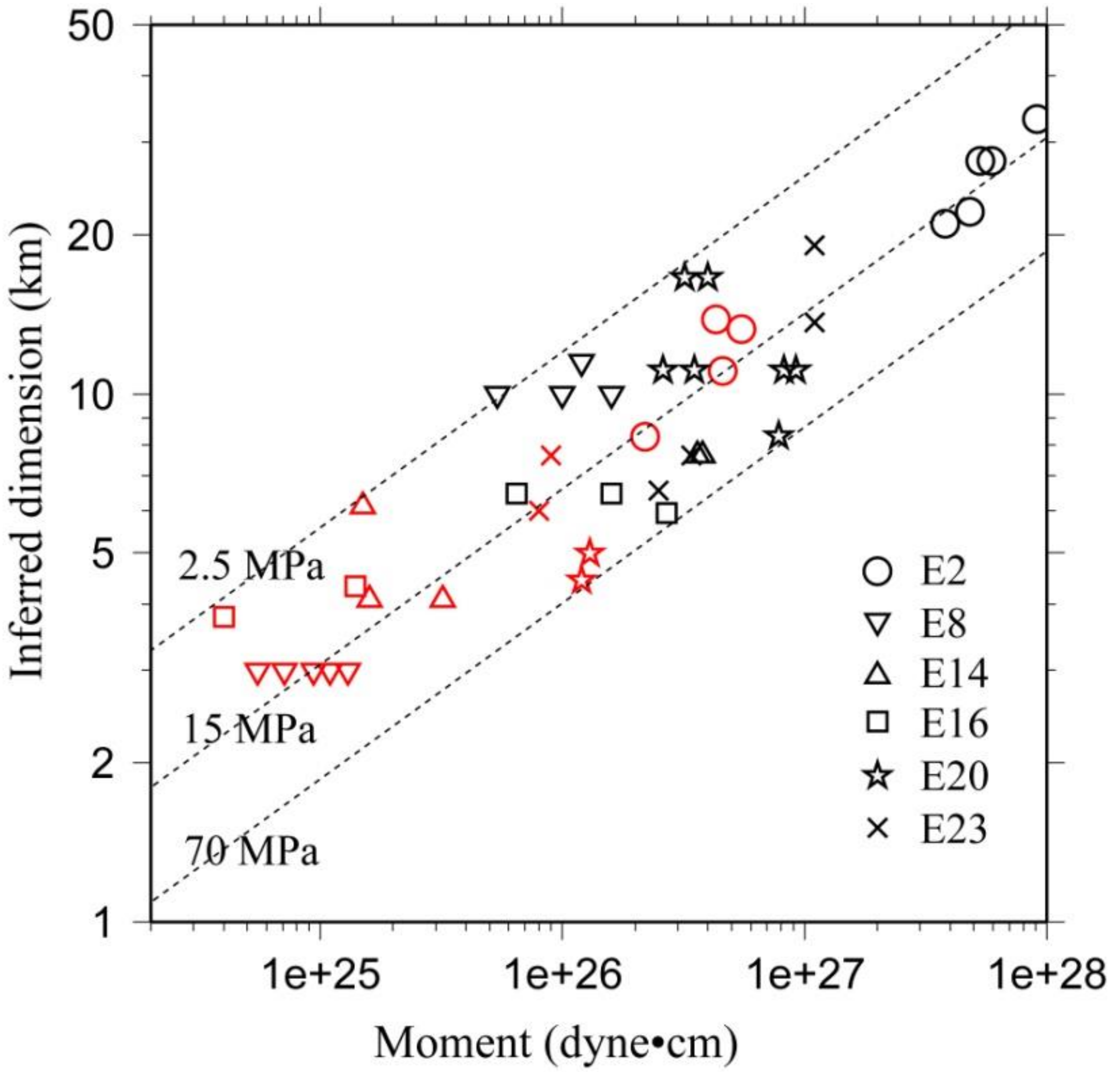

Fig. 5-4. Relationships between seismic moment and source duration of the best-fitting initiation and major sub-events of the earthquakes. Circles, inverted triangles, triangles, squares, stars and crosses represent the initiation sub-events (red) and the major sub-events (black) of earthquakes E2, E8, E14, E16, E20 and E23, respectively.

5.6. Discussion

The previous studies suggested that focal mechanisms of deep-focus earthquakes exhibit great variability in a close distance (Myhill, 2013; Yu and Wen, 2012). The great variability may be owing to orientation of the pre-existing weak zones (Chen and Wen, submitted) or great heterogeneity within the slab (Myhill, 2013). There is great variability among the focal mechanisms of the sub-events during the analyzed earthquakes. For example, the nine sub-events of earthquake E8 can be divided into three groups with similar focal mechanisms. Sub-events I1 and S4 can be classified into one group, sub-event I2, I3 and I4 into one group, and sub-event I5, S2, S3 and S4 into another group. The focal mechanisms deviate up to 30º from the GCMT solution. For example, the major sub-events of earthquake E14 are normal faulting (red beach balls in Fig. S5-3), while its initiation sub-events are combination of normal fault and strike-slip fault (green beach balls in Fig. S5-3). The great variability of focal mechanisms may be best explained by shear instabilities occurring on the pre-existing faulting (Chen and Wen, 2015).

The moment-dimension relationship is generally consistent with the previous studies (e.g. Frohlich, 2006, Vallee, 2013). The stress drops and strain rates are not fundamentally different between the initiation and major sub-events. The initiation sub-events of the great Bolivia earthquakes have the similar seismic moments and durations as the major sub-events of the other smaller earthquakes (E8, E14, E16, E20 and E23). Furthermore, the initiation sub-events of earthquakes E8, E14, E16, E20 and E23 can still be fit within the range between 2.5 MPa and 70 MPa. The relationship indicates that the initiation sub-events are not fundamentally different from the major sub-events, only with different magnitudes. The initiation process may be different from the shallow earthquakes (Scholz, 2002). The large deep-focus earthquakes can be best explained by a cascading failure of the sub-events with different magnitudes.

Six earthquakes are with clear weak initiation sub-events, seven earthquakes are with weak initiation sub-events observed in some azimuths, and thirteen earthquakes with impulsive onsets. First of all, the distribution of the three categories is not correlated with the subducted slabs or geographical locations. For example, E22 and E23 occurred 20 km apart, with E22 in category three and E23 in category one. No evidence shows that they are different types of earthquakes. One possible explanation is that the initiation sub-events are not necessary for deep-focus earthquakes and deep-focus earthquakes consist of smaller sub-events with different magnitudes, with a triggering relationship.

In addition, the spatio-temporal distribution of each earthquake (Table S5-1 – S5-6) is inconsistent with a unified source propagating velocity, which may also imply a triggering relationship. Overall, we suggest that the inferred results of our studied events can be best explained by a cascading of shear thermal instabilities in pre-existing weak zones, with the perturbation of stress generated by a shear instability triggering another and the orientations of the pre-existing weak zones controlling the focal mechanisms of these instabilities.

5.7. Conclusion

We investigate 26 deep-focus earthquakes from 1994 to 2013, with Mw > 7.0 and depth > 400 km. The earthquakes are classified into three categories in the presence of initiation phases: 1) category one, with clear initiation phases in most of the azimuth ranges, whose spatial distribution and focal mechanisms can be inferred, 2) category two, with the initiation phases observable in some azimuths but the azimuth range is not good enough to infer a reliable results, and 3) category three, without any observable initiation phases.

We apply our multiple source inversion method to study the source initiation processes of the six earthquakes (E2, E8, E14, E16, E20 and E23) in category one, based on waveform modeling of P, SH and pP waves. The initiation phases of the 6 studied deep-focus earthquakes can be modeled using two to five double couple point sources. The inferred sub-event models exhibit great complexity, with a complex spatio-temporal distribution and deviation of focal mechanisms up to 30º from the GCMT solutions.

We study the moment-duration relationship of all the sub-events of the analyzed earthquakes. All the sub-events can be fit within a range between 2.5 MPa and 70 MPa. The initiation sub-events are not fundamentally distinguishable from the major sub-events. The relationship suggests that the earthquakes consist of smaller sub-events with various magnitudes.

We further discuss that no correlation has been found between the earthquakes in different categories and geographical locations. We suggest that the inferred results of all the studied events can be best explained by a cascading failure of shear thermal instabilities in pre-existing weak zones, with the perturbation of stress generated by a shear instability triggering another and the orientations of the pre-existing weak zones controlling the focal mechanisms of these instabilities.

Reference

Antolik, M., Dreger, D., Romanowicz, B., 1996. Finite fault source study of the great 1994 deep Bolivia earthquake. Geophysical Research Letters 23, 1589-1592.

Antolik, M., Dreger, D., Romanowicz, B., 1999. Rupture processes of large deep-focus earthquakes from inversion of moment rate functions. Journal of Geophysical Research-Solid Earth 104, 863-894.

Boatwright, J., 1980. SPECTRAL THEORY FOR CIRCULAR SEISMIC SOURCES - SIMPLE ESTIMATES OF SOURCE DIMENSION, DYNAMIC STRESS DROP, AND RADIATED SEISMIC ENERGY. Bulletin of the Seismological Society of America 70, 1-27.

Brudzinski, M.R., Thurber, C.H., Hacker, B.R., Engdahl, E.R., 2007. Global prevalence of double Benioff zones. Science 316, 1472-1474.

Chen, M., Tromp, J., Helmberger, D., Kanamori, H., 2007. Waveform modeling of the slab beneath Japan. Journal of Geophysical Research-Solid Earth 112, 19.

Chen, Y., Wen, L., 2015. Global large deep-focus earthquakes: Source process and cascading failure of shear instability as a unified physical mechanism. Earth and Planetary Science Letters 423, 134-144.

Chen, Y., Wen, L., Ji, C., 2014. A cascading failure during the 24 May 2013 great Okhotsk deep earthquake. Journal of Geophysical Research-Solid Earth 119, 3035-3049.

Chu, R., Wei, S., Helmberger, D.V., Zhan, Z., Zhu, L., Kanamori, H., 2011. Initiation of the great M w 9.0 Tohoku–Oki earthquake. Earth and Planetary Science Letters 308, 277-283.

Dziewonski, A.M., Anderson, D.L., 1981. Preliminary reference Earth model. Physics of the Earth and Planetary Interiors 25, 297-356.

Ellsworth, W., Beroza, G., 1995. Seismic evidence for an earthquake nucleation phase. Science 268, 851-855.

Eshelby, J.D., 1957. The determination of the elastic field of an ellipsoidal inclusion, and related problems. Proceedings of the Royal Society of London Series a-Mathematical and Physical Sciences 241, 376-396.

Estabrook, C.H., 1999. Body wave inversion of the 1970 and 1963 South American large deep-focus earthquakes. Journal of Geophysical Research-Solid Earth 104, 28751-28767.

Estabrook, C.H., 2004. Seismic constraints on mechanisms of deep earthquake rupture. Journal of Geophysical Research-Solid Earth 109.

Frohlich, C., 2006. Deep earthquakes. Cambridge university press.

Goes, S., Ritsema, J., 1995. A broad-band P-wave analysis of the large deep Fiji island and Bolivia earthquakes OF 1994. Geophysical Research Letters 22, 2249-2252.

Green, H.W., 2007. Shearing instabilities accompanying high-pressure phase transformations and the mechanics of deep earthquakes. Proceedings of the National Academy of Sciences of the United States of America 104, 9133-9138.

Green, H.W., Burnley, P.C., 1989. A new self-organizing mechanism for deep-focus earthquakes. Nature 341, 733-737.

Green, H.W., Houston, H., 1995. The mechanisms of deep earthquakes. Annual Review of Earth and Planetary Sciences 23, 169-213.

Green, H.W., II, Chen, W.-P., Brudzinski, M.R., 2010. Seismic evidence of negligible water carried below 400-km depth in subducting lithosphere. Nature 467, 828-831.

Hayes, G.P., Wald, D.J., Johnson, R.L., 2012. Slab1.0: A three-dimensional model of global subduction zone geometries. Journal of Geophysical Research-Solid Earth 117, 15.

Helmberg, D.V., 1968. The crust-mantle transition in Bering sea. Bulletin of the Seismological Society of America 58, 179-214.

Hill, D.P., 2008. Dynamic stresses, Coulomb failure, and remote triggering. Bulletin of the Seismological Society of America 98, 66-92.

Hobbs, B.E., Ord, A., 1988a. PLASTIC INSTABILITIES - IMPLICATIONS FOR THE ORIGIN OF INTERMEDIATE AND DEEP-FOCUS EARTHQUAKES. Journal of Geophysical Research-Solid Earth and Planets 93, 10521-10540.

Hobbs, B.E., Ord, A., 1988b. Plastic instabilities - implications for the origin of intermedite and deep focus earthquakes. Journal of Geophysical Research-Solid Earth and Planets 93, 10521-10540.

Iidaka, T., Suetsugu, D., 1992. Seismological evidence for metastable olivine inside a subducting slab. Nature 356, 593-595.

Ji, C., Wald, D.J., Helmberger, D.V., 2002. Source description of the 1999 Hector Mine, California, earthquake, part I: Wavelet domain inversion theory and resolution analysis. Bulletin of the Seismological Society of America 92, 1192-1207.

Jiao, W.J., Silver, P.G., Fei, Y.W., Prewitt, C.T., 2000. Do intermediate- and deep-focus earthquakes occur on preexisting weak zones? An examination of the Tonga subduction zone. Journal of Geophysical Research-Solid Earth 105, 28125-28138.

Jung, H., Green, H.W., Dobrzhinetskaya, L.F., 2004. Intermediate-depth earthquake faulting by dehydration embrittlement with negative volume change. Nature 428, 545-549.

Kanamori, H., Anderson, D.L., Heaton, T.H., 1998. Frictional melting during the rupture of the 1994 Bolivian earthquake. Science 279, 839-842.

Karato, S., Riedel, M.R., Yuen, D.A., 2001. Rheological structure and deformation of subducted slabs in the mantle transition zone: implications for mantle circulation and deep earthquakes. Physics of the Earth and Planetary Interiors 127, 83-108.

Kawakatsu, H., 1991. Insignificant isotropic component in the moment tensor of deep earthquakes. Nature 351, 50-53.

Kelemen, P.B., Hirth, G., 2007. A periodic shear-heating mechanism for intermediate-depth earthquakes in the mantle. Nature 446, 787-790.

Kennett, B., Engdahl, E., 1991. Traveltimes for global earthquake location and phase identification. Geophysical Journal International 105, 429-465.

Kirby, S.H., 1987. Localized polymorphic phase-transformation in high-pressure faults and applications to the physical-mechanism of deep earthquakes. Journal of Geophysical Research-Solid Earth and Planets 92, 13789-13800.

Kirby, S.H., Stein, S., Okal, E.A., Rubie, D.C., 1996. Metastable mantle phase transformations and deep earthquakes in subducting oceanic lithosphere. Reviews of Geophysics 34, 261-306.

Kuge, K., Kawakatsu, H., 1990. Analysis of a deep “non double couple” earthquake using very broadband data. Geophysical Research Letters 17, 227-230.

Kuge, K., Kawakatsu, H., 1992. Deep and intermediate-depth non-double couple earthquakes - interpretation of moment tensor inversions using various passbands of very broad-band seismic data. Geophysical Journal International 111, 589-606.

Kuge, K., Kawakatsu, H., 1993. Significance of non-double couple components of deep and intermediate-depth earhtquakes - implications from moment tensor inversions of long-period seismic waves. Physics of the Earth and Planetary Interiors 75, 243-266.

Kuge, K., Lay, T., 1994. Systematic non-double-couple components of earthquakes mechanisms : The role of fault zone irregularity. Journal of Geophysical Research-Solid Earth 99, 15457-15467.

McGuire, J.J., Wiens, D.A., Shore, P.J., Bevis, M.G., 1997. The March 9, 1994 (M-w 7.6), deep Tonga earthquake: Rupture outside the seismically active slab. Journal of Geophysical Research-Solid Earth 102, 15163-15182.

Meade, C., Jeanloz, R., 1989. Acoustic emissions and shear instabilities during phase-transformations in Si and Ge at ultrahigh pressures. Nature 339, 616-618.

Meade, C., Jeanloz, R., 1991. Deep-focus earthquakes and recycling of water into the earths mantle. Science 252, 68-72.

Meng, L., Ampuero, J.-P., Buergmann, R., 2014. The 2013 Okhotsk deep-focus earthquake: Rupture beyond themetastable olivinewedge and thermally controlled rise time near the edge of a slab. Geophysical Research Letters 41, 3779-3785.

Meng, L., Ampuero, J.P., Stock, J., Duputel, Z., Luo, Y., Tsai, V.C., 2012. Earthquake in a Maze: Compressional Rupture Branching During the 2012 M-w 8.6 Sumatra Earthquake. Science 337, 724-726.

Myhill, R., 2013. Slab buckling and its effect on the distributions and focal mechanisms of deep-focus earthquakes. Geophysical Journal International 192, 837-853.

Myhill, R., Warren, L.M., 2012. Fault plane orientations of deep earthquakes in the Izu-Bonin-Marianas subduction zone. Journal of Geophysical Research-Solid Earth 117.

Ogawa, M., 1987. Shear instability in a viscoelastic material as the cause of deep-focus earthquakes. Journal of Geophysical Research-Solid Earth and Planets 92, 13801-13810.

Peacock, S.M., 2001. Are the lower planes of double seismic zones caused by serpentine dehydration in subducting oceanic mantle? Geology 29, 299-302.

Raleigh, C., Paterson, M., 1965. Experimental deformation of serpentinite and its tectonic implications. Journal of Geophysical Research 70, 3965-3985.

Scholz, C.H., 2002. The mechanics of earthquakes and faulting. Cambridge university press.

Silver, P.G., Beck, S.L., Wallace, T.C., Meade, C., Myers, S.C., James, D.E., Kuehnel, R., 1995. Rupture characteristics of the deep Bolivian earthquake of 9 June 1994 and the mechanisms of deep-focus earthquakes. Science 268, 69-73.

Tibi, R., Bock, G., Wiens, D.A., 2003a. Source characteristics of large deep earthquakes: Constraint on the faulting mechanism at great depths. Journal of Geophysical Research-Solid Earth 108, 25.

Tibi, R., Wiens, D.A., Hildebrand, J.A., 2001. Aftershock locations and rupture characteristics of the 1995 Mariana deep earthquake. Geophysical Research Letters 28, 4311-4314.

Tibi, R., Wiens, D.A., Inoue, H., 2003b. Remote triggering of deep earthquakes in the 2002 Tonga sequences. Nature 424, 921-925.

Vallee, M., 2013. Source time function properties indicate a strain drop independent of earthquake depth and magnitude. Nature communications 4, 2606-2606.

Wadati, K., 1928. shallow and deep earthquakes. Geophys. Mag 1, 161-202.

Wadati, K., 1929. shallow and deep earthquakes (2nd paper). Geophys. Mag 2, 1-36.

Warren, L.M., Hughes, A.N., Silver, P.G., 2007. Earthquake mechanics and deformation in the Tonga-Kermadec subduction zone from fault plane orientations of intermediate- and deep-focus earthquakes. Journal of Geophysical Research-Solid Earth 112.

Warren, L.M., Langstaff, M.A., Silver, P.G., 2008. Fault plane orientations of intermediate-depth earthquakes in the Middle America Trench. Journal of Geophysical Research-Solid Earth 113.

Wei, S.J., Helmberger, D., Zhan, Z.W., Graves, R., 2013. Rupture complexity of the M-w 8.3 sea of okhotsk earthquake: Rapid triggering of complementary earthquakes? Geophysical Research Letters 40, 5034-5039.

Wen, L., 2006. Localized temporal change of the Earth's inner core boundary. Science 314, 967-970.

Wiens, D.A., 1998. Source and aftershock properties of the 1996 Flores Sea deep earthquake. Geophysical Research Letters 25, 781-784.

Wiens, D.A., 2001. Seismological constraints on the mechanism of deep earthquakes: temperature dependence of deep earthquake source properties. Physics of the Earth and Planetary Interiors 127, 145-163.

Wiens, D.A., Gilbert, H.J., 1996. Effect of slab temperature on deep-earthquake aftershock productivity and magnitude-frequency relations. Nature 384, 153-156.

Wiens, D.A., McGuire, J.J., 1995. The 1994 Bolivia and Tonga events - fundamental different types of deep earthquakes. Geophysical Research Letters 22, 2245-2248.

Wiens, D.A., McGuire, J.J., Shore, P.J., 1993. Evidence for transformational faulting from a deep double seismic zone in Tonga. Nature 364, 790-793.

Wiens, D.A., McGuire, J.J., Shore, P.J., Bevis, M.G., Draunidalo, K., Prasad, G., Helu, S.P., 1994. A deep earthquake aftershock sequence and implications for the rupture mechanism of deep earthuqakes. Nature 372, 540-543.

Ye, L., Lay, T., Kanamori, H., Koper, K.D., 2013. Energy Release of the 2013 Mw 8.3 Sea of Okhotsk Earthquake and Deep Slab Stress Heterogeneity. Science 341, 1380-1384.

Yu, W.-c., Wen, L., 2012. Deep-Focus Repeating Earthquakes in the Tonga-Fiji Subduction Zone. Bulletin of the Seismological Society of America 102, 1829-1849.

Yue, H., Lay, T., Koper, K.D., 2012. En echelon and orthogonal fault ruptures of the 11 April 2012 great intraplate earthquakes. Nature 490, 245-249.

Zhan, Z., Kanamori, H., Tsai, V.C., Helmberger, D.V., Wei, S., 2014a. Rupture complexity of the 1994 Bolivia and 2013 Sea of Okhotsk deep earthquakes. Earth and Planetary Science Letters 385, 89-96.

Zhan, Z.W., Helmberger, D.V., Kanamori, H., Shearer, P.M., 2014b. Supershear rupture in a M-w 6.7 aftershock of the 2013 Sea of Okhotsk earthquake. Science 345, 204-207.

Supplementary Information

Supplementary figures for Chapter 2 include:

Figs. S2-1 to S2-4

Supplementary tables and figures for Chapter 3 include:

Tables S3-1 to S3-5

Figs. S3-1 to S3-6

Supplementary information for Chapter 4 include:

Tables S4-0 to S4-26

Figs. S4-1 to S4-26

Supplementary tables and figures for Chapter 5 include:

Tables S5-1 to S5-6

Figs. S5-1 to S5-6

Supplementary Figures for Chapter 2

(Fig. S2-1)

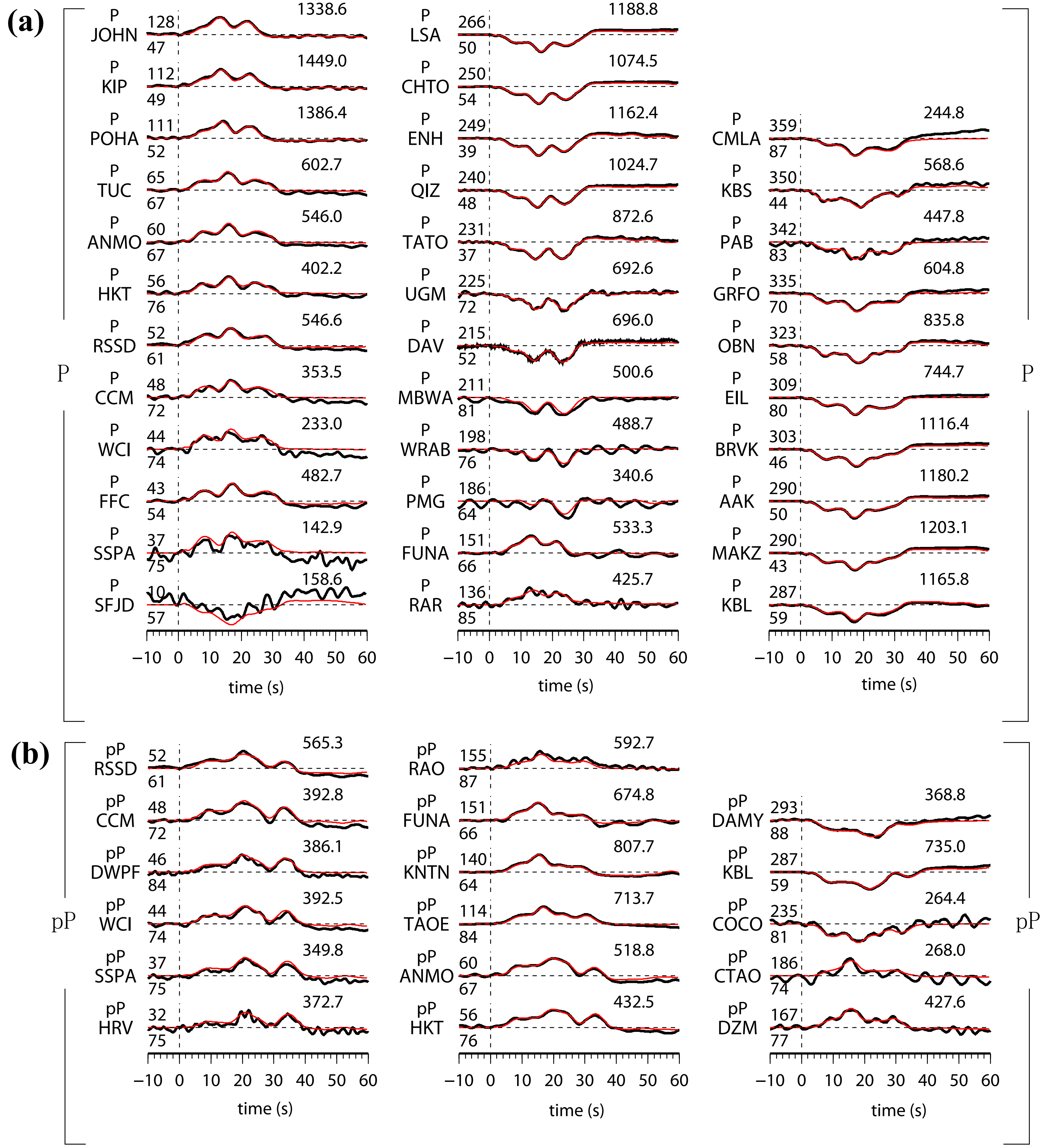

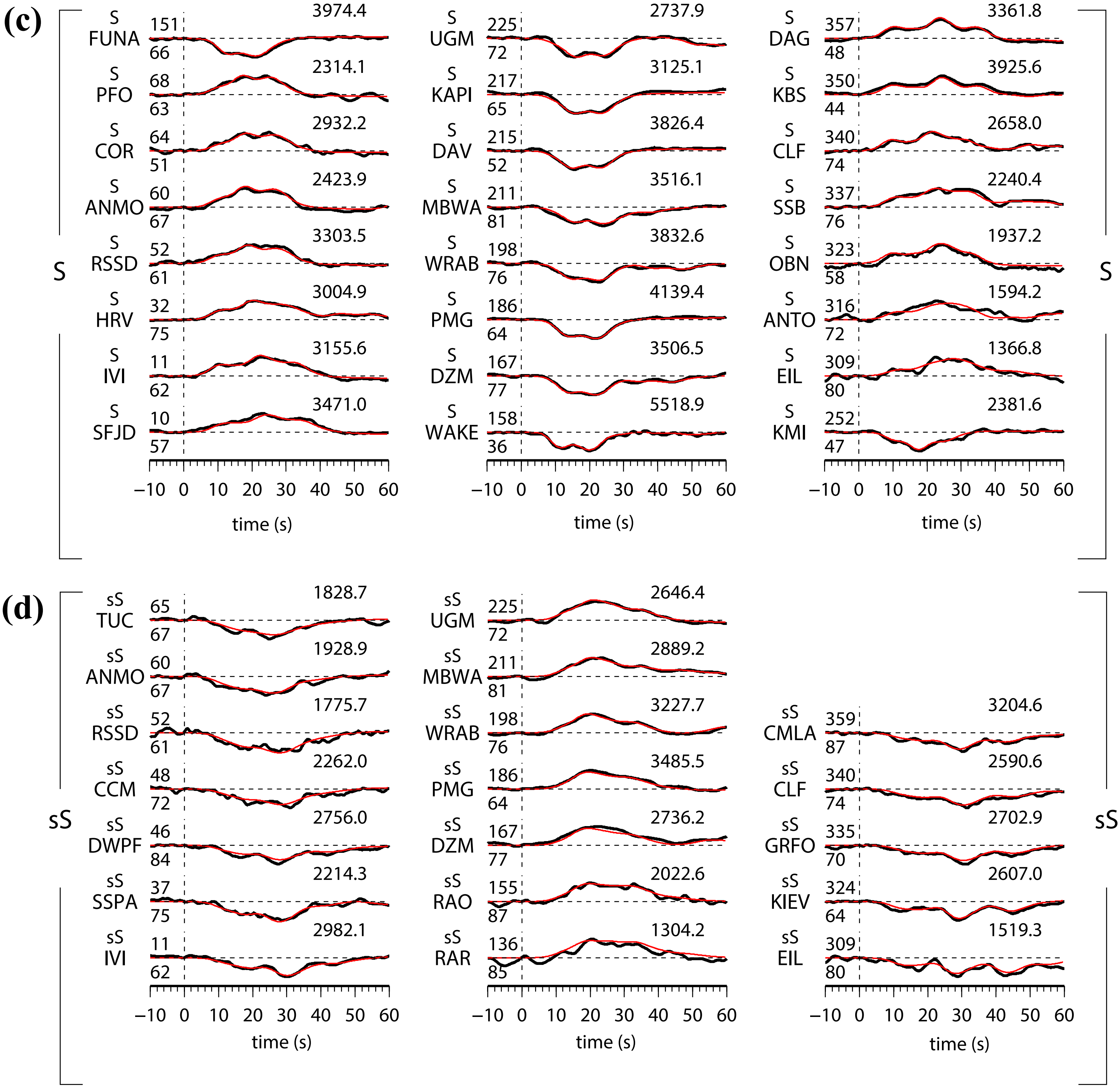

Fig. S2-1. Synthetics (black traces) of the test model (Table 2-1) comparing with synthetics (red traces) predicted based on the inverted six subevent model (Table 2-2) based on fitting the synthetics of the test model for, (a) P phase (vertical displacement), (b) pP phase (vertical displacement), (c) SH phase (tangential displacement), and (d) sSH phase (tangential displacement).

(Fig. S2-2)

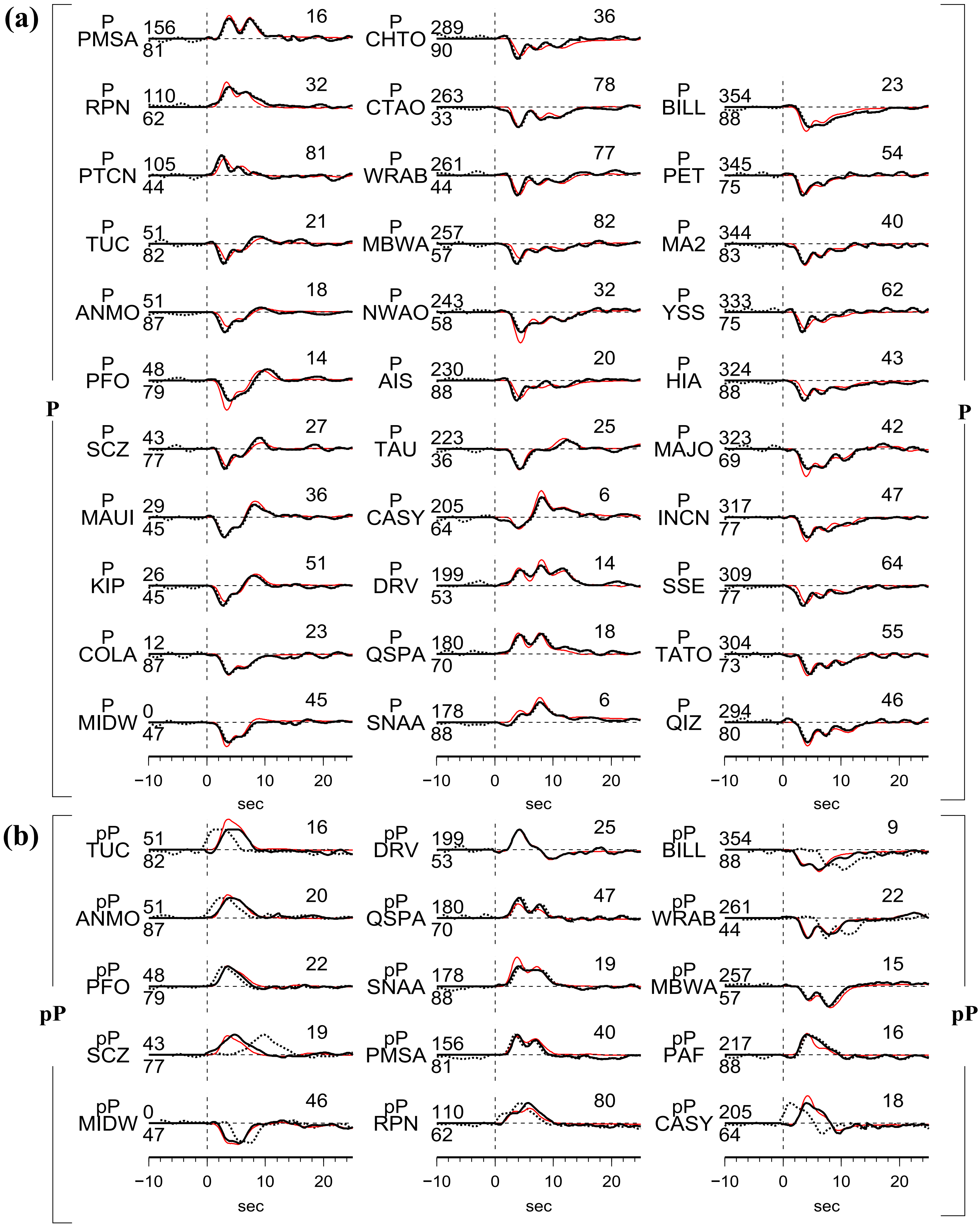
(a)
P
PMSA
156
81
16
P
CHTO
289
90
36
P
RPN
110
62
32
P
CTAO
263
33
78
P
BILL
354
88
23
P
PTCN
105
44
81
P
WRAB
261
44
77
P
PET
345
75
54
P
TUC
51
82
21
P
MBWA
257
57
82
P
MA2
344
83
40
P
ANMO
51
87
18
P
NWAO
243
58
32
P
YSS
333
75
62
P
PFO
48
79
14
P
AIS
230
88
20
P
HIA
324
88
43
P
SCZ
43
77
27
P
TAU
223
36
25
P
MAJO
323
69
42
P
MAUI
29
45
36
P
CASY
205
64
6
P
INCN
317
77
47
P
KIP
26
45
51
P
DRV
199
53
14
P
SSE
309
77
64
P
COLA
12
87
23
P
QSPA
180
70
18
P
TATO
304
73
55
P
MIDW
0
47
45
P
SNAA
178
88
6
P
QIZ
294
80
46
−10
0
10
20
sec
P
P
(b)
pP
TUC
51
82
16
pP
DRV
199
53
25
pP
BILL
354
88
9
pP
ANMO
51
87
20
pP
QSPA
180
70
47
pP
WRAB
261
44
22
pP
PFO
48
79
22
pP
SNAA
178
88
19
pP
MBWA
257
57
15
pP
SCZ
43
77
19
pP
PMSA
156
81
40
pP
PAF
217
88
16
pP
MIDW
0
47
46
pP
RPN
110
62
80
pP
CASY
205
64
18
−10
0
10
20
sec
pP
pP

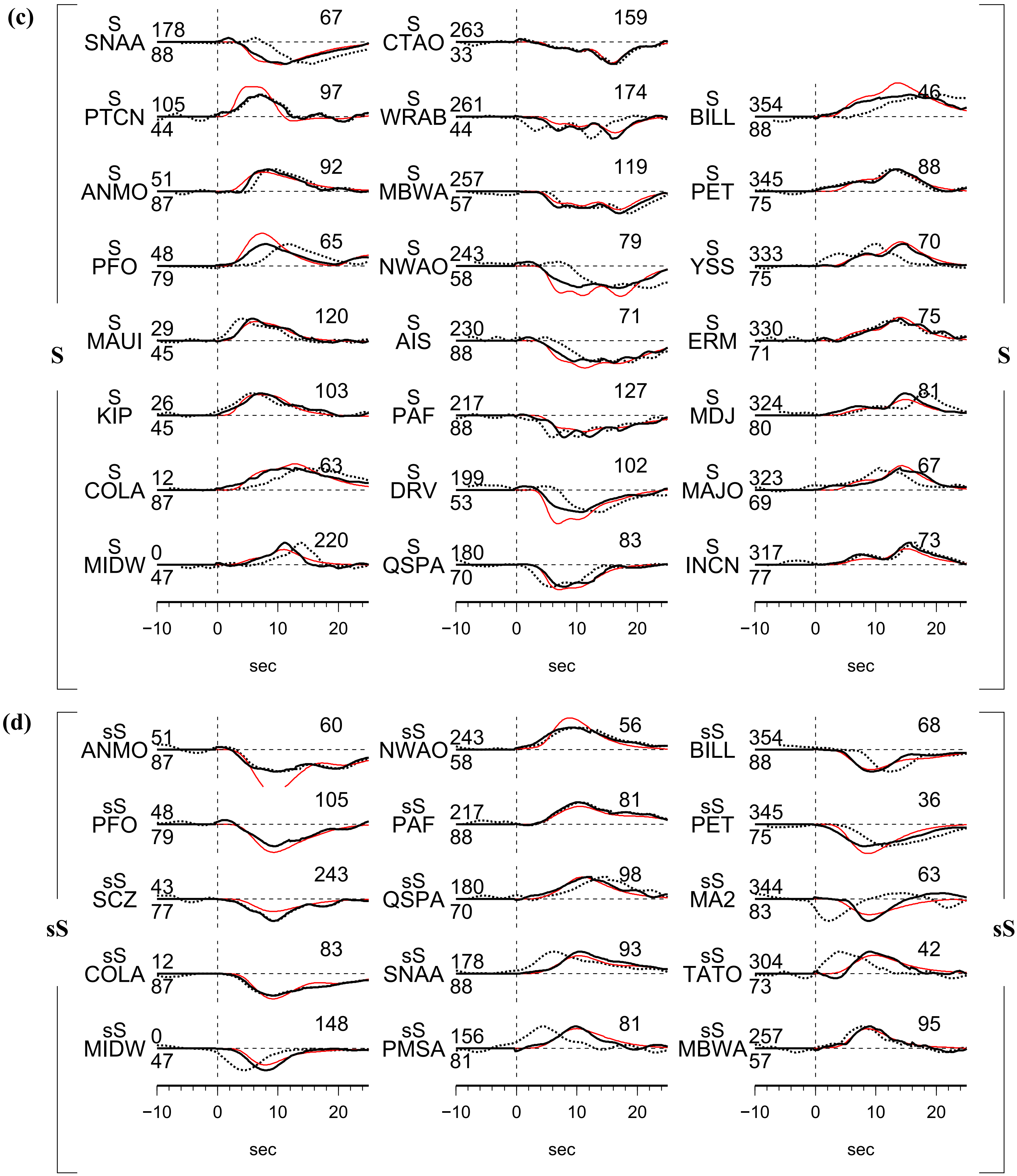

Figs. S2-2. (a) – (d) Synthetic seismograms in presence of noise, large initial misalignments and waveform distortions (black dash traces) comparing with synthetics (red traces) predicted by the best-fitting source model and synthetic seismograms aligned by iterative inversion procedure (black traces), for (a) P waves, (b) pP waves, (c) SH waves and (d) sSH waves.

(Fig. S2-3)

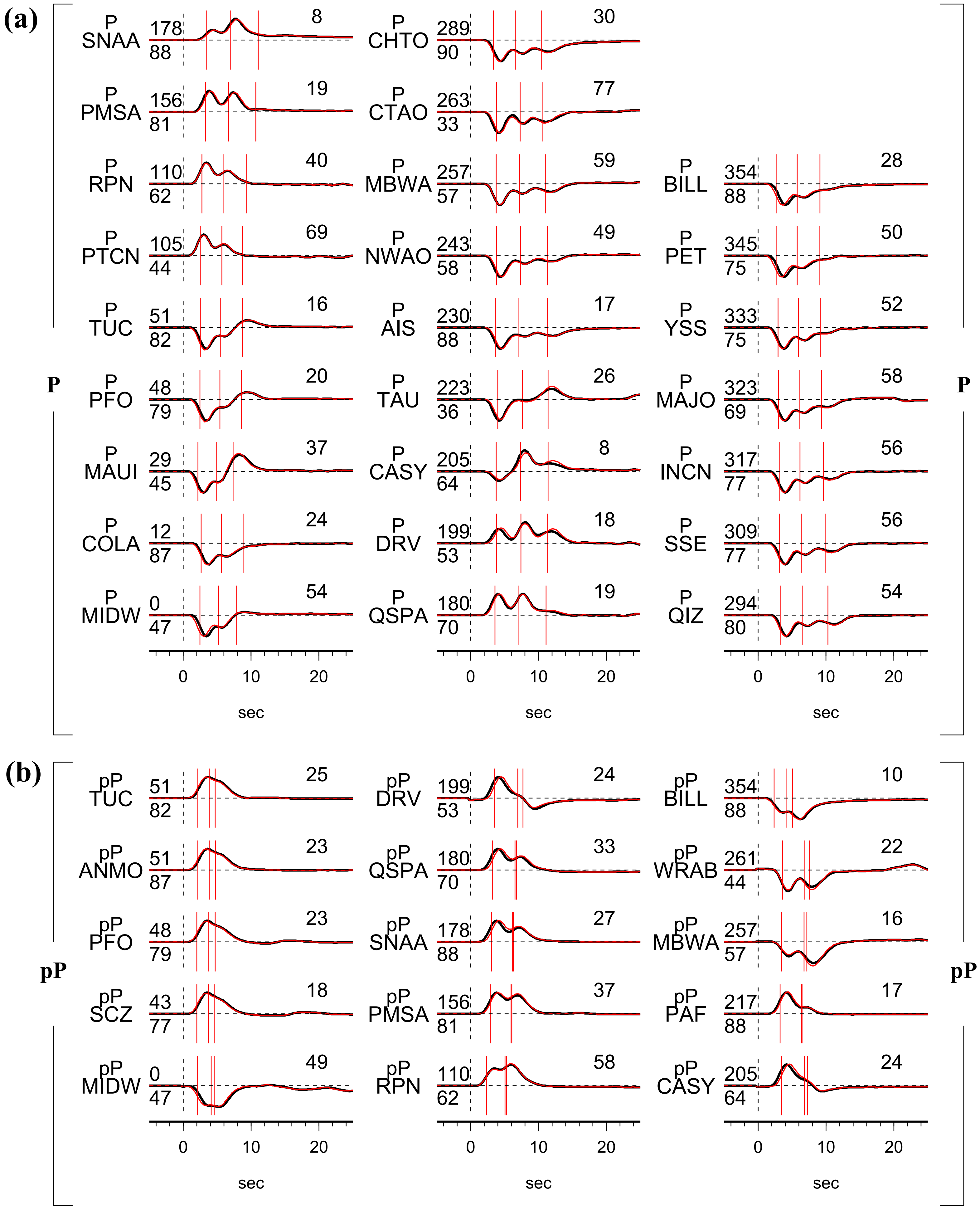
(a)
P
P SNAA 178 88 8
P CHTO 289 90 30
P PMSA 156 81 19
P CTAO 263 33 77
P RPN 110 62 40
P MBWA 257 57 59
P BILL 354 88 28
P PTCN 105 44 69
P NWAO 243 58 49
P PET 345 75 50
P TUC 51 82 16
P AIS 230 88 17
P YSS 333 75 52
P PFO 48 79 20
P TAU 223 36 26
P MAJO 323 69 58
P MAUI 29 45 37
P CASY 205 64 8
P INCN 317 77 56
P COLA 12 87 24
P DRV 199 53 18
P SSE 309 77 56
P MIDW 0 47 54
P QSPA 180 70 19
P QIZ 294 80 54
0
10
20
sec
(b)
pP
pP TUC 51 82 25
pP DRV 199 53 24
pP BILL 354 88 10
pP ANMO 51 87 23
pP QSPA 180 70 33
pP WRAB 261 44 22
pP PFO 48 79 23
pP SNAA 178 88 27
pP MBWA 257 57 16
pP SCZ 43 77 18
pP PMSA 156 81 37
pP PAF 217 88 17
pP MIDW 0 47 49
pP RPN 110 62 58
pP CASY 205 64 24
0
10
20
sec

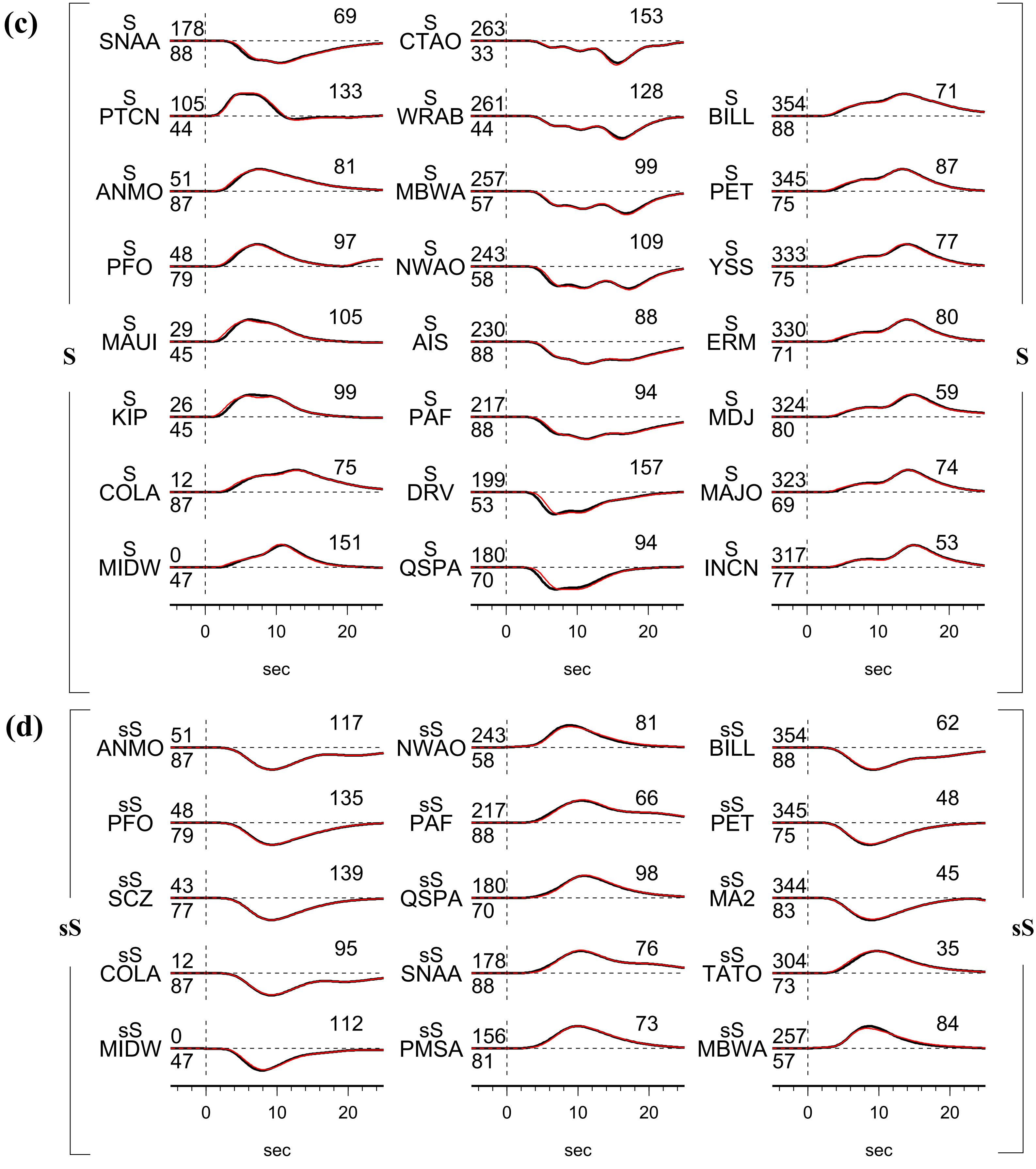

Figs. S2-3. (a) The misfits (RMS) of amplitudes between the synthetics predicted by the best-fitting model, and the synthetics predicted by the inferred model with sub-event 1 moved 0 – 10 km away from it best-fitting location. (b) – (e) Synthetics (black traces) preditected by the best-fitting model comparing with synthetics (red traces) predicted by the inferred modeled with sub-event 1 moved 5 km away from its best-fitting location, for (b) P waves, (c) pP waves, (d) SH waves and (e) sSH waves.

(Fig. S2-4)

(a)

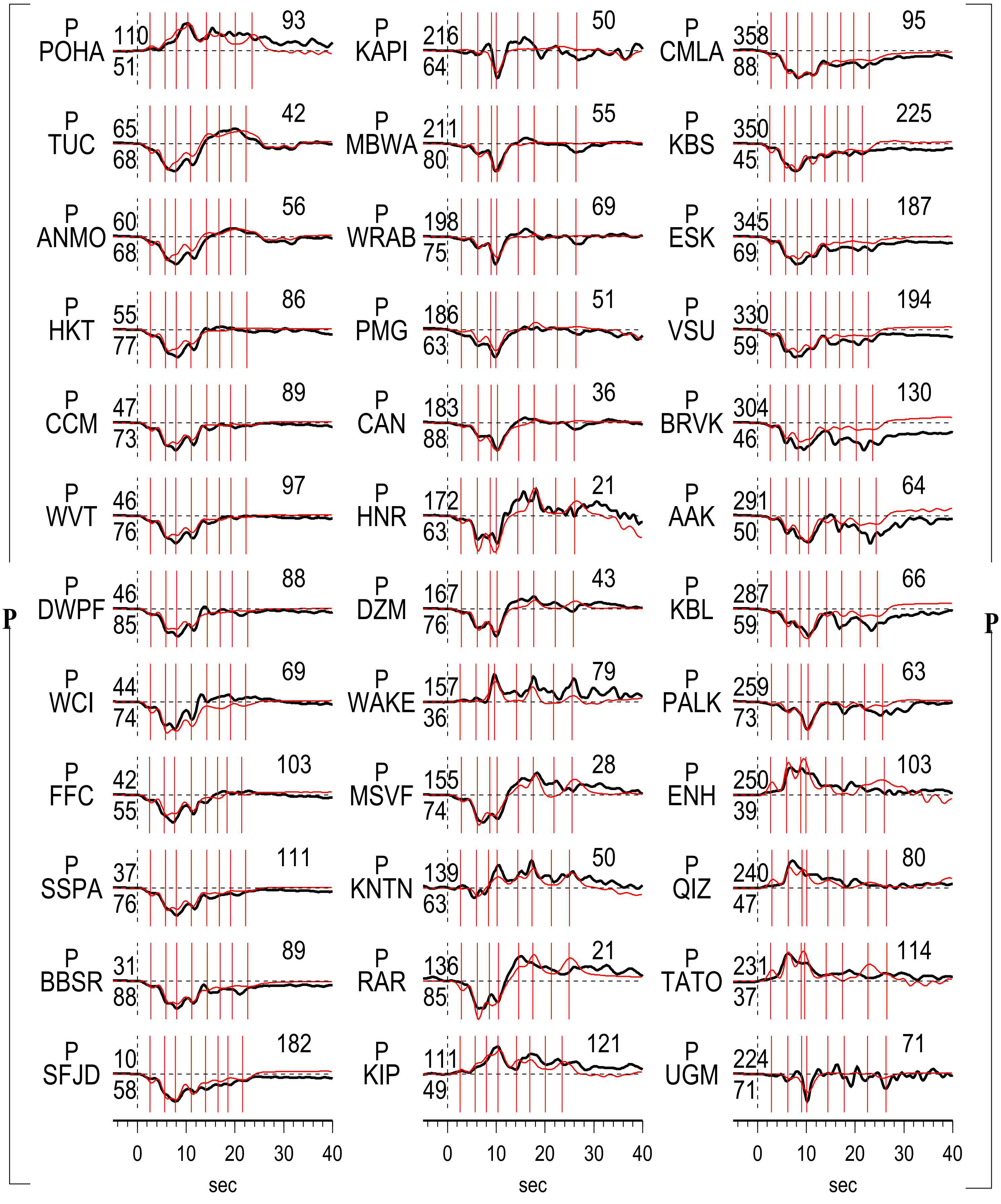
P
POHA
110
51
93
P
KAPI
216
64
50
P
CMLA
358
88
95
P
TUC
65
68
42
P
MBWA
211
80
55
P
KBS
350
45
225
P
ANMO
60
68
56
P
WRAB
198
75
69
P
ESK
345
69
187
P
HKT
55
77
86
P
PMG
186
63
51
P
VSU
330
59
194
P
CCM
47
73
89
P
CAN
183
88
36
P
BRVK
304
46
130
P
WVT
46
76
97
P
HNR
172
63
21
P
AAK
291
50
64
P
DWPF
46
85
88
P
DZM
167
76
43
P
KBL
287
59
66
P
WCI
44
74
69
P
WAKE
157
36
79
P
PALK
259
73
63
P
FFC
42
55
103
P
MSVF
155
74
28
P
ENH
250
39
103
P
SSPA
37
76
111
P
KNTN
139
63
50
P
QIZ
240
47
80
P
BBSR
31
88
89
P
RAR
136
85
21
P
TATO
231
37
114
P
SFJD
10
58
182
P
KIP
111
49
121
P
UGM
224
71
71
0
10
20
30
40
sec
P
P

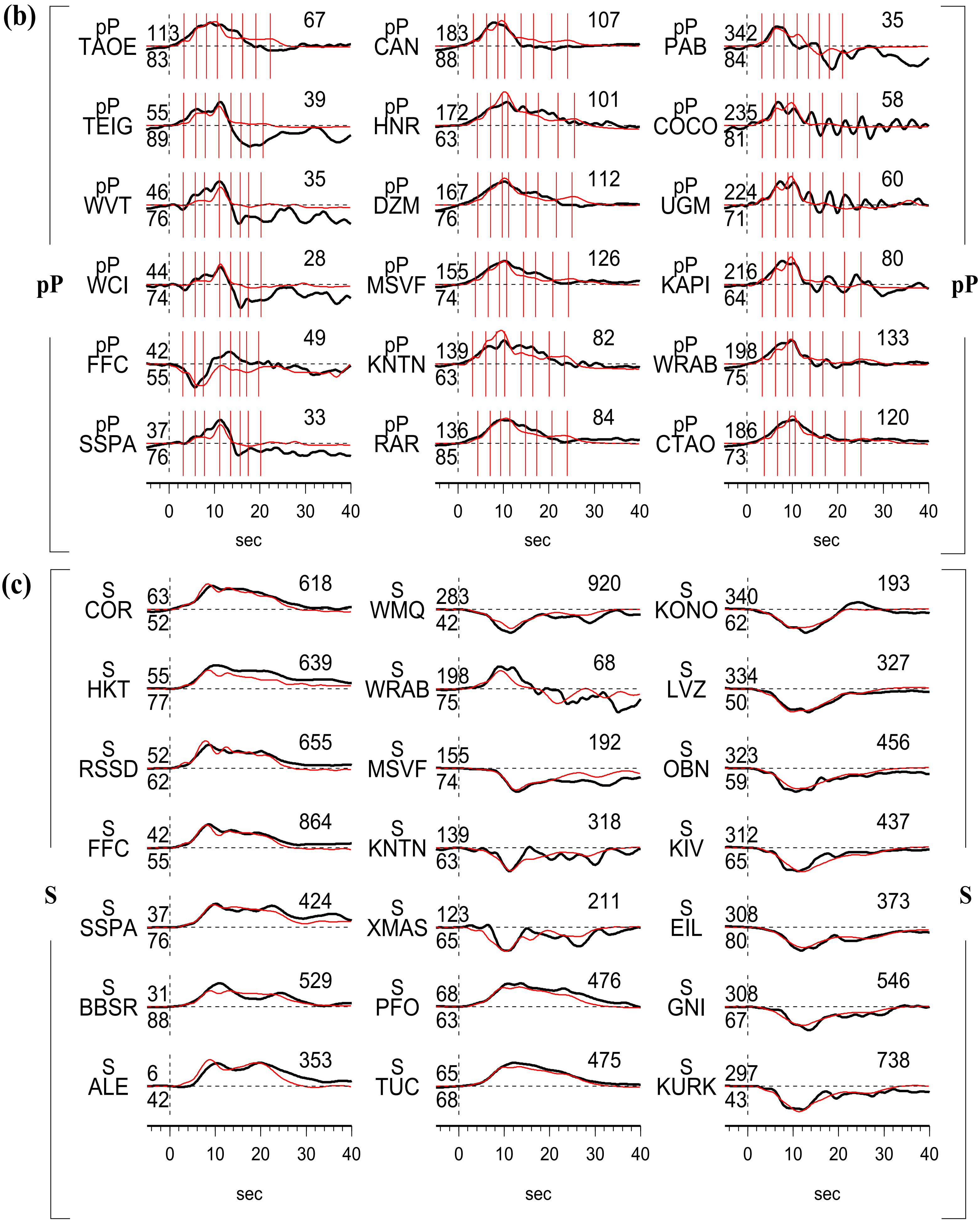
(b)
pP
pP TAOE 113 83 67
pP CAN 183 88 107
pP PAB 342 84 35
pP TEIG 55 89 39
pP HNR 172 63 101
pP COCO 235 81 58
pP WVT 46 76 35
pP DZM 167 76 112
pP UGM 224 71 60
pP WCI 44 74 28
pP MSVF 155 74 126
pP KAPI 216 64 80
pP FFC 42 55 49
pP KNTN 139 63 82
pP WRAB 198 75 133
pP SSPA 37 76 33
pP RAR 136 85 84
pP CTAO 186 73 120
0
10
20
30
40
sec
(c)
S
S COR 63 52 618
S WMQ 283 42 920
S KONO 340 62 193
S HKT 55 77 639
S WRAB 198 75 68
S LVZ 334 50 327
S RSSD 52 62 655
S MSVF 155 74 192
S OBN 323 59 456
S FFC 42 55 864
S KNTN 139 63 318
S KIV 312 65 437
S SSPA 37 76 424
S XMAS 123 65 211
S EIL 308 80 373
S BBSR 31 88 529
S PFO 68 63 476
S GNI 308 67 546
S ALE 6 42 353
S TUC 65 68 475
S KURK 297 43 738
0
10
20
30
40
sec

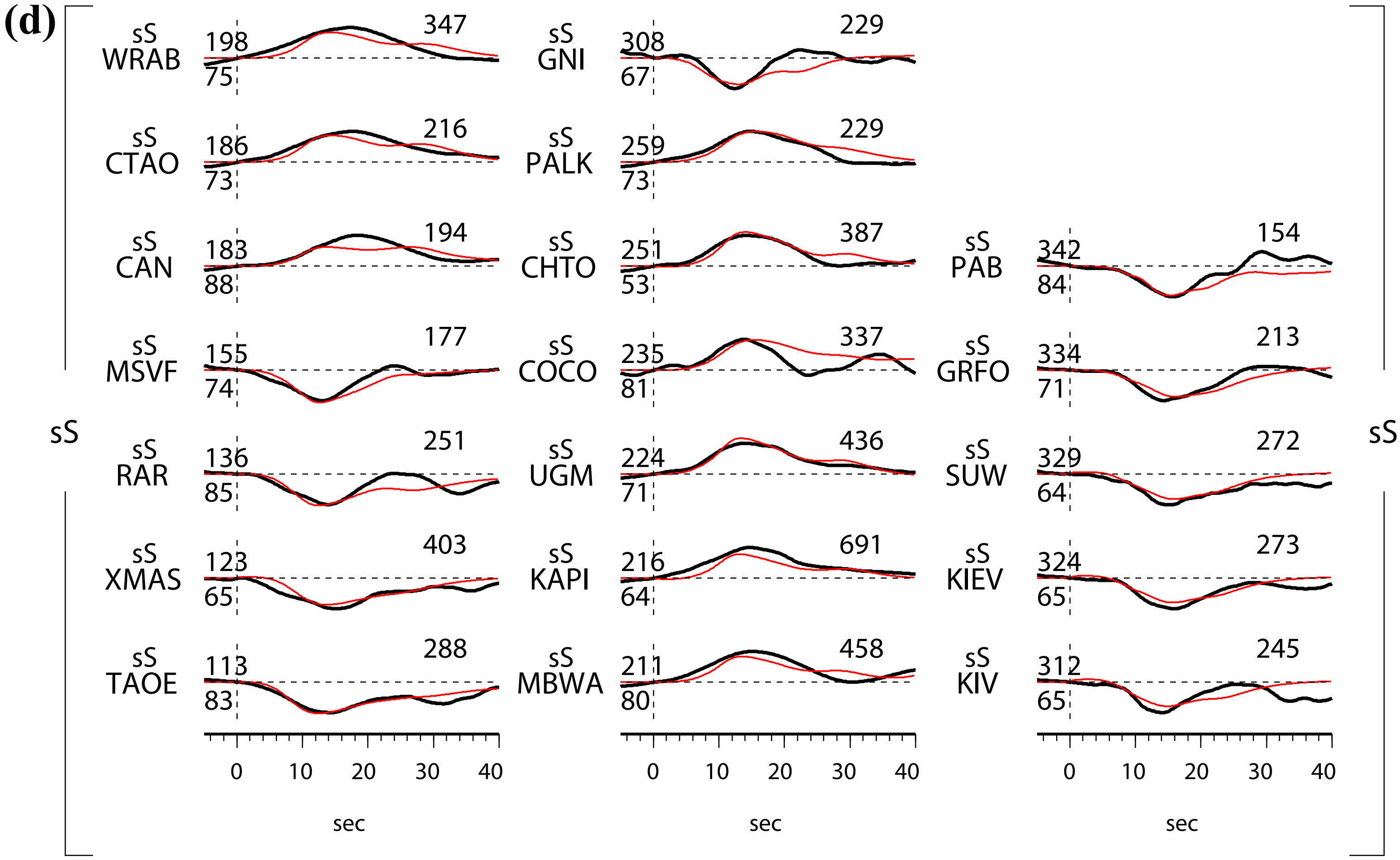

Figs. S2-4. (a) – (d) Observed seismograms low-passed filtered to 0.5 Hz (black traces) comparing with synthetics low-passed filtered to 0.5 Hz (red traces) predicted by the best-fitting source model, for (a) P waves, (b) pP waves, (c) SH waves and (d) sSH waves. The red lines label the peak times of the sub-events predicted by the best-fitting model.

Supplementary tables and figures for Chapter 3

Table S3-1. Source parameters of inverted six sub-events on the GCMT sub-horizontal plane

Sub-event	dt (s)	dn (km)	de (km)	dz (km)	duration (s)	moment (dyn-cm)	strike (°)	dip (°)	slip (°)
0	0	0	0	0	3.0	3.0E+26	191.0	11.2	264.7
1a	1.5	3.9	4.6	-0.7	11.8	6.7E+27	191.0	11.2	268.3
1b	7.0	-13.4	6.6	-1.8	12.0	6.4E+27	191.0	11.2	260.7
2	11.6	-32.0	2.3	-1.6	9.0	7.0E+27	191.0	11.2	270.1
3	16.0	-29.2	10.8	-3.1	12.0	9.7E+27	191.0	11.2	270.0
4	23.0	-51.5	-11.4	0.3	12.0	5.7E+27	191.0	11.2	277.0

Table S3-2. Source parameters of inverted six sub-events on the GCMT sub-horizontal plane based on P wave data only

Sub-event	dt (s)	dn (km)	de (km)	dz (km)	duration (s)	moment (dyn-cm)	strike (°)	dip (°)	slip (°)
0	0	0	0	0	3.2	2.5E+26	191.0	11.2	300.2
1a	1.8	4.4	1.8	-0.2	12.0	6.1E+27	191.0	11.2	274.5
1b	7.1	-14.2	8.9	-2.2	10.0	4.5E+27	191.0	11.2	261.3
2	10.8	-32.5	14.1	-3.9	9.0	9.1E+27	191.0	11.2	269.9
3	16.2	-21.9	8.9	-2.5	12.0	1.0E+28	191.0	11.2	271.7
4	22.1	-55.0	-4.2	1.2	12.0	6.3E+27	191.0	11.2	272.2

Table S3-3. Source parameters of inverted six sub-events on the GCMT sub-vertical plane

Sub-event	dt (s)	dn (km)	de (km)	dz (km)	duration (s)	moment (dyn-cm)	strike (°)	dip (°)	slip (°)
0	0	0	0	0	3.2	3.0E+26	13.5	78.8	285.1
1a	1.5	4.6	1.2	0.8	12.0	7.0E+27	13.5	78.8	277.3
1b	7.5	1.8	-0.2	-3.2	12.0	6.2E+27	13.5	78.8	280.4
2	11.5	-41.2	-7.0	12.8	9.0	7.2E+27	13.5	78.8	269.2
3	15.8	-20.8	-3.9	4.6	12.0	8.6E+27	13.5	78.8	268.2
4	22.8	-50.6	-5.6	30.4	12.0	7.0E+27	13.5	78.8	268.3

Table S3-4. Source parameters of inverted six sub-events on a plane that best connects the inverted sub-events (Table 1) in the main text

Sub-event	dt (s)	dn (km)	de (km)	dz (km)	duration (s)	moment (dyn-cm)	strike (°)	dip (°)	slip (°)
0	0	0	0	0	3	2.9E+26	-12.0	65.0	290.6
1a	1.7	3.1	1.7	4.9	11.4	7.0E+27	-12.0	65.0	294.1
1b	7.0	-10.3	4.3	4.4	11.8	6.6E+27	-12.0	65.0	300.1
2	11.9	-40.1	15.7	15.1	8.8	8.8E+27	-12.0	65.0	287.7
3	15.7	-27.6	9.7	8.1	12.0	9.2E+27	-12.0	65.0	287.9
4	22.8	-53.4	28.1	35.1	12.0	8.5E+27	-12.0	65.0	276.4

Table S3-5. Source parameters of inverted six sub-events when compeling the subevent 4 to 90 km south to the initiation of the earthquake

Sub-event	dt (s)	dn (km)	de (km)	dz (km)	duration (s)	moment (dyn-cm)	strike (°)	dip (°)	slip (°)
0	0	0	0	0	2.5	3.0E+26	17.6	88.0	285.8
1a	1.7	4.2	4.7	1.8	11.8	6.7E+27	12.2	85.9	281.2
1b	7.5	-4.6	9.5	-4.6	11.9	6.4E+27	22.7	86.8	265.0
2	12.0	-44.4	16.5	13.4	8.9	7.9E+27	4.7	78.2	281.0
3	16.6	-25.6	14.6	1.5	12.0	8.7E+27	18.4	85.9	261.7
4	22.5	-90.8	11.2	27.9	12.0	6.8E+27	-7.8	69.5	268.8

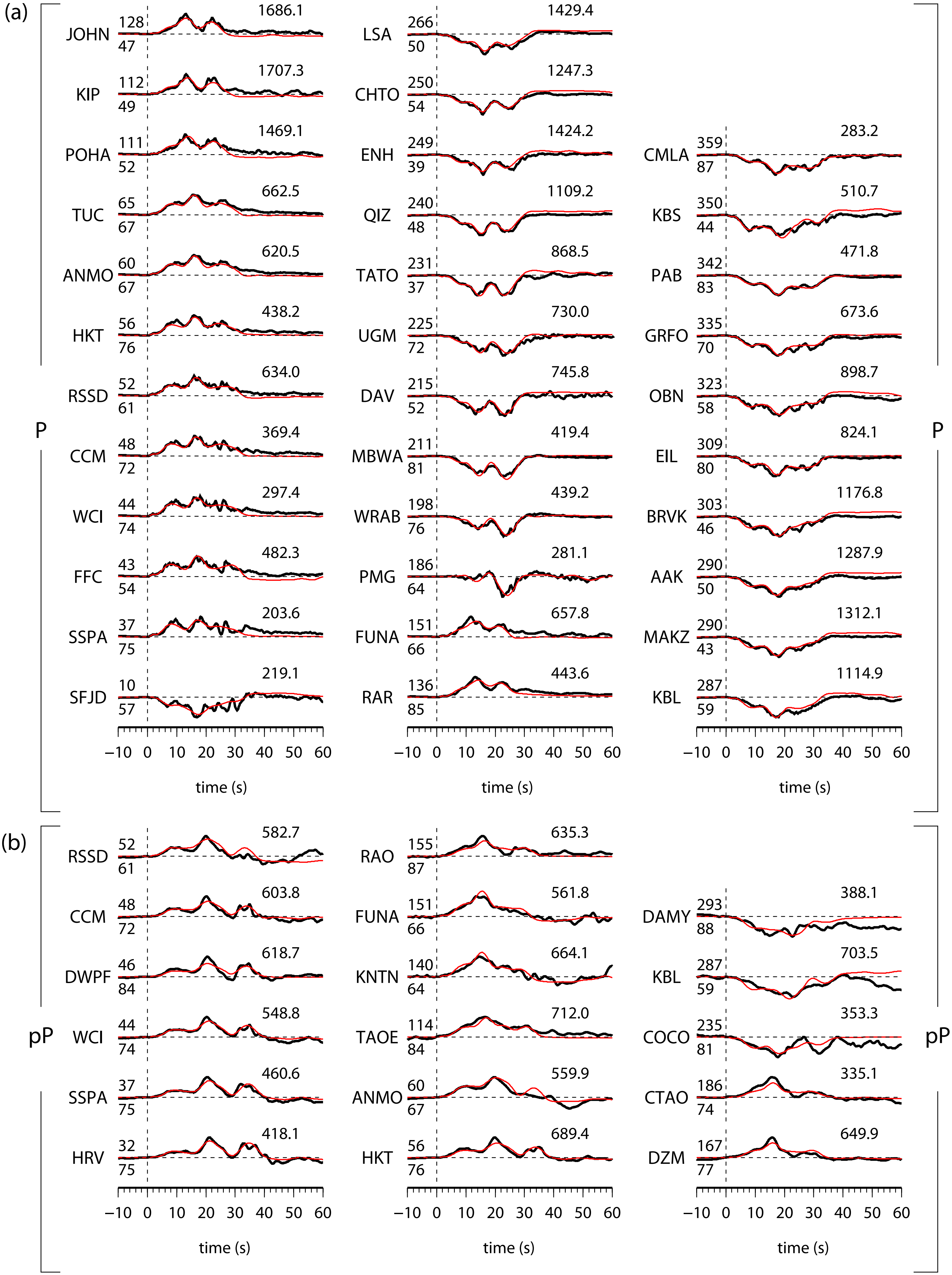
(a)
P
JOHN 128 47 1686.1
KIP 112 49 1707.3
POHA 111 52 1469.1
TUC 65 67 662.5
ANMO 60 67 620.5
HKT 56 76 438.2
RSSD 52 61 634.0
CCM 48 72 369.4
WCI 44 74 297.4
FFC 43 54 482.3
SSPA 37 75 203.6
SFJD 10 57 219.1
LSA 266 50 1429.4
CHTO 250 54 1247.3
ENH 249 39 1424.2
QIZ 240 48 1109.2
TATO 231 37 868.5
UGM 225 72 730.0
DAV 215 52 745.8
MBWA 211 81 419.4
WRAB 198 76 439.2
PMG 186 64 281.1
FUNA 151 66 657.8
RAR 136 85 443.6
CMLA 359 87 283.2
KBS 350 44 510.7
PAB 342 83 471.8
GRFO 335 70 673.6
OBN 323 58 898.7
EIL 309 80 824.1
BRVK 303 46 1176.8
AAK 290 50 1287.9
MAKZ 290 43 1312.1
KBL 287 59 1114.9
−10 0 10 20 30 40 50 60
time (s)
(b)
pP
RSSD 52 61 582.7
CCM 48 72 603.8
DWPF 46 84 618.7
WCI 44 74 548.8
SSPA 37 75 460.6
HRV 32 75 418.1
RAO 155 87 635.3
FUNA 151 66 561.8
KNTN 140 64 664.1
TAOE 114 84 712.0
ANMO 60 67 559.9
HKT 56 76 689.4
DAMY 293 88 388.1
KBL 287 59 703.5
COCO 235 81 353.3
CTAO 186 74 335.1
DZM 167 77 649.9
−10 0 10 20 30 40 50 60
time (s)

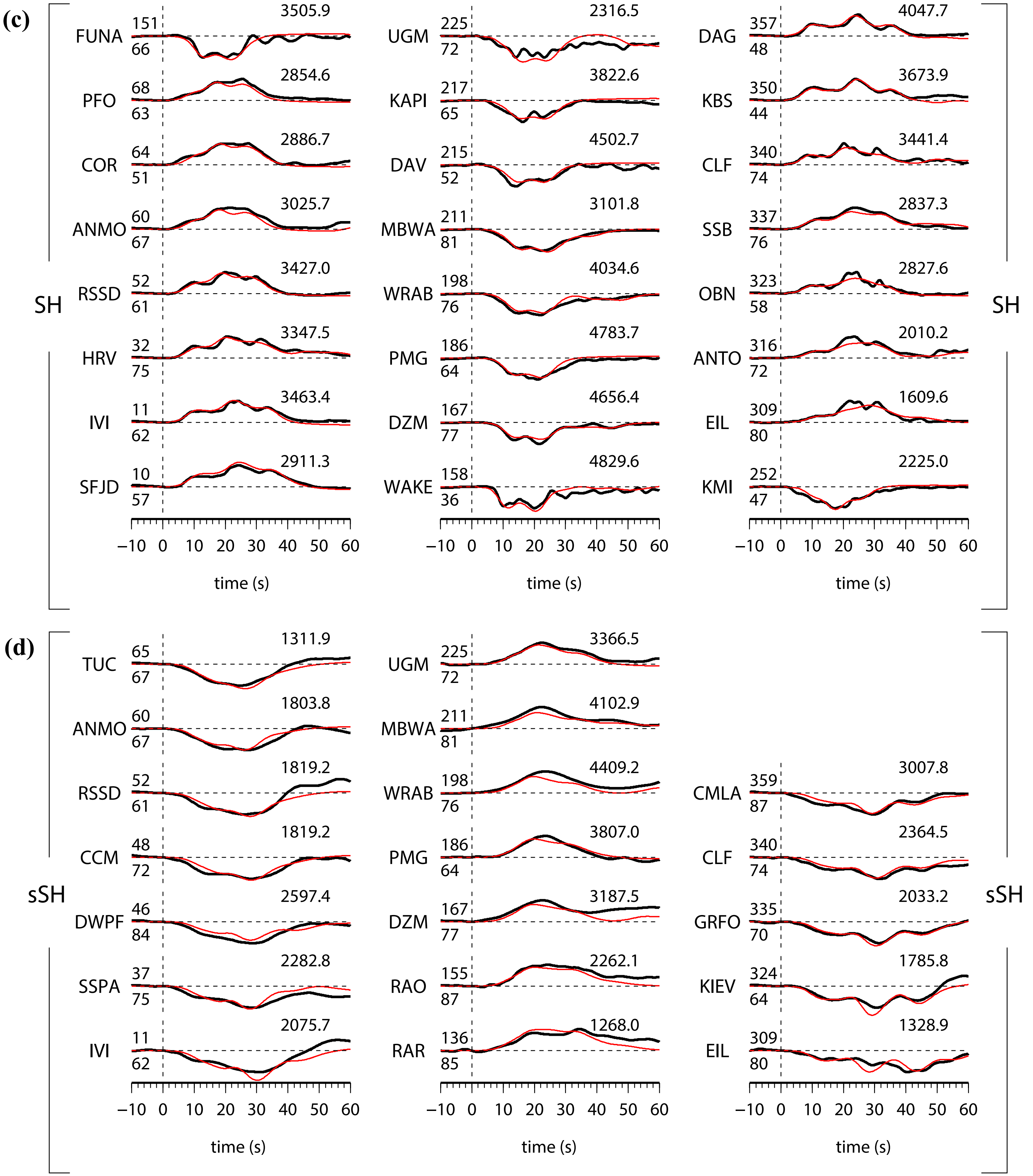

Fig. S3-1. Observed seismograms (black traces) comparing with synthetics (red traces) predicted based on the inverted six subevent model in the main text (Table 2-1) for, (a) P phase (vertical displacement), (b) pP phase (vertical displacement), (c) SH phase (tangential displacement), and (d) sSH phase (tangential displacement).

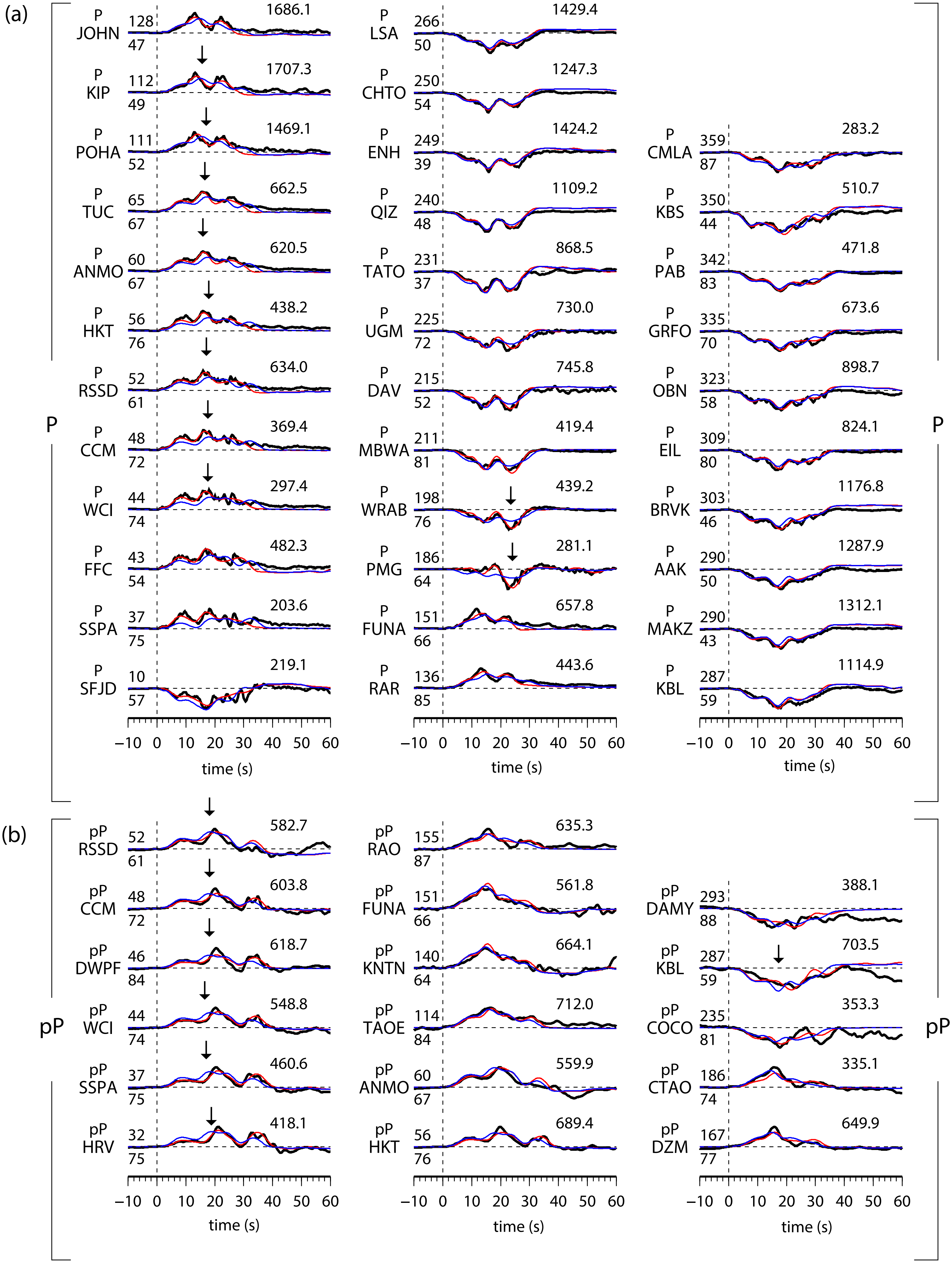
(a)
P
P JOHN 128 47 1686.1
P KIP 112 49 1707.3
P POHA 111 52 1469.1
P TUC 65 67 662.5
P ANMO 60 67 620.5
P HKT 56 76 438.2
P RSSD 52 61 634.0
P CCM 48 72 369.4
P WCI 44 74 297.4
P FFC 43 54 482.3
P SSPA 37 75 203.6
P SFJD 10 57 219.1
P LSA 266 50 1429.4
P CHTO 250 54 1247.3
P ENH 249 39 1424.2
P QIZ 240 48 1109.2
P TATO 231 37 868.5
P UGM 225 72 730.0
P DAV 215 52 745.8
P MBWA 211 81 419.4
P WRAB 198 76 439.2
P PMG 186 64 281.1
P FUNA 151 66 657.8
P RAR 136 85 443.6
P CMLA 359 87 283.2
P KBS 350 44 510.7
P PAB 342 83 471.8
P GRFO 335 70 673.6
P OBN 323 58 898.7
P EIL 309 80 824.1
P BRVK 303 46 1176.8
P AAK 290 50 1287.9
P MAKZ 290 43 1312.1
P KBL 287 59 1114.9
–10 0 10 20 30 40 50 60
time (s)
(b)
pP
pP RSSD 52 61 582.7
pP CCM 48 72 603.8
pP DWPF 46 84 618.7
pP WCI 44 74 548.8
pP SSPA 37 75 460.6
pP HRV 32 75 418.1
pP RAO 155 87 635.3
pP FUNA 151 66 561.8
pP KNTN 140 64 664.1
pP TAOE 114 84 712.0
pP ANMO 60 67 559.9
pP HKT 56 76 689.4
pP DAMY 293 88 388.1
pP KBL 287 59 703.5
pP COCO 235 81 353.3
pP CTAO 186 74 335.1
pP DZM 167 77 649.9
–10 0 10 20 30 40 50 60
time (s)

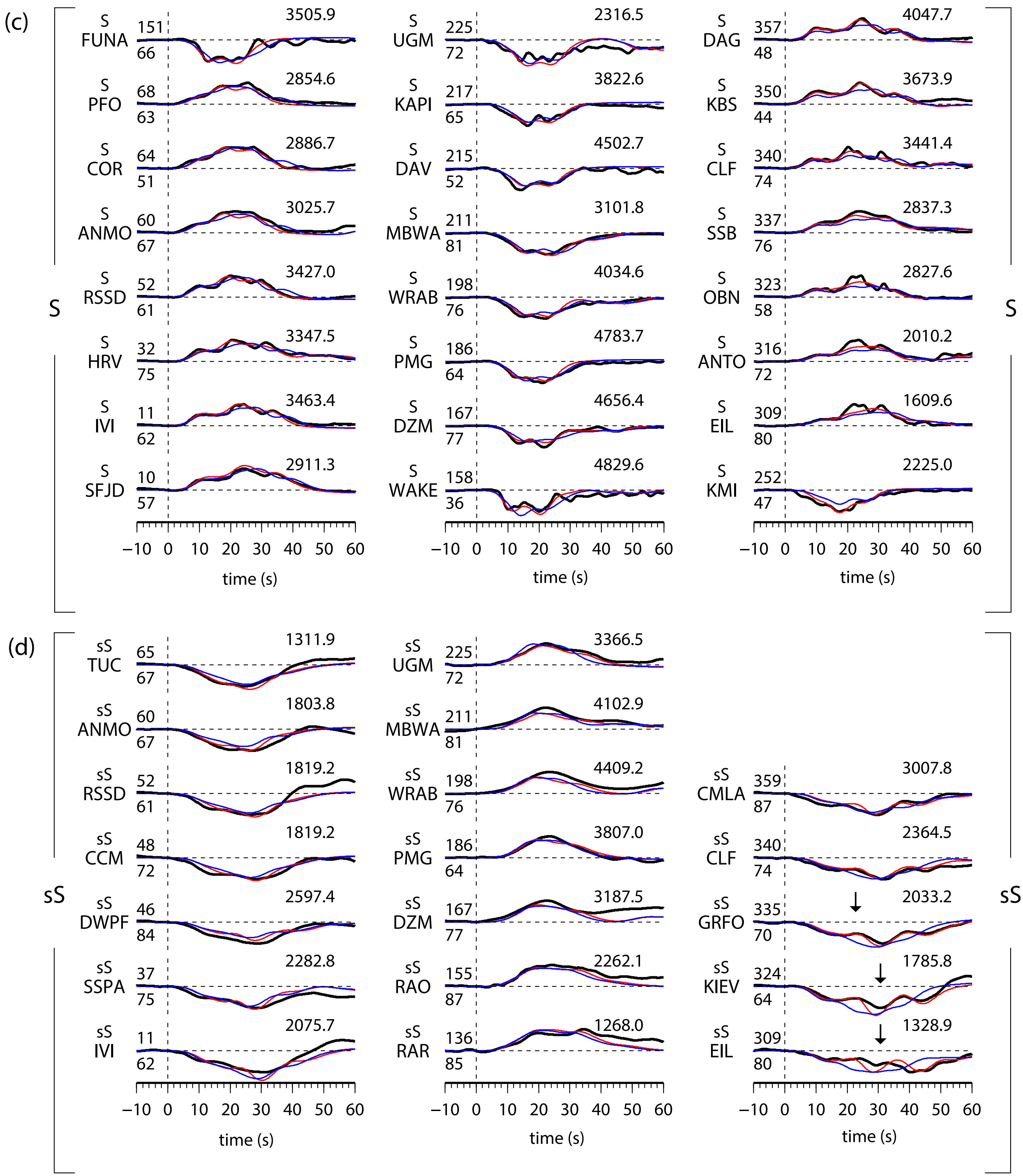

Fig. S3-2. Observed seismograms (black traces) comparing with synthetics (red traces) predicted by the best-fitting source model in the main text (Table 2-1) and synthetics (blue traces) predicted by the best-fitting source model (Table S3-1) on the CMT sub-horizontal plane for, (a) P phase (vertical displacement), (b) pP phase (vertical displacement), (c) SH phase (tangential displacement), and (d) sSH phase (tangential displacement).

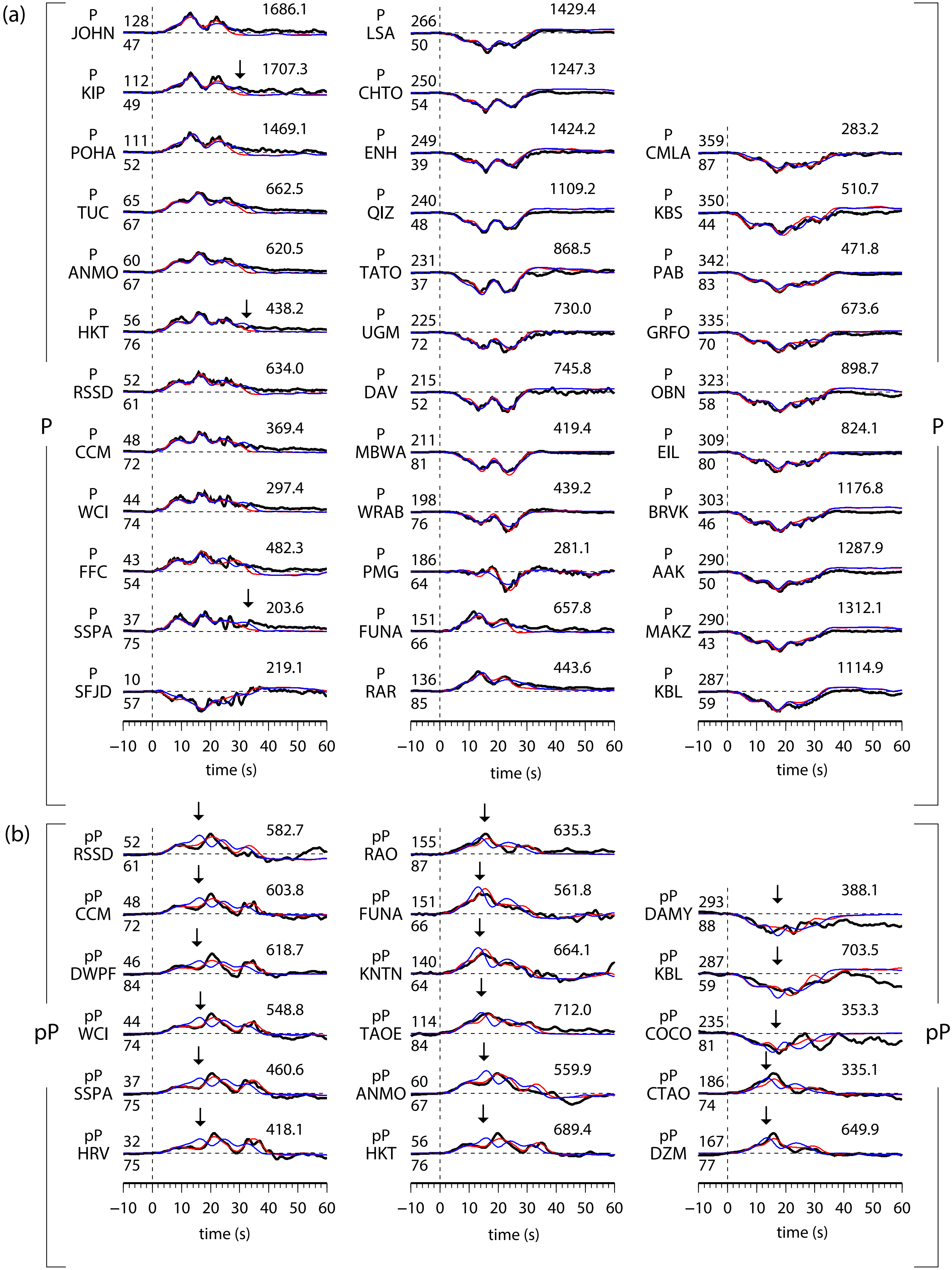
(a)
P
P JOHN 128 47 1686.1
P KIP 112 49 1707.3
P POHA 111 52 1469.1
P TUC 65 67 662.5
P ANMO 60 67 620.5
P HKT 56 76 438.2
P RSSD 52 61 634.0
P CCM 48 72 369.4
P WCI 44 74 297.4
P FFC 43 54 482.3
P SSPA 37 75 203.6
P SFJD 10 57 219.1
P LSA 266 50 1429.4
P CHTO 250 54 1247.3
P ENH 249 39 1424.2
P QIZ 240 48 1109.2
P TATO 231 37 868.5
P UGM 225 72 730.0
P DAV 215 52 745.8
P MBWA 211 81 419.4
P WRAB 198 76 439.2
P PMG 186 64 281.1
P FUNA 151 66 657.8
P RAR 136 85 443.6
P CMLA 359 87 283.2
P KBS 350 44 510.7
P PAB 342 83 471.8
P GRFO 335 70 673.6
P OBN 323 58 898.7
P EIL 309 80 824.1
P BRVK 303 46 1176.8
P AAK 290 50 1287.9
P MAKZ 290 43 1312.1
P KBL 287 59 1114.9
−10 0 10 20 30 40 50 60
time (s)
(b)
pP
pP RSSD 52 61 582.7
pP CCM 48 72 603.8
pP DWPF 46 84 618.7
pP WCI 44 74 548.8
pP SSPA 37 75 460.6
pP HRV 32 75 418.1
pP RAO 155 87 635.3
pP FUNA 151 66 561.8
pP KNTN 140 64 664.1
pP TAOE 114 84 712.0
pP ANMO 60 67 559.9
pP HKT 56 76 689.4
pP DAMY 293 88 388.1
pP KBL 287 59 703.5
pP COCO 235 81 353.3
pP CTAO 186 74 335.1
pP DZM 167 77 649.9
−10 0 10 20 30 40 50 60
time (s)

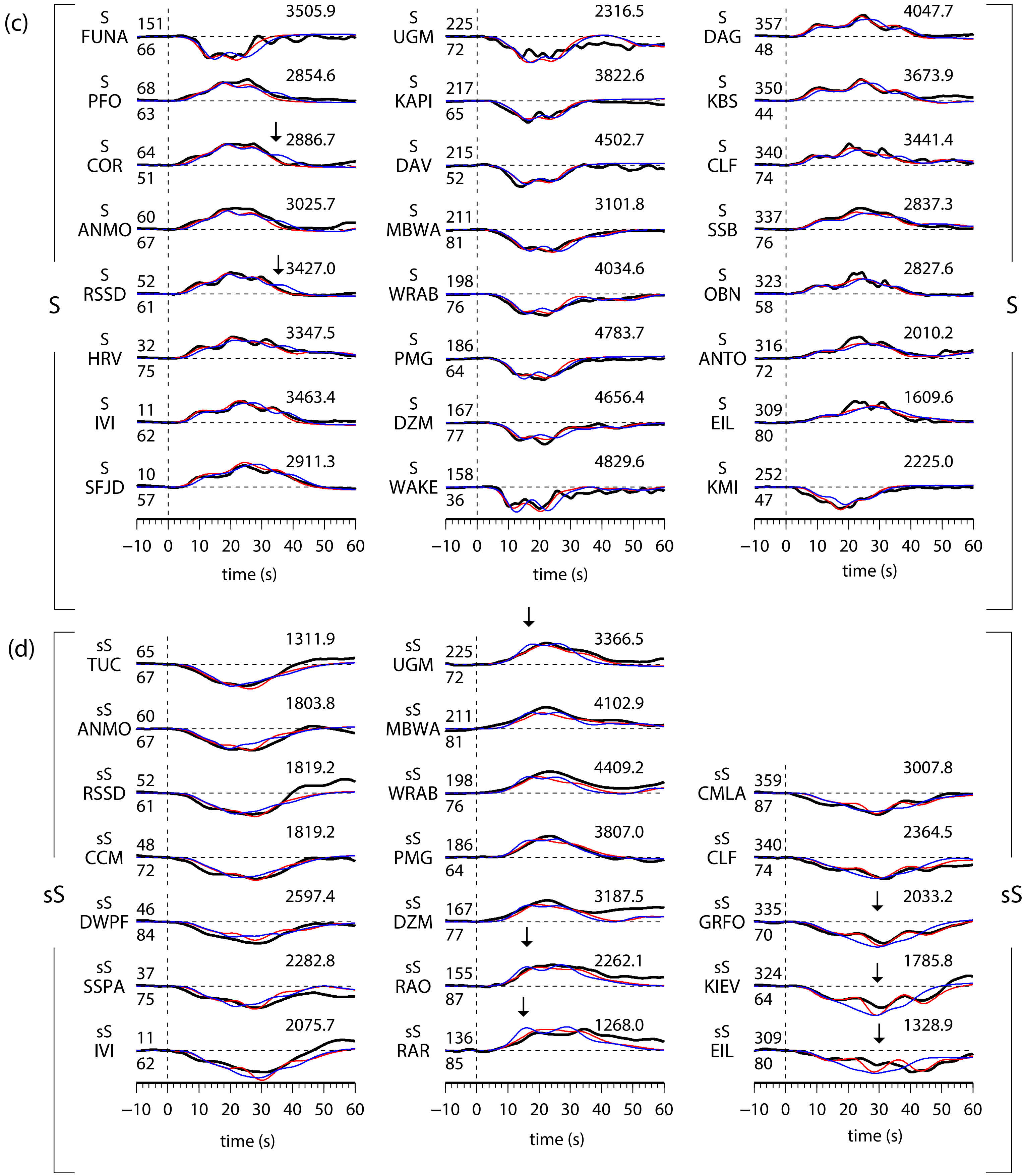

Fig. S3-3. Observed seismograms (black traces) comparing with synthetics (red traces) predicted by thebest-fitting source model in the main text (Table 2 - 1) and synthetics (blue traces) predicted by the best-fitting source model (Table S3-2) on the CMT sub-horizontal plane based on P wave data only for, (a) P phase (vertical displacement), (b) pP phase (vertical displacement), (c) SH phase (tangential displacement), and (d) sSH phase (tangential displacement).

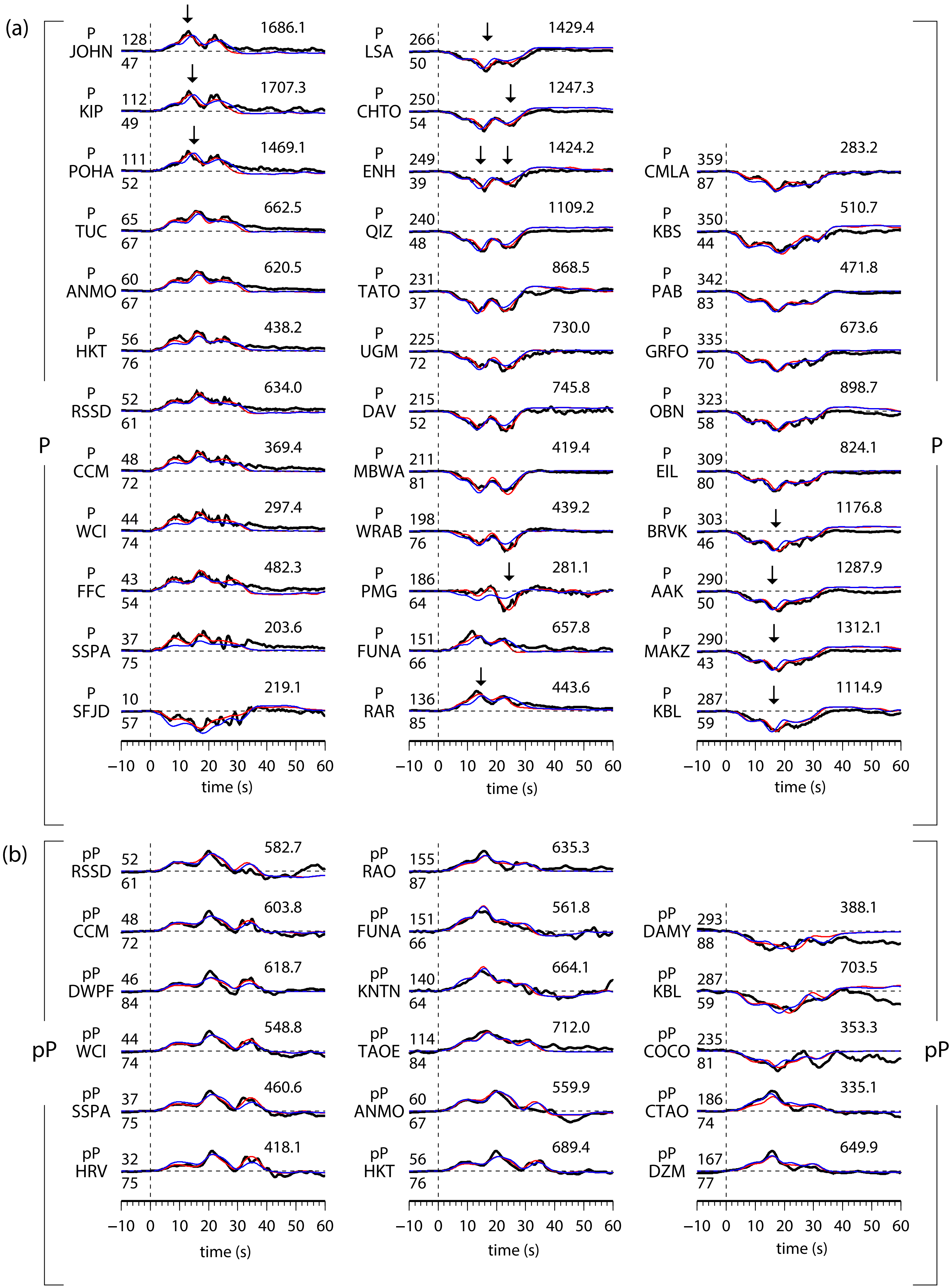

(a)
P
P JOHN 128 47 1686.1
P KIP 112 49 1707.3
P POHA 111 52 1469.1
P TUC 65 67 662.5
P ANMO 60 67 620.5
P HKT 56 76 438.2
P RSSD 52 61 634.0
P CCM 48 72 369.4
P WCI 44 74 297.4
P FFC 43 54 482.3
P SSPA 37 75 203.6
P SFJD 10 57 219.1
P LSA 266 50 1429.4
P CHTO 250 54 1247.3
P ENH 249 39 1424.2
P QIZ 240 48 1109.2
P TATO 231 37 868.5
P UGM 225 72 730.0
P DAV 215 52 745.8
P MBWA 211 81 419.4
P WRAB 198 76 439.2
P PMG 186 64 281.1
P FUNA 151 66 657.8
P RAR 136 85 443.6
P CMLA 359 87 283.2
P KBS 350 44 510.7
P PAB 342 83 471.8
P GRFO 335 70 673.6
P OBN 323 58 898.7
P EIL 309 80 824.1
P BRVK 303 46 1176.8
P AAK 290 50 1287.9
P MAKZ 290 43 1312.1
P KBL 287 59 1114.9
−10 0 10 20 30 40 50 60
time (s)
(b)
pP
pP RSSD 52 61 582.7
pP CCM 48 72 603.8
pP DWPF 46 84 618.7
pP WCI 44 74 548.8
pP SSPA 37 75 460.6
pP HRV 32 75 418.1
pP RAO 155 87 635.3
pP FUNA 151 66 561.8
pP KNTN 140 64 664.1
pP TAOE 114 84 712.0
pP ANMO 60 67 559.9
pP HKT 56 76 689.4
pP DAMY 293 88 388.1
pP KBL 287 59 703.5
pP COCO 235 81 353.3
pP CTAO 186 74 335.1
pP DZM 167 77 649.9
−10 0 10 20 30 40 50 60
time (s)

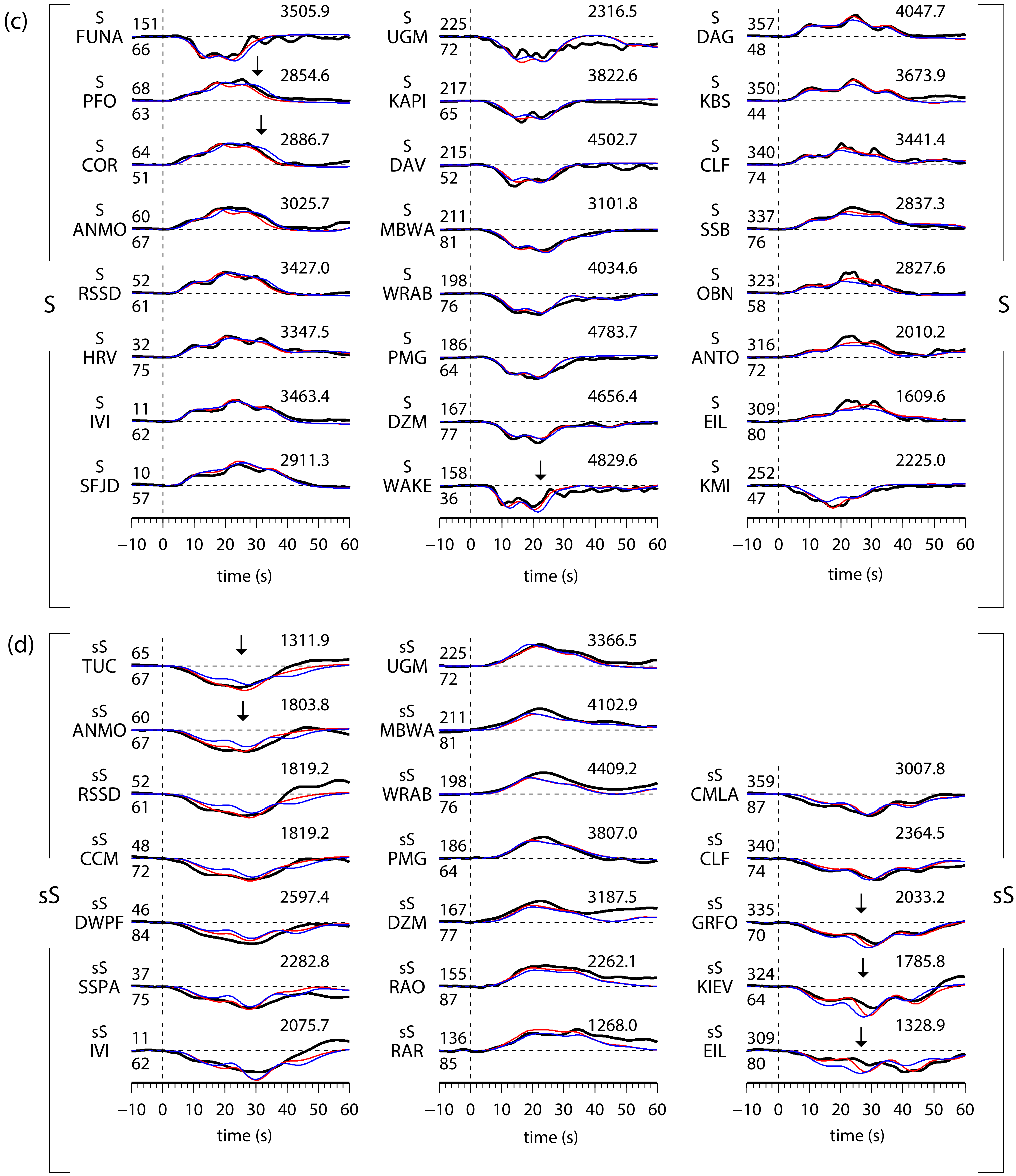

Fig. S3-4. Observed seismograms (black traces) comparing with synthetics (red traces) predicted by the best-fitting source model in the main text (Table 2 - 1) and synthetics (blue traces) predicted by the best-fitting source model (Table S3-3) on the CMT sub-vertical plane for, (a) P phase (vertical displacement), (b) pP phase (vertical displacement), (c) SH phase (tangential displacement), and (d) sSH phase (tangential displacement).

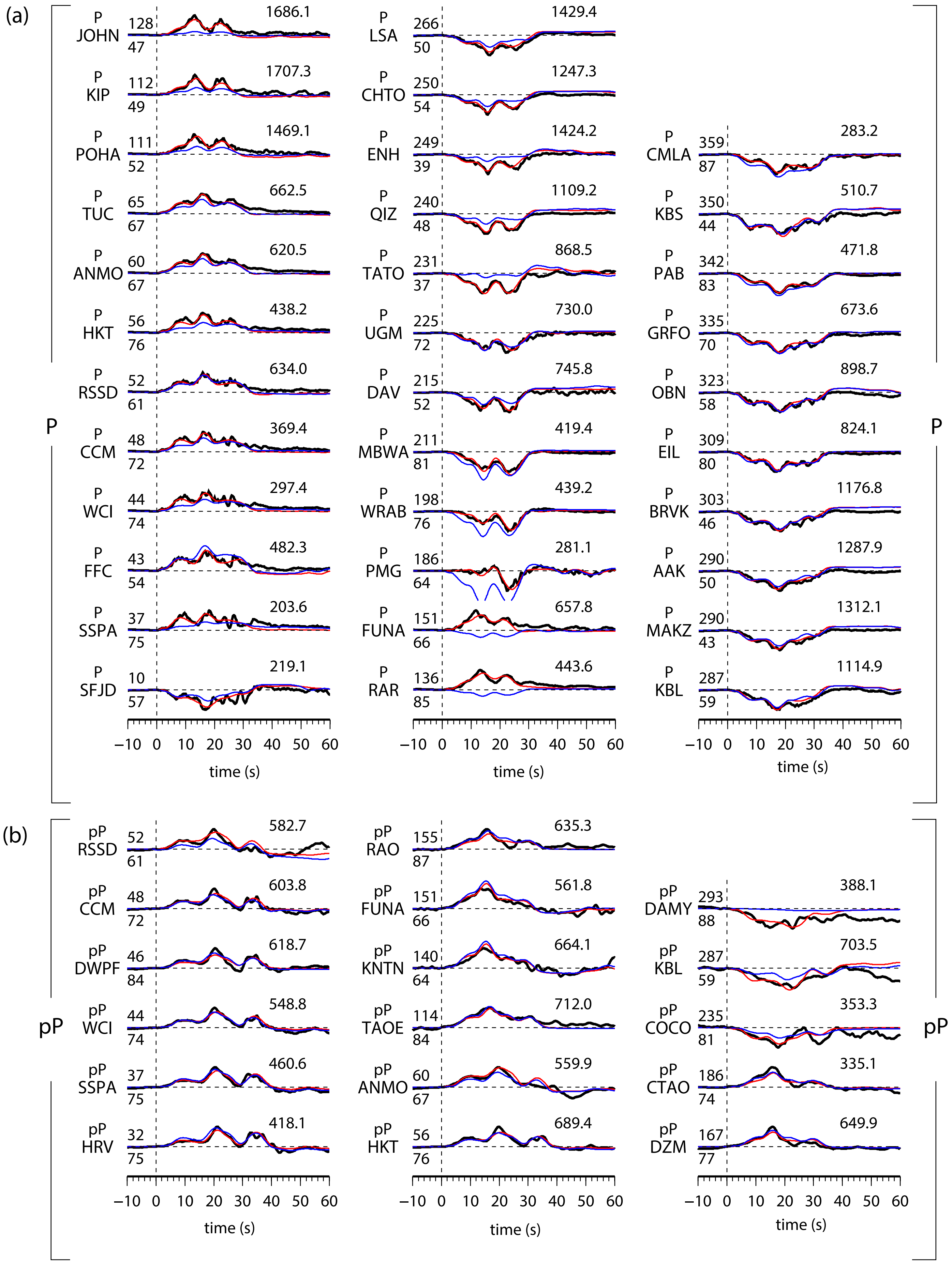
(a)
P
P JOHN 128 47 1686.1
P KIP 112 49 1707.3
P POHA 111 52 1469.1
P TUC 65 67 662.5
P ANMO 60 67 620.5
P HKT 56 76 438.2
P RSSD 52 61 634.0
P CCM 48 72 369.4
P WCI 44 74 297.4
P FFC 43 54 482.3
P SSPA 37 75 203.6
P SFJD 10 57 219.1
P LSA 266 50 1429.4
P CHTO 250 54 1247.3
P ENH 249 39 1424.2
P QIZ 240 48 1109.2
P TATO 231 37 868.5
P UGM 225 72 730.0
P DAV 215 52 745.8
P MBWA 211 81 419.4
P WRAB 198 76 439.2
P PMG 186 64 281.1
P FUNA 151 66 657.8
P RAR 136 85 443.6
P CMLA 359 87 283.2
P KBS 350 44 510.7
P PAB 342 83 471.8
P GRFO 335 70 673.6
P OBN 323 58 898.7
P EIL 309 80 824.1
P BRVK 303 46 1176.8
P AAK 290 50 1287.9
P MAKZ 290 43 1312.1
P KBL 287 59 1114.9
−10 0 10 20 30 40 50 60
time (s)
P
(b)
pP
pP RSSD 52 61 582.7
pP CCM 48 72 603.8
pP DWPF 46 84 618.7
pP WCI 44 74 548.8
pP SSPA 37 75 460.6
pP HRV 32 75 418.1
pP RAO 155 87 635.3
pP FUNA 151 66 561.8
pP KNTN 140 64 664.1
pP TAOE 114 84 712.0
pP ANMO 60 67 559.9
pP HKT 56 76 689.4
pP DAMY 293 88 388.1
pP KBL 287 59 703.5
pP COCO 235 81 353.3
pP CTAO 186 74 335.1
pP DZM 167 77 649.9
−10 0 10 20 30 40 50 60
time (s)
pP

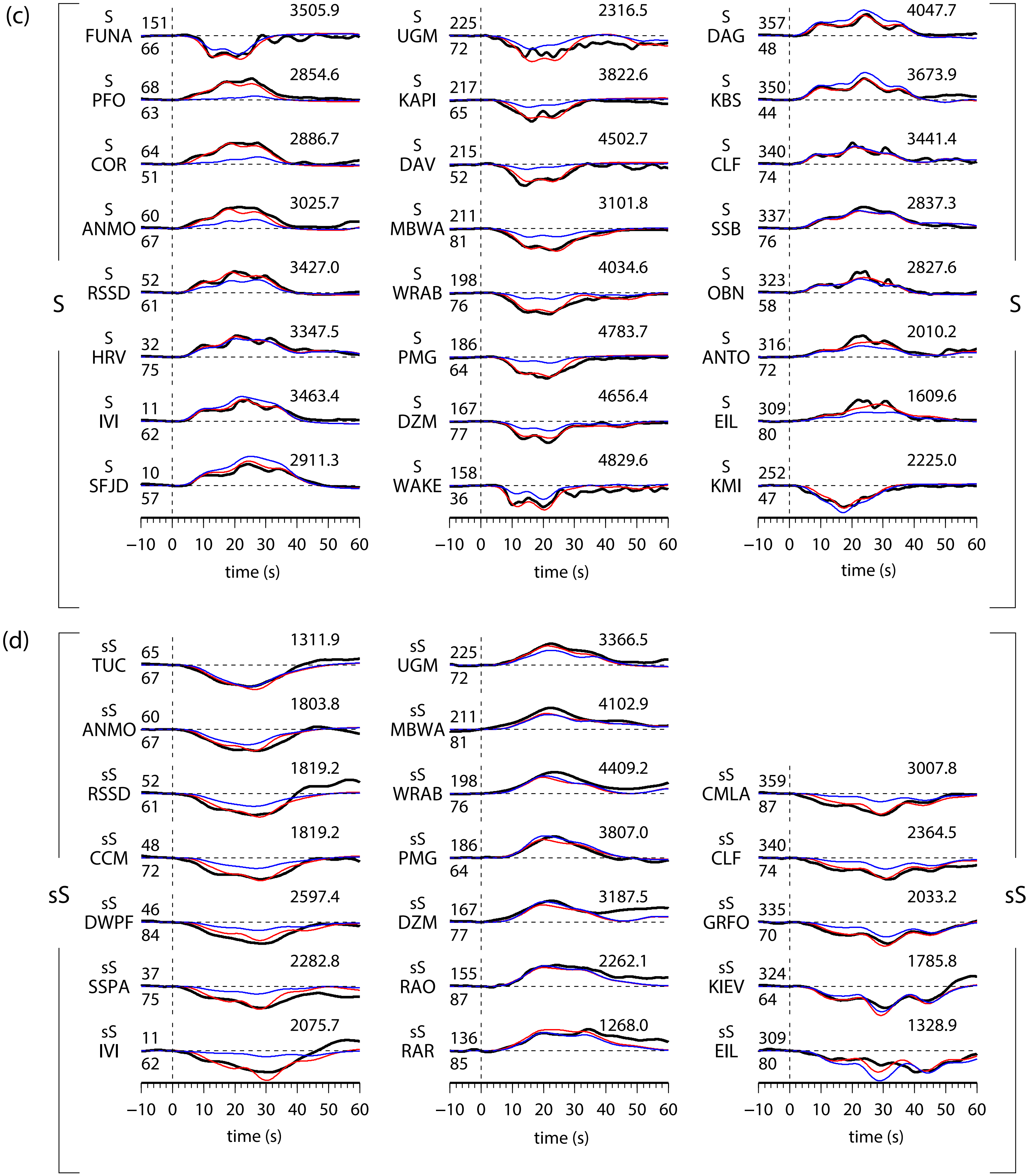

Fig. S3-5. Observed seismograms (black traces) comparing with synthetics (red traces) predicted by the best-fitting source model in the main text (Table 2 - 1) and synthetics (blue traces) predicted by the best-fitting source model (Table S3-4) on a plane that best connects the inferred subevents in Table 2 - 1, for, (a) P phase (vertical displacement), (b) pP phase (vertical displacement), (c) SH phase (tangential displacement), and (d) sSH phase (tangential displacement).

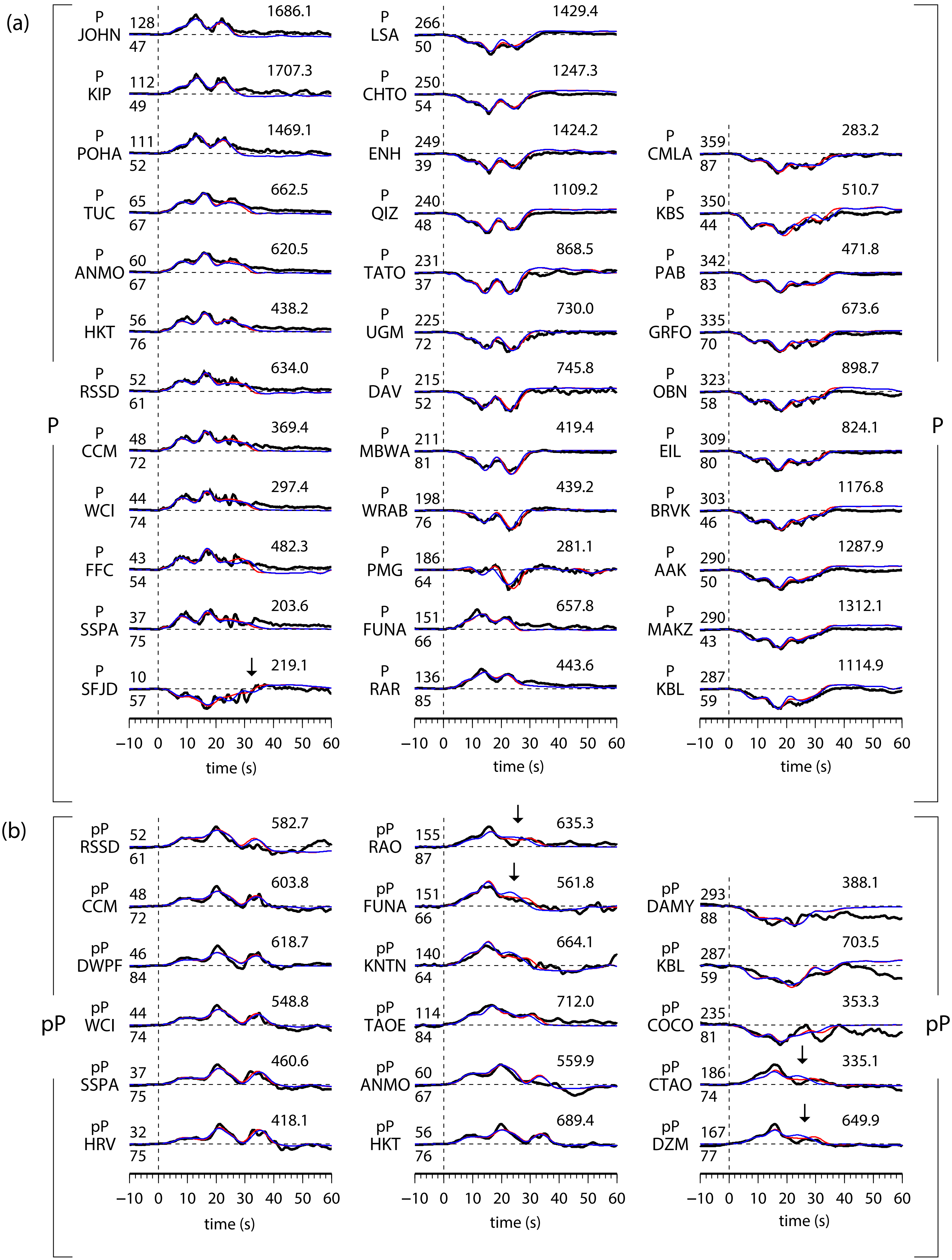
(a)
P
P
JOHN
128
47
1686.1
P
KIP
112
49
1707.3
P
POHA
111
52
1469.1
P
TUC
65
67
662.5
P
ANMO
60
67
620.5
P
HKT
56
76
438.2
P
RSSD
52
61
634.0
P
CCM
48
72
369.4
P
WCI
44
74
297.4
P
FFC
43
54
482.3
P
SSPA
37
75
203.6
P
SFJD
10
57
219.1
P
LSA
266
50
1429.4
P
CHTO
250
54
1247.3
P
ENH
249
39
1424.2
P
QIZ
240
48
1109.2
P
TATO
231
37
868.5
P
UGM
225
72
730.0
P
DAV
215
52
745.8
P
MBWA
211
81
419.4
P
WRAB
198
76
439.2
P
PMG
186
64
281.1
P
FUNA
151
66
657.8
P
RAR
136
85
443.6
P
CMLA
359
87
283.2
P
KBS
350
44
510.7
P
PAB
342
83
471.8
P
GRFO
335
70
673.6
P
OBN
323
58
898.7
P
EIL
309
80
824.1
P
BRVK
303
46
1176.8
P
AAK
290
50
1287.9
P
MAKZ
290
43
1312.1
P
KBL
287
59
1114.9
−10
0
10
20
30
40
50
60
time (s)
(b)
pP
pP
RSSD
52
61
582.7
pP
CCM
48
72
603.8
pP
DWPF
46
84
618.7
pP
WCI
44
74
548.8
pP
SSPA
37
75
460.6
pP
HRV
32
75
418.1
pP
RAO
155
87
635.3
pP
FUNA
151
66
561.8
pP
KNTN
140
64
664.1
pP
TAOE
114
84
712.0
pP
ANMO
60
67
559.9
pP
HKT
56
76
689.4
pP
DAMY
293
88
388.1
pP
KBL
287
59
703.5
pP
COCO
235
81
353.3
pP
CTAO
186
74
335.1
pP
DZM
167
77
649.9
−10
0
10
20
30
40
50
60
time (s)

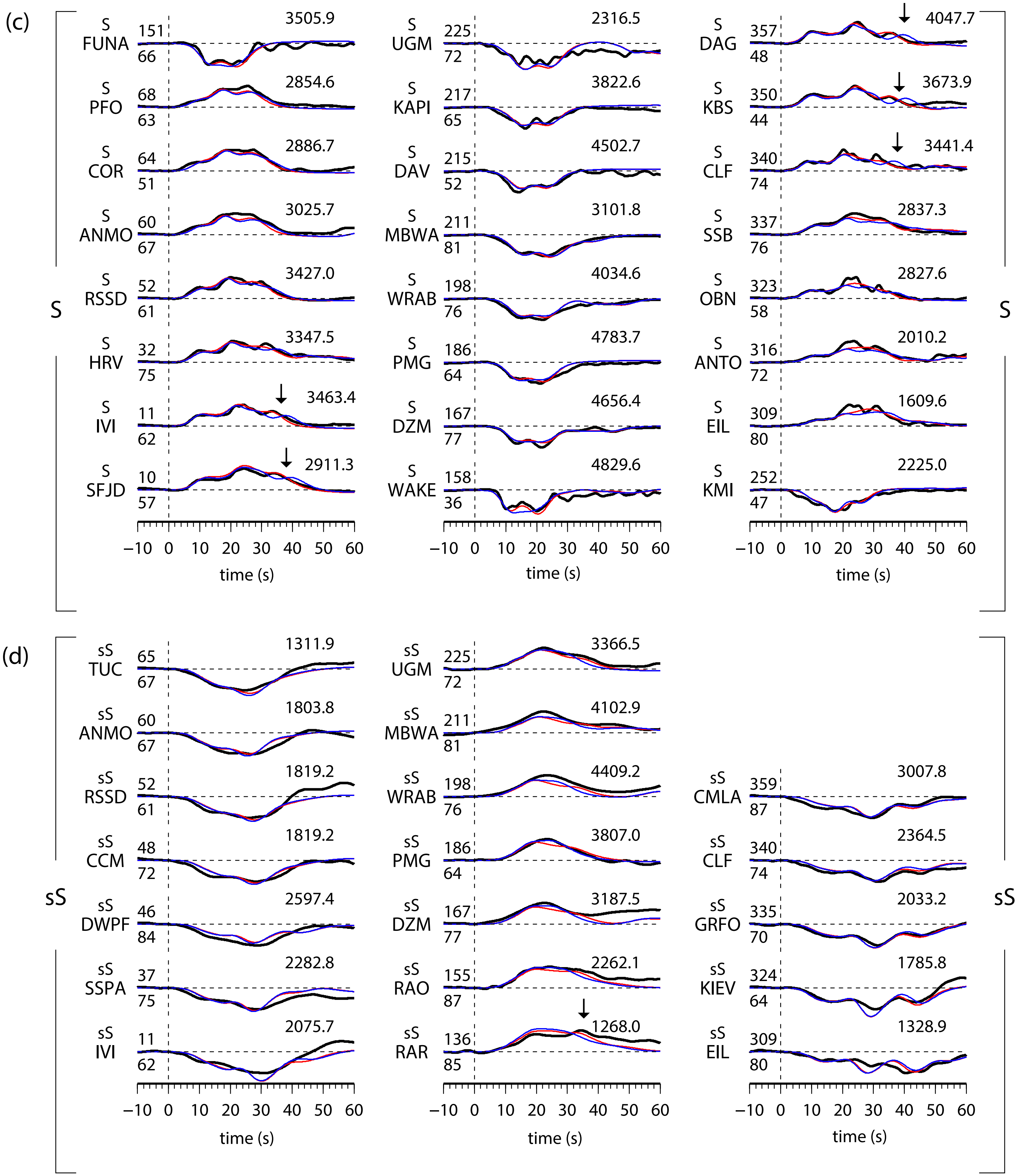

Fig. S3-6. Observed seismograms (black traces) comparing with synthetics (red traces) predicted by the best-fitting source model in the main text (Table 2 - 1) and synthetics (blue traces) predicted by the best -fitting source model (Table S3-5) by compeling the subevent 4 to 90 km south to the initiation of the earthquake for, (a) P phase (vertical displacement), (b) pP phase (vertical displacement), (c) SH phase (tangential displacement), and (d) sSH phase (tangential displacement).

Supplementary Information for Chapter 4

Multiple source inversion results

We investigate 26 deep-focus earthquakes with Mw > 7.0 and depth > 400 km, based on waveform modeling of P, pP, SH, sSH wave data. The information of each analyzed earthquake is presented in Table S4-0, including the date, time, epicenter, moment magnitude and the GCMT fault planes. The event epicenters by 2008 are corrected based on ISC EHB catalog. The events E11, E23 and E25 are relocated relative to E9, E22 and E12, respectively. Each earthquake process is delineated with a description, a table of the best-fitting model, a figure of comparison between the best-fitting sub-event model and the best planar model, and waveform comparisons among the seismic data (black traces) and the synthetics predicted by the best-fitting model (red traces) and the best planar model (blue traces) for P, pP, SH ans sSH wave data.

Figure caption

Because Figs. S4-1 – S4-26 have similar figure captions, we present an example figure caption for all the events E1 – E26. Figs. S4-2b, S4-6b and S4-19b are presented as Figs. 4-4b, 4-5b and 4-6b, respectively, in the main text.

Figs. S4-1 – S4-26 (a) Location and the GCMT focal mechanism of the earthquake (red beach ball) and used seismic stations (blue triangles), labeled with station names. The green traces are the ray paths from the earthquake and seismic stations. (b) Locations of the best-fitting sub-event model (red points) and the best planar model (blue points), and the initiated location (black star) of the earthquake (E1 – E26), along with slab depth contours (black traces, labelled with slab depths). Black beach ball describes GCMT focal mechanism of the event. Red and blue beach balls represent inferred focal mechanisms of the sub-events of the best-fitting model and the best planar model, labeled with the sub-event peak times and depths. (c) – (f) Observed seismograms (black traces) comparing with synthetics (red traces) predicted by the best-fitting source model and synthetics (blue traces) predicted by the best planar model, for (c) P waves, (d) pP waves,

(e) SH waves and (f) sSH waves. The red and blue lines label the peak times of the sub-events predicted by the best-fitting model and the best planar model.

Table S4-0. Analyzed global major deep-focus earthquakes

ID	Date	Time	Lat (˚)	Lon (˚)	Depth (km)	M_W	Low-angle Plane	High-angle Plane
E1	1994/03/09	23:28:08	-17.95	-178.37	562	7.6	250/27/330	7/77/246
E2	1994/06/09	00:33:17	-13.86	-67.51	631	8.2	302/10/300	92/81/265
E3	1994/07/21	18:36:32	42.32	132.87	471	7.3	64/34/178	155/89/56
E4	1995/08/23	07:06:04	18.80	145.32	595	7.0	136/42/242	351/53/293
E5	1996/06/17	11:22:19	-7.14	122.51	587	7.8	225/50/229	98/54/308
E6	1996/08/05	22:38:23	-20.79	-178.22	550	7.4	213/20/261	43/70/273
E7	1998/03/29	19:48:17	-17.73	-178.91	543	7.1	359/53/156	104/71/40
E8	1998/08/20	06:40:56	28.97	139.40	425	7.0	83/27/198	337/82/296
E9	1999/04/08	13:10:34	43.61	130.39	566	7.1	81/25/160	189/82/67
E10	2000/04/23	09:27:24	-28.32	-62.93	610	7.0	290/5/210	171/88/274
E11#	2002/06/28	17:19:31	43.75	130.57	564	7.3	27/13/105	192/77/86
E12	2002/08/19	11:01:02	-21.73	-179.36	580	7.6	149/22/219	22/76/288
E13	2002/08/19	11:08:25	-23.93	178.55	675	7.7	50/3/83	237/87/90
E14	2002/11/17	04:53:49	47.97	146.40	459	7.3	316/9/30	197/86/98
E15	2003/06/20	06:19:39	-7.65	-71.67	553	7.0	353/47/295	139/49/246
E16	2004/07/15	04:27:14	-17.76	-178.70	560	7.1	345/44/137	109/62/55
E17	2004/07/25	14:35:19	-2.53	103.93	581	7.3	108/45/231	337/56/303
E18	2005/02/05	12:23:20	5.29	123.38	536	7.1	158/14/246	3/77/276
E19	2006/01/02	22:13:41	-19.96	-178.09	593	7.2	281/22/320	49/76/253
E20	2008/07/05	02:12:04	53.95	152.92	632	7.7	143/48/226	18/58/308
E21	2008/11/24	09:02:58	54.23	154.31	490	7.3	276/19/331	34/81/254
E22	2010/07/23	22:08:11	6.72	123.41	607	7.3	263/19/329	22/80/254
E23#	2010/07/23	22:51:12	6.56	123.53	587	7.6	233/18/322	359/79/255
E24	2011/01/01	09:56:58	-26.79	-63.09	577	7.0	360/20/296	152/72/261
E25#	2011/09/15	19:31:04	-21.53	-179.30	604	7.3	312/38/353	48/85/232
E26*	2009/11/09	10:44:54	-17.24	178.34	591	7.3	172/42/33	56/68/127
E27*	2010/07/23	23:15:10	6.78	123.26	641	7.4	254/22/308	34/73/256
E28*	2012/08/14	02:59:38	49.80	145.06	582	7.7	27/33/59	243/63/108

#s label the events relocated based on the adjacent events.

*s label the discarded events in the catalog.

E1. The 09 Mar 1994 Mw 7.6 earthquake

Earthquake E1 occurred 562 km beneath Fiji islands region (Table S4-0), which is well known as a deep earthquake with numerous aftershocks (Wiens et al., 1994). The aftershock locations (Wiens et al., 1994) and the mainshock directivity (Warren et al., 2007) suggested that the earthquake ruptured on the GCMT sub-vertical fault plane. We infer source process of the earthquake using 19 P, 13 pP, 14 S and 11 sS (Fig. S4-1a). The major energy of the earthquake can be modeled by three sub-events reasonably well (Table S4-1, Fig. S4-1b – S4-1f). We compare synthetics predicted by the best-fitting sub-event model (red traces) and the best planar model (blue traces) that compels the sub-events distributed on the GCMT sub-vertical plane. The sub-event arrival times of the best-fitting model and the best planar model is similar (Figs. S4-1c – S4-1f), representing that they propagate around the sub-vertical plane. However, radiation pattern of synthetics predicted by the best planar model do not fit that of seismic data. Focal mechanisms of the sub-events can be modeled by plane rupture.

Table S4-1. Source parameters of inferred sub-events of E1

Sub-event	dt (s)	dn (km)	de (km)	dz (km)	duration (s)	Mw	strike (°)	dip (°)	slip (°)
1	2.4	1.7	3.0	1.0	4.0	7.3	27.4	70.2	258.4
2	6.0	21.2	3.1	-4.3	6.0	7.4	-4.5	77.0	246.4
3	9.2	10.0	12.3	-12.8	7.8	7.3	-18.1	91.6	230.8

(Fig. S4-1)

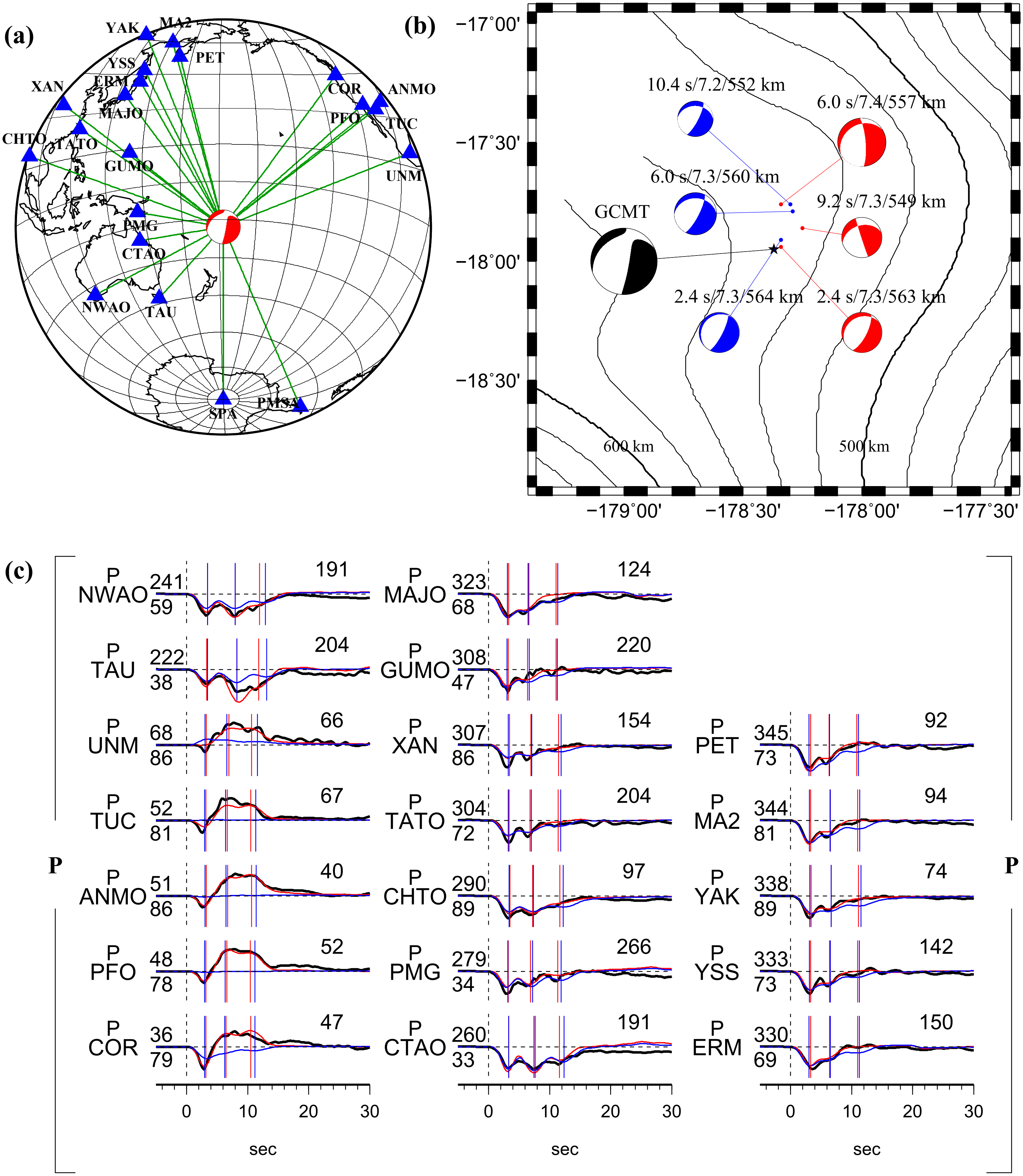

(a)
YAK
MA2
PET
YSS
ERM
XAN
MAJO
CHTO
TATO
GUMO
PMG
CTAO
NWAO
TAU
SPA
PMSA
COR
ANMO
PFO
TUC
UNM
(b)
−17˚00'
−17˚30'
−18˚00'
−18˚30'
−179˚00'
−178˚30'
−178˚00'
−177˚30'
10.4 s/7.2/552 km
6.0 s/7.4/557 km
6.0 s/7.3/560 km
9.2 s/7.3/549 km
GCMT
2.4 s/7.3/564 km
2.4 s/7.3/563 km
600 km
500 km
(c)
P
NWAO 241 59 191
P
MAJO 323 68 124
P
TAU 222 38 204
P
GUMO 308 47 220
P
UNM 68 86 66
P
XAN 307 86 154
P
PET 345 73 92
P
TUC 52 81 67
P
TATO 304 72 204
P
MA2 344 81 94
P
ANMO 51 86 40
P
CHTO 290 89 97
P
YAK 338 89 74
P
PFO 48 78 52
P
PMG 279 34 266
P
YSS 333 73 142
P
COR 36 79 47
P
CTAO 260 33 191
P
ERM 330 69 150
0
10
20
30
sec
P
P

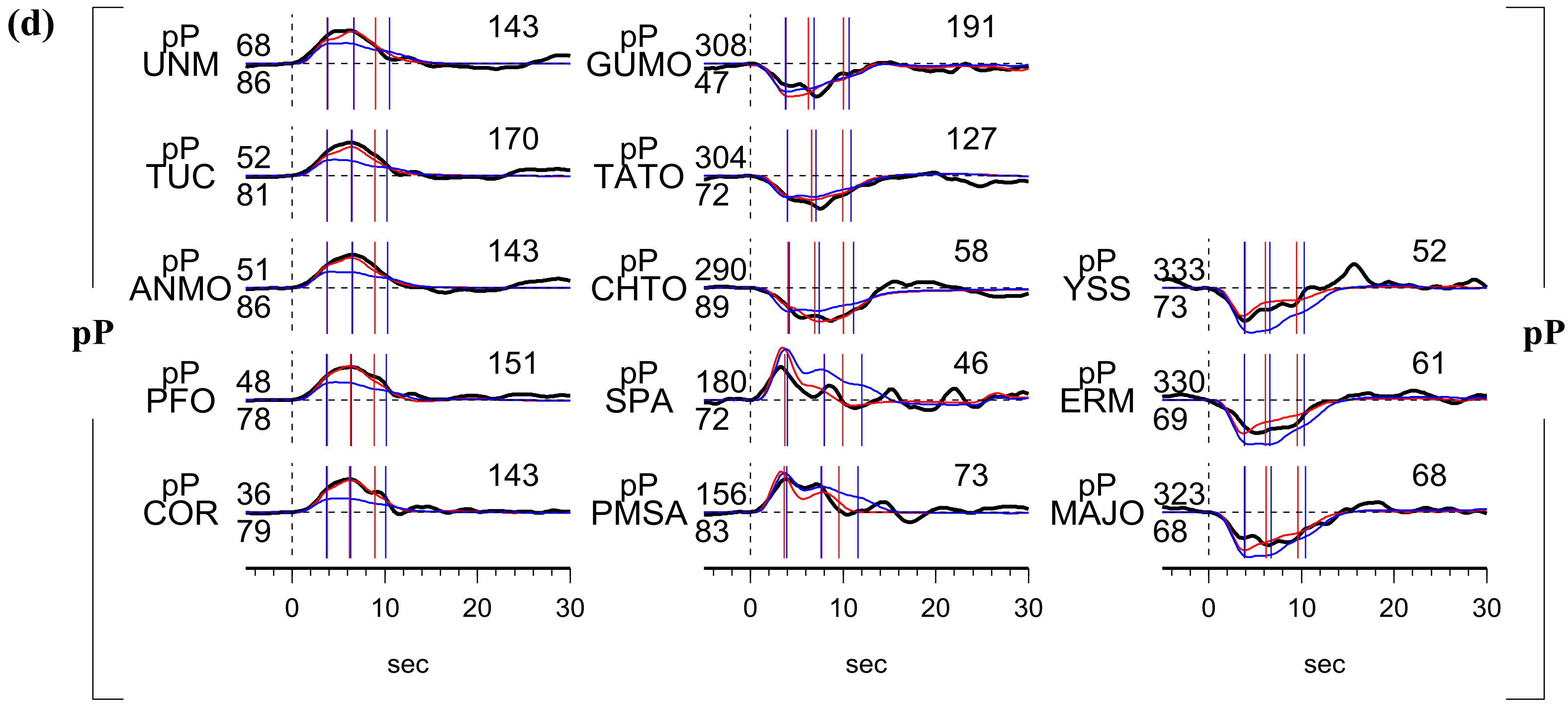

(d)
pP
pP
pP UNM 68 86 143
pP GUMO 308 47 191
pP TUC 52 81 170
pP TATO 304 72 127
pP ANMO 51 86 143
pP CHTO 290 89 58
pP YSS 333 73 52
pP PFO 48 78 151
pP SPA 180 72 46
pP ERM 330 69 61
pP COR 36 79 143
pP PMSA 156 83 73
pP MAJO 323 68 68
0 10 20 30
sec

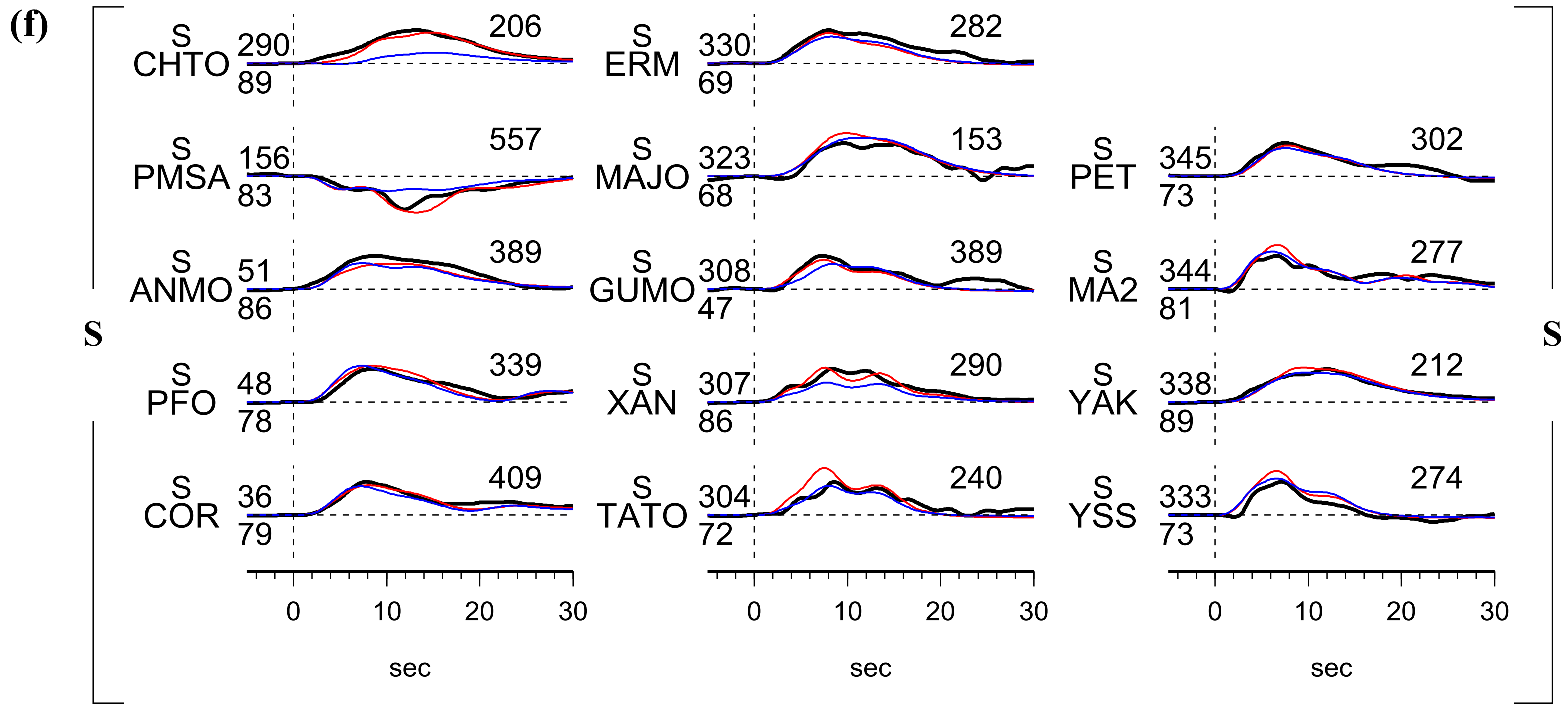

(f)
S
S
S CHTO 290 89 206
S ERM 330 69 282
S PMSA 156 83 557
S MAJO 323 68 153
S PET 345 73 302
S ANMO 51 86 389
S GUMO 308 47 389
S MA2 344 81 277
S PFO 48 78 339
S XAN 307 86 290
S YAK 338 89 212
S COR 36 79 409
S TATO 304 72 240
S YSS 333 73 274
0 10 20 30
sec

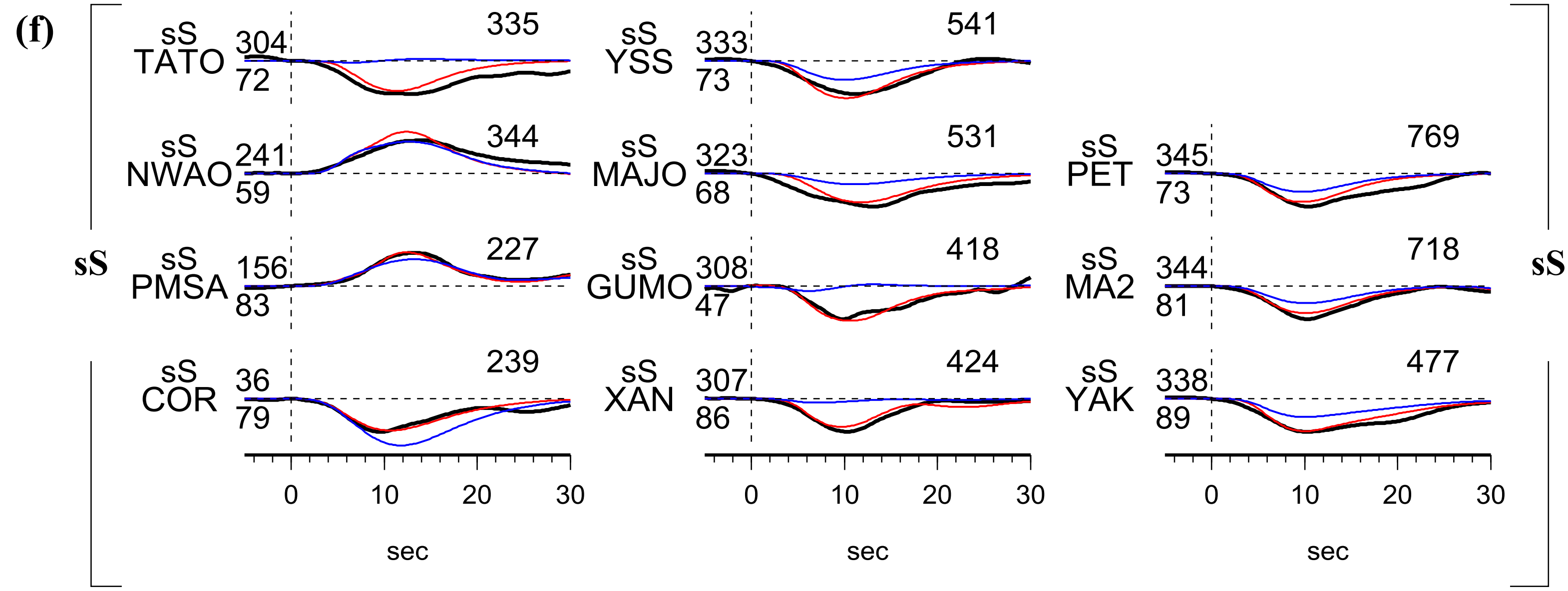

(f)
sS
sS
sS TATO 304 72 335
sS YSS 333 73 541
sS NWAO 241 59 344
sS MAJO 323 68 531
sS PET 345 73 769
sS PMSA 156 83 227
sS GUMO 308 47 418
sS MA2 344 81 718
sS COR 36 79 239
sS XAN 307 86 424
sS YAK 338 89 477
0 10 20 30
sec

E2. The 09 Jun 1994 Mw 8.2 earthquake

Earthquake E2 occurred 631 km beneath Northern Bolivia (Table S4-0). We infer the source process using 15 P, 8 pP, 13 S and 9 sS (Fig. S4-2a). Five sub-events (Table S4-2, Fig. 4-3a) are used to model the main energy after a 10 s initiation (Zhan et al., 2014). The best-fitting plane fits the data reasonably well, while the best planar model (the GCMT sub-horizontal model) does not predict the arrival times of the last two sub-events (Figs. S4-2c – S4-2f). The detail analysis is presented in the main text.

Table S4-2. Source parameters of inferred sub-events of E2

Sub-event	dt (s)	dn (km)	de (km)	dz (km)	duration (s)	Mw	strike (°)	dip (°)	slip (°)
1	15.4	2.6	20.4	8.9	7.6	7.7	297.1	14.5	288.3
2	19.2	5.6	25.5	5.0	8.0	7.8	293.4	7.3	286.1
3	24.6	15.4	14.5	5.1	10.0	7.8	312.2	11.2	308.7
4	30.8	21.7	22.6	18.0	12.0	7.9	313.4	8.4	311.0
5	38.4	20.2	41.2	39.0	10.0	7.8	311.6	10.0	305.9

(Fig. S4-2)

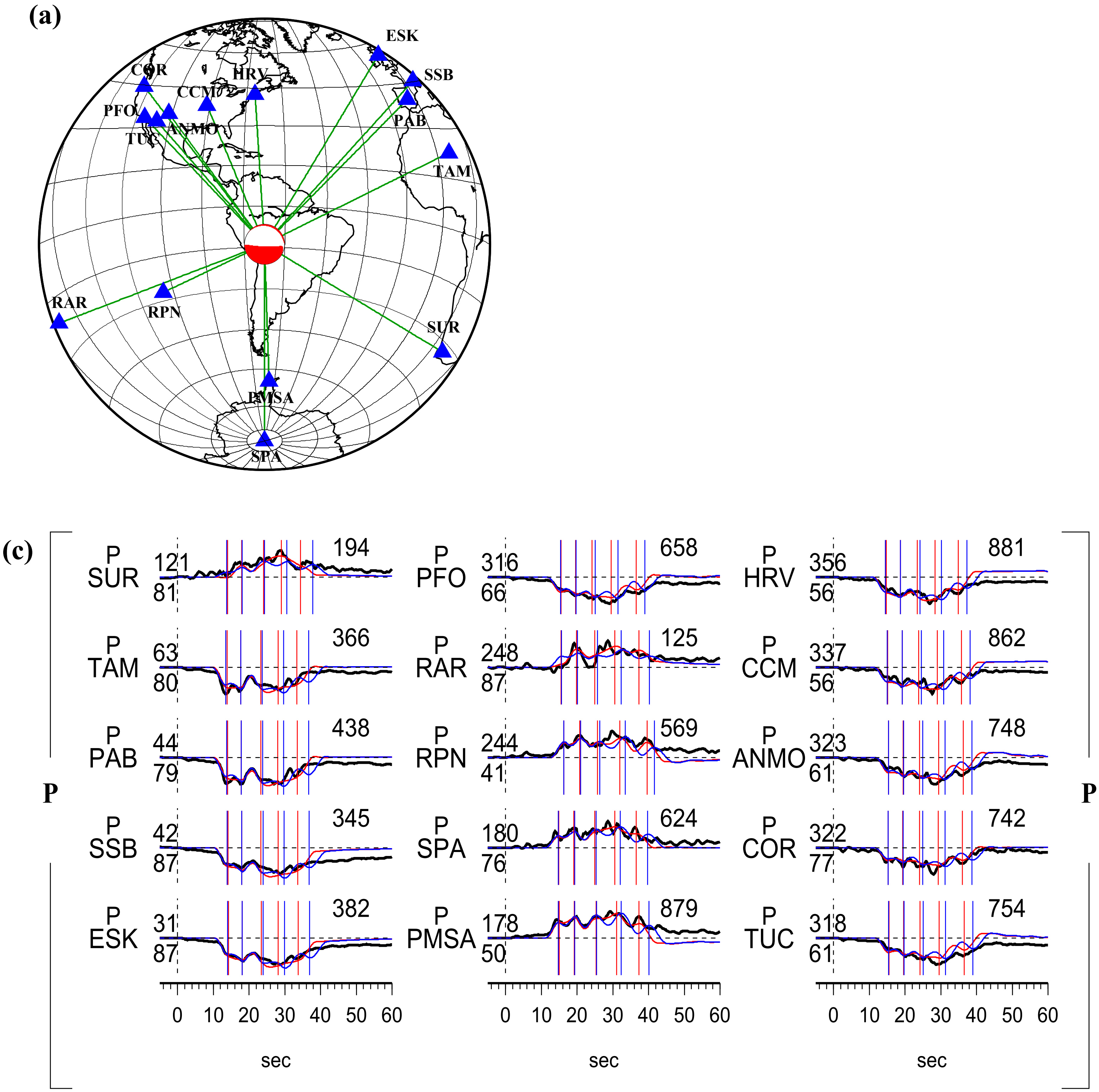
(a)
ESK
SSB
COR
HRV
CCM
PFO
PAB
ANMO
TUC
TAM
RAR
RPN
SUR
PMSA
SPA
(c)
P
P
P SUR 121 81 194
P TAM 63 80 366
P PAB 44 79 438
P SSB 42 87 345
P ESK 31 87 382
P PFO 316 66 658
P RAR 248 87 125
P RPN 244 41 569
P SPA 180 76 624
P PMSA 178 50 879
P HRV 356 56 881
P CCM 337 56 862
P ANMO 323 61 748
P COR 322 77 742
P TUC 318 61 754
0 10 20 30 40 50 60
sec

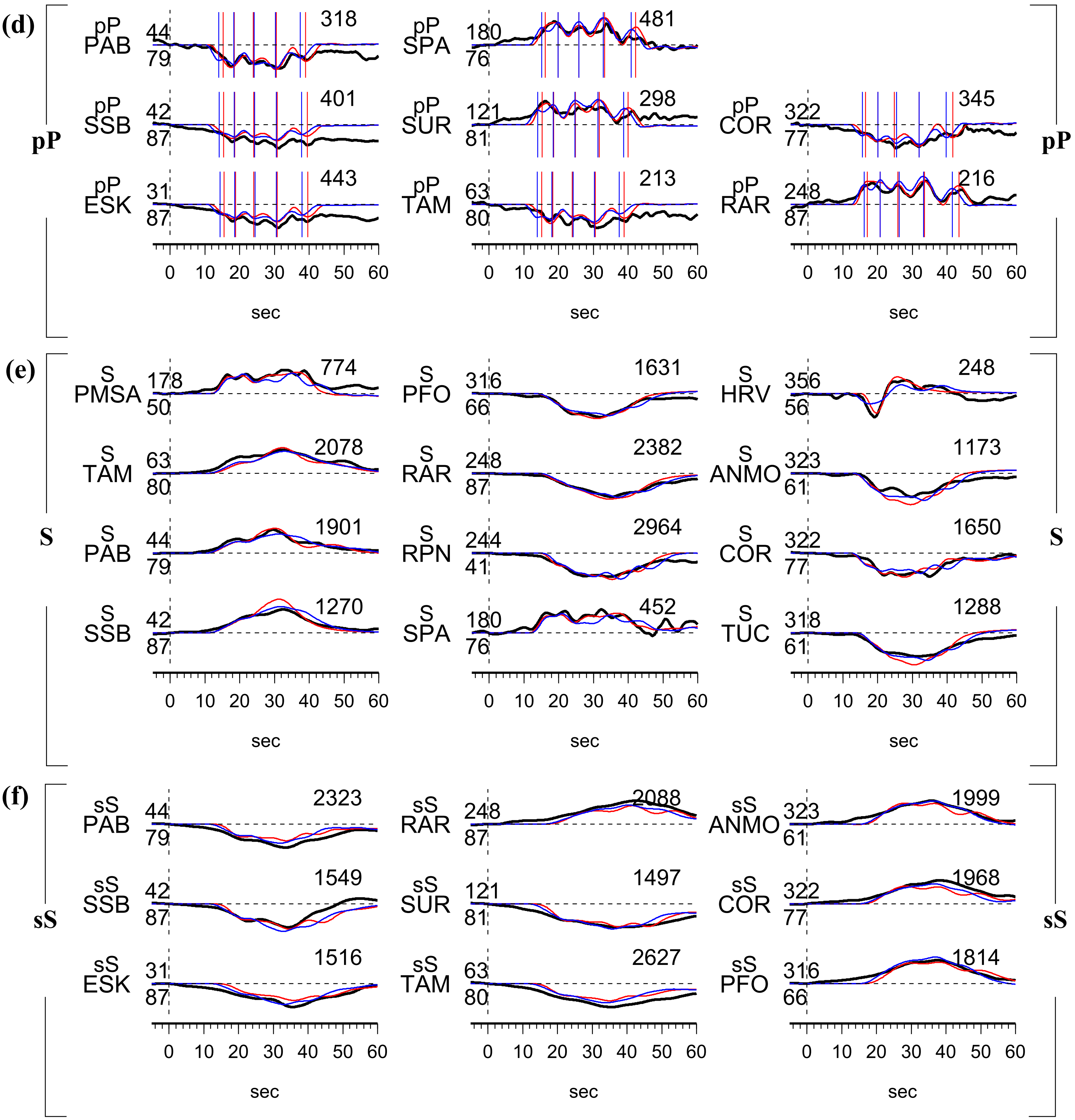
(d)
pP
pP PAB 44 79 318
pP SPA 180 76 481
pP SSB 42 87 401
pP SUR 121 81 298
pP COR 322 77 345
pP ESK 31 87 443
pP TAM 63 80 213
pP RAR 248 87 216
0 10 20 30 40 50 60
sec
(e)
S
S PMSA 178 50 774
S PFO 316 66 1631
S HRV 356 56 248
S TAM 63 80 2078
S RAR 248 87 2382
S ANMO 323 61 1173
S PAB 44 79 1901
S RPN 244 41 2964
S COR 322 77 1650
S SSB 42 87 1270
S SPA 180 76 452
S TUC 318 61 1288
0 10 20 30 40 50 60
sec
(f)
sS
sS PAB 44 79 2323
sS RAR 248 87 2088
sS ANMO 323 61 1999
sS SSB 42 87 1549
sS SUR 121 81 1497
sS COR 322 77 1968
sS ESK 31 87 1516
sS TAM 63 80 2627
sS PFO 316 66 1814
0 10 20 30 40 50 60
sec

E3. The 21 Jul 1994 Mw 7.3 earthquake

Earthquake E3 occurred 471 km beneath Sea of Japan (Table S4-0). We infer the source process using 26 P, 20 pP, 18 S and 20 sS data which constitute good azimuth coverage (Fig. S4-3a). Two energy pulses were observed in the first order (Antolik et al., 1999). However, four sub-events can be observed when looked into detail (ADK and OBN, Fig. S4-3c). The strong directivity of the two major pulses also require four sub-events (Table S4-3) to model the data (narrower at AFI and broader at AAK, Fig. S4-3c). The inferred sub-events propagate to the southeast and downward, consistent with the previous finite fault inversion result (Antolik et al., 1999). The sub-events propagate close to the nodal axis of the GCMT sub-horizontal and sub-vertical fault planes (Fig. S4-3b), consistent with the previous directivity analysis (Warren and Silver, 2006). However, synthetics (blue traces) predicted by the best planar model can fit the radiation patterns of the seismic data (black traces, Figs. S4-3c-S4-3f), especially the P wave data in the azimuth of 322° to 335° (Fig. S4-3c).

Table S4-3. Source parameters of inferred sub-events of E3

Sub-event	dt (s)	dn (km)	de (km)	dz (km)	duration (s)	Mw	strike (°)	dip (°)	slip (°)
1	1.1	-0.5	0.5	0.0	2.0	6.8	61.9	53.6	196.0
2	2.3	-2.7	4.4	2.2	2.0	6.8	68.7	39.9	177.5
3	5.0	-5.1	5.8	8.1	3.0	6.8	70.7	30.0	178.5
4	6.6	-18.3	10.1	10	4.0	7.0	70.7	30.9	174.8

(Fig. S4-3)

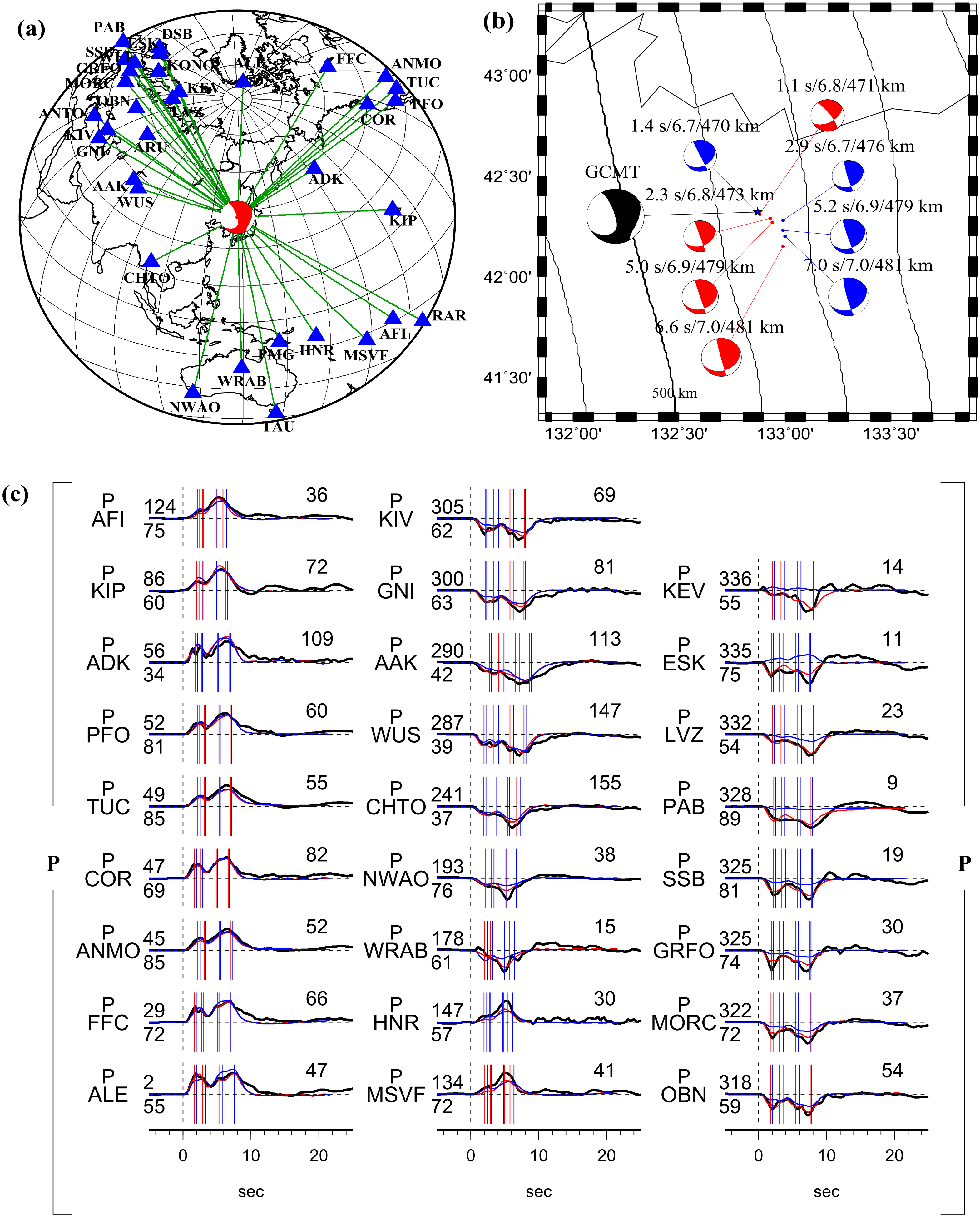
(a)
PAB
DSB
ESK
SSB
WLF
GRFO
MORC
KONO
KEV
ALE
FFC
ANMO
TUC
PFO
OBN
LVZ
ANTO
KIV
GNI
ARU
COR
AAK
WUS
ADK
KIP
CHTO
RAR
AFI
PMG
HNR
MSVF
WRAB
NWAO
TAU
(b)
43˚00'
42˚30'
42˚00'
41˚30'
132˚00'
132˚30'
133˚00'
133˚30'
GCMT
1.1 s/6.8/471 km
1.4 s/6.7/470 km
2.9 s/6.7/476 km
2.3 s/6.8/473 km
5.2 s/6.9/479 km
5.0 s/6.9/479 km
7.0 s/7.0/481 km
6.6 s/7.0/481 km
500 km
(c)
P AFI 124 75 36
P KIP 86 60 72
P ADK 56 34 109
P PFO 52 81 60
P TUC 49 85 55
P COR 47 69 82
P ANMO 45 85 52
P FFC 29 72 66
P ALE 2 55 47
P KIV 305 62 69
P GNI 300 63 81
P AAK 290 42 113
P WUS 287 39 147
P CHTO 241 37 155
P NWAO 193 76 38
P WRAB 178 61 15
P HNR 147 57 30
P MSVF 134 72 41
P KEV 336 55 14
P ESK 335 75 11
P LVZ 332 54 23
P PAB 328 89 9
P SSB 325 81 19
P GRFO 325 74 30
P MORC 322 72 37
P OBN 318 59 54
P
P
0
10
20
sec

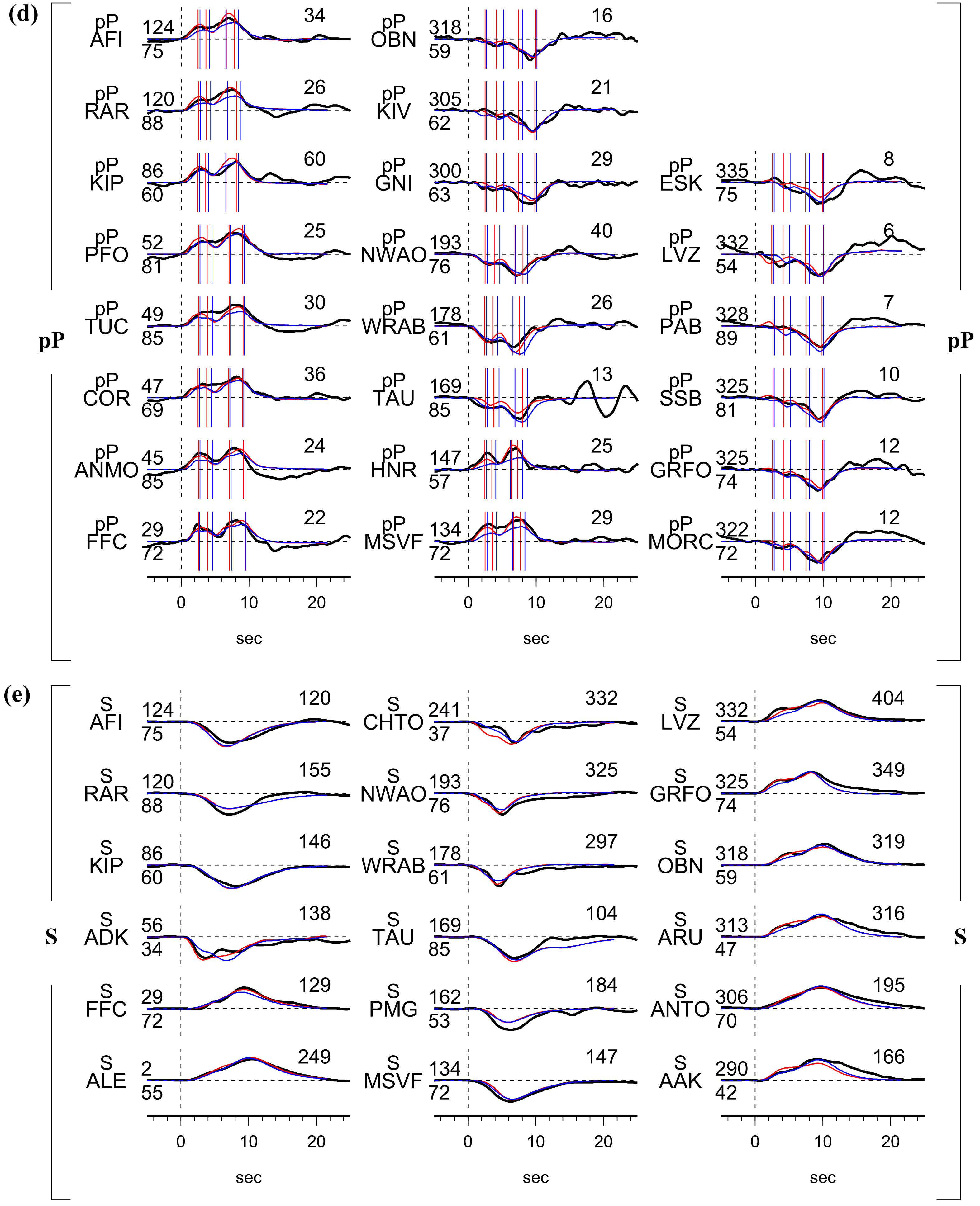
(d)
pP
pP AFI 124 75 34
pP RAR 120 88 26
pP KIP 86 60 60
pP PFO 52 81 25
pP TUC 49 85 30
pP COR 47 69 36
pP ANMO 45 85 24
pP FFC 29 72 22
pP OBN 318 59 16
pP KIV 305 62 21
pP GNI 300 63 29
pP NWAO 193 76 40
pP WRAB 178 61 26
pP TAU 169 85 13
pP HNR 147 57 25
pP MSVF 134 72 29
pP ESK 335 75 8
pP LVZ 332 54 6
pP PAB 328 89 7
pP SSB 325 81 10
pP GRFO 325 74 12
pP MORC 322 72 12
0
10
20
sec
(e)
S
S AFI 124 75 120
S RAR 120 88 155
S KIP 86 60 146
S ADK 56 34 138
S FFC 29 72 129
S ALE 2 55 249
S CHTO 241 37 332
S NWAO 193 76 325
S WRAB 178 61 297
S TAU 169 85 104
S PMG 162 53 184
S MSVF 134 72 147
S LVZ 332 54 404
S GRFO 325 74 349
S OBN 318 59 319
S ARU 313 47 316
S ANTO 306 70 195
S AAK 290 42 166
0
10
20
sec

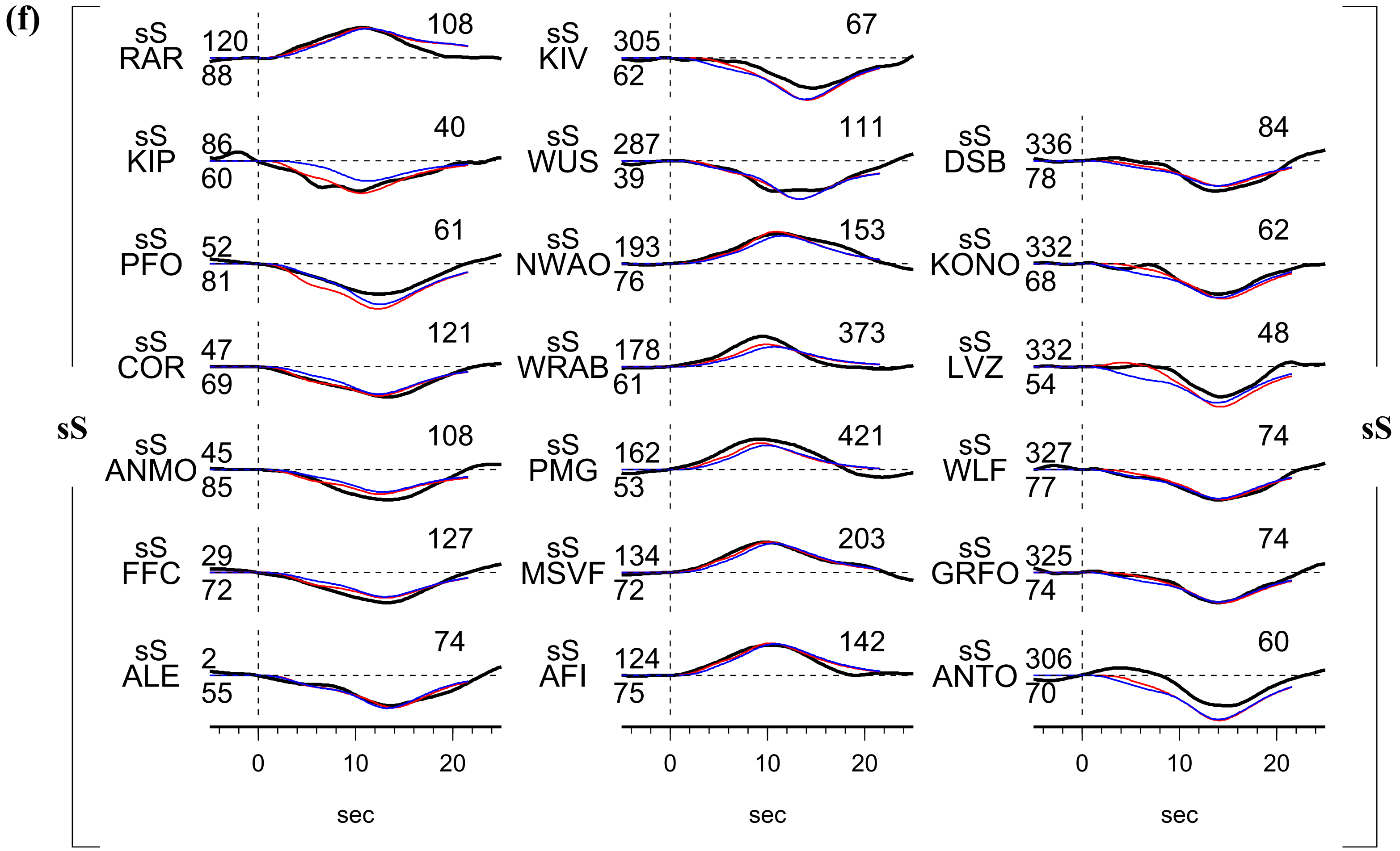
(f)
sS
sS
sS RAR 120 88 108
sS KIV 305 62 67
sS KIP 86 60 40
sS WUS 287 39 111
sS DSB 336 78 84
sS PFO 52 81 61
sS NWAO 193 76 153
sS KONO 332 68 62
sS COR 47 69 121
sS WRAB 178 61 373
sS LVZ 332 54 48
sS ANMO 45 85 108
sS PMG 162 53 421
sS WLF 327 77 74
sS FFC 29 72 127
sS MSVF 134 72 203
sS GRFO 325 74 74
sS ALE 2 55 74
sS AFI 124 75 142
sS ANTO 306 70 60
0
10
20
sec
0
10
20
sec
0
10
20
sec

E4. The 23 Aug 1995 Mw 7.0 earthquake

Earthquake E4 occurred 595 km beneath Mariana Islands (Table S4-0). We inferred the source process by fitting 20 P, 13 pP, 21 S and 9 sS data (Fig. S4-4a). The seismic energy can be modeled by two sub-events propagating to the southwest with a duration of 5.5 s and the second sub-event is 11 km from the initiation point (Fig. S4-4b, Table S4-4). Synthetics predicted by the best planar (135˚/42˚/242˚, low-angle plane) fit the seismic data as well as synthetics predicted by the best-fitting model (Fig. S4-4c – S4-4f). The result of plane rupture on the GCMT low-angle plane is consistent with the previous directivity analysis (Myhill, 2012) and finite fault inversion (Antolik, 1999).

Table S4-4. Source parameters of inferred sub-events of E4

Sub-event	dt (s)	dn (km)	de (km)	dz (km)	duration (s)	Mw	strike (°)	dip (°)	slip (°)
1	1.5	-1.4	-2.0	0.0	2.2	6.6	149.0	43.7	255.4
2	4.0	-3.6	-6.5	7.8	3.0	6.9	132.8	43.9	235.2

(Fig. S4-4)

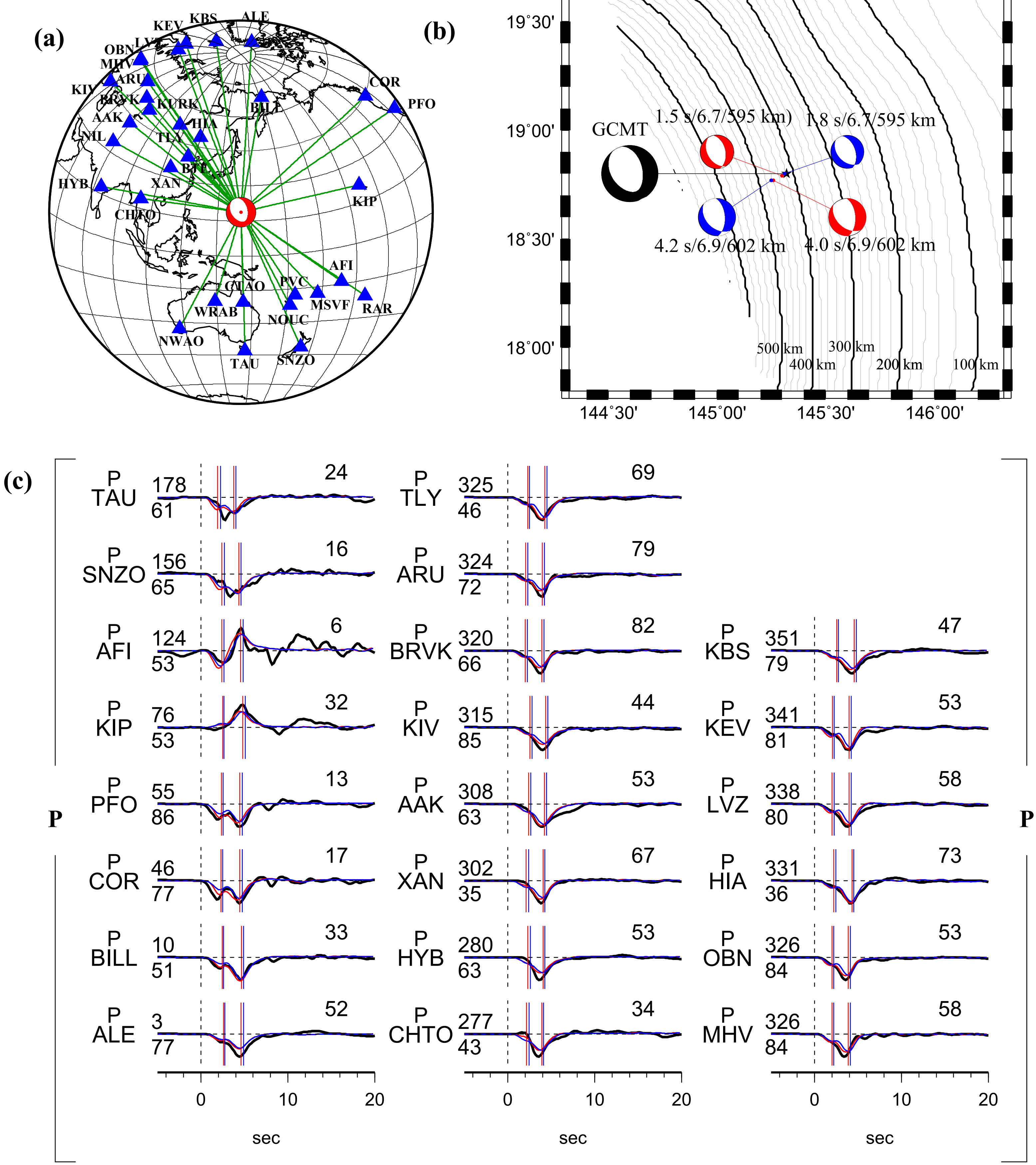

(a)
KEV
KBS
ALE
OBN
LVZ
MHV
ARU
KIV
BRVK
KURK
AAK
HIA
NIL
TLY
BILL
COR
PFO
BJT
XAN
HYB
CHTO
KIP
AFI
CTAO
PVC
MSVF
RAR
WRAB
NOUC
NWAO
TAU
SNZO
(b)
19˚30'
19˚00'
18˚30'
18˚00'
144˚30'
145˚00'
145˚30'
146˚00'
GCMT
1.5 s/6.7/595 km)
1.8 s/6.7/595 km
4.2 s/6.9/602 km
4.0 s/6.9/602 km
500 km
400 km
300 km
200 km
100 km
(c)
P
P TAU 178 61 24
P SNZO 156 65 16
P AFI 124 53 6
P KIP 76 53 32
P PFO 55 86 13
P COR 46 77 17
P BILL 10 51 33
P ALE 3 77 52
P TLY 325 46 69
P ARU 324 72 79
P BRVK 320 66 82
P KIV 315 85 44
P AAK 308 63 53
P XAN 302 35 67
P HYB 280 63 53
P CHTO 277 43 34
P KBS 351 79 47
P KEV 341 81 53
P LVZ 338 80 58
P HIA 331 36 73
P OBN 326 84 53
P MHV 326 84 58
0
10
20
sec

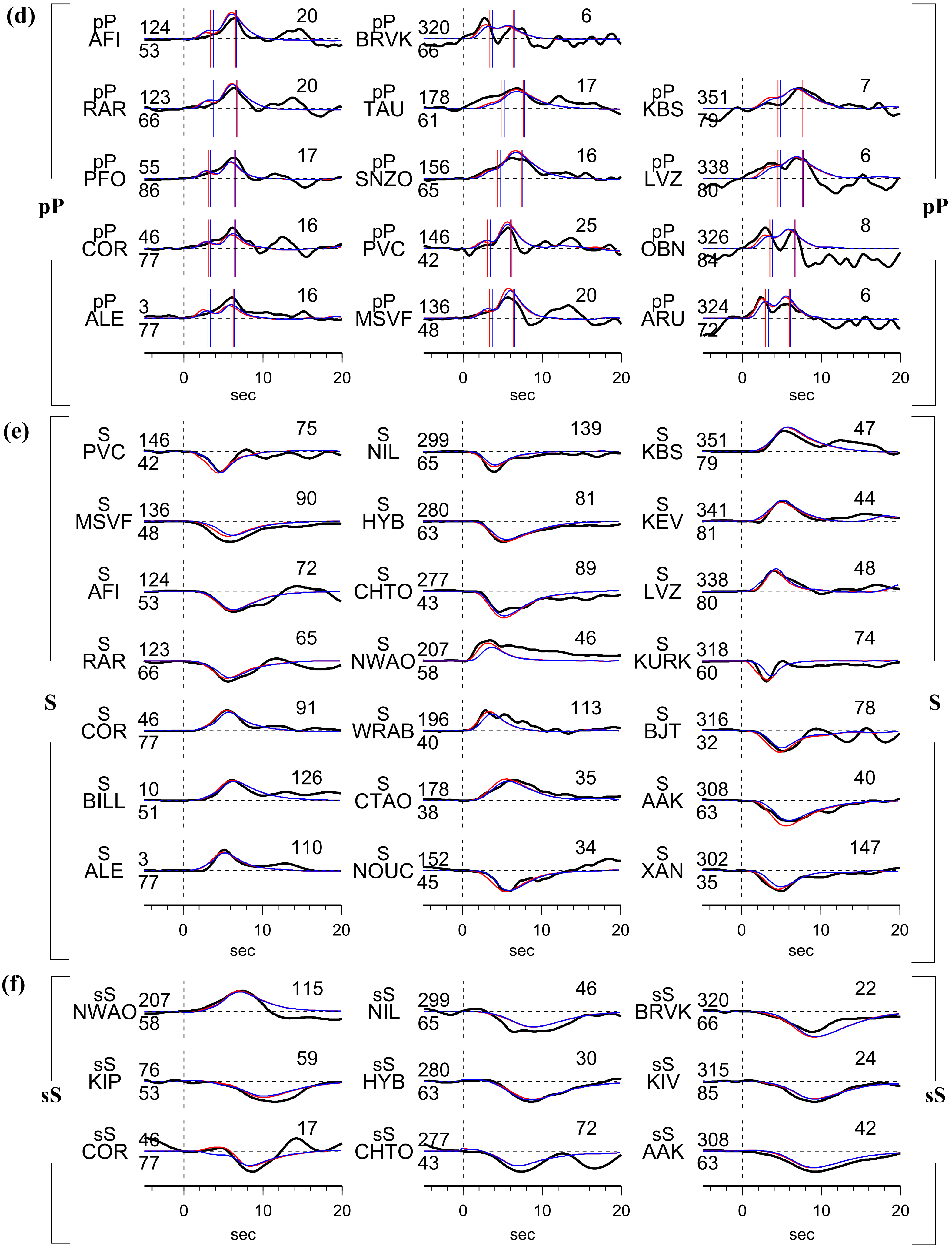
(d)
pP
pP AFI 124 53 20
pP BRVK 320 66 6
pP RAR 123 66 20
pP TAU 178 61 17
pP KBS 351 79 7
pP PFO 55 86 17
pP SNZO 156 65 16
pP LVZ 338 80 6
pP COR 46 77 16
pP PVC 146 42 25
pP OBN 326 84 8
pP ALE 3 77 16
pP MSVF 136 48 20
pP ARU 324 72 6
0
10
20
sec
(e)
S
S PVC 146 42 75
S NIL 299 65 139
S KBS 351 79 47
S MSVF 136 48 90
S HYB 280 63 81
S KEV 341 81 44
S AFI 124 53 72
S CHTO 277 43 89
S LVZ 338 80 48
S RAR 123 66 65
S NWAO 207 58 46
S KURK 318 60 74
S COR 46 77 91
S WRAB 196 40 113
S BJT 316 32 78
S BILL 10 51 126
S CTAO 178 38 35
S AAK 308 63 40
S ALE 3 77 110
S NOUC 152 45 34
S XAN 302 35 147
0
10
20
sec
(f)
sS
sS NWAO 207 58 115
sS NIL 299 65 46
sS BRVK 320 66 22
sS KIP 76 53 59
sS HYB 280 63 30
sS KIV 315 85 24
sS COR 46 77 17
sS CHTO 277 43 72
sS AAK 308 63 42
0
10
20
sec

E5. The 17 Jun 1996 Mw 7.8 earthquake

Earthquake E5 occurred 587 km beneath Flores Sea (Table S4-0). We infer the source process using 24 P, 12 pP, 21 S and 10 sS with good azimuth coverage (Fig. S4-5a). The seismic data exhibit great complexity and the seismic energy are sometimes with different polarities (Fig. S4-5c). The complex waveforms are owing to the variability of fault orientation, and the sensitivity of the seismograms which take off near the nodal planes. The seismic energy can be modeled by five sub-events, propagating to the east and downward, with a large horizontal extension of 70 km (Table S4-5, Fig. S4-5b). The arrival times of the best-fitting model and best planar model are roughly the same for the first four sub-events, while the fifth sub-event has a little depth difference between the two models. The best-fitting model match the radiation pattern much better, especially for the SH and sSH waves (Figs. S4-5c – S4-5f).

Table S4-5. Source parameters of inferred sub-events of E5

Sub-event	dt (s)	dn (km)	de (km)	dz (km)	duration (s)	Mw	strike (°)	dip (°)	slip (°)
1	3.7	-3.6	-4.0	0.4	6.0	7.1	90.9	54.1	319.2
2	7.9	-23.3	8.5	9.8	4.0	7.4	78.9	43.4	317.2
3	10.3	-15.3	15.5	7.8	4.0	7.5	103.8	54.2	316.2
4	15.0	-0.9	49.7	5.3	7.2	7.5	110.6	59.3	316.3
5	20.9	-12.1	63.1	25.5	6.4	7.4	81.5	52.3	305.5

(Fig. S4-5)

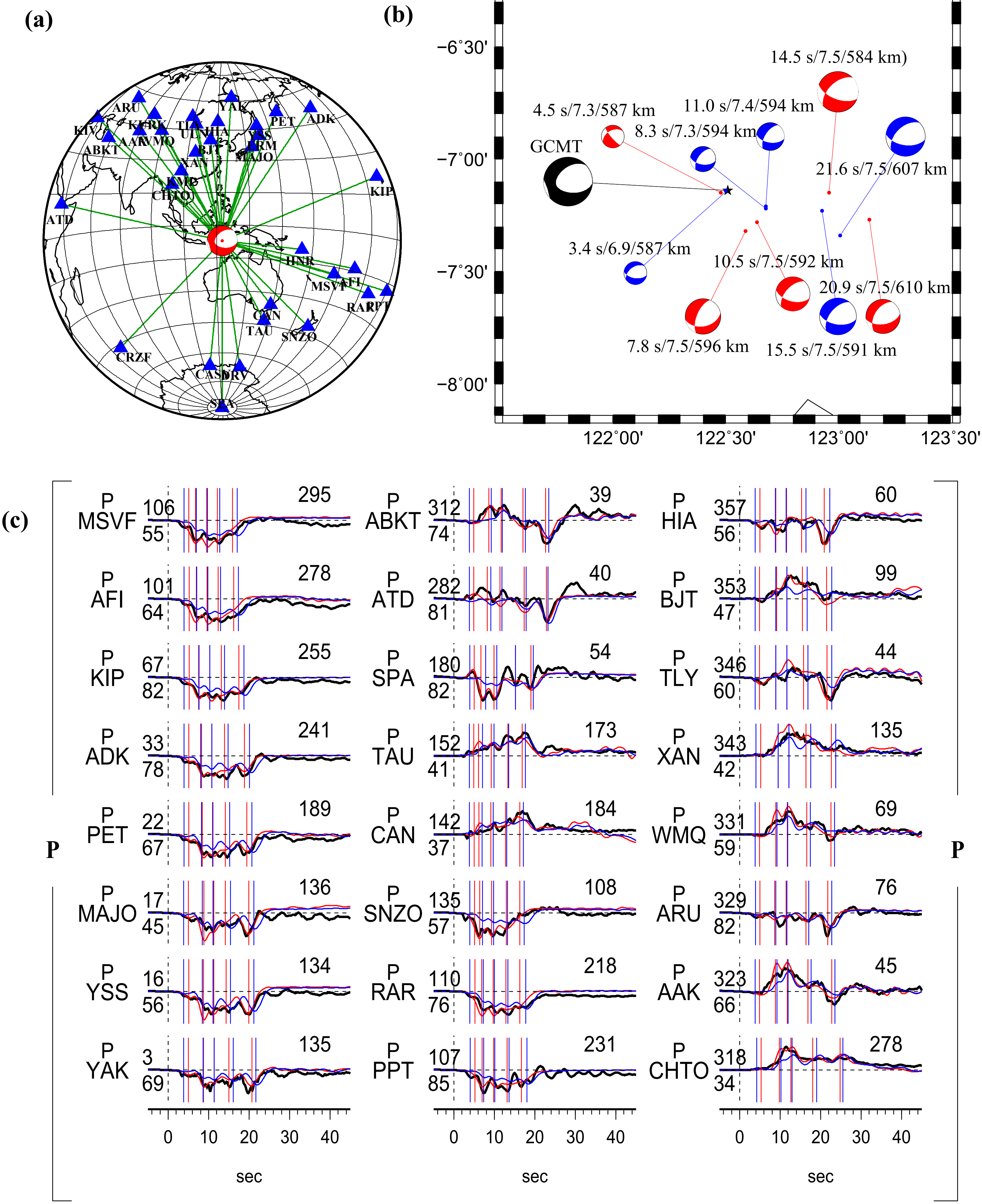

(a)
ARU
YAK
PET
ADK
KIV
KURK
TLY
HIA
AAK
WMQ
ULN
YSS
ABKT
BJT
ERM
MAJO
XAN
KMI
CHTO
KIP
ATD
HNR
AFI
MSVF
RAR
PPT
CAN
TAU
SNZO
CRZF
CASY
DRV
SPA
(b)
−6˚30'
−7˚00'
−7˚30'
−8˚00'
122˚00'
122˚30'
123˚00'
123˚30'
14.5 s/7.5/584 km)
4.5 s/7.3/587 km
11.0 s/7.4/594 km
8.3 s/7.3/594 km
GCMT
21.6 s/7.5/607 km
3.4 s/6.9/587 km
10.5 s/7.5/592 km
20.9 s/7.5/610 km
7.8 s/7.5/596 km
15.5 s/7.5/591 km
(c)
P MSVF 106 55 295
P AFI 101 64 278
P KIP 67 82 255
P ADK 33 78 241
P PET 22 67 189
P MAJO 17 45 136
P YSS 16 56 134
P YAK 3 69 135
P ABKT 312 74 39
P ATD 282 81 40
P SPA 180 82 54
P TAU 152 41 173
P CAN 142 37 184
P SNZO 135 57 108
P RAR 110 76 218
P PPT 107 85 231
P HIA 357 56 60
P BJT 353 47 99
P TLY 346 60 44
P XAN 343 42 135
P WMQ 331 59 69
P ARU 329 82 76
P AAK 323 66 45
P CHTO 318 34 278
P
P
0
10
20
30
40
sec

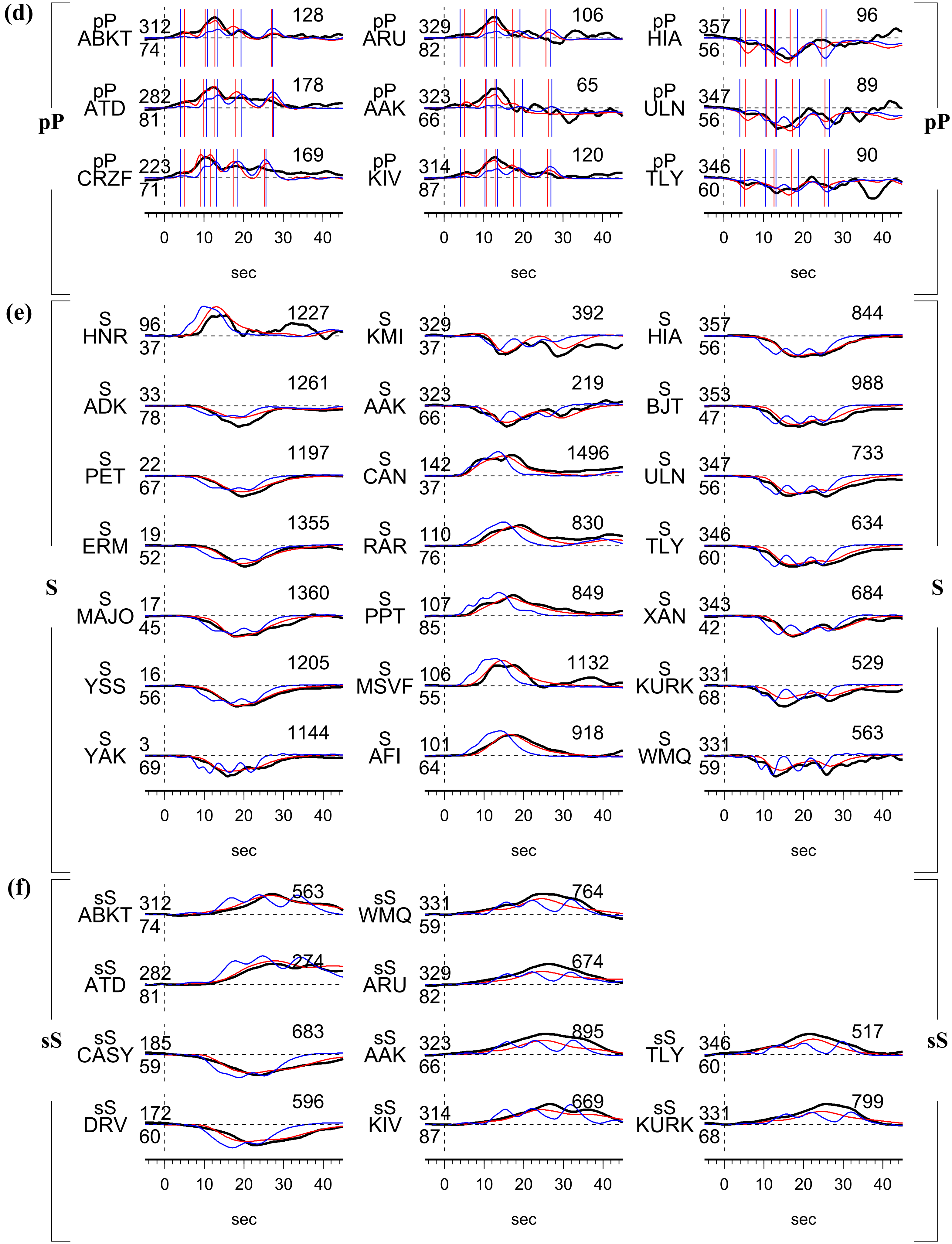
(d)
pP
pP ABKT 312 74 128
pP ARU 329 82 106
pP HIA 357 56 96
pP ATD 282 81 178
pP AAK 323 66 65
pP ULN 347 56 89
pP CRZF 223 71 169
pP KIV 314 87 120
pP TLY 346 60 90
0 10 20 30 40
sec
(e)
S
S HNR 96 37 1227
S KMI 329 37 392
S HIA 357 56 844
S ADK 33 78 1261
S AAK 323 66 219
S BJT 353 47 988
S PET 22 67 1197
S CAN 142 37 1496
S ULN 347 56 733
S ERM 19 52 1355
S RAR 110 76 830
S TLY 346 60 634
S MAJO 17 45 1360
S PPT 107 85 849
S XAN 343 42 684
S YSS 16 56 1205
S MSVF 106 55 1132
S KURK 331 68 529
S YAK 3 69 1144
S AFI 101 64 918
S WMQ 331 59 563
0 10 20 30 40
sec
(f)
sS
sS ABKT 312 74 563
sS WMQ 331 59 764
sS ATD 282 81 274
sS ARU 329 82 674
sS CASY 185 59 683
sS AAK 323 66 895
sS TLY 346 60 517
sS DRV 172 60 596
sS KIV 314 87 669
sS KURK 331 68 799
0 10 20 30 40
sec

E6. The 05 Aug 1996 Mw 7.4 earthquake

Earthquake E6 occurred 550 km beneath Fiji Islands Region (Table S4-0). We infer the source process using 29 P, 16 pP, 20 S and 10 sS constitute good azimuth coverage (Fig. S4-6a). The comparison of waveform fitting is showed in Figs. S4-6c – S4-6f. The analysis is presented in the main text.

Table S4-6. Source parameters of inferred sub-events of E6

Sub-event	dt (s)	dn (km)	de (km)	dz (km)	duration (s)	Mw	strike (°)	dip (°)	slip (°)
1	2.0	-3.3	4.5	-2.0	2.0	6.8	196.6	22.7	242.6
2	4.2	7.2	3.2	-5.0	3.0	7.1	197.3	22.3	246.5
3	6.4	1.7	1.7	-6.9	4.0	7.0	220.4	15.3	268.4
4	9.6	18.2	2.9	2.3	3.8	6.7	194.6	12.4	237.1

(Fig. S4-6)

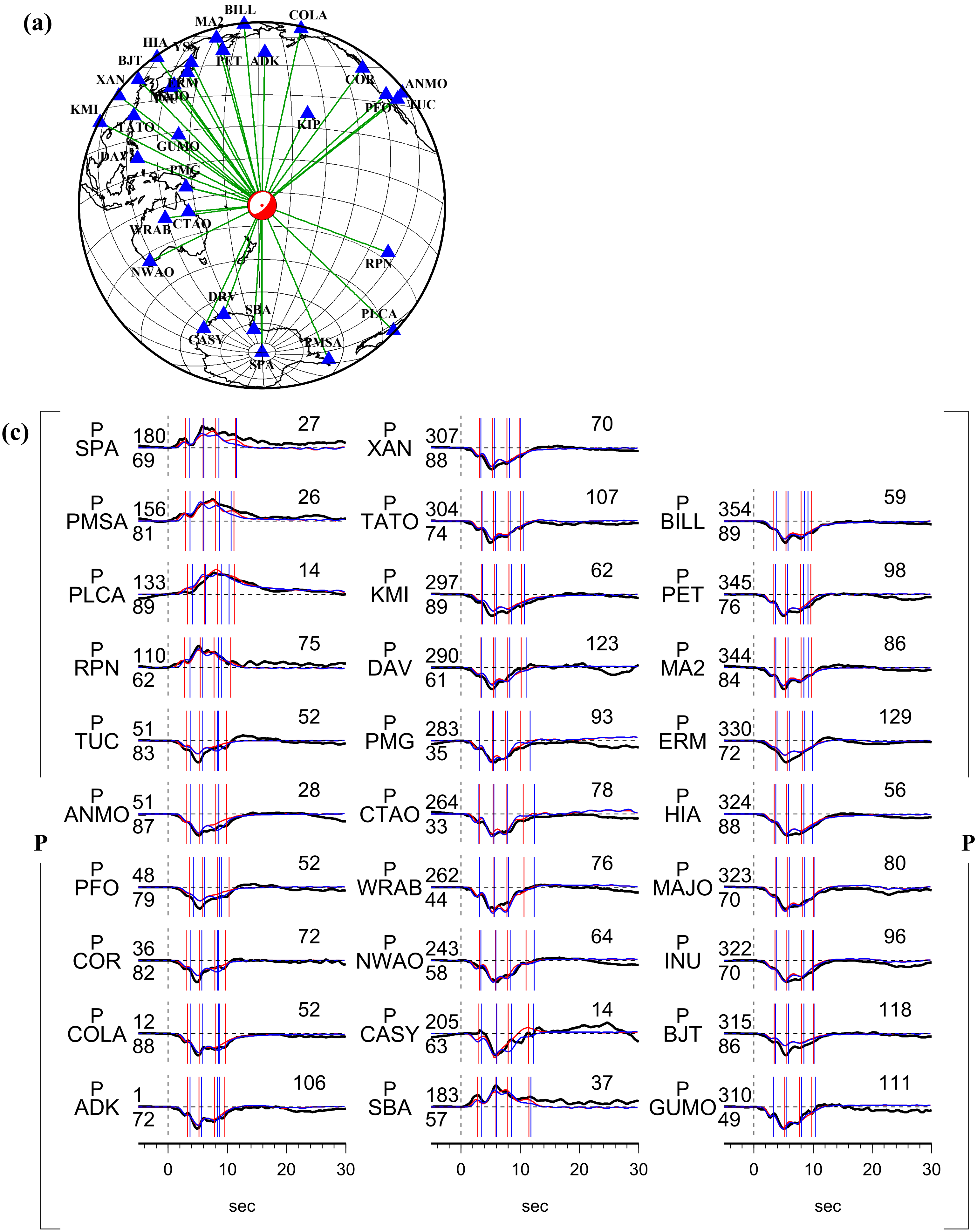

(a)
BILL
MA2
COLA
HIA
YSS
BJT
PET
ADK
XAN
ERM
COR
ANMO
MAJO
INU
KMI
PFO
TUC
KIP
TATO
GUMO
DAV
PMG
WRAB
CTAO
RPN
NWAO
DRV
SBA
PLCA
CASY
PMSA
SPA
(c)
P SPA 180 69 27
P PMSA 156 81 26
P PLCA 133 89 14
P RPN 110 62 75
P TUC 51 83 52
P ANMO 51 87 28
P PFO 48 79 52
P COR 36 82 72
P COLA 12 88 52
P ADK 1 72 106
P XAN 307 88 70
P TATO 304 74 107
P KMI 297 89 62
P DAV 290 61 123
P PMG 283 35 93
P CTAO 264 33 78
P WRAB 262 44 76
P NWAO 243 58 64
P CASY 205 63 14
P SBA 183 57 37
P BILL 354 89 59
P PET 345 76 98
P MA2 344 84 86
P ERM 330 72 129
P HIA 324 88 56
P MAJO 323 70 80
P INU 322 70 96
P BJT 315 86 118
P GUMO 310 49 111
0
10
20
30
sec
0
10
20
30
sec
0
10
20
30
sec
P
P

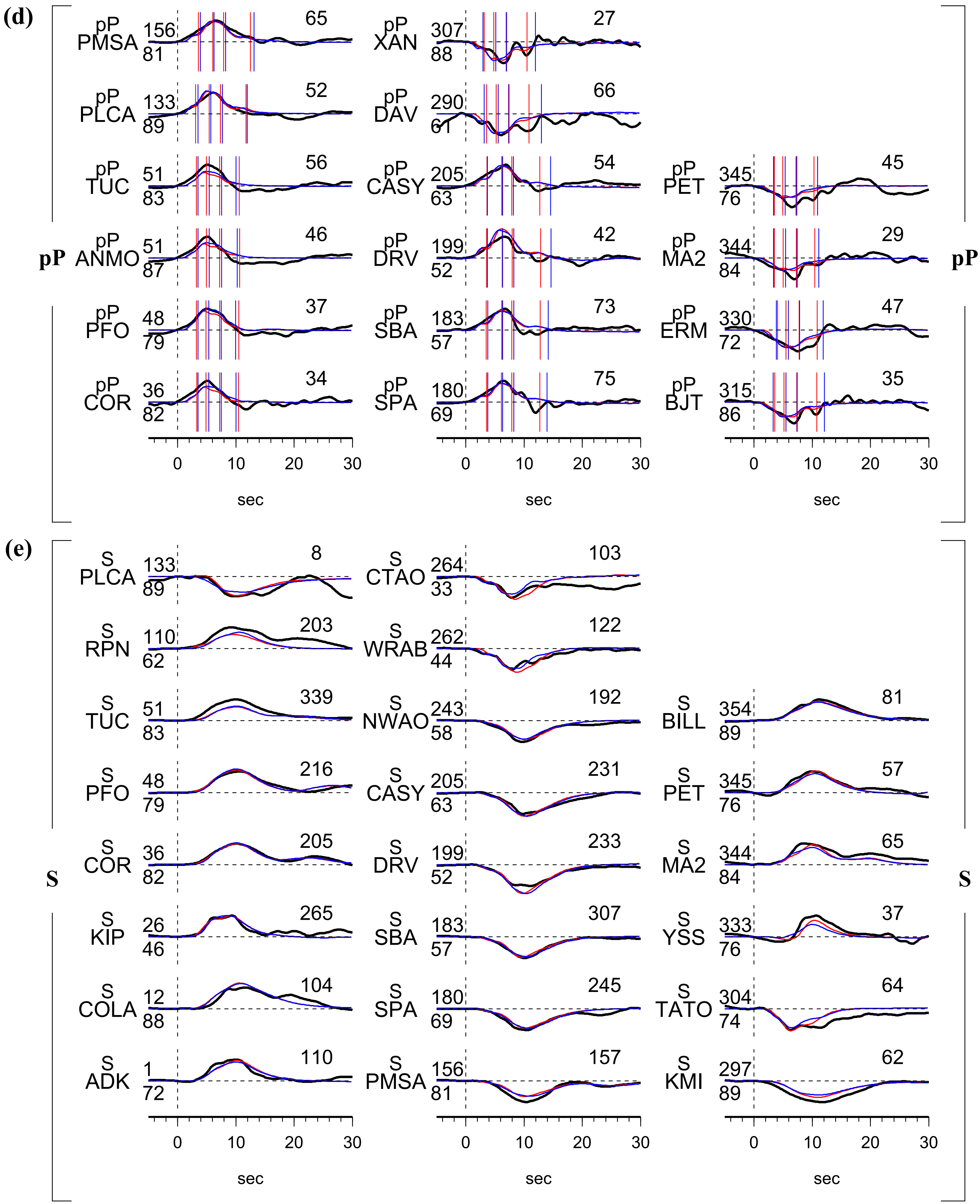
(d)
pP
pP PMSA 156 81 65
pP XAN 307 88 27
pP PLCA 133 89 52
pP DAV 290 61 66
pP TUC 51 83 56
pP CASY 205 63 54
pP PET 345 76 45
pP ANMO 51 87 46
pP DRV 199 52 42
pP MA2 344 84 29
pP PFO 48 79 37
pP SBA 183 57 73
pP ERM 330 72 47
pP COR 36 82 34
pP SPA 180 69 75
pP BJT 315 86 35
0 10 20 30
sec
(e)
S
S PLCA 133 89 8
S CTAO 264 33 103
S RPN 110 62 203
S WRAB 262 44 122
S TUC 51 83 339
S NWAO 243 58 192
S BILL 354 89 81
S PFO 48 79 216
S CASY 205 63 231
S PET 345 76 57
S COR 36 82 205
S DRV 199 52 233
S MA2 344 84 65
S KIP 26 46 265
S SBA 183 57 307
S YSS 333 76 37
S COLA 12 88 104
S SPA 180 69 245
S TATO 304 74 64
S ADK 1 72 110
S PMSA 156 81 157
S KMI 297 89 62
0 10 20 30
sec

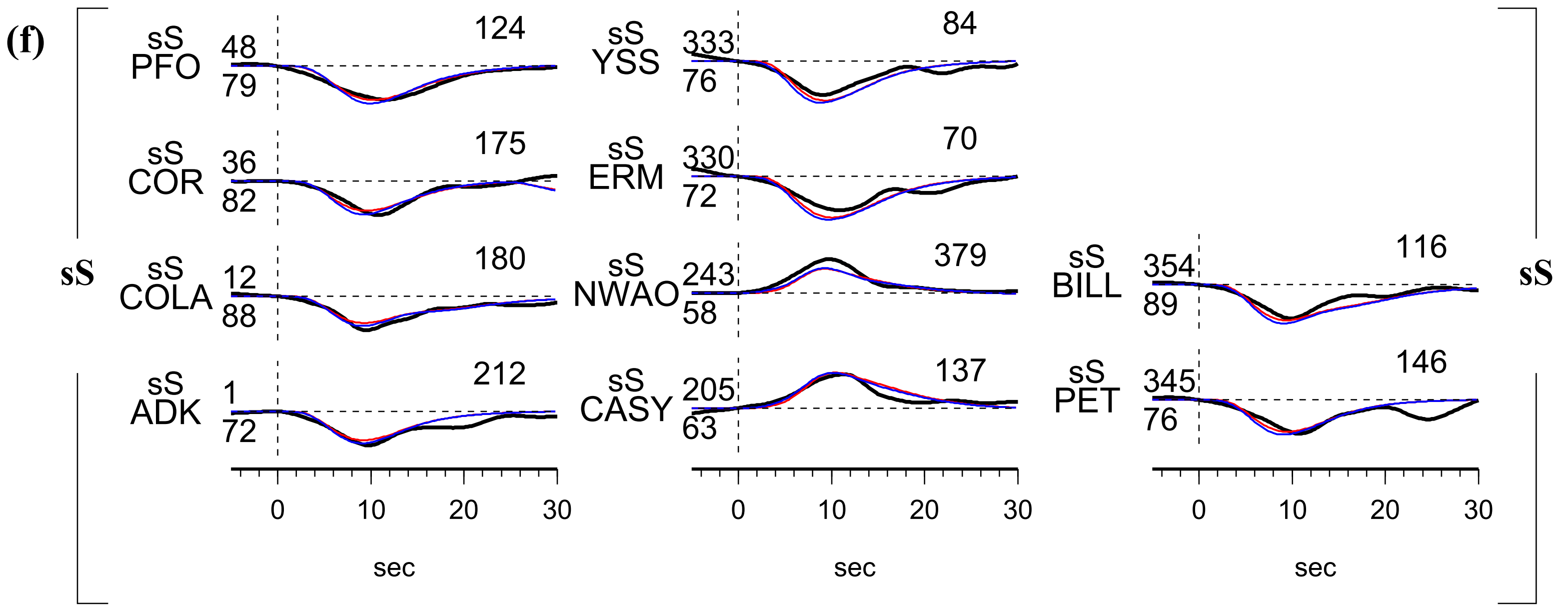
(f)
sS
sS
sS PFO 48 79 124
sS YSS 333 76 84
sS COR 36 82 175
sS ERM 330 72 70
sS COLA 12 88 180
sS NWAO 243 58 379
sS BILL 354 89 116
sS ADK 1 72 212
sS CASY 205 63 137
sS PET 345 76 146
0
10
20
30
sec

E7. The 29 Mar 1998 Mw 7.1 earthquake

Earthquake E7 occurred 543 km beneath Fiji Islands region (Table S4-0). The seismograms constitute good azimuthal coverage with 26 P, 10 pP, 24 S and 16 sS wave data (Fig. S4-7a). The earthquake has one major sub-event only, which is 8 km away from the initiation point (Fig. S4-7b). The inferred source parameter is consistent with the GCMT solution (Table S4-7). The previous directivity analysis was not able to distinguish the fault planes (Warren et al., 2007). We suggest that the source region is too small to detect its directivity. The best-fitting model is able to model the seismic data reasonably well (Figs, S4-7c – S4-7f). We do not perform the plane tests, because one sub-event can be naturally fit into plane rupture.

Table S4-7. Source parameters of inferred sub-events of E7

Sub-event	dt (s)	dn (km)	de (km)	dz (km)	duration (s)	Mw	strike (°)	dip (°)	slip (°)
1	2.8	-1.4	5.4	-4.4	3.0	7.1	101.9	72.0	41.6

(Fig. S4-7)

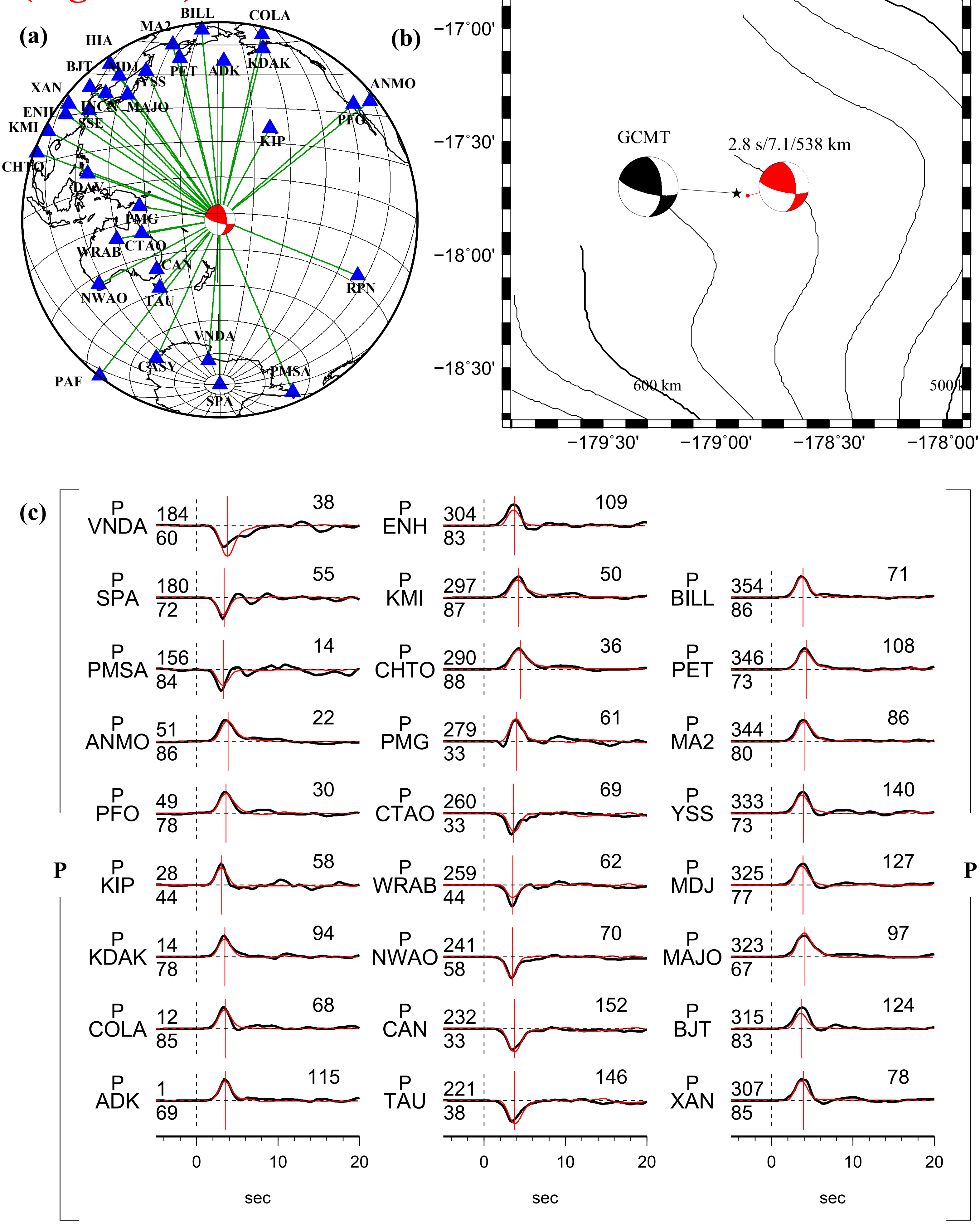
(a)
BILL
COLA
MA2
HIA
PET
ADK
KDAK
BJT
MDJ
YSS
XAN
ANMO
INCN
MAJO
ENH
SSE
PFO
KMI
KIP
CHTO
DAV
PMG
CTAO
WRAB
CAN
RPN
NWAO
TAU
VNDA
CASY
PMSA
PAF
SPA
(b)
−17˚00'
−17˚30'
−18˚00'
−18˚30'
GCMT
2.8 s/7.1/538 km
600 km
500 k
−179˚30'
−179˚00'
−178˚30'
−178˚00'
(c)
P VNDA 184 60 38
P ENH 304 83 109
P SPA 180 72 55
P KMI 297 87 50
P BILL 354 86 71
P PMSA 156 84 14
P CHTO 290 88 36
P PET 346 73 108
P ANMO 51 86 22
P PMG 279 33 61
P MA2 344 80 86
P PFO 49 78 30
P CTAO 260 33 69
P YSS 333 73 140
P KIP 28 44 58
P WRAB 259 44 62
P MDJ 325 77 127
P KDAK 14 78 94
P NWAO 241 58 70
P MAJO 323 67 97
P COLA 12 85 68
P CAN 232 33 152
P BJT 315 83 124
P ADK 1 69 115
P TAU 221 38 146
P XAN 307 85 78
P
P
0
10
20
sec
0
10
20
sec
0
10
20
sec

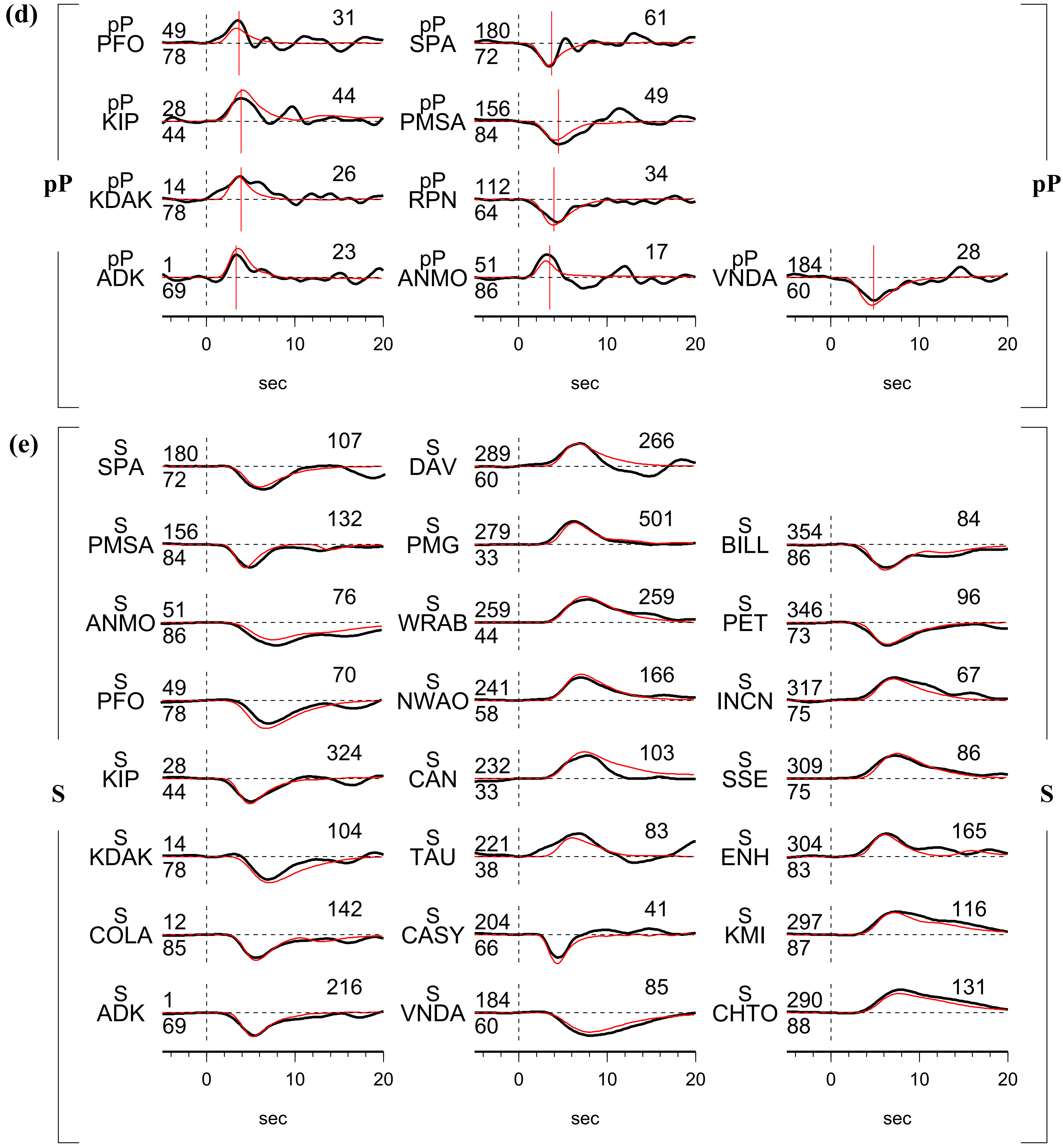
(d)
pP
pP
pP PFO 49 78 31
pP SPA 180 72 61
pP KIP 28 44 44
pP PMSA 156 84 49
pP KDAK 14 78 26
pP RPN 112 64 34
pP ADK 1 69 23
pP ANMO 51 86 17
pP VNDA 184 60 28
0
10
20
sec
sec
sec
(e)
S
S
S SPA 180 72 107
S DAV 289 60 266
S PMSA 156 84 132
S PMG 279 33 501
S BILL 354 86 84
S ANMO 51 86 76
S WRAB 259 44 259
S PET 346 73 96
S PFO 49 78 70
S NWAO 241 58 166
S INCN 317 75 67
S KIP 28 44 324
S CAN 232 33 103
S SSE 309 75 86
S KDAK 14 78 104
S TAU 221 38 83
S ENH 304 83 165
S COLA 12 85 142
S CASY 204 66 41
S KMI 297 87 116
S ADK 1 69 216
S VNDA 184 60 85
S CHTO 290 88 131
0
10
20
sec
sec
sec

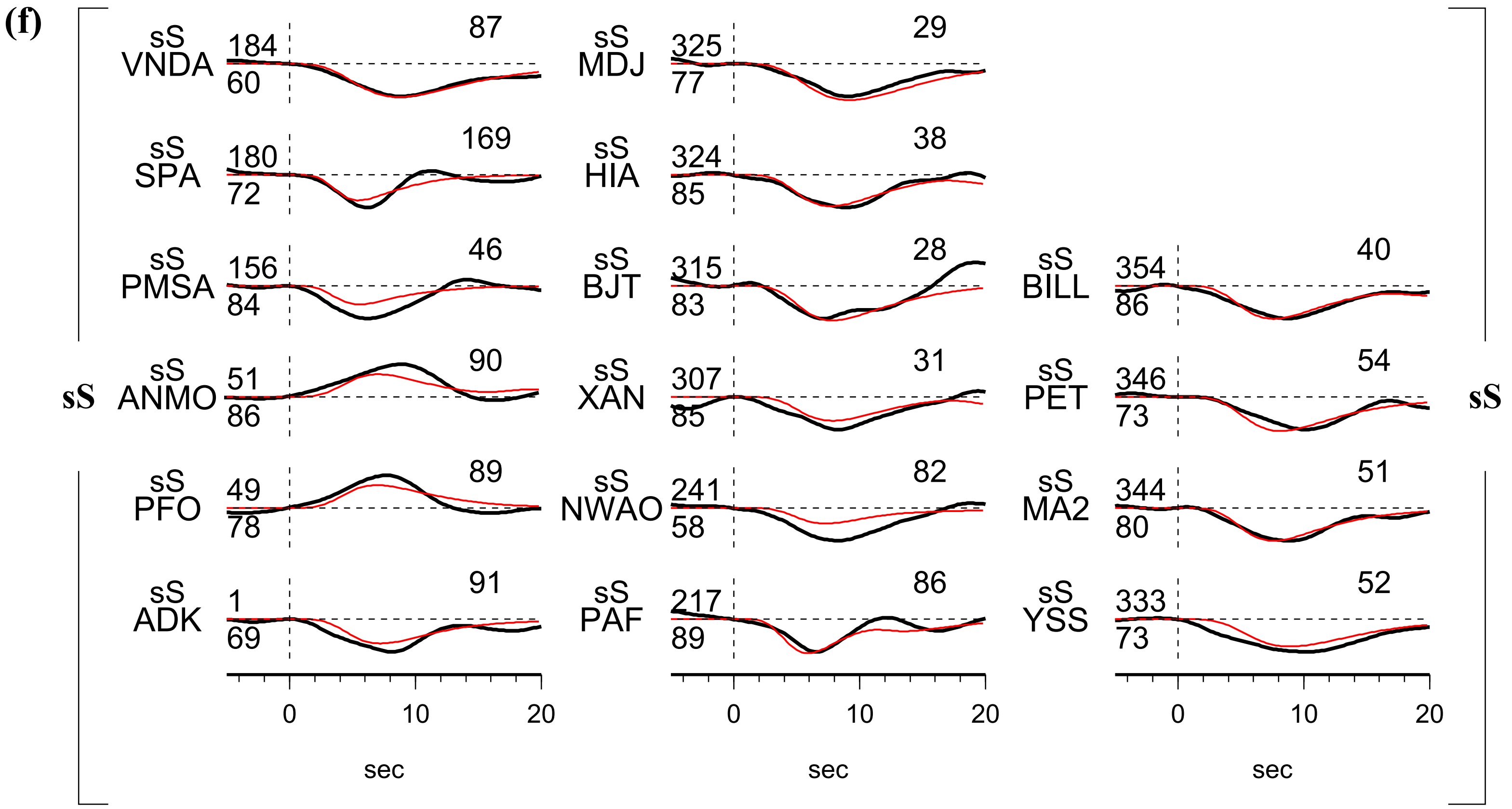
(f)
sS
sS
sS VNDA 184 60 87
sS MDJ 325 77 29
sS SPA 180 72 169
sS HIA 324 85 38
sS PMSA 156 84 46
sS BJT 315 83 28
sS BILL 354 86 40
sS ANMO 51 86 90
sS XAN 307 85 31
sS PET 346 73 54
sS PFO 49 78 89
sS NWAO 241 58 82
sS MA2 344 80 51
sS ADK 1 69 91
sS PAF 217 89 86
sS YSS 333 73 52
0
10
20
sec

E8. The 20 Aug 1998 Mw 7.0 earthquake

Earthquake E8 occurred 425 km beneath Bonin Islands region (Table S4-0). The seismograms constitute a good azimuthal coverage with 29 P, 22 pP, 34 S and 19 sS wave data (Fig. S4-8a). The earthquake is inferred by four major sub-events (Table S4-8, Fig. S4-8b). The first sub-event is southeast to the initiation point, the second and third sub-events are to the northeast of the initiation point, and the fourth is to the northwest (Fig. S4-8b). It is interesting to note that, this earthquake has a longer duration with well-separated sub-events, comparing to most of the other analyzed earthquakes with Mw ~7.0. The sub-events propagated around the GCMT sub-horizontal fault plane, consistent with the previous analysis (Myhill and Warren, 2012). Synthetics predicted by the best planar model match the arrival times of energy pulses of the data as well as synthetics predicted by the best-fitting model, as well as the amplitude for most of the seismogram. However, the best-fitting model can fit much better at the stations near the nodal plane, for example, P waveforms at the stations SFJ, ALE, KEV and KBS. It is worth to mention that, the nodal plane data might be critical to resolve focal mechanisms of the deep earthquakes.

Table S4-8. Source parameters of inferred sub-events of E8

Sub-event	dt (s)	dn (km)	de (km)	dz (km)	duration (s)	Mw	strike (°)	dip (°)	slip (°)
1	9.9	-7.3	6.3	-2.5	4.0	6.6	94.5	20.3	198.6
2	14.1	8.7	12.7	-4.4	4.0	6.8	89.9	29.1	201.0
3	17.2	27.0	12.4	-4.0	4.6	6.7	90.5	33.1	206.8
4	23.8	24.5	-14.7	-8.1	5.0	6.5	56.4	14.0	158.9

(Fig. S4-8)

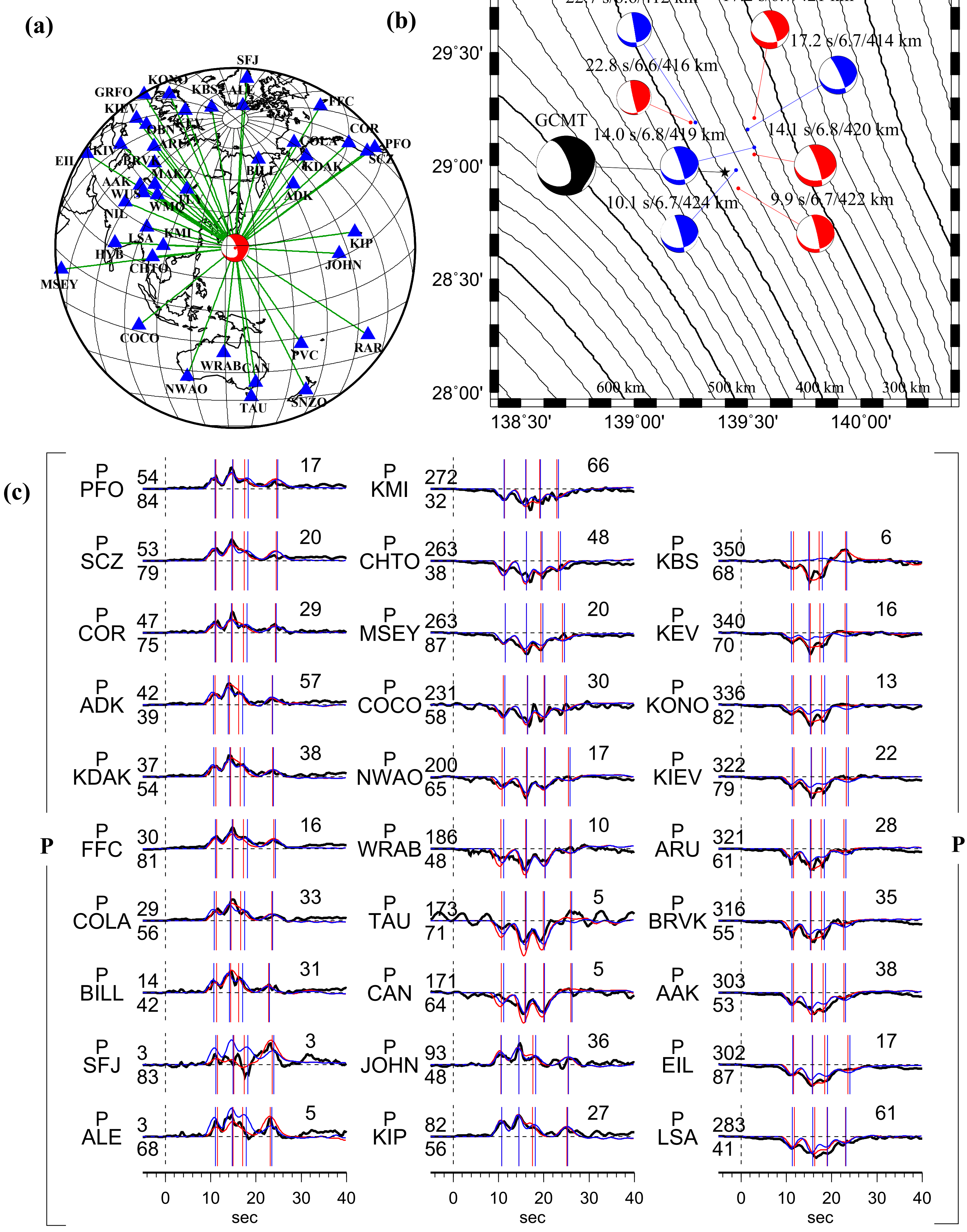

(a)
SFJ
KONO
GRFO
KBS
ALE
FFC
KIEV
KEV
OBN
ARU
COLA
COR
PFO
EIL
KIV
BRVK
BILL
KDAK
SCZ
MAKZ
AAK
WUS
TLY
ADK
WMQ
NIL
KMI
KIP
LSA
HYB
CHTO
JOHN
MSEY
COCO
RAR
PVC
WRAB
CAN
NWAO
TAU
SNZO
(b)
22.7 s/6.6/412 km
17.2 s/6.7/421 km
17.2 s/6.7/414 km
22.8 s/6.6/416 km
GCMT
14.0 s/6.8/419 km
14.1 s/6.8/420 km
10.1 s/6.7/424 km
9.9 s/6.7/422 km
29˚30'
29˚00'
28˚30'
28˚00'
600 km
500 km
400 km
300 km
138˚30'
139˚00'
139˚30'
140˚00'
(c)
P
P PFO 54 84 17
P SCZ 53 79 20
P COR 47 75 29
P ADK 42 39 57
P KDAK 37 54 38
P FFC 30 81 16
P COLA 29 56 33
P BILL 14 42 31
P SFJ 3 83 3
P ALE 3 68 5
P KMI 272 32 66
P CHTO 263 38 48
P MSEY 263 87 20
P COCO 231 58 30
P NWAO 200 65 17
P WRAB 186 48 10
P TAU 173 71 5
P CAN 171 64 5
P JOHN 93 48 36
P KIP 82 56 27
P KBS 350 68 6
P KEV 340 70 16
P KONO 336 82 13
P KIEV 322 79 22
P ARU 321 61 28
P BRVK 316 55 35
P AAK 303 53 38
P EIL 302 87 17
P LSA 283 41 61
0
10
20
30
40
sec

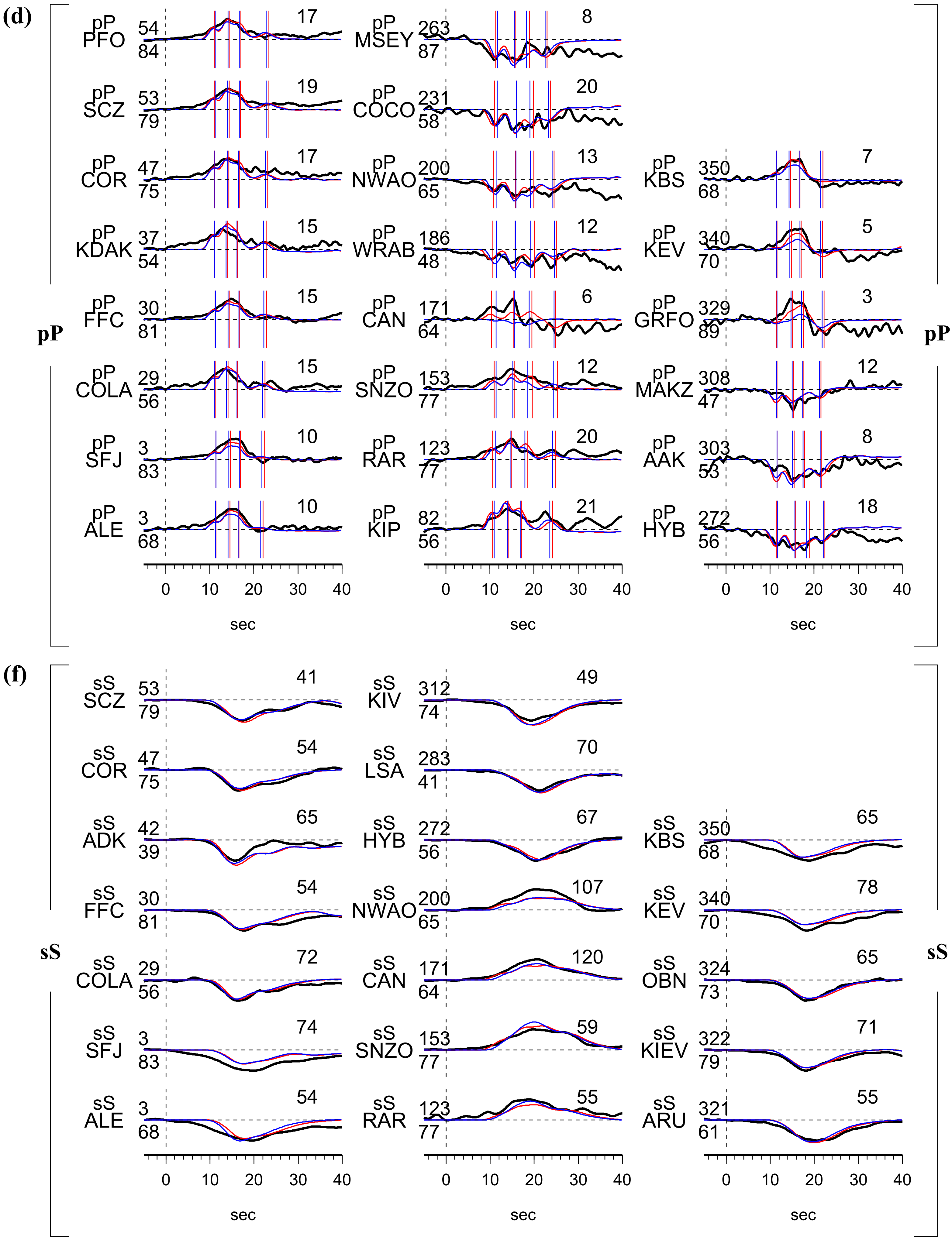
(d)
pP
pP PFO 54 84 17
pP MSEY 263 87 8
pP SCZ 53 79 19
pP COCO 231 58 20
pP COR 47 75 17
pP NWAO 200 65 13
pP KBS 350 68 7
pP KDAK 37 54 15
pP WRAB 186 48 12
pP KEV 340 70 5
pP FFC 30 81 15
pP CAN 171 64 6
pP GRFO 329 89 3
pP COLA 29 56 15
pP SNZO 153 77 12
pP MAKZ 308 47 12
pP SFJ 3 83 10
pP RAR 123 77 20
pP AAK 303 53 8
pP ALE 3 68 10
pP KIP 82 56 21
pP HYB 272 56 18
0 10 20 30 40
sec
(f)
sS
sS SCZ 53 79 41
sS KIV 312 74 49
sS COR 47 75 54
sS LSA 283 41 70
sS ADK 42 39 65
sS HYB 272 56 67
sS KBS 350 68 65
sS FFC 30 81 54
sS NWAO 200 65 107
sS KEV 340 70 78
sS COLA 29 56 72
sS CAN 171 64 120
sS OBN 324 73 65
sS SFJ 3 83 74
sS SNZO 153 77 59
sS KIEV 322 79 71
sS ALE 3 68 54
sS RAR 123 77 55
sS ARU 321 61 55
0 10 20 30 40
sec

(e)

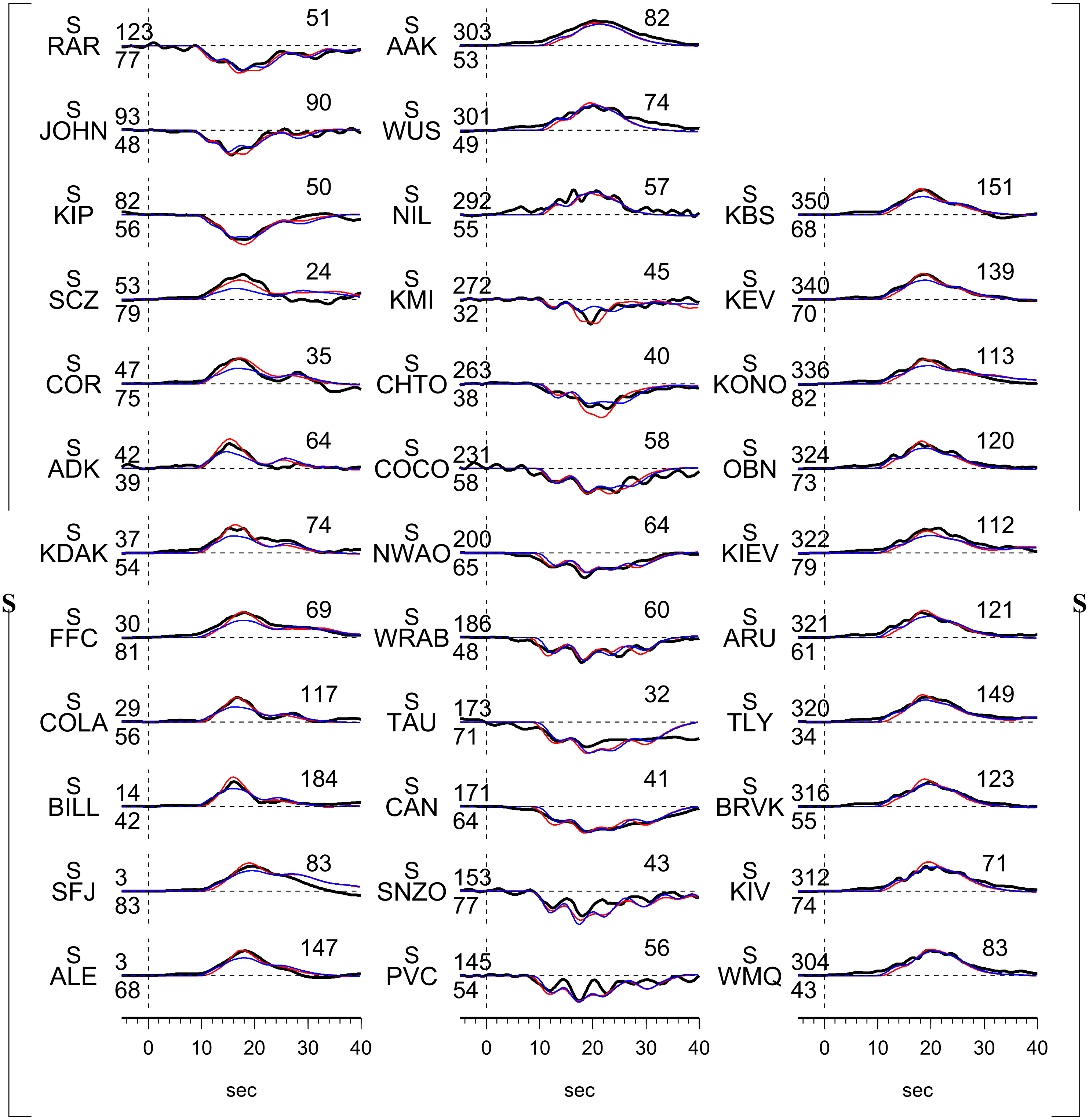

S
S
RAR 123 77 51
AAK 303 53 82
JOHN 93 48 90
WUS 301 49 74
KIP 82 56 50
NIL 292 55 57
KBS 350 68 151
SCZ 53 79 24
KMI 272 32 45
KEV 340 70 139
COR 47 75 35
CHTO 263 38 40
KONO 336 82 113
ADK 42 39 64
COCO 231 58 58
OBN 324 73 120
KDAK 37 54 74
NWAO 200 65 64
KIEV 322 79 112
FFC 30 81 69
WRAB 186 48 60
ARU 321 61 121
COLA 29 56 117
TAU 173 71 32
TLY 320 34 149
BILL 14 42 184
CAN 171 64 41
BRVK 316 55 123
SFJ 3 83 83
SNZO 153 77 43
KIV 312 74 71
ALE 3 68 147
PVC 145 54 56
WMQ 304 43 83
0
10
20
30
40
sec

E9. The 08 Apr 1999 Mw 7.1 earthquake

Earthquake E9 occurred 566 km beneath Sea of Japan (Table S4-0). The seismograms constitute good azimuthal coverage with 34 P, 23 pP, 30 S and 25 sS wave data (Fig. S4-9a). The seismic energy can be modeled by three sub-events (Table S4-9, Fig. S4-9b). The first sub-event is 5 km to the east of the initiation. The second sub-event is 7.0 km to the east, and the third sub-event is 11 km to the southeast (Fig. S4-9b). Focal mechanism of the second sub-event is different from that of the other two sub-events to the south (Fig. S4-9b). The GCMT sub-horizontal plane can predict the synthetics better than the sub-vertical one, but not as well as the best-fitting model (Figs. S4-9c – S4-9f), due to fault plane orientation change of the second sub-event (Table S4-9).

Table S4-9. Source parameters of inferred sub-events of E9

Sub-event	dt (s)	dn (km)	de (km)	dz (km)	duration (s)	Mw	strike (°)	dip (°)	slip (°)
1	1.5	-0.4	4.5	0.1	2.0	6.8	90.6	32.4	167.1
2	3.1	1.0	7.0	-3.1	2.4	6.9	98.3	9.7	191.9
3	5.2	-9.1	7.0	4.1	2.0	6.6	84.3	44.4	151.3

(Fig. S4-9)

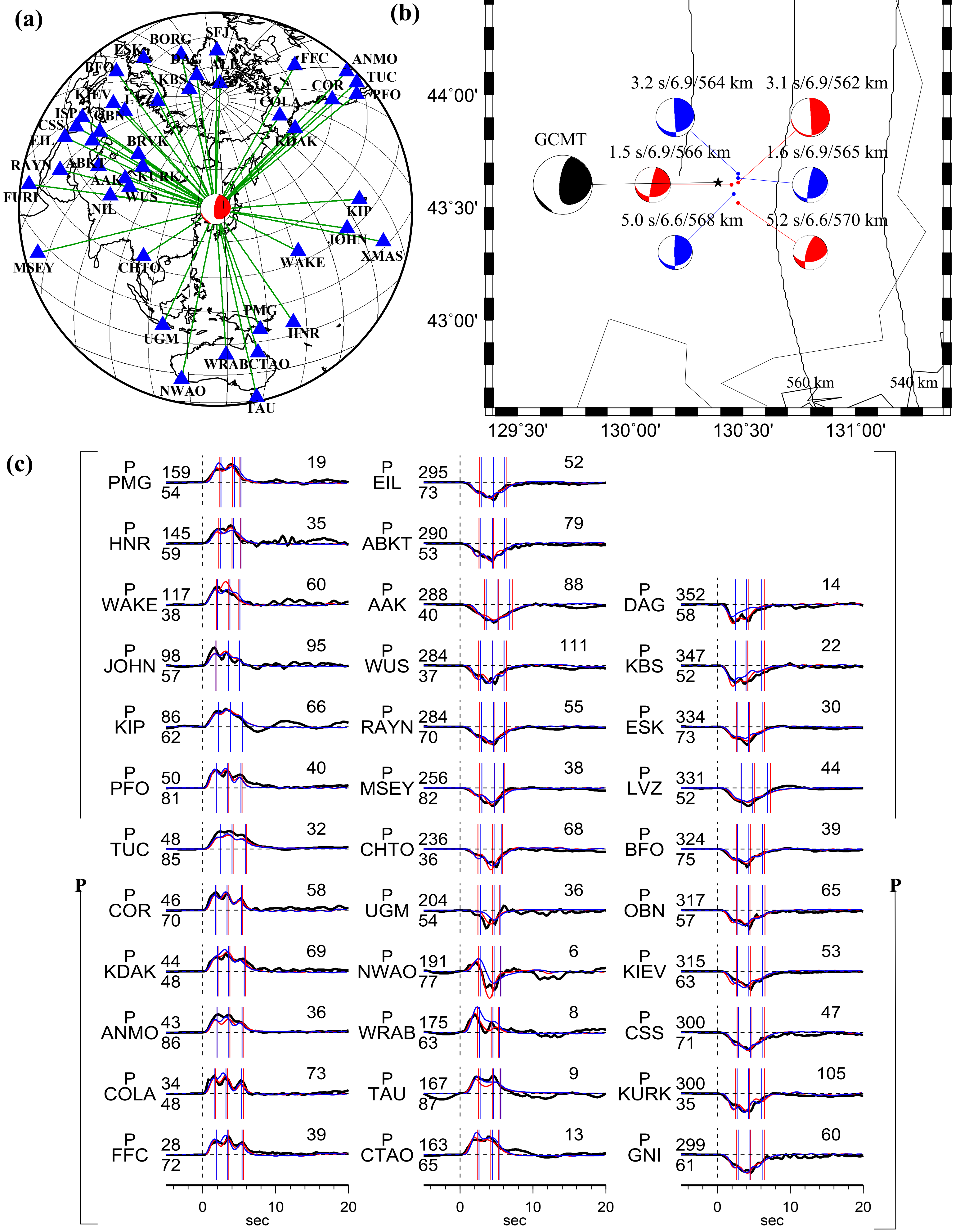

(a)
BORG
SFJ
ESK
DAG
FFC
ANMO
BFO
ALE
KBS
TUC
COR
PFO
KIEV
LVZ
ISP
OBN
COLA
CSS
EIL
BRVK
KDAK
RAYN
ABKT
AAK
KURK
FURI
WUS
NIL
KIP
JOHN
XMAS
MSEY
CHTO
WAKE
PMG
HNR
UGM
WRAB
CTAO
NWAO
TAU
(b)
44˚30'
44˚00'
43˚30'
43˚00'
129˚30'
130˚00'
130˚30'
131˚00'
GCMT
3.2 s/6.9/564 km
3.1 s/6.9/562 km
1.5 s/6.9/566 km
1.6 s/6.9/565 km
5.0 s/6.6/568 km
5.2 s/6.6/570 km
560 km
540 km
(c)
P PMG 159 54 19
P HNR 145 59 35
P WAKE 117 38 60
P JOHN 98 57 95
P KIP 86 62 66
P PFO 50 81 40
P TUC 48 85 32
P COR 46 70 58
P KDAK 44 48 69
P ANMO 43 86 36
P COLA 34 48 73
P FFC 28 72 39
P EIL 295 73 52
P ABKT 290 53 79
P AAK 288 40 88
P WUS 284 37 111
P RAYN 284 70 55
P MSEY 256 82 38
P CHTO 236 36 68
P UGM 204 54 36
P NWAO 191 77 6
P WRAB 175 63 8
P TAU 167 87 9
P CTAO 163 65 13
P DAG 352 58 14
P KBS 347 52 22
P ESK 334 73 30
P LVZ 331 52 44
P BFO 324 75 39
P OBN 317 57 65
P KIEV 315 63 53
P CSS 300 71 47
P KURK 300 35 105
P GNI 299 61 60
P
P
0
10
20
sec

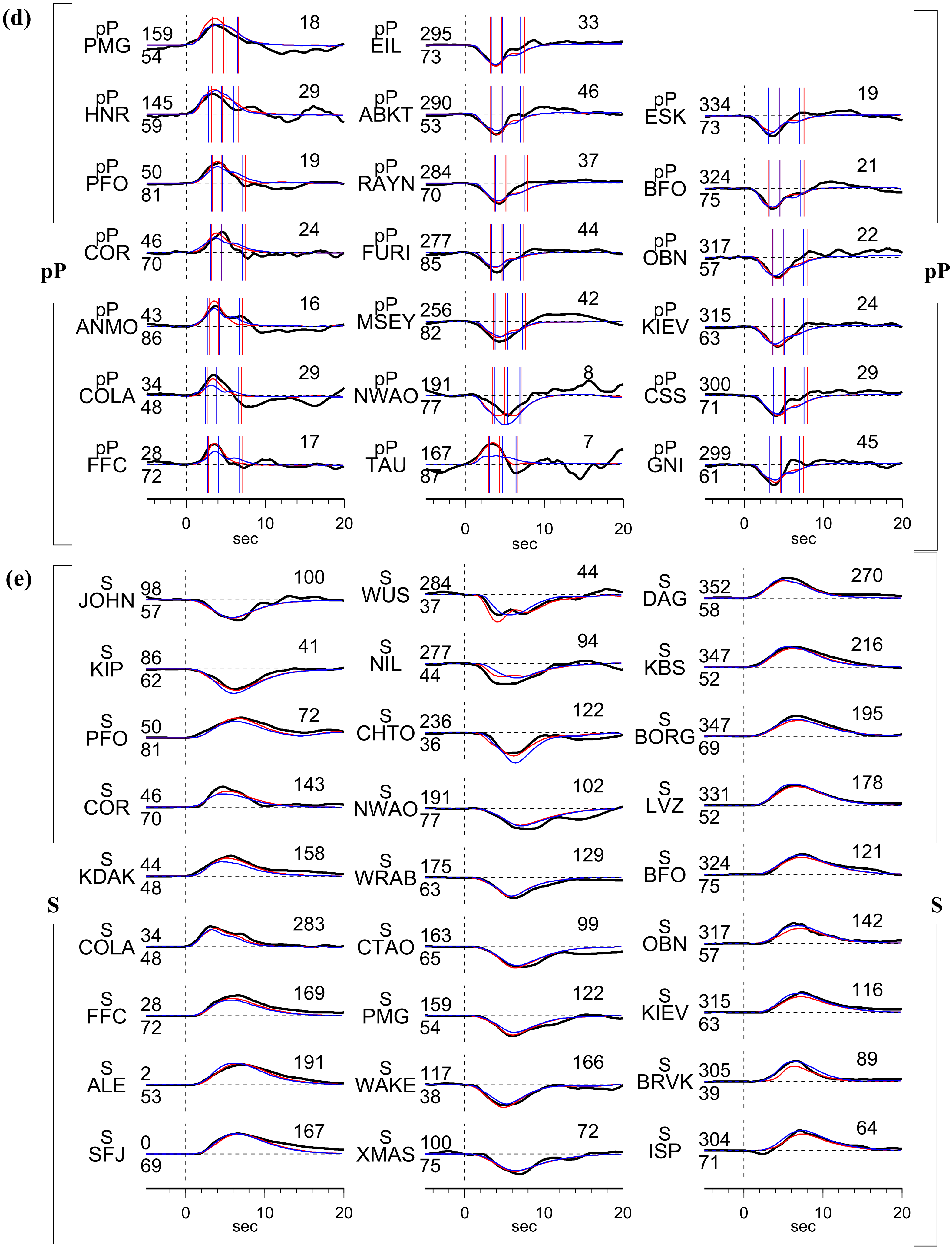
(d)
pP
pP PMG 159 54 18
pP EIL 295 73 33
pP HNR 145 59 29
pP ABKT 290 53 46
pP ESK 334 73 19
pP PFO 50 81 19
pP RAYN 284 70 37
pP BFO 324 75 21
pP COR 46 70 24
pP FURI 277 85 44
pP OBN 317 57 22
pP ANMO 43 86 16
pP MSEY 256 82 42
pP KIEV 315 63 24
pP COLA 34 48 29
pP NWAO 191 77 8
pP CSS 300 71 29
pP FFC 28 72 17
pP TAU 167 87 7
pP GNI 299 61 45
0
10
20
sec
(e)
S
S JOHN 98 57 100
S WUS 284 37 44
S DAG 352 58 270
S KIP 86 62 41
S NIL 277 44 94
S KBS 347 52 216
S PFO 50 81 72
S CHTO 236 36 122
S BORG 347 69 195
S COR 46 70 143
S NWAO 191 77 102
S LVZ 331 52 178
S KDAK 44 48 158
S WRAB 175 63 129
S BFO 324 75 121
S COLA 34 48 283
S CTAO 163 65 99
S OBN 317 57 142
S FFC 28 72 169
S PMG 159 54 122
S KIEV 315 63 116
S ALE 2 53 191
S WAKE 117 38 166
S BRVK 305 39 89
S SFJ 0 69 167
S XMAS 100 75 72
S ISP 304 71 64
0
10
20
sec

(f)

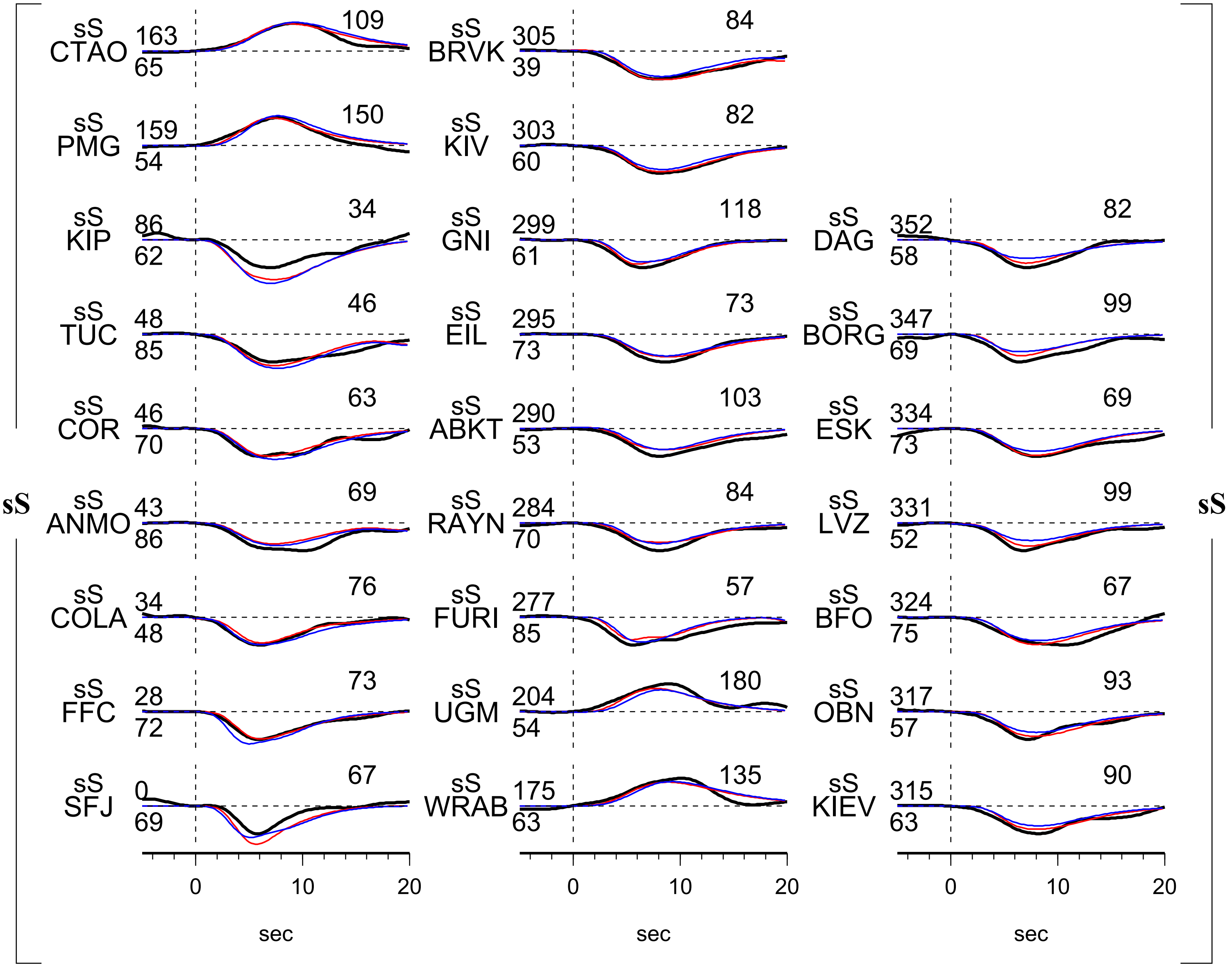
sS
sS
sS CTAO 163 65 109
sS BRVK 305 39 84
sS PMG 159 54 150
sS KIV 303 60 82
sS KIP 86 62 34
sS GNI 299 61 118
sS DAG 352 58 82
sS TUC 48 85 46
sS EIL 295 73 73
sS BORG 347 69 99
sS COR 46 70 63
sS ABKT 290 53 103
sS ESK 334 73 69
sS ANMO 43 86 69
sS RAYN 284 70 84
sS LVZ 331 52 99
sS COLA 34 48 76
sS FURI 277 85 57
sS BFO 324 75 67
sS FFC 28 72 73
sS UGM 204 54 180
sS OBN 317 57 93
sS SFJ 0 69 67
sS WRAB 175 63 135
sS KIEV 315 63 90
0
10
20
sec
0
10
20
sec
0
10
20
sec

E10. The 23 Apr 2000 Mw 7.0 earthquake

Earthquake E10 occurred 610 km beneath South America (Table S4-0). The seismograms constitute good azimuth coverage with 26 P, 20 pP, 24 S and 20 sS wave data (Fig. S4-10a). The earthquake has two sub-events located to the northeast and southeast of the initiation point (Fig. S4-10b). Synthetics predicted by the GCMT sub-horizontal plane can fit the seismic data as well as the best-fitting sub-event model. These two sub-events are well separated. It is interesting to note that, the two sub-events are with consistent source propagating velocities of ~3.4 km/s from the initiation point.

Table S4-10. Source parameters of inferred sub-events of E10

Sub-event	dt (s)	dn (km)	de (km)	dz (km)	duration (s)	Mw	strike (°)	dip (°)	slip (°)
1	2.3	4.8	5.9	-0.9	2.4	6.8	289.9	0.2	210.3
2	5.5	-14.1	13.1	0.0	3.0	6.6	309.9	12.8	219.2

(Fig. S4-10)

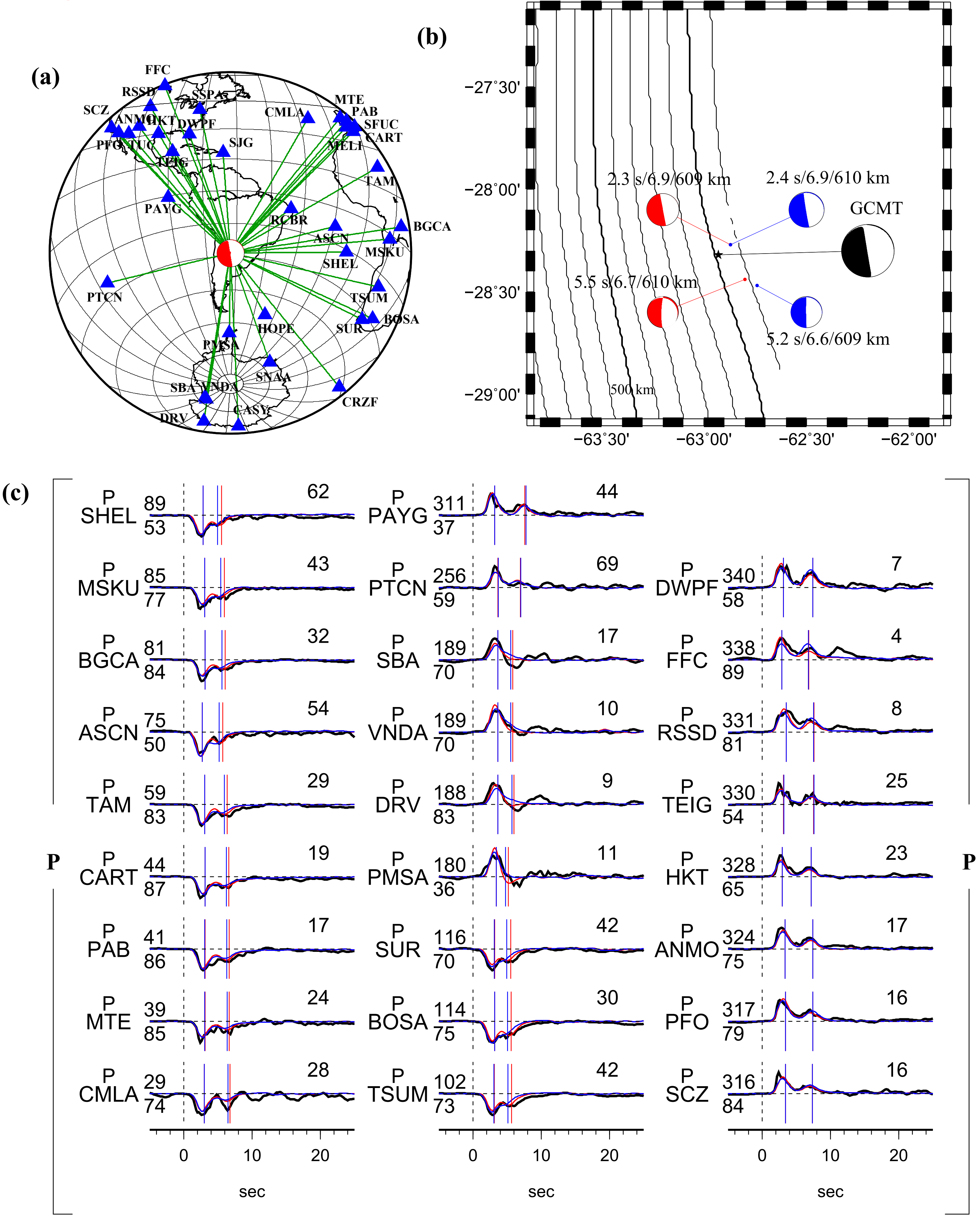
(a)
FFC
RSSD
SSPA
SCZ
ANMO
HKT
DWPF
CMLA
MTE
PAB
SFUC
CART
PFO
TUC
SJG
MELI
TEIG
TAM
PAYG
RCBR
BGCA
ASCN
MSKU
SHEL
PTCN
TSUM
HOPE
SUR
BOSA
PMSA
SNAA
SBA
VNDA
CRZF
CASY
DRV
(b)
-27˚30'
-28˚00'
-28˚30'
-29˚00'
-63˚30'
-63˚00'
-62˚30'
-62˚00'
2.3 s/6.9/609 km
2.4 s/6.9/610 km
GCMT
5.5 s/6.7/610 km
5.2 s/6.6/609 km
500 km
(c)
P SHEL 89 53 62
P PAYG 311 37 44
P MSKU 85 77 43
P PTCN 256 59 69
P DWPF 340 58 7
P BGCA 81 84 32
P SBA 189 70 17
P FFC 338 89 4
P ASCN 75 50 54
P VNDA 189 70 10
P RSSD 331 81 8
P TAM 59 83 29
P DRV 188 83 9
P TEIG 330 54 25
P CART 44 87 19
P PMSA 180 36 11
P HKT 328 65 23
P PAB 41 86 17
P SUR 116 70 42
P ANMO 324 75 17
P MTE 39 85 24
P BOSA 114 75 30
P PFO 317 79 16
P CMLA 29 74 28
P TSUM 102 73 42
P SCZ 316 84 16
P
P
0
10
20
sec

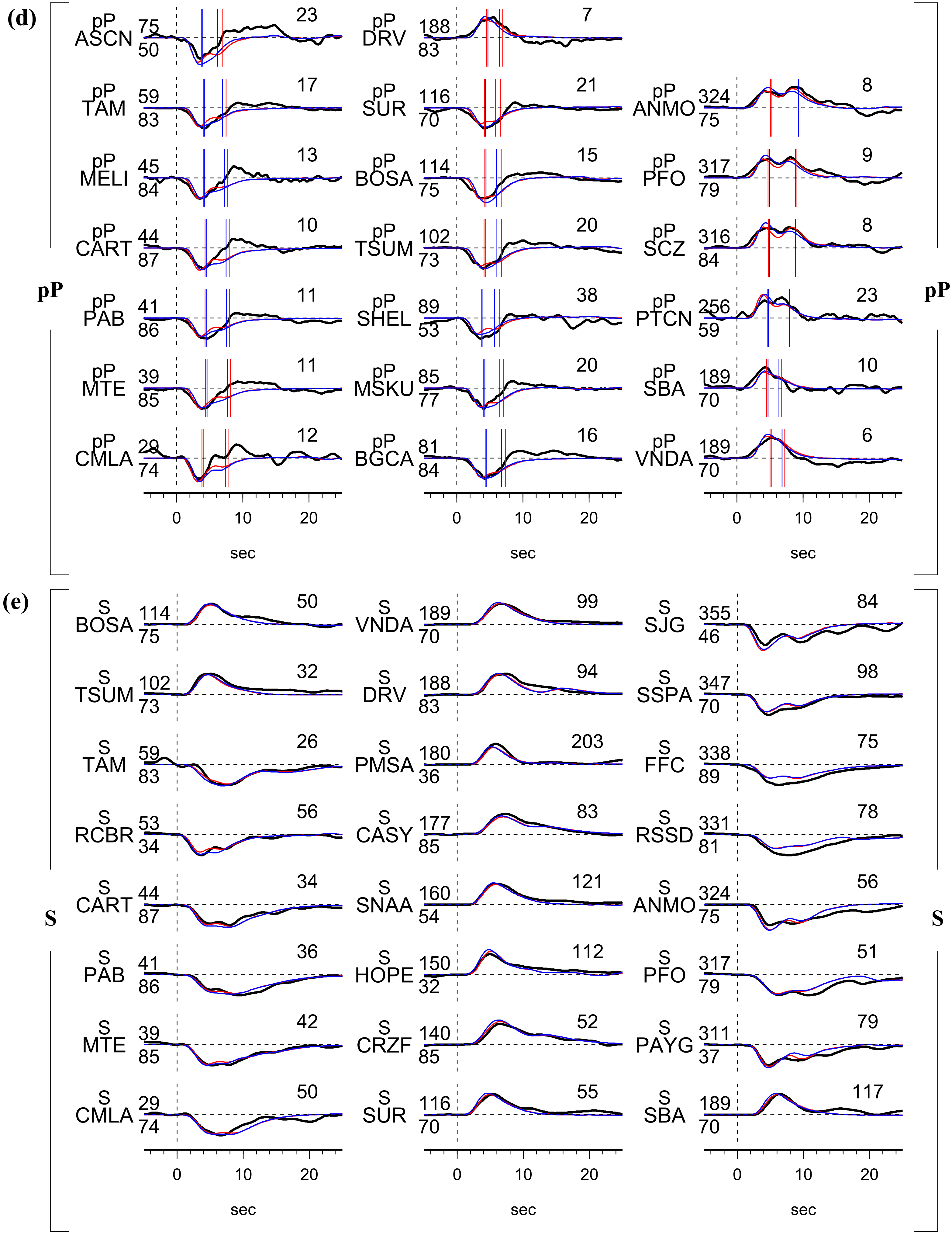
(d)
pP
pP
pP ASCN 75 50 23
pP DRV 188 83 7
pP TAM 59 83 17
pP SUR 116 70 21
pP ANMO 324 75 8
pP MELI 45 84 13
pP BOSA 114 75 15
pP PFO 317 79 9
pP CART 44 87 10
pP TSUM 102 73 20
pP SCZ 316 84 8
pP PAB 41 86 11
pP SHEL 89 53 38
pP PTCN 256 59 23
pP MTE 39 85 11
pP MSKU 85 77 20
pP SBA 189 70 10
pP CMLA 29 74 12
pP BGCA 81 84 16
pP VNDA 189 70 6
0
10
20
sec
(e)
S
S
S BOSA 114 75 50
S VNDA 189 70 99
S SJG 355 46 84
S TSUM 102 73 32
S DRV 188 83 94
S SSPA 347 70 98
S TAM 59 83 26
S PMSA 180 36 203
S FFC 338 89 75
S RCBR 53 34 56
S CASY 177 85 83
S RSSD 331 81 78
S CART 44 87 34
S SNAA 160 54 121
S ANMO 324 75 56
S PAB 41 86 36
S HOPE 150 32 112
S PFO 317 79 51
S MTE 39 85 42
S CRZF 140 85 52
S PAYG 311 37 79
S CMLA 29 74 50
S SUR 116 70 55
S SBA 189 70 117
0
10
20
sec

(f)

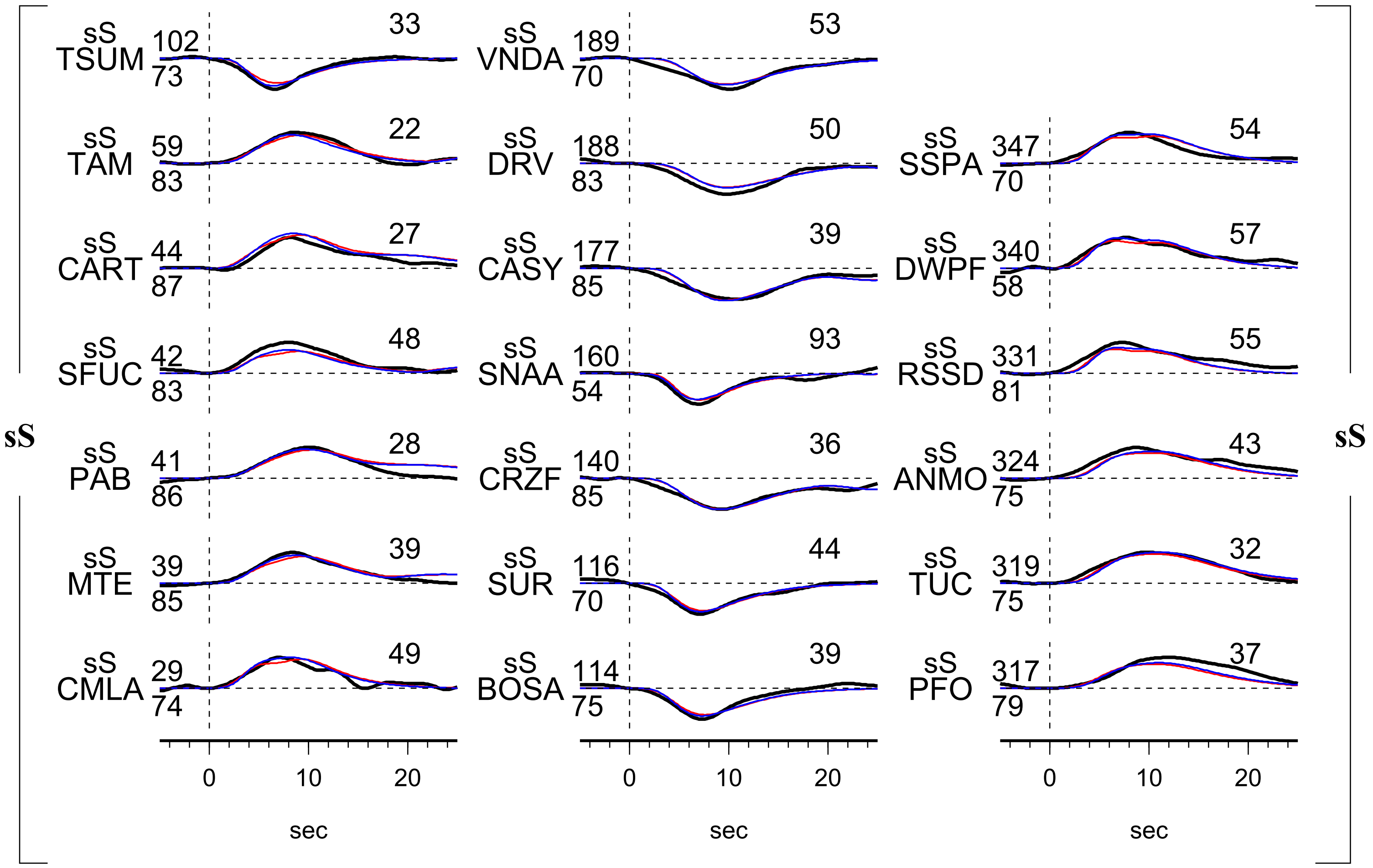
sS
sS
sS TSUM 102 73 33
sS VNDA 189 70 53
sS TAM 59 83 22
sS DRV 188 83 50
sS SSPA 347 70 54
sS CART 44 87 27
sS CASY 177 85 39
sS DWPF 340 58 57
sS SFUC 42 83 48
sS SNAA 160 54 93
sS RSSD 331 81 55
sS PAB 41 86 28
sS CRZF 140 85 36
sS ANMO 324 75 43
sS MTE 39 85 39
sS SUR 116 70 44
sS TUC 319 75 32
sS CMLA 29 74 49
sS BOSA 114 75 39
sS PFO 317 79 37
0
10
20
sec

E11. The 28 Jun 2002 Mw 7.3 earthquake

Earthquake E11 occurred 564 km beneath Sea of Japan (Table S4-0). We model the earthquake by four sub-events (Table S4-11), with good azimuth coverage of 35 P, 27 pP, 28 S and 27 sS wave data (Fig. S4-11a). The inferred sub-events propagate to the west like a rectangle distribution (Fig. S4-11b). The sub-events are close to the GCMT sub-horizontal plane, but radiation pattern of the third sub-event cannot be modeled on the planar model (Fig. S4-11c – S4-11f), due to different fault plane orientation (Table S4-11).

Table S4-11. Source parameters of inferred sub-events of E11

Sub-event	dt (s)	dn (km)	de (km)	dz (km)	duration (s)	Mw	strike (°)	dip (°)	slip (°)
1	2.7	0.0	-9.5	-1.6	4.6	6.9	26.0	2.9	118.2
2	6.6	-5.2	-11.0	3.6	3.0	6.9	46.5	10.9	123.8
3	8.8	0.1	-24.8	0.4	2.2	6.9	46.6	20.6	125.9
4	10.6	5.1	-22.7	2.3	4.0	6.7	46.7	8.3	117.4

(Fig. S4-11)

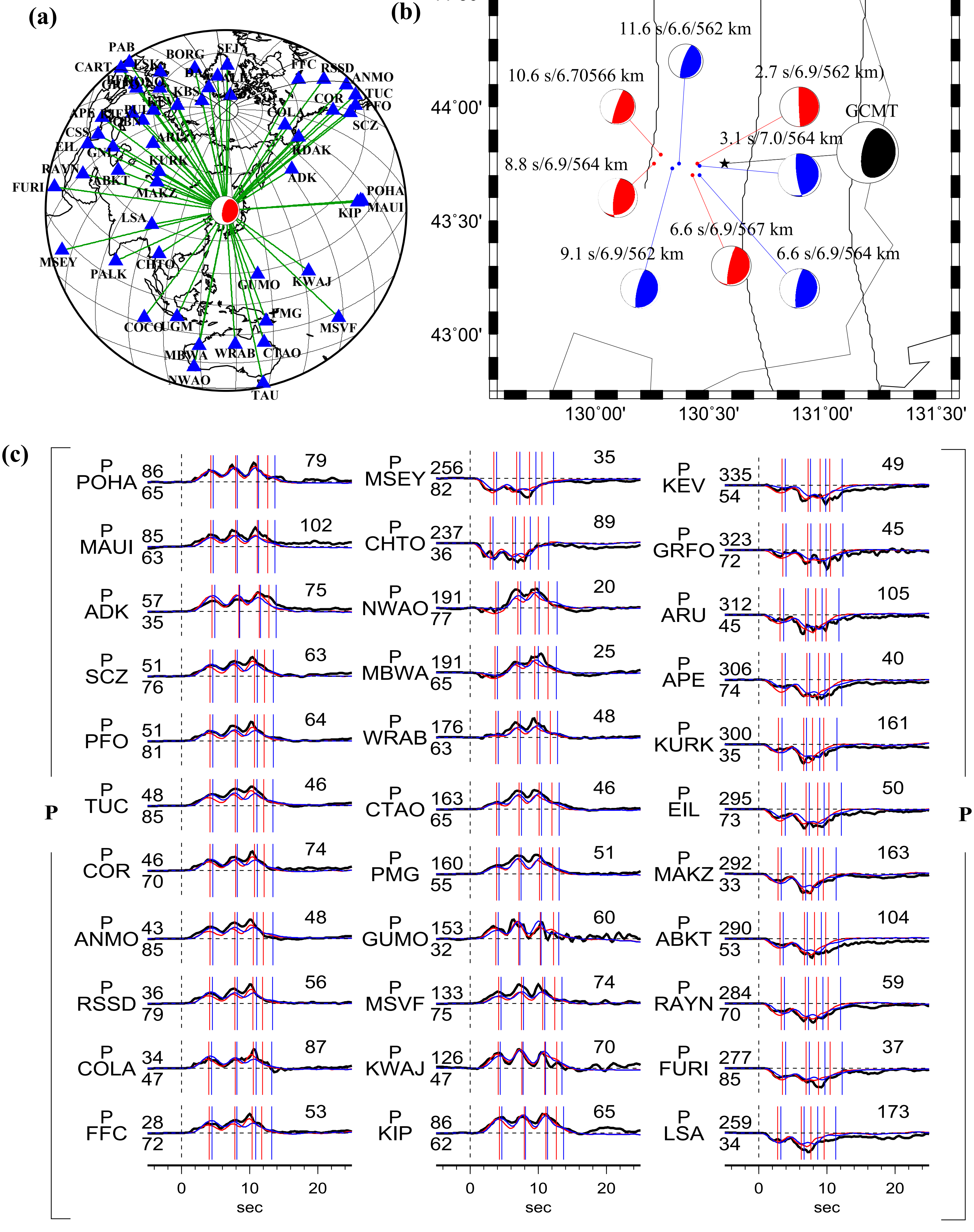
(a)
PAB
CART
ESK
BORG
SFJ
BA
ALE
FFC
RSSD
ANMO
TUC
PFO
SCZ
COR
COLA
KBS
KEV
PUL
OBN
APE
CSS
EIL
GNI
ARU
KURK
KDAK
ADK
RAYN
ABKT
FURI
MAKZ
POHA
MAUI
KIP
LSA
MSEY
PALK
CHTO
GUMO
KWAJ
PMG
MSVF
COCO
UGM
MBWA
WRAB
CTAO
NWAO
TAU
(b)
44˚30'
44˚00'
43˚30'
43˚00'
130˚00'
130˚30'
131˚00'
131˚30'
11.6 s/6.6/562 km
10.6 s/6.70566 km
2.7 s/6.9/562 km)
GCMT
3.1 s/7.0/564 km
8.8 s/6.9/564 km
6.6 s/6.9/567 km
9.1 s/6.9/562 km
6.6 s/6.9/564 km
(c)
P POHA 86 65 79
P MAUI 85 63 102
P ADK 57 35 75
P SCZ 51 76 63
P PFO 51 81 64
P TUC 48 85 46
P COR 46 70 74
P ANMO 43 85 48
P RSSD 36 79 56
P COLA 34 47 87
P FFC 28 72 53
P MSEY 256 82 35
P CHTO 237 36 89
P NWAO 191 77 20
P MBWA 191 65 25
P WRAB 176 63 48
P CTAO 163 65 46
P PMG 160 55 51
P GUMO 153 32 60
P MSVF 133 75 74
P KWAJ 126 47 70
P KIP 86 62 65
P KEV 335 54 49
P GRFO 323 72 45
P ARU 312 45 105
P APE 306 74 40
P KURK 300 35 161
P EIL 295 73 50
P MAKZ 292 33 163
P ABKT 290 53 104
P RAYN 284 70 59
P FURI 277 85 37
P LSA 259 34 173
P
P
0
10
20
sec

(d)

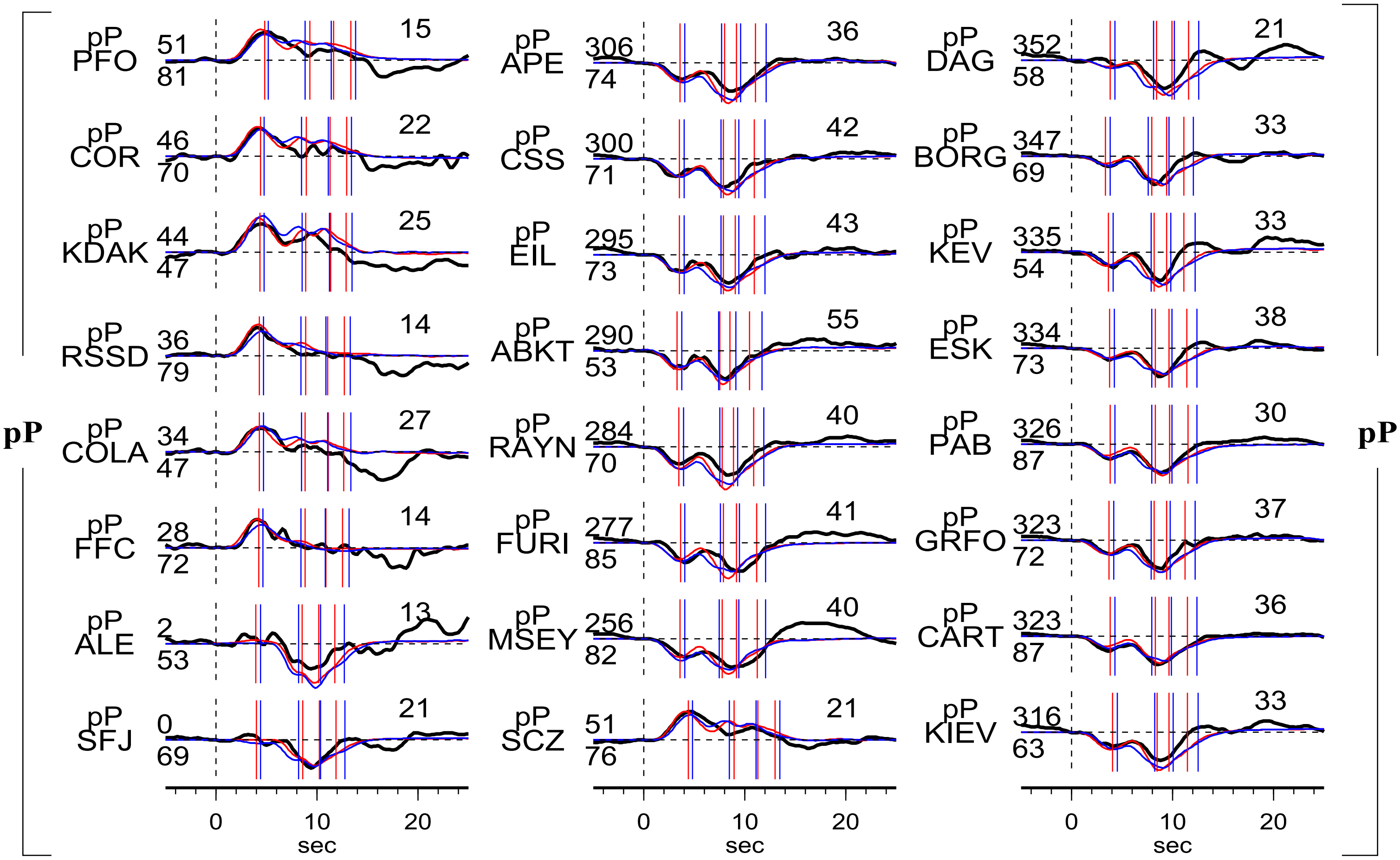
pP
pP PFO 51 81 15
pP COR 46 70 22
pP KDAK 44 47 25
pP RSSD 36 79 14
pP COLA 34 47 27
pP FFC 28 72 14
pP ALE 2 53 13
pP SFJ 0 69 21
pP APE 306 74 36
pP CSS 300 71 42
pP EIL 295 73 43
pP ABKT 290 53 55
pP RAYN 284 70 40
pP FURI 277 85 41
pP MSEY 256 82 40
pP SCZ 51 76 21
pP DAG 352 58 21
pP BORG 347 69 33
pP KEV 335 54 33
pP ESK 334 73 38
pP PAB 326 87 30
pP GRFO 323 72 37
pP CART 323 87 36
pP KIEV 316 63 33
0
10
20
sec
pP

(e)

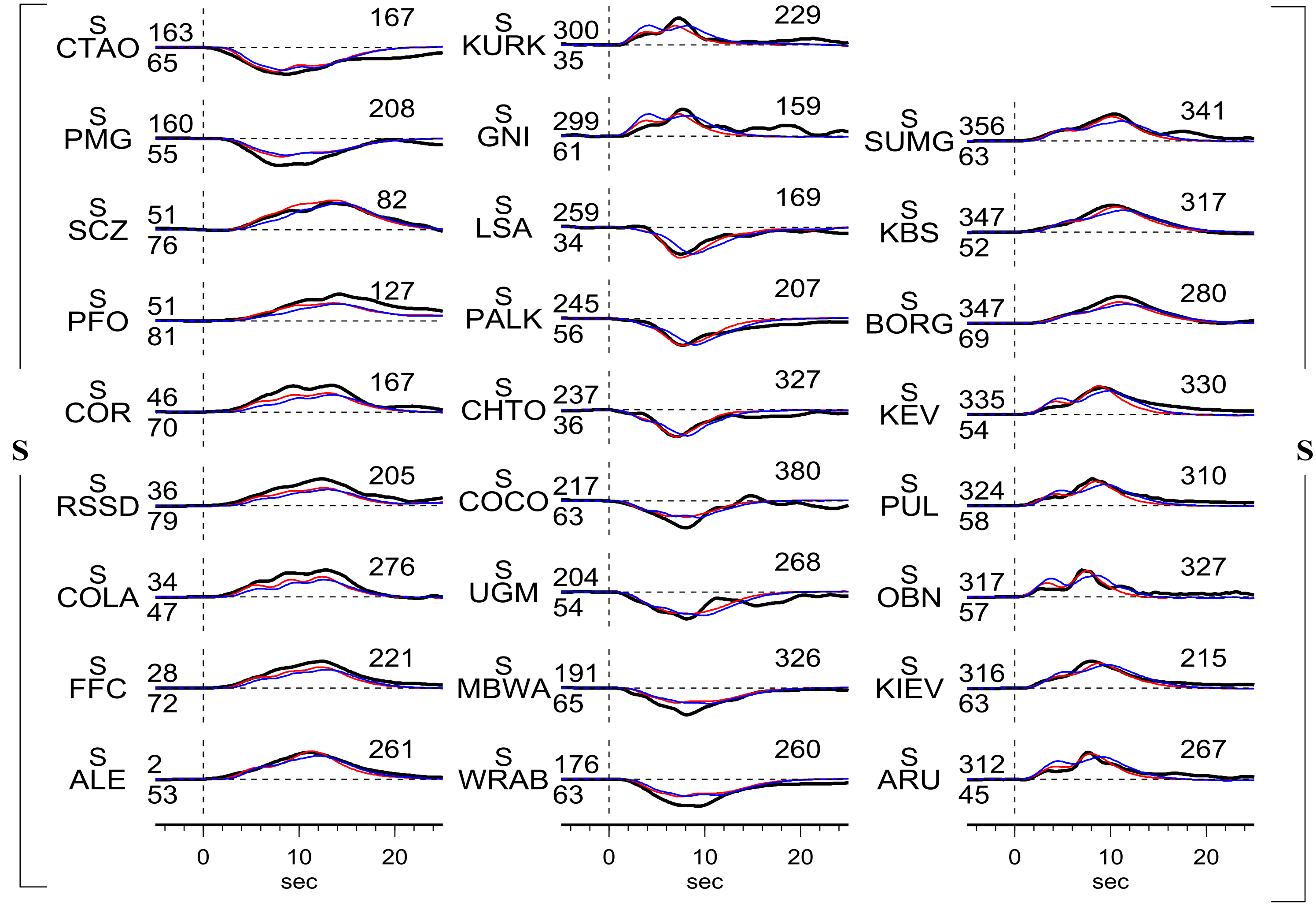
S
S CTAO 163 65 167
S PMG 160 55 208
S SCZ 51 76 82
S PFO 51 81 127
S COR 46 70 167
S RSSD 36 79 205
S COLA 34 47 276
S FFC 28 72 221
S ALE 2 53 261
S KURK 300 35 229
S GNI 299 61 159
S LSA 259 34 169
S PALK 245 56 207
S CHTO 237 36 327
S COCO 217 63 380
S UGM 204 54 268
S MBWA 191 65 326
S WRAB 176 63 260
S SUMG 356 63 341
S KBS 347 52 317
S BORG 347 69 280
S KEV 335 54 330
S PUL 324 58 310
S OBN 317 57 327
S KIEV 316 63 215
S ARU 312 45 267
0
10
20
sec
S

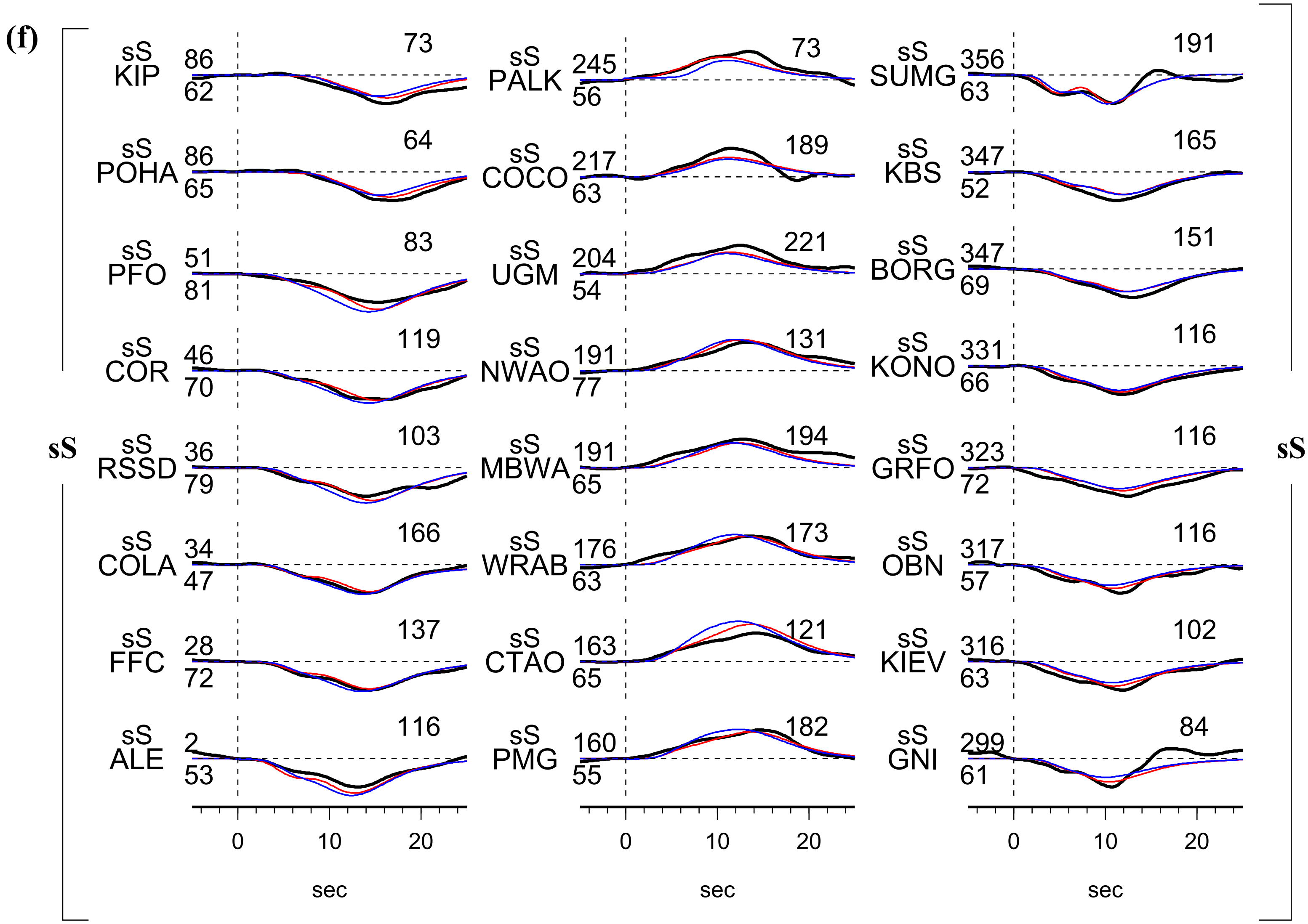

(f)
sS
sS
sS KIP 86 62 73
sS PALK 245 56 73
sS SUMG 356 63 191
sS POHA 86 65 64
sS COCO 217 63 189
sS KBS 347 52 165
sS PFO 51 81 83
sS UGM 204 54 221
sS BORG 347 69 151
sS COR 46 70 119
sS NWAO 191 77 131
sS KONO 331 66 116
sS RSSD 36 79 103
sS MBWA 191 65 194
sS GRFO 323 72 116
sS COLA 34 47 166
sS WRAB 176 63 173
sS OBN 317 57 116
sS FFC 28 72 137
sS CTAO 163 65 121
sS KIEV 316 63 102
sS ALE 2 53 116
sS PMG 160 55 182
sS GNI 299 61 84
0
10
20
sec
0
10
20
sec
0
10
20
sec

E12. The 19 Aug 2002 Mw 7.6 earthquake

Earthquake E12 occurred 580 km beneath Tonga region (Table S4-0). The seismograms constitute good azimuth coverage with 36 P, 23 pP, 26 S and 27 sS wave data (Fig. S4-12a). The seismic energy can be modeled by four sub-events (Table S4-12, Fig. S4-12b). The first sub-event is about 5 km to the northeast of and 5 km below the initiation point. The following three sub-events are about 20 km to 30 km below the initiation point. The sub-events are close to the GCMT sub-vertical plane, roughly consistent with the previous directivity analysis (Warren et al., 2007). The seismograms exhibit great complexity with different polarities. The focal mechanisms cannot be modeled on the planar model, especially the P waves (Fig. S4-12c – S4-12f).

Table S4-12. Source parameters of inferred sub-events of E12

Sub-event	dt (s)	dn (km)	de (km)	dz (km)	duration (s)	Mw	strike (°)	dip (°)	slip (°)
1	1.9	4.5	2.2	4.5	2.2	7.0	32.1	86.8	289.0
2	7.5	13.6	7.2	25.3	2.8	7.4	15.7	71.9	302.3
3	10.1	-0.9	2.0	25.5	5.0	7.3	35.2	74.8	272.1
4	14.2	1.7	-7.6	26.7	4.0	7.1	32.1	92.3	277.4

(Fig. S4-12)

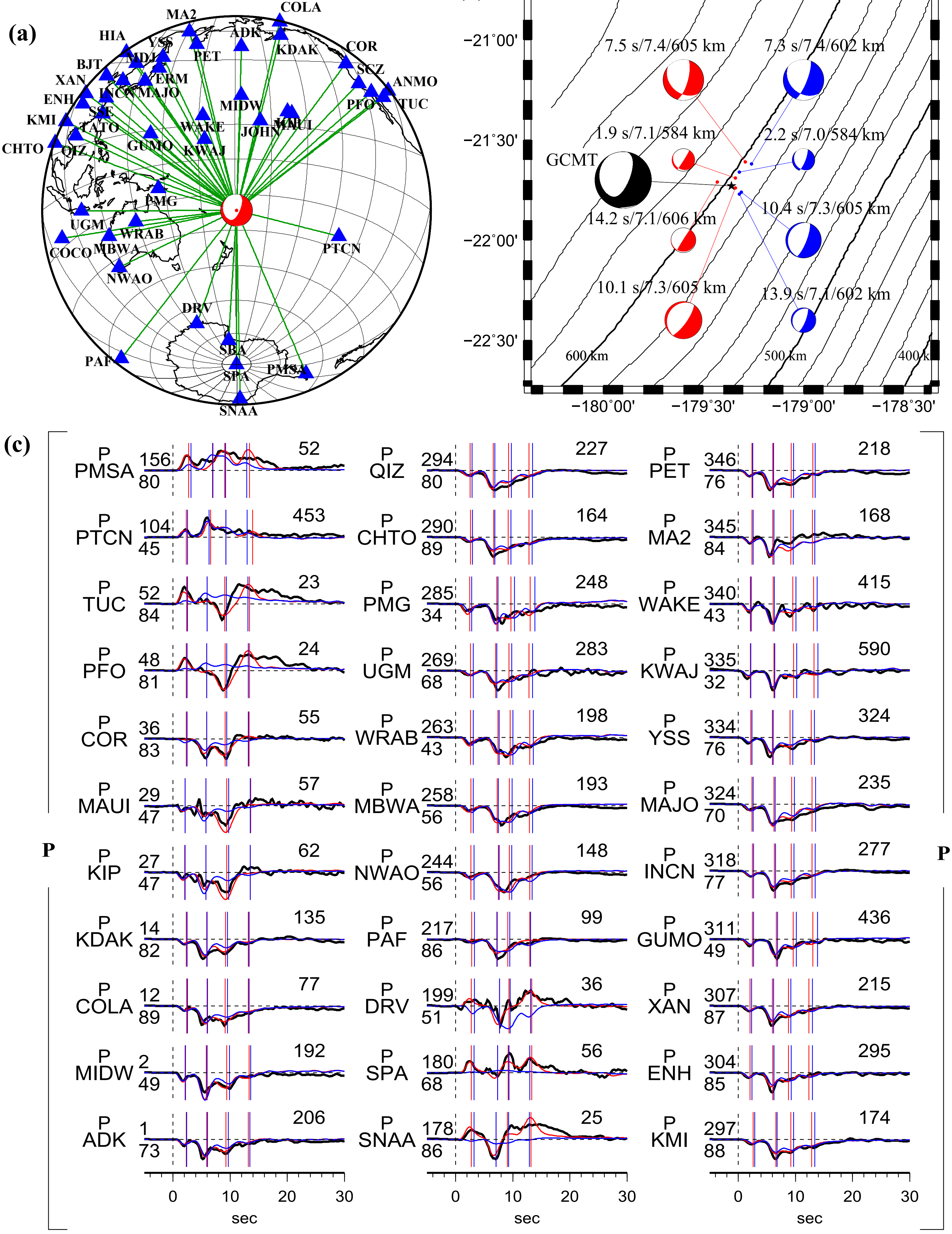
(a)
COLA
MA2
ADK
KDAK
HIA
YSS
PET
MDJ
COR
BJT
ERM
SCZ
XAN
INCN
MAJO
ANMO
ENH
SSE
MIDW
PFO
TUC
KMI
TATO
WAKE
JOHN
KIP
MAUI
CHTO
QIZ
GUMO
KWAJ
PMG
UGM
WRAB
PTCN
COCO
MBWA
NWAO
DRV
SBA
PAF
SPA
PMSA
SNAA
(b)
−21˚00'
−21˚30'
−22˚00'
−22˚30'
−180˚00'
−179˚30'
−179˚00'
−178˚30'
7.5 s/7.4/605 km
7.3 s/7.4/602 km
1.9 s/7.1/584 km
2.2 s/7.0/584 km
GCMT
14.2 s/7.1/606 km
10.4 s/7.3/605 km
10.1 s/7.3/605 km
13.9 s/7.1/602 km
600 km
500 km
400 k
(c)
P PMSA 156 80 52
P QIZ 294 80 227
P PET 346 76 218
P PTCN 104 45 453
P CHTO 290 89 164
P MA2 345 84 168
P TUC 52 84 23
P PMG 285 34 248
P WAKE 340 43 415
P PFO 48 81 24
P UGM 269 68 283
P KWAJ 335 32 590
P COR 36 83 55
P WRAB 263 43 198
P YSS 334 76 324
P MAUI 29 47 57
P MBWA 258 56 193
P MAJO 324 70 235
P KIP 27 47 62
P NWAO 244 56 148
P INCN 318 77 277
P KDAK 14 82 135
P PAF 217 86 99
P GUMO 311 49 436
P COLA 12 89 77
P DRV 199 51 36
P XAN 307 87 215
P MIDW 2 49 192
P SPA 180 68 56
P ENH 304 85 295
P ADK 1 73 206
P SNAA 178 86 25
P KMI 297 88 174
0
10
20
30
sec
P
P

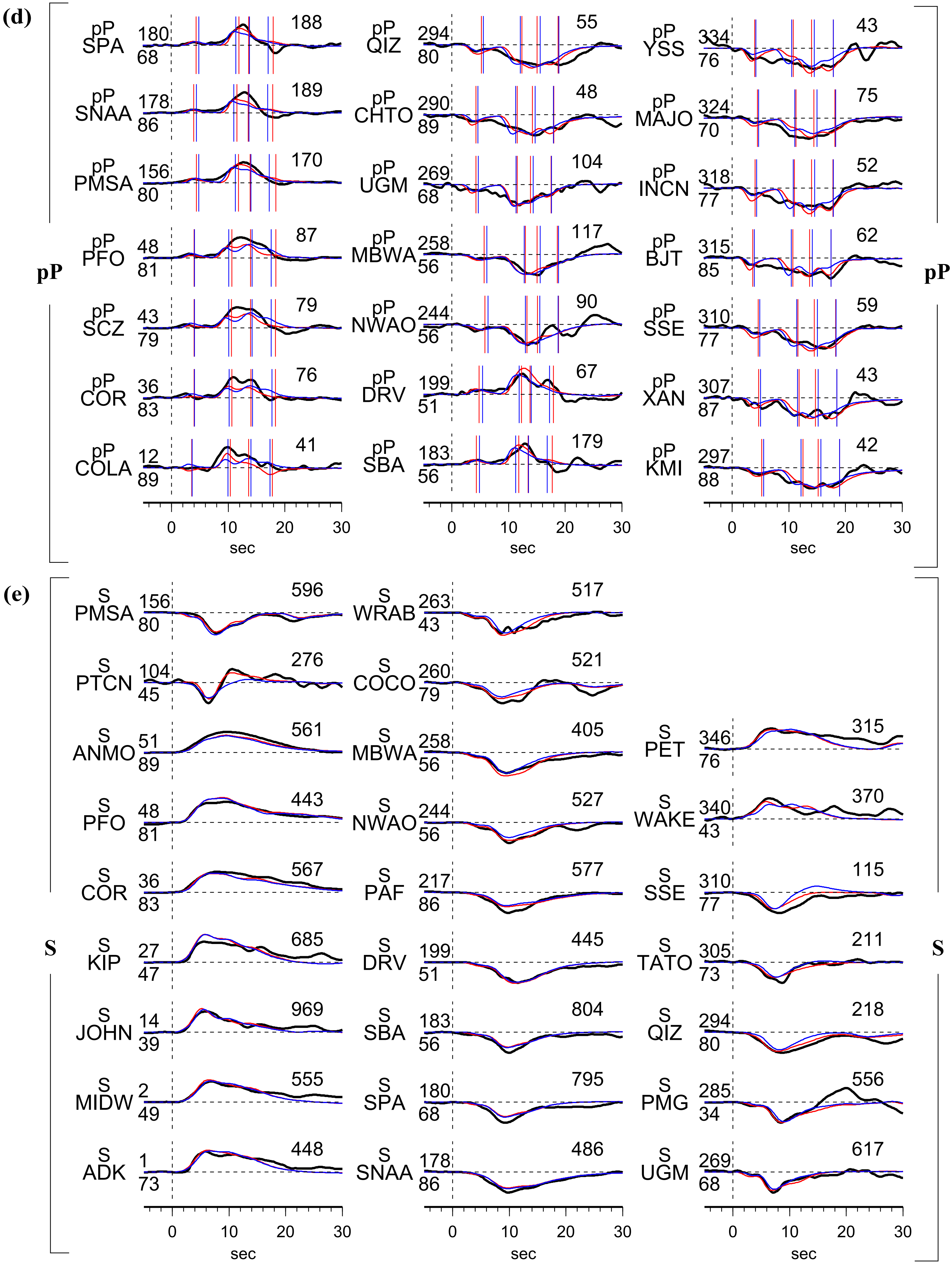
(d)
pP
pP
pP SPA 180 68 188
pP QIZ 294 80 55
pP YSS 334 76 43
pP SNAA 178 86 189
pP CHTO 290 89 48
pP MAJO 324 70 75
pP PMSA 156 80 170
pP UGM 269 68 104
pP INCN 318 77 52
pP PFO 48 81 87
pP MBWA 258 56 117
pP BJT 315 85 62
pP SCZ 43 79 79
pP NWAO 244 56 90
pP SSE 310 77 59
pP COR 36 83 76
pP DRV 199 51 67
pP XAN 307 87 43
pP COLA 12 89 41
pP SBA 183 56 179
pP KMI 297 88 42
0
10
20
30
sec
(e)
S
S
S PMSA 156 80 596
S WRAB 263 43 517
S PTCN 104 45 276
S COCO 260 79 521
S ANMO 51 89 561
S MBWA 258 56 405
S PET 346 76 315
S PFO 48 81 443
S NWAO 244 56 527
S WAKE 340 43 370
S COR 36 83 567
S PAF 217 86 577
S SSE 310 77 115
S KIP 27 47 685
S DRV 199 51 445
S TATO 305 73 211
S JOHN 14 39 969
S SBA 183 56 804
S QIZ 294 80 218
S MIDW 2 49 555
S SPA 180 68 795
S PMG 285 34 556
S ADK 1 73 448
S SNAA 178 86 486
S UGM 269 68 617
0
10
20
30
sec

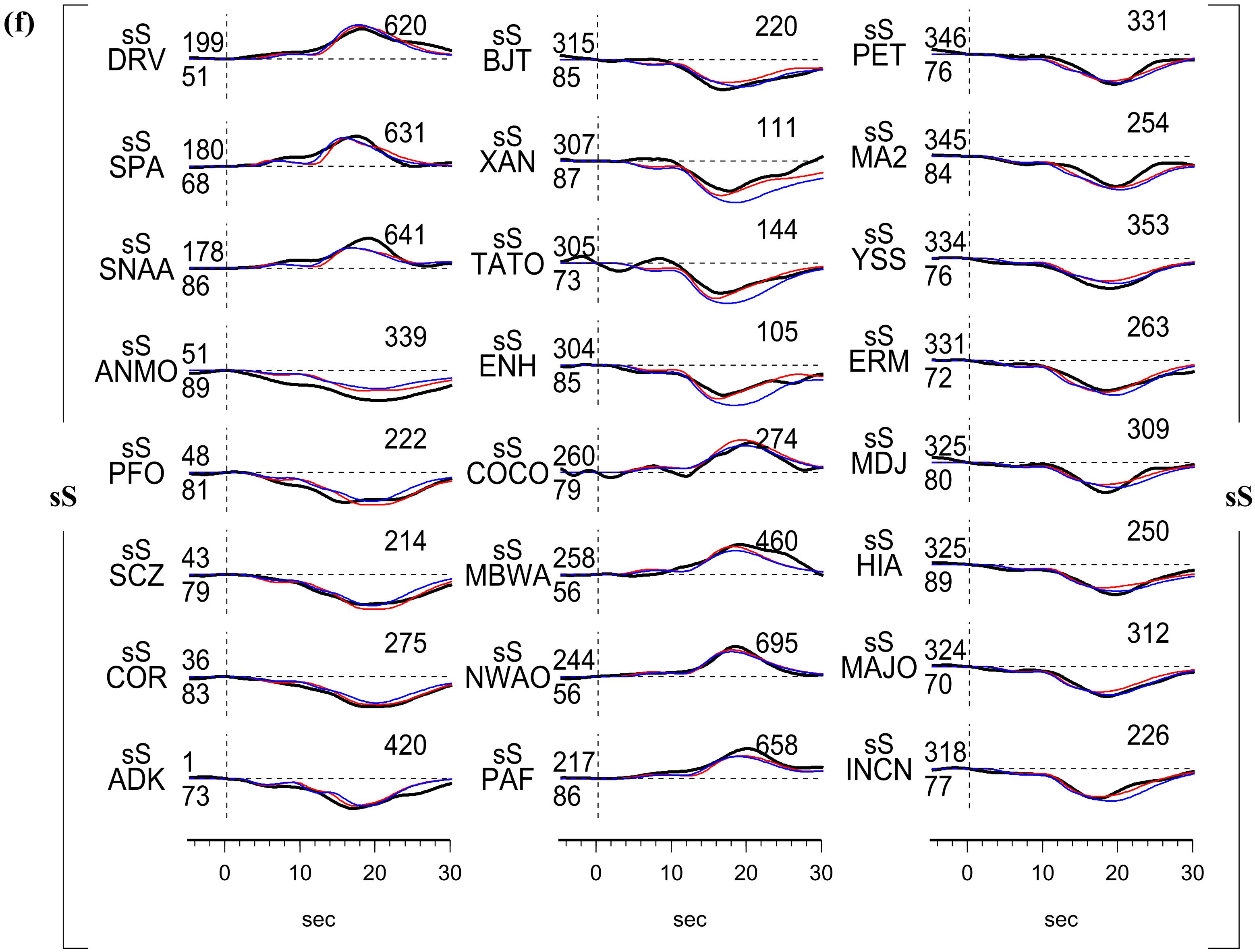
(f)
sS
sS
sS DRV 199 51 620
sS BJT 315 85 220
sS PET 346 76 331
sS SPA 180 68 631
sS XAN 307 87 111
sS MA2 345 84 254
sS SNAA 178 86 641
sS TATO 305 73 144
sS YSS 334 76 353
sS ANMO 51 89 339
sS ENH 304 85 105
sS ERM 331 72 263
sS PFO 48 81 222
sS COCO 260 79 274
sS MDJ 325 80 309
sS SCZ 43 79 214
sS MBWA 258 56 460
sS HIA 325 89 250
sS COR 36 83 275
sS NWAO 244 56 695
sS MAJO 324 70 312
sS ADK 1 73 420
sS PAF 217 86 658
sS INCN 318 77 226
0
10
20
30
sec
0
10
20
30
sec
0
10
20
30
sec

E13. The 19 Aug 2002 Mw 7.7 earthquake

Earthquake E13 occurred 675 km beneath Tonga region (Table S4-0), which is one of the deepest earthquakes. It occurred ~7 minutes after the E12. The seismograms constitute good azimuth coverage with 32 P, 19 pP, 26 S and 16 sS wave data (Fig. S4-13a). The seismic energy can be modeled by three sub-events (Table S4-13, Fig. S4-13b). The first sub-event occurred ~5km to the northwest of the initiation, the second 32 km to the southeast and the third 20 km to the south. The planar model prefers the sub-horizontal plane, consistent with the previous directivity analysis (Warren et al., 2007). However, synthetics predicted by the sub-horizontal plane cannot model radiation pattern of the seismic data (Fig. S4-13c – S4-13f).

Table S4-13. Source parameters of inferred sub-events of E13

Sub-event	dt (s)	dn (km)	de (km)	dz (km)	duration (s)	Mw	strike (°)	dip (°)	slip (°)
1	4.1	3.1	-4.7	0.0	6.0	7.4	56.4	2.1	69.7
2	5.9	-28.0	15.0	-5.7	5.8	7.5	67.2	-5.4	111.6
3	9.3	-20.7	-3.7	17.1	3.6	7.3	45.5	3.9	84.3

(Fig. S4-13)

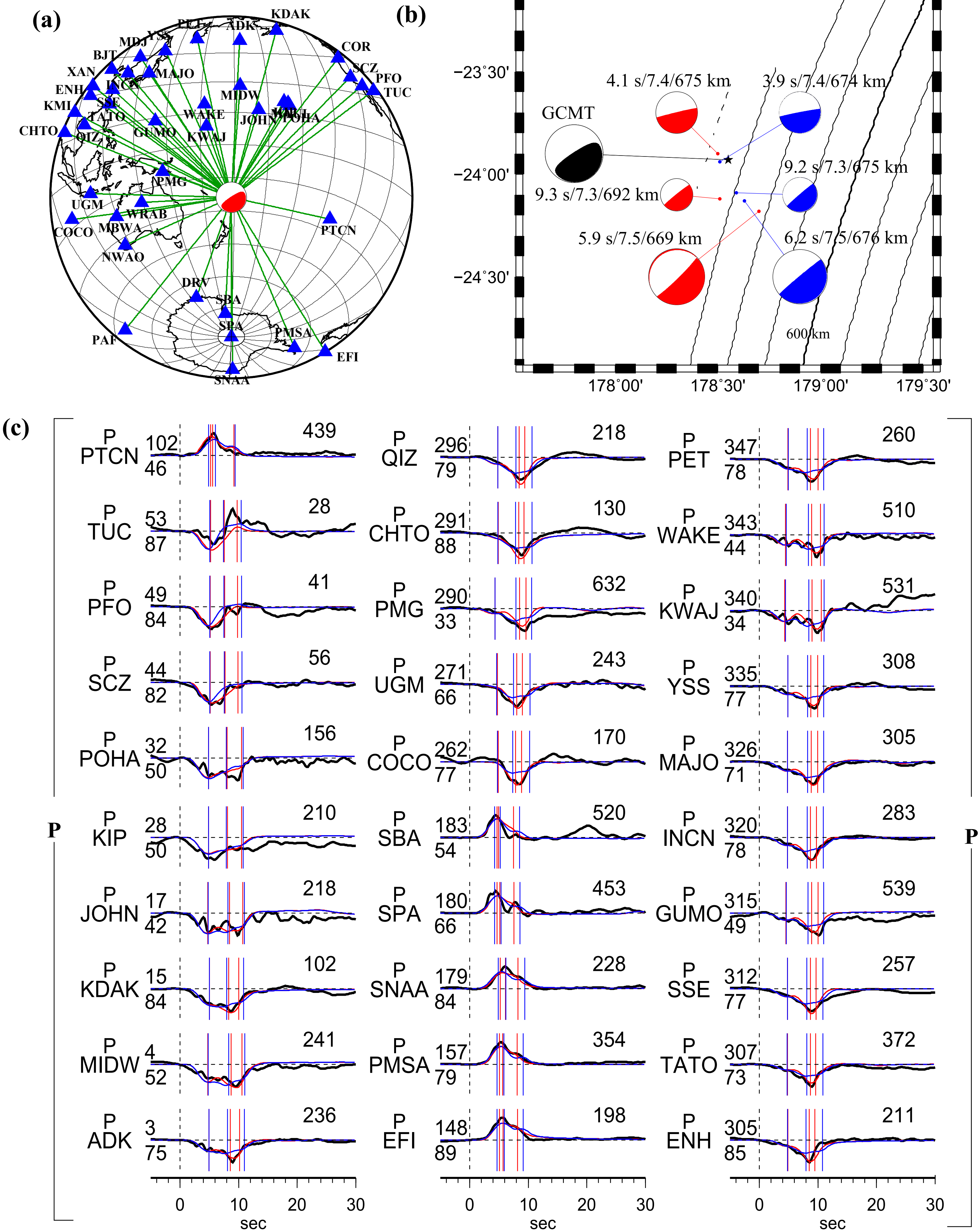

(a)
KDAK
PET
ADK
YSS
MDJ
BJT
MAJO
XAN
INCN
ENH
SSE
KMI
TATO
CHTO
QIZ
GUMO
MIDW
WAKE
KWAJ
JOHN
KIP
POHA
COR
SCZ
PFO
TUC
PMG
UGM
WRAB
COCO
MBWA
NWAO
PTCN
DRV
SBA
SPA
PMSA
PAF
EFI
SNAA
(b)
−23˚00'
−23˚30'
−24˚00'
−24˚30'
178˚00'
178˚30'
179˚00'
179˚30'
GCMT
4.1 s/7.4/675 km
3.9 s/7.4/674 km
9.3 s/7.3/692 km
9.2 s/7.3/675 km
5.9 s/7.5/669 km
6.2 s/7.5/676 km
600 km
(c)
P PTCN 102 46 439
P QIZ 296 79 218
P PET 347 78 260
P TUC 53 87 28
P CHTO 291 88 130
P WAKE 343 44 510
P PFO 49 84 41
P PMG 290 33 632
P KWAJ 340 34 531
P SCZ 44 82 56
P UGM 271 66 243
P YSS 335 77 308
P POHA 32 50 156
P COCO 262 77 170
P MAJO 326 71 305
P KIP 28 50 210
P SBA 183 54 520
P INCN 320 78 283
P JOHN 17 42 218
P SPA 180 66 453
P GUMO 315 49 539
P KDAK 15 84 102
P SNAA 179 84 228
P SSE 312 77 257
P MIDW 4 52 241
P PMSA 157 79 354
P TATO 307 73 372
P ADK 3 75 236
P EFI 148 89 198
P ENH 305 85 211
0
10
20
30
sec
P
P

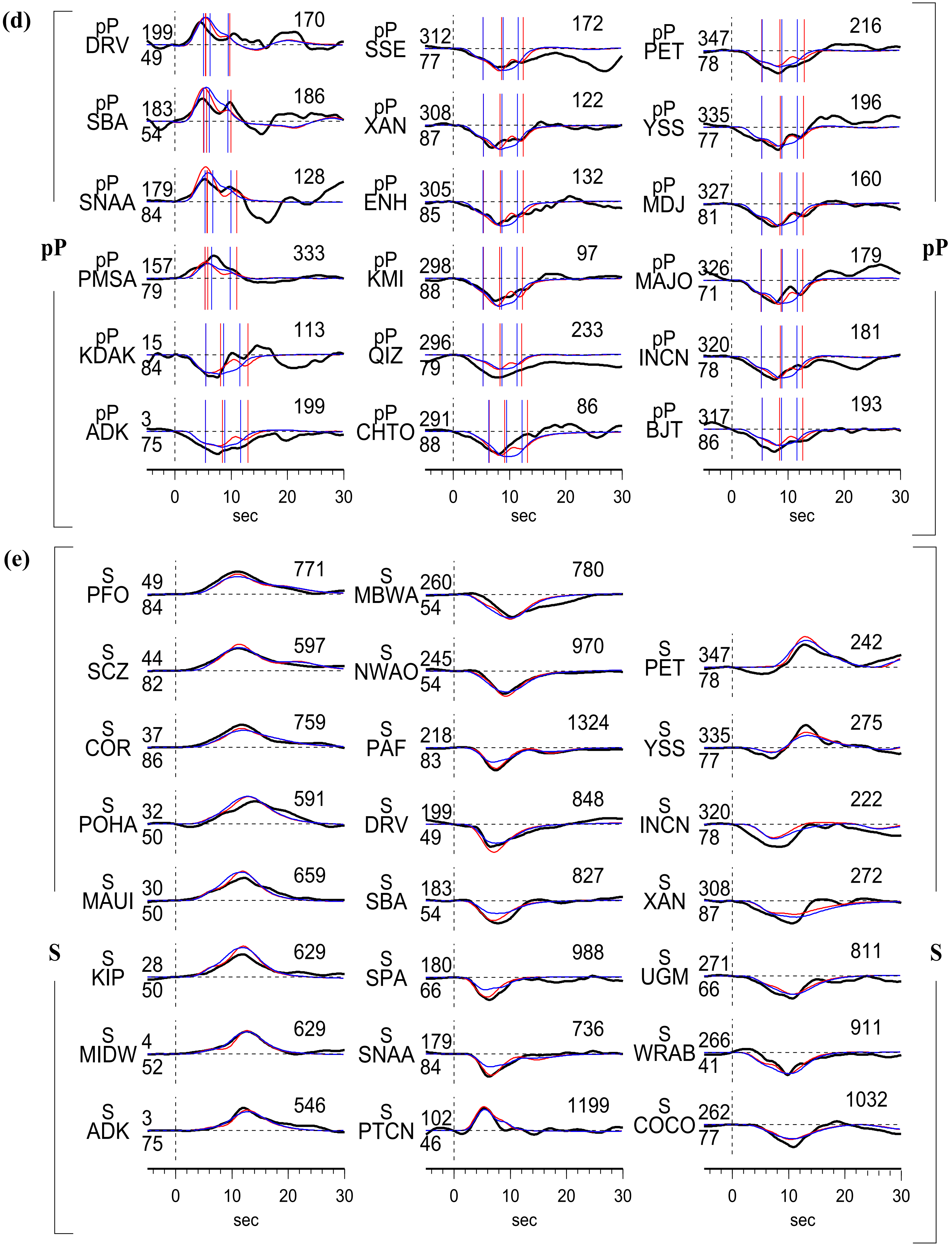

(d)
pP DRV 199 49 170
pP SSE 312 77 172
pP PET 347 78 216
pP SBA 183 54 186
pP XAN 308 87 122
pP YSS 335 77 196
pP SNAA 179 84 128
pP ENH 305 85 132
pP MDJ 327 81 160
pP
pP PMSA 157 79 333
pP KMI 298 88 97
pP MAJO 326 71 179
pP
pP KDAK 15 84 113
pP QIZ 296 79 233
pP INCN 320 78 181
pP ADK 3 75 199
pP CHTO 291 88 86
pP BJT 317 86 193
0
10
20
30
sec
(e)
S PFO 49 84 771
S MBWA 260 54 780
S SCZ 44 82 597
S NWAO 245 54 970
S PET 347 78 242
S COR 37 86 759
S PAF 218 83 1324
S YSS 335 77 275
S POHA 32 50 591
S DRV 199 49 848
S INCN 320 78 222
S MAUI 30 50 659
S SBA 183 54 827
S XAN 308 87 272
S
S KIP 28 50 629
S SPA 180 66 988
S UGM 271 66 811
S
S MIDW 4 52 629
S SNAA 179 84 736
S WRAB 266 41 911
S ADK 3 75 546
S PTCN 102 46 1199
S COCO 262 77 1032
0
10
20
30
sec

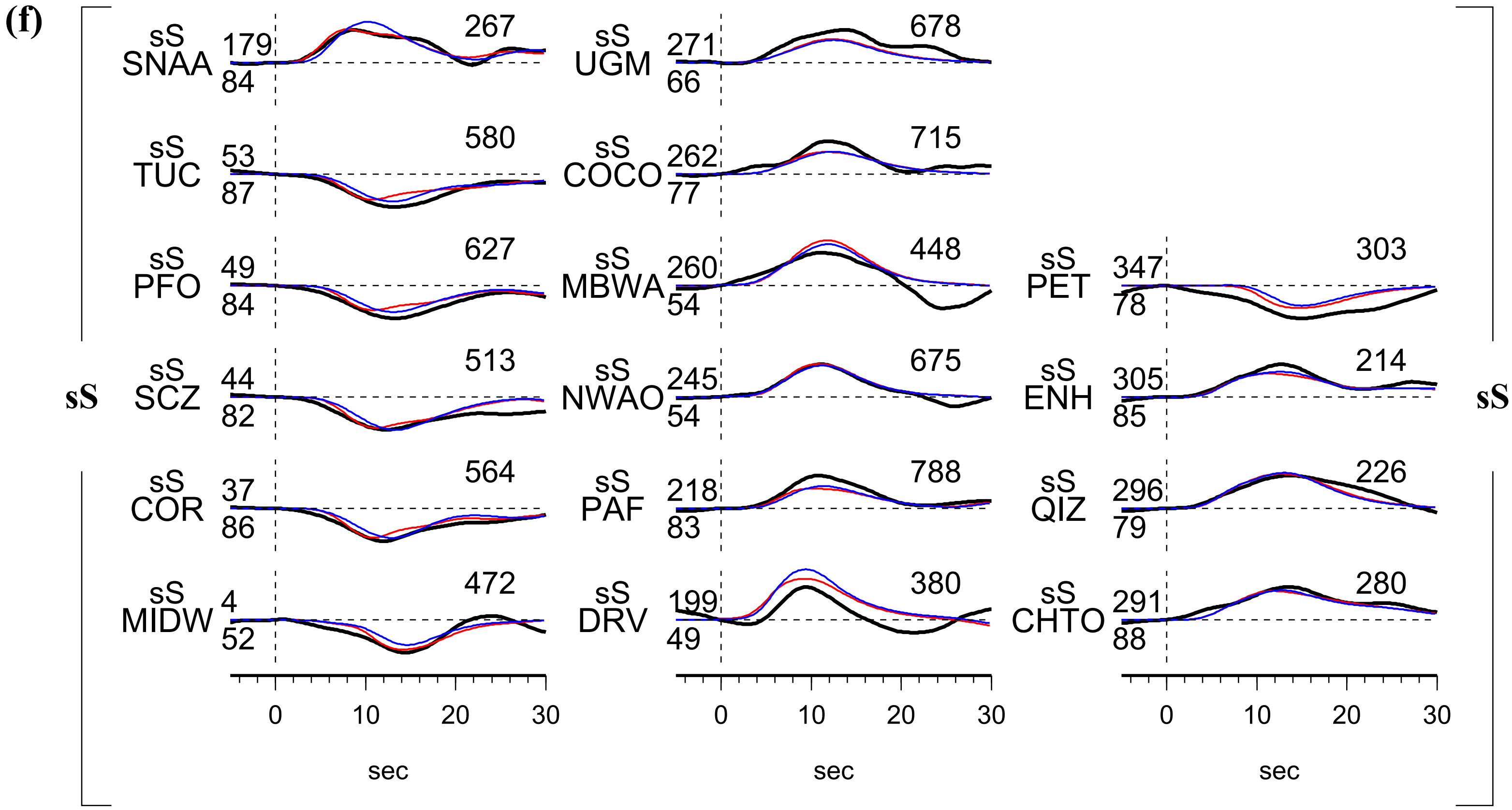
(f)
sS
sS
sS SNAA 179 84 267
sS UGM 271 66 678
sS TUC 53 87 580
sS COCO 262 77 715
sS PFO 49 84 627
sS MBWA 260 54 448
sS PET 347 78 303
sS SCZ 44 82 513
sS NWAO 245 54 675
sS ENH 305 85 214
sS COR 37 86 564
sS PAF 218 83 788
sS QIZ 296 79 226
sS MIDW 4 52 472
sS DRV 199 49 380
sS CHTO 291 88 280
0
10
20
30
sec
0
10
20
30
sec
0
10
20
30
sec

E14. The 17 Nov 2002 Mw 7.3 earthquake

Earthquake E14 occurred 459 km beneath Sea of Okhotsk (Table S4-0). The seismograms constitute good azimuth coverage with 33 P, 27 pP, 30 S and 25 sS waveforms (Fig. S4-14a). The seismic energy can be modeled by two major sub-events after a ~6 s weak initiation (Table S4-14, Fig. S4-14b). The first sub-event is 16 km to the south of the initiation point, but the second is 10 km to the southeast. The sub-events can be inferred on both the GCMT sub-horizontal plane model and the best-fitting sub-event model (Fig. S4-14c – S4-14f).

Table S4-14. Source parameters of inferred sub-events of E14

Sub-event	dt (s)	dn (km)	de (km)	dz (km)	duration (s)	Mw	strike (°)	dip (°)	slip (°)
1	7.9	-15.9	1.6	-0.6	3.0	7.0	314.2	6.5	27.7
2	10.1	-8.5	5.3	3.1	3.0	7.0	326.0	9.6	40.8

(Fig. S4-14)

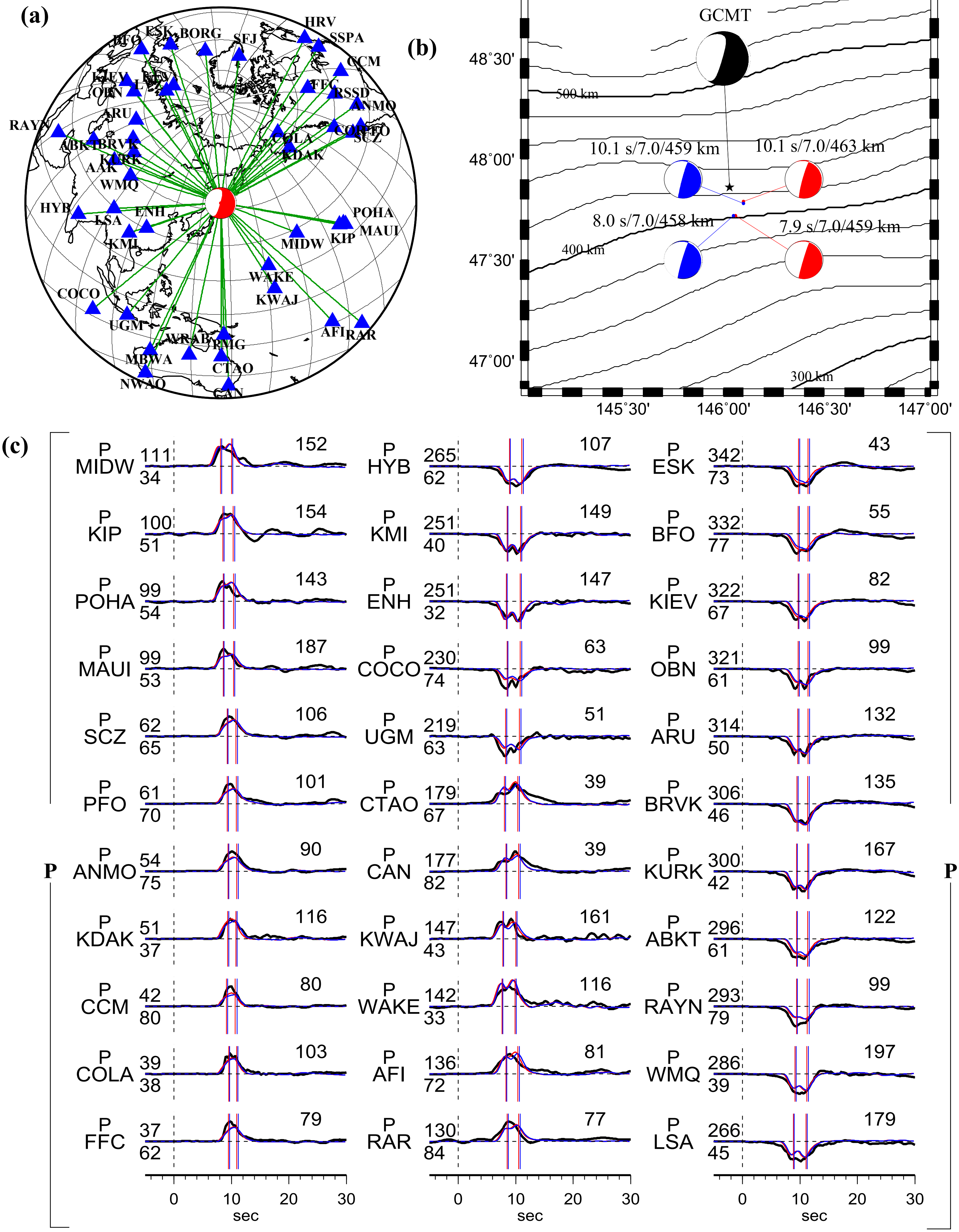

(a)
HRV
SSPA
CCM
BFO
ESK
BORG
SFJ
KIEV
OBN
FFC
RSSD
ANMO
ARU
RAYN
COR
PFO
SCZ
COLA
ABKT
BRVK
KDAK
KURK
AAK
WMQ
HYB
ENH
LSA
POHA
MAUI
KIP
KMI
MIDW
WAKE
KWAJ
COCO
UGM
AFI
RAR
WRAB
PMG
MBWA
CTAO
NWAO
CAN
(b)
GCMT
48˚30'
48˚00'
47˚30'
47˚00'
500 km
400 km
300 km
10.1 s/7.0/459 km
10.1 s/7.0/463 km
8.0 s/7.0/458 km
7.9 s/7.0/459 km
145˚30'
146˚00'
146˚30'
147˚00'
(c)
P MIDW 111 34 152
P KIP 100 51 154
P POHA 99 54 143
P MAUI 99 53 187
P SCZ 62 65 106
P PFO 61 70 101
P ANMO 54 75 90
P KDAK 51 37 116
P CCM 42 80 80
P COLA 39 38 103
P FFC 37 62 79
P HYB 265 62 107
P KMI 251 40 149
P ENH 251 32 147
P COCO 230 74 63
P UGM 219 63 51
P CTAO 179 67 39
P CAN 177 82 39
P KWAJ 147 43 161
P WAKE 142 33 116
P AFI 136 72 81
P RAR 130 84 77
P ESK 342 73 43
P BFO 332 77 55
P KIEV 322 67 82
P OBN 321 61 99
P ARU 314 50 132
P BRVK 306 46 135
P KURK 300 42 167
P ABKT 296 61 122
P RAYN 293 79 99
P WMQ 286 39 197
P LSA 266 45 179
P
P
0
10
20
30
sec

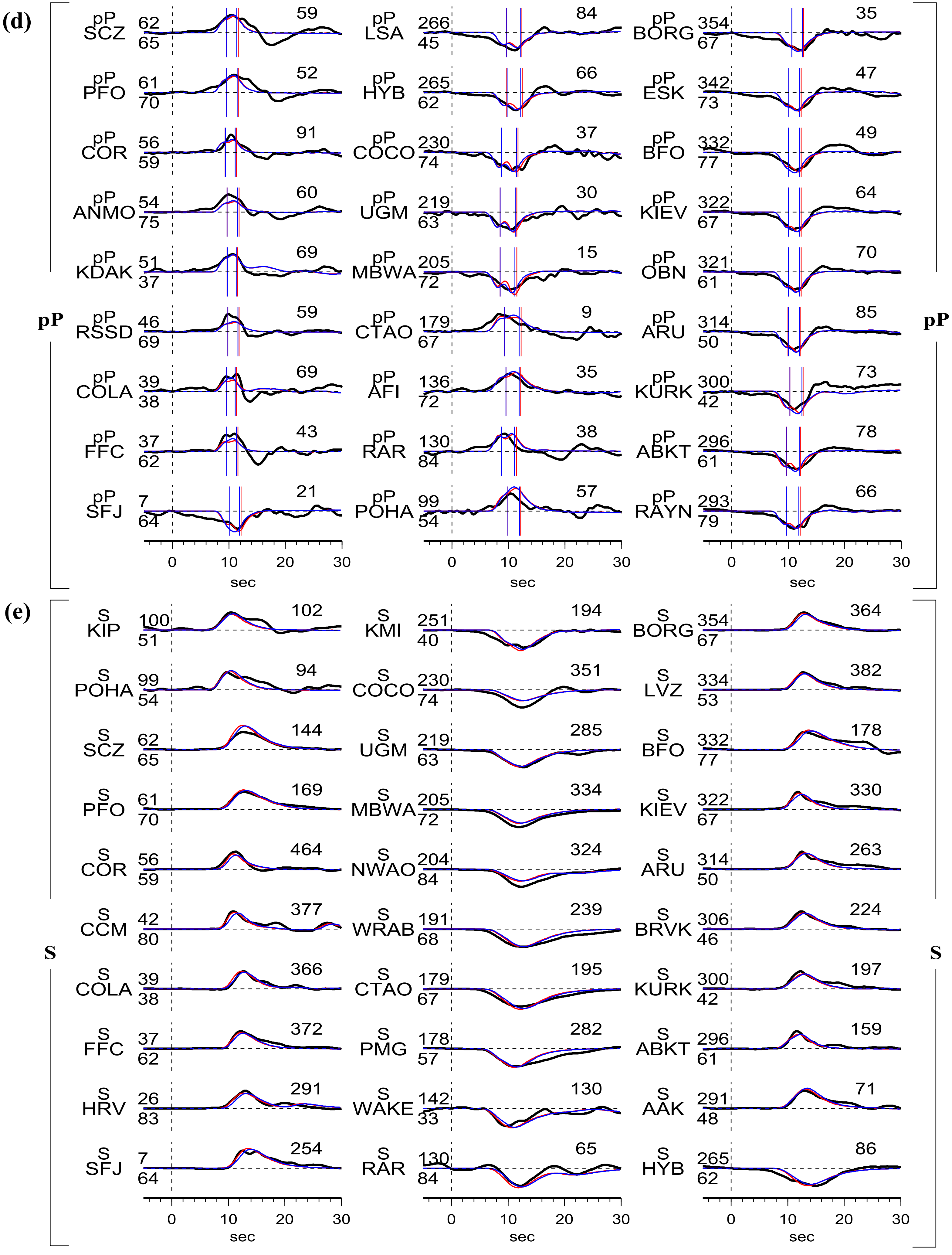

(d)
pP
pP SCZ 62 65 59
pP PFO 61 70 52
pP COR 56 59 91
pP ANMO 54 75 60
pP KDAK 51 37 69
pP RSSD 46 69 59
pP COLA 39 38 69
pP FFC 37 62 43
pP SFJ 7 64 21
pP LSA 266 45 84
pP HYB 265 62 66
pP COCO 230 74 37
pP UGM 219 63 30
pP MBWA 205 72 15
pP CTAO 179 67 9
pP AFI 136 72 35
pP RAR 130 84 38
pP POHA 99 54 57
pP BORG 354 67 35
pP ESK 342 73 47
pP BFO 332 77 49
pP KIEV 322 67 64
pP OBN 321 61 70
pP ARU 314 50 85
pP KURK 300 42 73
pP ABKT 296 61 78
pP RAYN 293 79 66
0
10
20
30
sec
(e)
S
S KIP 100 51 102
S POHA 99 54 94
S SCZ 62 65 144
S PFO 61 70 169
S COR 56 59 464
S CCM 42 80 377
S COLA 39 38 366
S FFC 37 62 372
S HRV 26 83 291
S SFJ 7 64 254
S KMI 251 40 194
S COCO 230 74 351
S UGM 219 63 285
S MBWA 205 72 334
S NWAO 204 84 324
S WRAB 191 68 239
S CTAO 179 67 195
S PMG 178 57 282
S WAKE 142 33 130
S RAR 130 84 65
S BORG 354 67 364
S LVZ 334 53 382
S BFO 332 77 178
S KIEV 322 67 330
S ARU 314 50 263
S BRVK 306 46 224
S KURK 300 42 197
S ABKT 296 61 159
S AAK 291 48 71
S HYB 265 62 86
0
10
20
30
sec

(f)

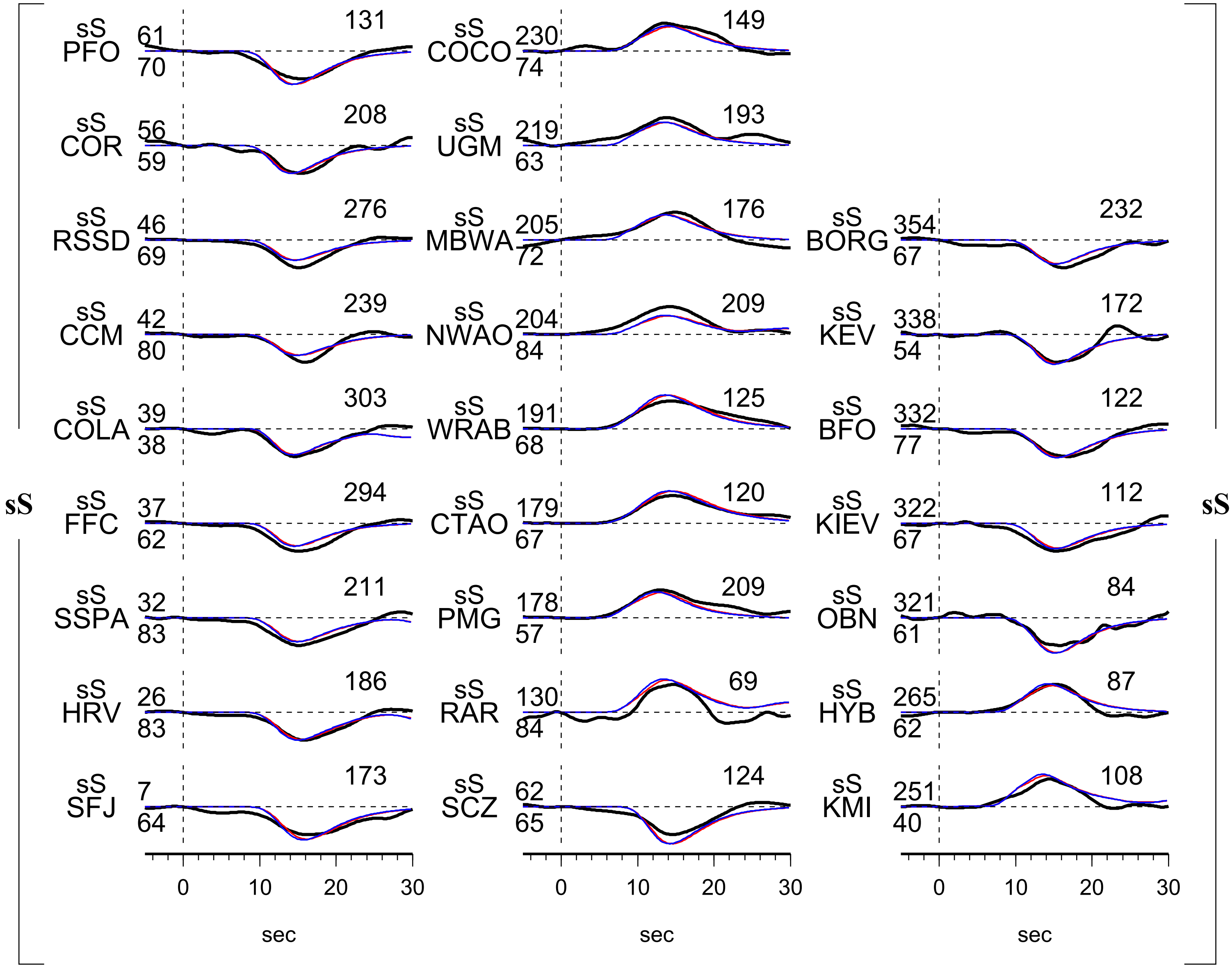
sS PFO 61 70 131
sS COCO 230 74 149
sS COR 56 59 208
sS UGM 219 63 193
sS RSSD 46 69 276
sS MBWA 205 72 176
sS BORG 354 67 232
sS CCM 42 80 239
sS NWAO 204 84 209
sS KEV 338 54 172
sS COLA 39 38 303
sS WRAB 191 68 125
sS BFO 332 77 122
sS FFC 37 62 294
sS CTAO 179 67 120
sS KIEV 322 67 112
sS SSPA 32 83 211
sS PMG 178 57 209
sS OBN 321 61 84
sS HRV 26 83 186
sS RAR 130 84 69
sS HYB 265 62 87
sS SFJ 7 64 173
sS SCZ 62 65 124
sS KMI 251 40 108
sS
sS
0
10
20
30
sec

E15. The 20 Jun 2003 Mw 7.0 earthquake

Earthquake E15 occurred 553 km beneath South America (Table S4-0). The seismograms constitute good azimuth coverage with 32 P, 27 pP, 20 S and 8 sS wave data (Fig. S4-15a). The seismic energy can be modeled by five major sub-events with a horizontal extension of ~70 km and a vertical extension of 30 km (Table S4-15, Fig. S4-15b). The earthquake has a huge source extension, but a short duration of 12 s and a moment magnitude of 7.0. The average propagating velocity of the source process is ~5.4 km/s, close to the S wave velocity at this depth. The five pulses are separated enough in the azimuth of 180° and merge in the azimuth of 0° (Figs. S4-15c – S4-15f). The planar model (blue traces) can model the P and pP data (Figs. S4-15c, S4-15d) almost as well as the best-fitting model (red traces), but have great misfit to radiation patterns of the S and sS waves (Figs. S4-15e and S4-15f). Although the sub-events have different fault plane orientations, but still propagate close to the higher angle plane.

Table S4-15. Source parameters of inferred sub-events of E15

Sub-event	dt (s)	dn (km)	de (km)	dz (km)	duration (s)	Mw	strike (°)	dip (°)	slip (°)
1	1.9	2.1	-1.3	2.4	3.6	6.6	128.7	48.0	247.6
2	4.3	9.6	-1.4	0.3	4.0	6.6	157.6	41.0	249.2
3	6.9	29.0	-4.7	-15.7	3.8	6.6	134.0	47.5	241.7
4	9.5	45.6	-7.5	-25.5	4.0	6.6	115.9	56.6	240.5
5	11.3	54.8	-12.3	-29.9	2.8	6.4	156.4	48.4	264.2

(Fig. S4-15)

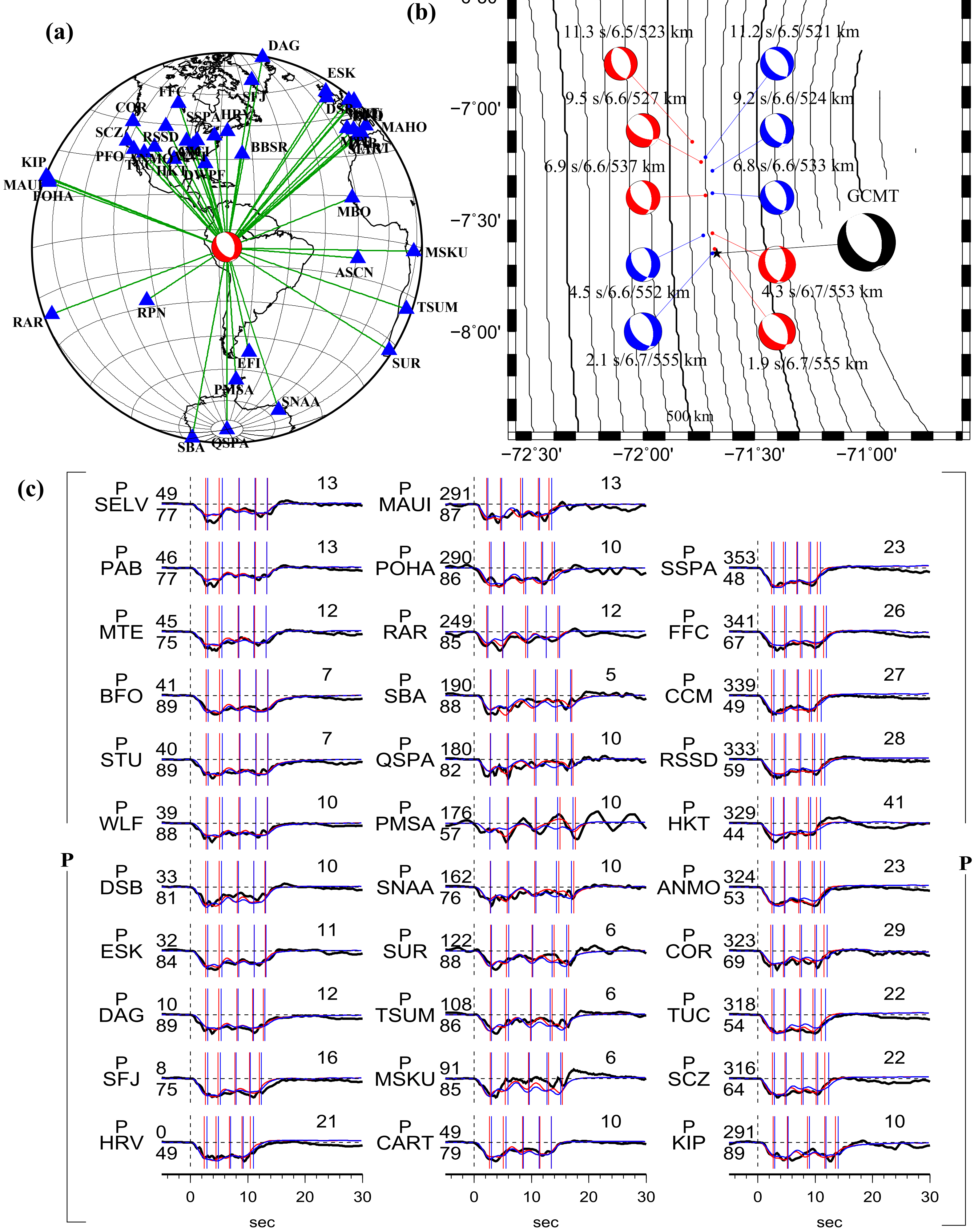
(a)
DAG
ESK
FFC
SFJ
COR
SSPA
HRV
DSB
MAHO
SCZ
RSSD
PFO
BBSR
KIP
MAUI
POHA
MBO
MSKU
ASCN
RAR
RPN
TSUM
SUR
EFI
PMSA
SNAA
SBA
QSPA
(b)
−6˚30'
−7˚00'
−7˚30'
−8˚00'
−72˚30'
−72˚00'
−71˚30'
−71˚00'
11.3 s/6.5/523 km
11.2 s/6.5/521 km
9.5 s/6.6/527 km
9.2 s/6.6/524 km
6.9 s/6.6/537 km
6.8 s/6.6/533 km
GCMT
4.5 s/6.6/552 km
4.3 s/6.7/553 km
2.1 s/6.7/555 km
1.9 s/6.7/555 km
500 km
(c)
P SELV 49 77 13
P MAUI 291 87 13
P PAB 46 77 13
P POHA 290 86 10
P SSPA 353 48 23
P MTE 45 75 12
P RAR 249 85 12
P FFC 341 67 26
P BFO 41 89 7
P SBA 190 88 5
P CCM 339 49 27
P STU 40 89 7
P QSPA 180 82 10
P RSSD 333 59 28
P WLF 39 88 10
P PMSA 176 57 10
P HKT 329 44 41
P DSB 33 81 10
P SNAA 162 76 10
P ANMO 324 53 23
P ESK 32 84 11
P SUR 122 88 6
P COR 323 69 29
P DAG 10 89 12
P TSUM 108 86 6
P TUC 318 54 22
P SFJ 8 75 16
P MSKU 91 85 6
P SCZ 316 64 22
P HRV 0 49 21
P CART 49 79 10
P KIP 291 89 10
P
P
0
10
20
30
sec

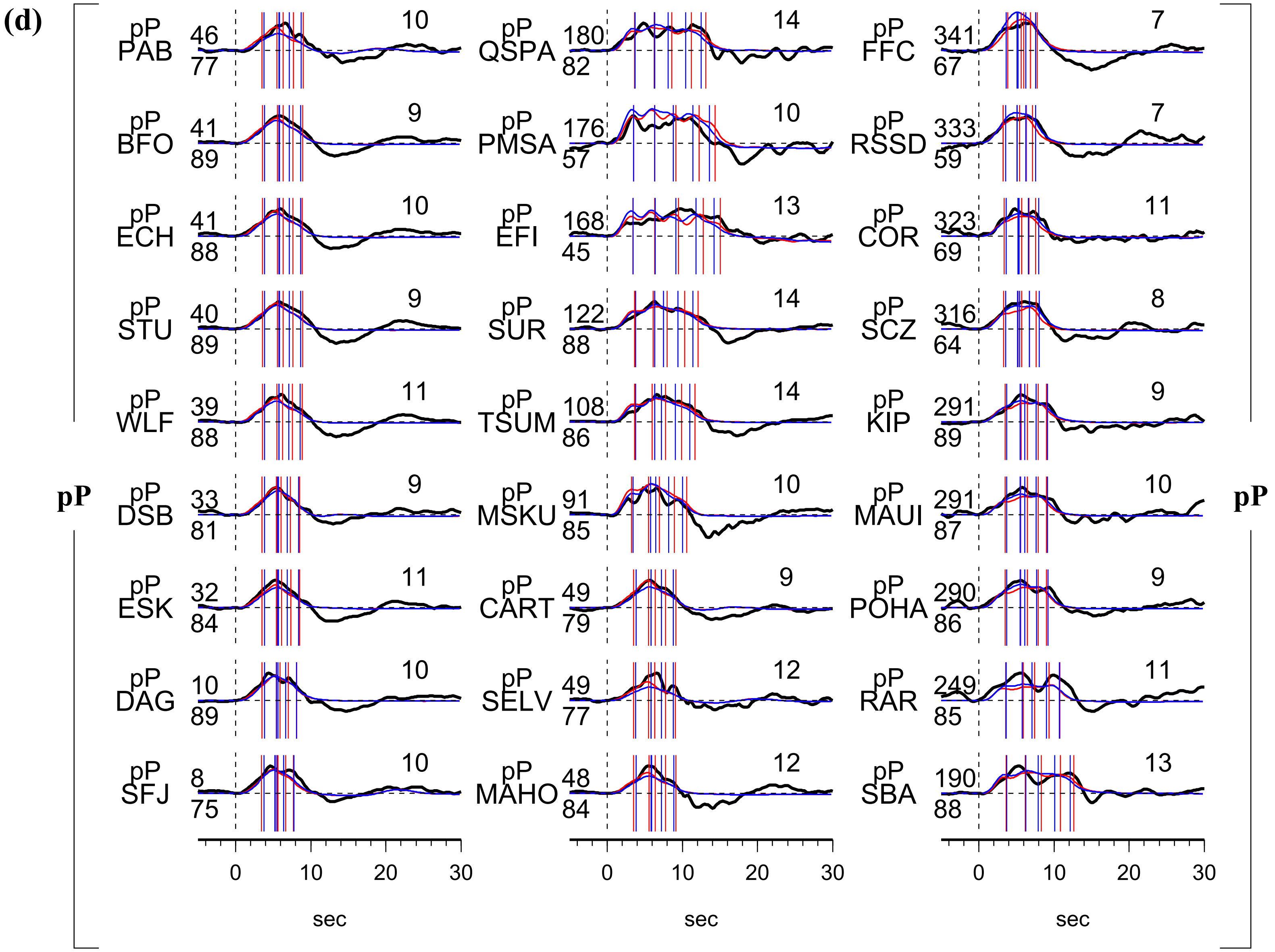
(d)
pP
pP
pP PAB 46 77 10
pP BFO 41 89 9
pP ECH 41 88 10
pP STU 40 89 9
pP WLF 39 88 11
pP DSB 33 81 9
pP ESK 32 84 11
pP DAG 10 89 10
pP SFJ 8 75 10
pP QSPA 180 82 14
pP PMSA 176 57 10
pP EFI 168 45 13
pP SUR 122 88 14
pP TSUM 108 86 14
pP MSKU 91 85 10
pP CART 49 79 9
pP SELV 49 77 12
pP MAHO 48 84 12
pP FFC 341 67 7
pP RSSD 333 59 7
pP COR 323 69 11
pP SCZ 316 64 8
pP KIP 291 89 9
pP MAUI 291 87 10
pP POHA 290 86 9
pP RAR 249 85 11
pP SBA 190 88 13
0
10
20
30
sec
0
10
20
30
sec
0
10
20
30
sec

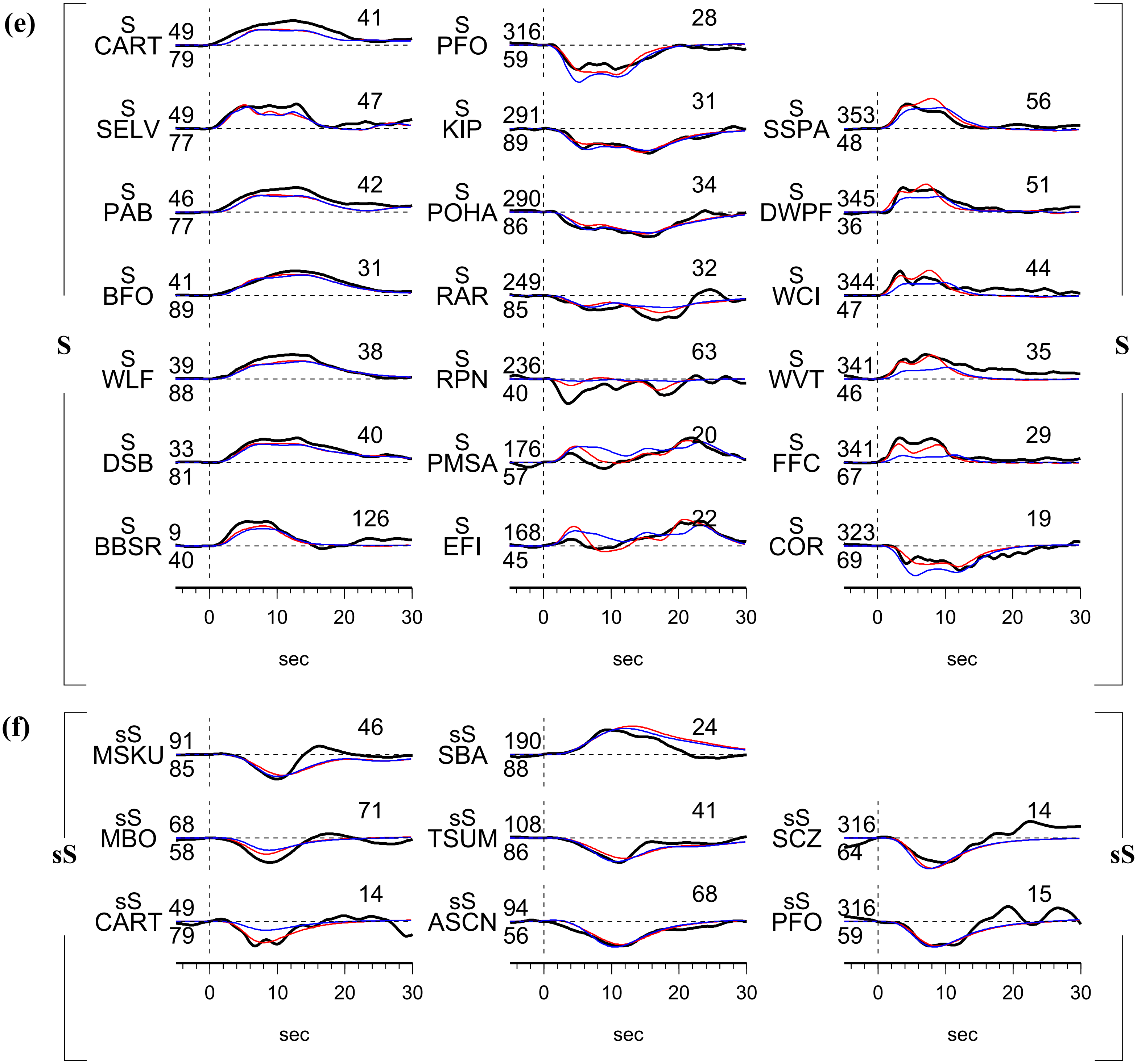
(e)
S
S CART 49 79 41
S PFO 316 59 28
S SELV 49 77 47
S KIP 291 89 31
S SSPA 353 48 56
S PAB 46 77 42
S POHA 290 86 34
S DWPF 345 36 51
S BFO 41 89 31
S RAR 249 85 32
S WCI 344 47 44
S WLF 39 88 38
S RPN 236 40 63
S WVT 341 46 35
S DSB 33 81 40
S PMSA 176 57 20
S FFC 341 67 29
S BBSR 9 40 126
S EFI 168 45 22
S COR 323 69 19
0
10
20
30
sec
(f)
sS
sS MSKU 91 85 46
sS SBA 190 88 24
sS MBO 68 58 71
sS TSUM 108 86 41
sS SCZ 316 64 14
sS CART 49 79 14
sS ASCN 94 56 68
sS PFO 316 59 15
0
10
20
30
sec

E16. The 15 Jul 2004 Mw 7.1 earthquake

Earthquake E16 occurred 560 km beneath Tonga region (Table S4-0). The seismograms constitute good azimuth coverage with 34 P, 20 pP, 24 S and 16 sS wave data (Fig. S4-16a). The seismic energy can be modeled three sub-events after ~6 s initiation (Table S4-16). The sub-events propagated to the northwest along the intersection of the two GCMT fault planes (Fig. S4-16b). Previous study cannot distinguish the fault plane by directivity (Warren et al., 2007). The planar model cannot model the varying radiation pattern of the seismic data (Fig. S4-16c – S4-16f).

Table S4-16. Source parameters of inferred sub-events of E16

Sub-event	dt (s)	dn (km)	de (km)	dz (km)	duration (s)	Mw	strike (°)	dip (°)	slip (°)
1	7.3	6.5	-4.6	4.8	2.2	6.9	342.9	33.9	126.1
2	9.3	13.2	-10.8	1.3	2.4	6.8	345.2	50.7	138.2
3	12.0	16.9	-25.3	5.8	2.4	6.5	329.4	66.0	125.7

(Fig. S4-16)

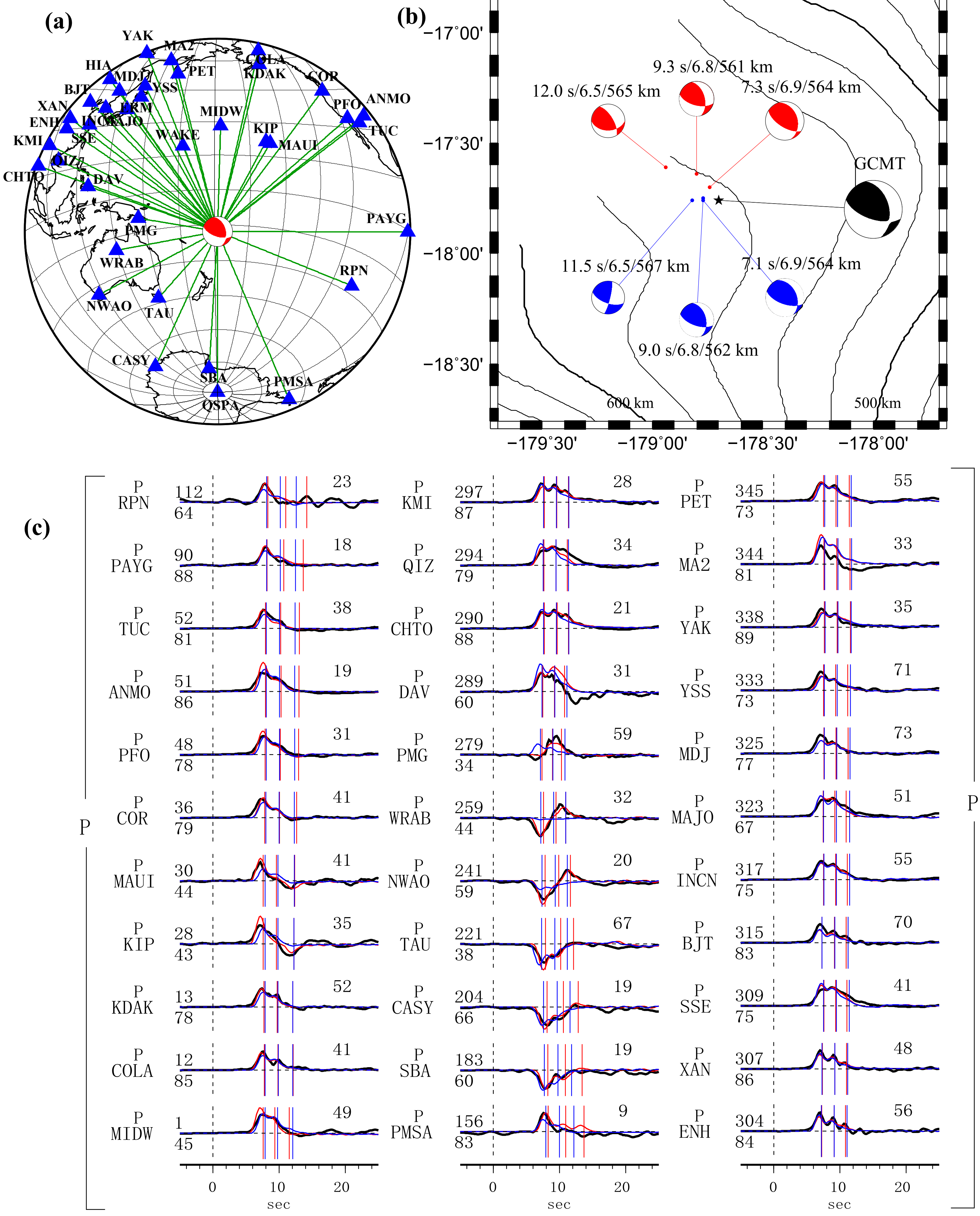
(a)
YAK
MA2
PET
HIA
MDJ
YSS
COLA
KDAK
COR
BJT
XAN
ERM
INCN
MAJO
ENH
PFO
ANMO
TUC
KMI
SSE
MIDW
WAKE
KIP
MAUI
QIZ
CHTO
DAV
PMG
PAYG
WRAB
RPN
NWAO
TAU
CASY
SBA
PMSA
QSPA
(b)
9.3 s/6.8/561 km
12.0 s/6.5/565 km
7.3 s/6.9/564 km
GCMT
11.5 s/6.5/567 km
7.1 s/6.9/564 km
9.0 s/6.8/562 km
600 km
500 km
−17˚00'
−17˚30'
−18˚00'
−18˚30'
−179˚30'
−179˚00'
−178˚30'
−178˚00'
(c)
P RPN 112 64 23
P PAYG 90 88 18
P TUC 52 81 38
P ANMO 51 86 19
P PFO 48 78 31
P COR 36 79 41
P MAUI 30 44 41
P KIP 28 43 35
P KDAK 13 78 52
P COLA 12 85 41
P MIDW 1 45 49
P KMI 297 87 28
P QIZ 294 79 34
P CHTO 290 88 21
P DAV 289 60 31
P PMG 279 34 59
P WRAB 259 44 32
P NWAO 241 59 20
P TAU 221 38 67
P CASY 204 66 19
P SBA 183 60 19
P PMSA 156 83 9
P PET 345 73 55
P MA2 344 81 33
P YAK 338 89 35
P YSS 333 73 71
P MDJ 325 77 73
P MAJO 323 67 51
P INCN 317 75 55
P BJT 315 83 70
P SSE 309 75 41
P XAN 307 86 48
P ENH 304 84 56
0
10
20
sec
P
P

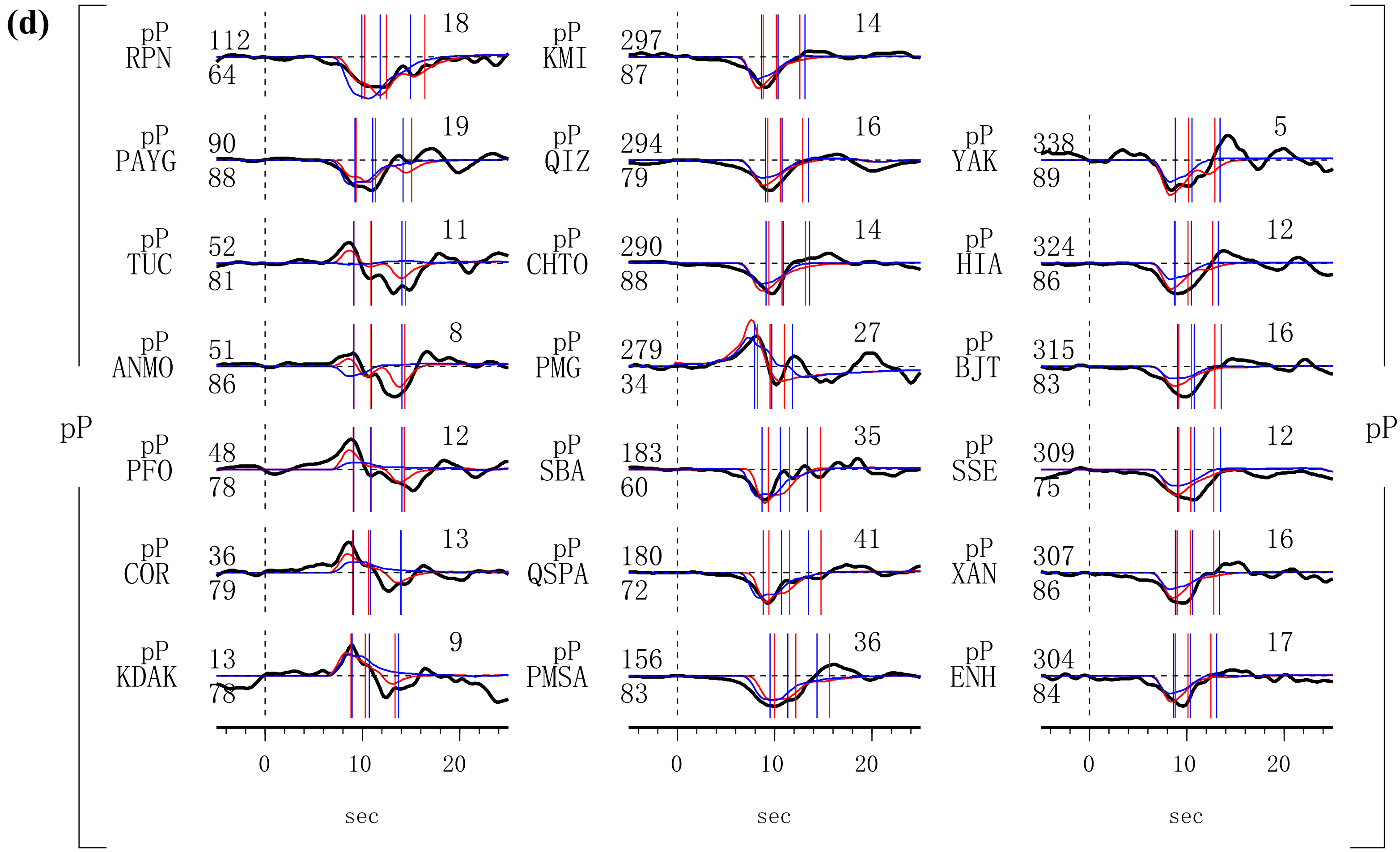
(d)
pP
pP RPN 112 64 18
pP KMI 297 87 14
pP PAYG 90 88 19
pP QIZ 294 79 16
pP YAK 338 89 5
pP TUC 52 81 11
pP CHTO 290 88 14
pP HIA 324 86 12
pP ANMO 51 86 8
pP PMG 279 34 27
pP BJT 315 83 16
pP PFO 48 78 12
pP SBA 183 60 35
pP SSE 309 75 12
pP COR 36 79 13
pP QSPA 180 72 41
pP XAN 307 86 16
pP KDAK 13 78 9
pP PMSA 156 83 36
pP ENH 304 84 17
0 10 20
sec

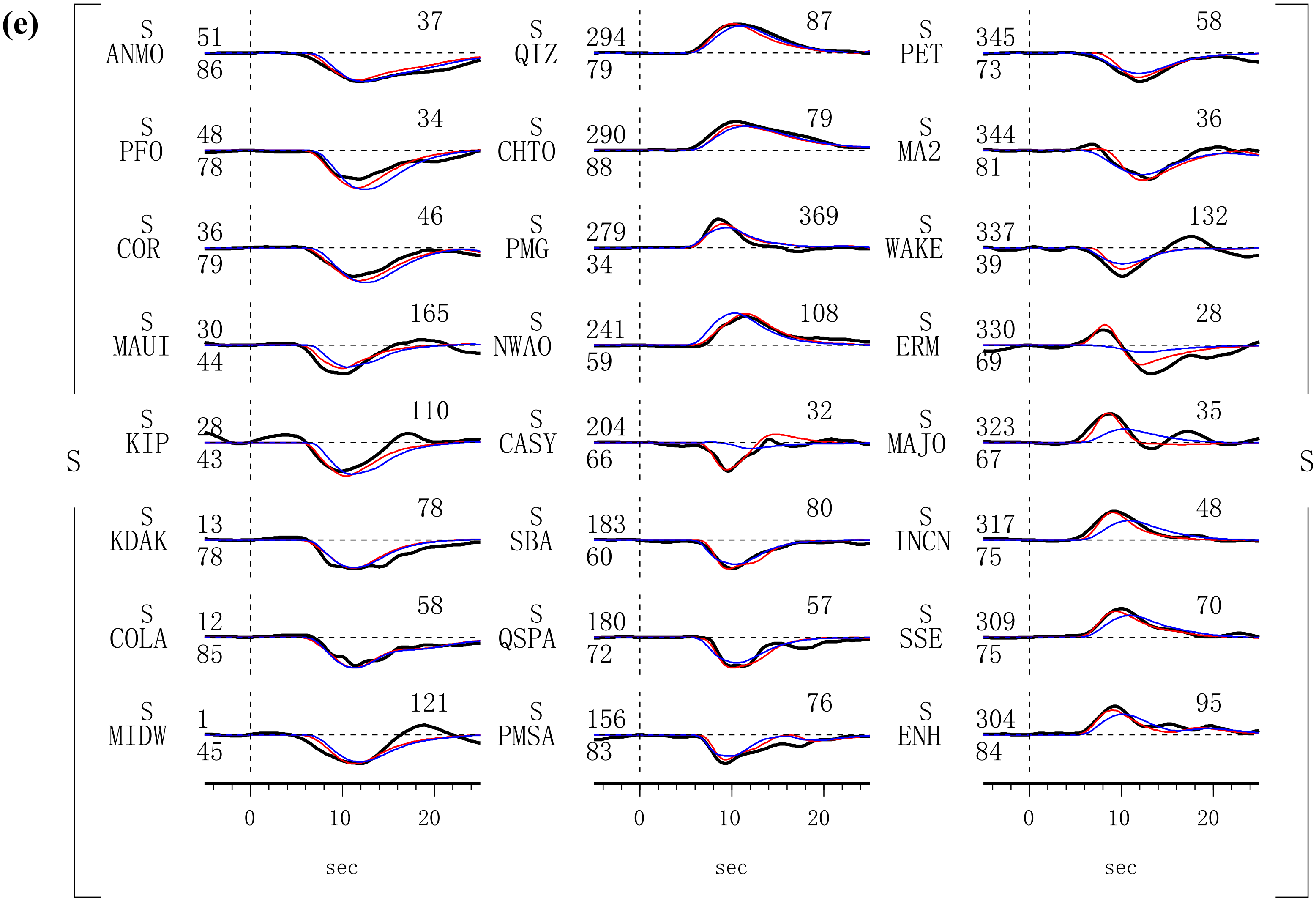
(e)
S
S ANMO 51 86 37
S QIZ 294 79 87
S PET 345 73 58
S PFO 48 78 34
S CHTO 290 88 79
S MA2 344 81 36
S COR 36 79 46
S PMG 279 34 369
S WAKE 337 39 132
S MAUI 30 44 165
S NWAO 241 59 108
S ERM 330 69 28
S KIP 28 43 110
S CASY 204 66 32
S MAJO 323 67 35
S KDAK 13 78 78
S SBA 183 60 80
S INCN 317 75 48
S COLA 12 85 58
S QSPA 180 72 57
S SSE 309 75 70
S MIDW 1 45 121
S PMSA 156 83 76
S ENH 304 84 95
0 10 20
sec

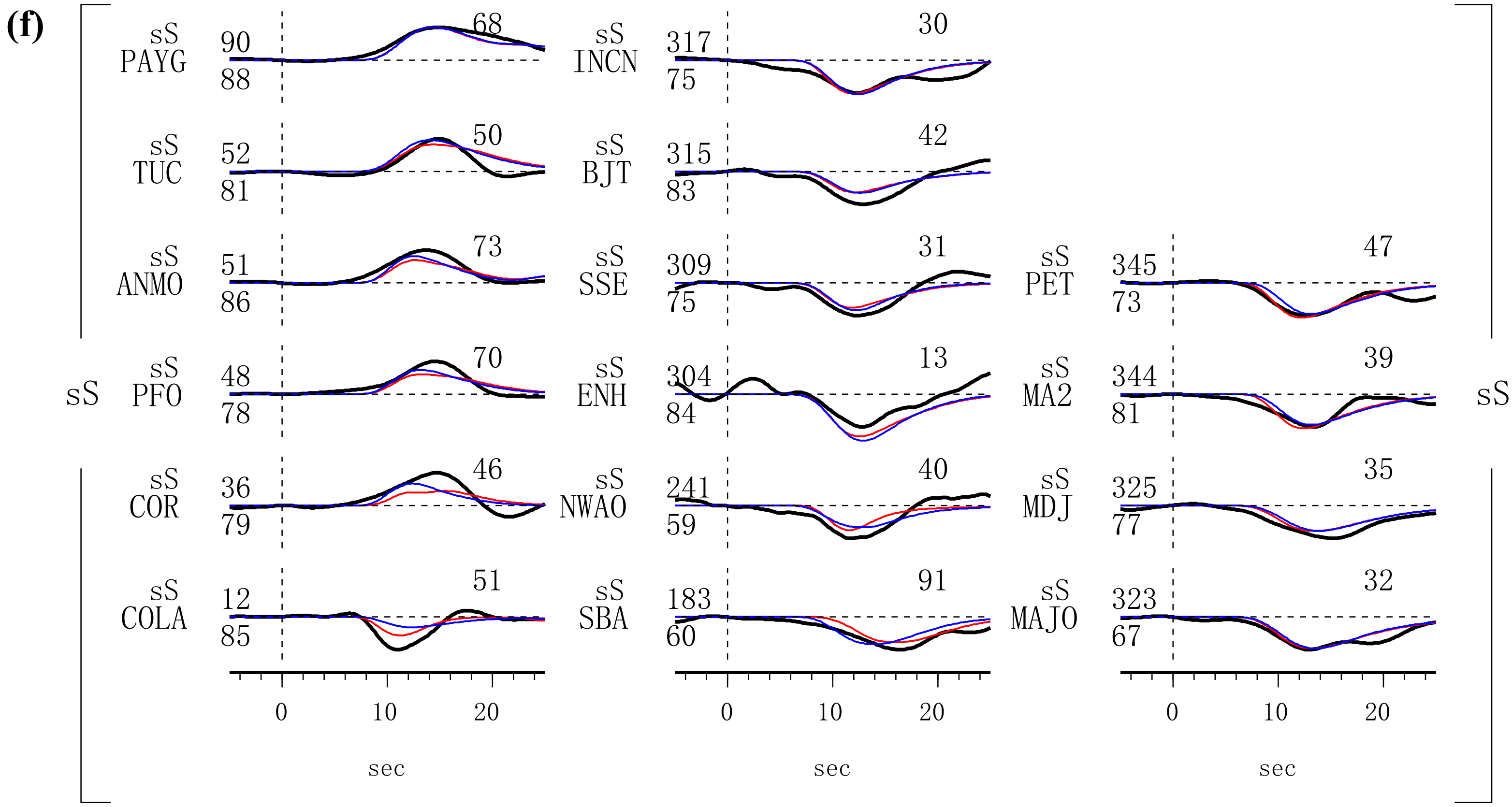
(f)
sS
PAYG 90 88 68
INCN 317 75 30
TUC 52 81 50
BJT 315 83 42
ANMO 51 86 73
SSE 309 75 31
PET 345 73 47
PFO 48 78 70
ENH 304 84 13
MA2 344 81 39
COR 36 79 46
NWAO 241 59 40
MDJ 325 77 35
COLA 12 85 51
SBA 183 60 91
MAJO 323 67 32
0
10
20
sec

E17. The 25 Jul 2004 Mw 7.3 earthquake

Earthquake E17 occurred 581 km beneath Java Sea (Table S4-0). The seismograms constitute good azimuth coverage with 35 P, 16 pP, 27 S and 18 sS wave data (Fig. S4-17a). The seismic energy can be modeled by four sub-events (Table S4-17, Fig. S4-17b), however, the fourth sub-event cannot be well resolved, since it can be clearly observed between the azimuth of 100˚ and 180˚ in P wave data only (Fig. S4-17c). The first three sub-events propagated to the south, the second and the third is to the southeast, and the fourth is geographically between the first and second but with a greater depth. Radiation patterns of the seismic data cannot be modeled on a plane.

Table S4-17. Source parameters of inferred sub-events of E17

Sub-event	dt (s)	dn (km)	de (km)	dz (km)	duration (s)	Mw	strike (°)	dip (°)	slip (°)
1	1.7	-8.2	-0.4	3.9	3.0	6.8	329.4	55.7	293.7
2	5.2	-20.5	19.2	14.1	2.0	6.7	317.9	49.1	304.0
3	7.9	-18.3	26.8	18.7	3.0	7.1	342.3	60.3	304.6
4	16.0	-15.2	8.9	35.7	3.0	6.4	388.5	91.3	253.7

(Fig. S4-17)

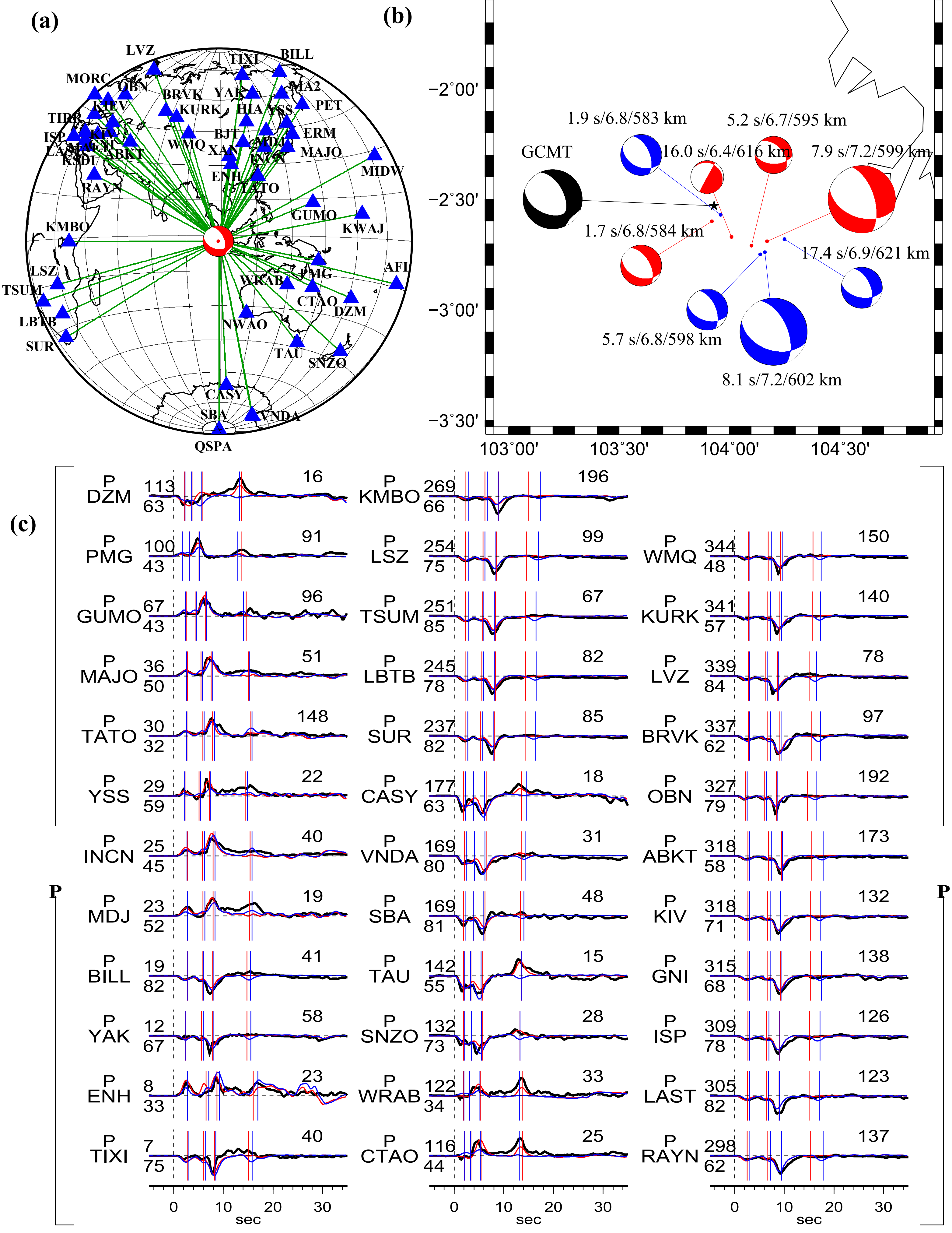
(a)
LVZ
TIXI
BILL
MORC
OBN
BRVK
YAK
MA2
KIEV
KURK
HIA
YSS
PET
TIRR
ISP
BJT
ERM
WMQ
XAN
MDJ
MAJO
LAST
GNI
KSDI
ABKT
INCN
ENH
MIDW
RAYN
TATO
GUMO
KMBO
KWAJ
LSZ
PMG
AFI
TSUM
WRAB
CTAO
DZM
LBTB
NWAO
SUR
TAU
SNZO
CASY
SBA
VNDA
QSPA
(b)
GCMT
1.9 s/6.8/583 km
5.2 s/6.7/595 km
16.0 s/6.4/616 km
7.9 s/7.2/599 km
1.7 s/6.8/584 km
17.4 s/6.9/621 km
5.7 s/6.8/598 km
8.1 s/7.2/602 km
−2˚00'
−2˚30'
−3˚00'
−3˚30'
103˚00'
103˚30'
104˚00'
104˚30'
(c)
P DZM 113 63 16
P PMG 100 43 91
P GUMO 67 43 96
P MAJO 36 50 51
P TATO 30 32 148
P YSS 29 59 22
P INCN 25 45 40
P MDJ 23 52 19
P BILL 19 82 41
P YAK 12 67 58
P ENH 8 33 23
P TIXI 7 75 40
P KMBO 269 66 196
P LSZ 254 75 99
P TSUM 251 85 67
P LBTB 245 78 82
P SUR 237 82 85
P CASY 177 63 18
P VNDA 169 80 31
P SBA 169 81 48
P TAU 142 55 15
P SNZO 132 73 28
P WRAB 122 34 33
P CTAO 116 44 25
P WMQ 344 48 150
P KURK 341 57 140
P LVZ 339 84 78
P BRVK 337 62 97
P OBN 327 79 192
P ABKT 318 58 173
P KIV 318 71 132
P GNI 315 68 138
P ISP 309 78 126
P LAST 305 82 123
P RAYN 298 62 137
P
P
0
10
20
30
sec

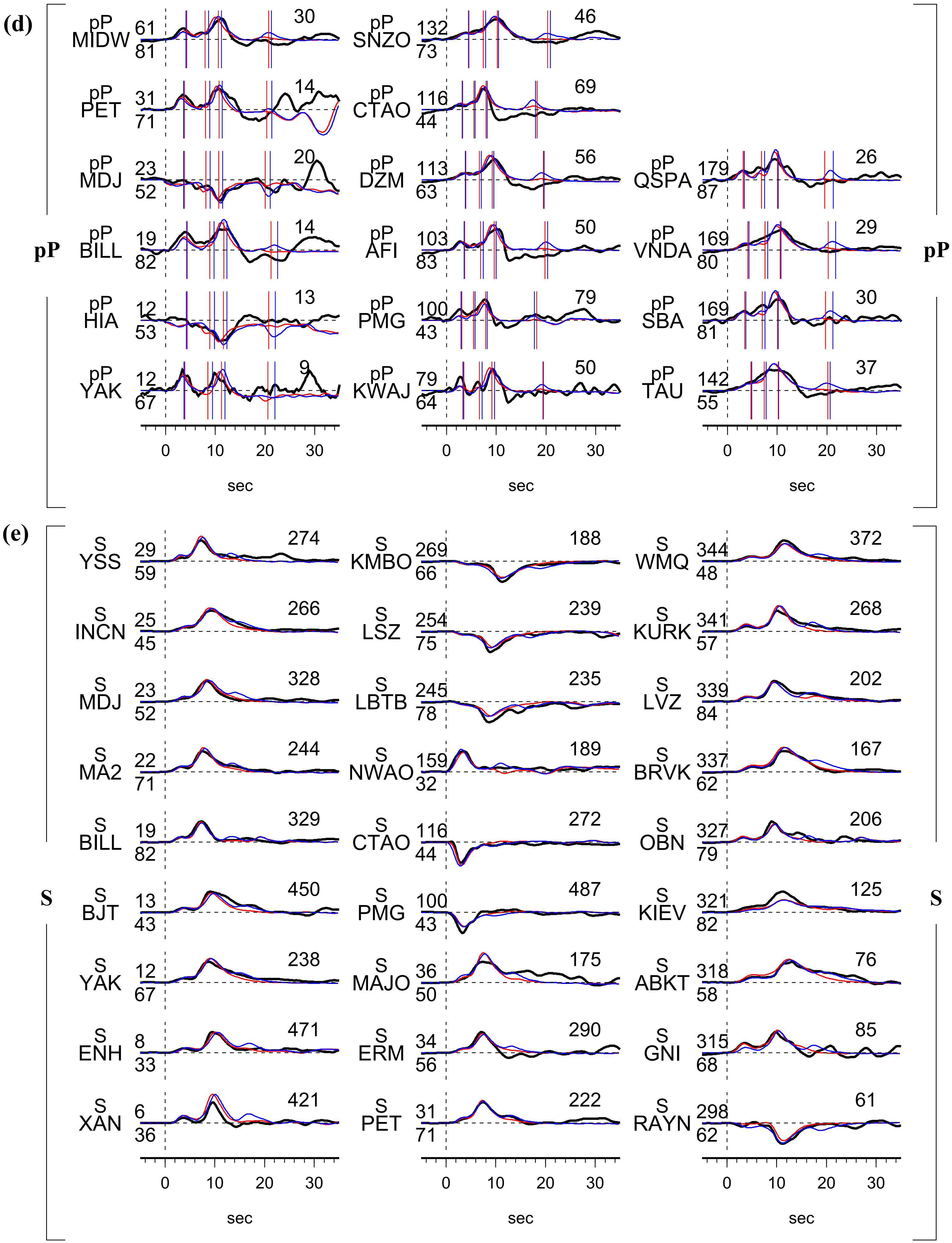
(d)
pP
pP MIDW 61 81 30
pP SNZO 132 73 46
pP PET 31 71 14
pP CTAO 116 44 69
pP MDJ 23 52 20
pP DZM 113 63 56
pP QSPA 179 87 26
pP BILL 19 82 14
pP AFI 103 83 50
pP VNDA 169 80 29
pP HIA 12 53 13
pP PMG 100 43 79
pP SBA 169 81 30
pP YAK 12 67 9
pP KWAJ 79 64 50
pP TAU 142 55 37
0
10
20
30
sec
(e)
S
S
S YSS 29 59 274
S KMBO 269 66 188
S WMQ 344 48 372
S INCN 25 45 266
S LSZ 254 75 239
S KURK 341 57 268
S MDJ 23 52 328
S LBTB 245 78 235
S LVZ 339 84 202
S MA2 22 71 244
S NWAO 159 32 189
S BRVK 337 62 167
S BILL 19 82 329
S CTAO 116 44 272
S OBN 327 79 206
S BJT 13 43 450
S PMG 100 43 487
S KIEV 321 82 125
S YAK 12 67 238
S MAJO 36 50 175
S ABKT 318 58 76
S ENH 8 33 471
S ERM 34 56 290
S GNI 315 68 85
S XAN 6 36 421
S PET 31 71 222
S RAYN 298 62 61
0
10
20
30
sec

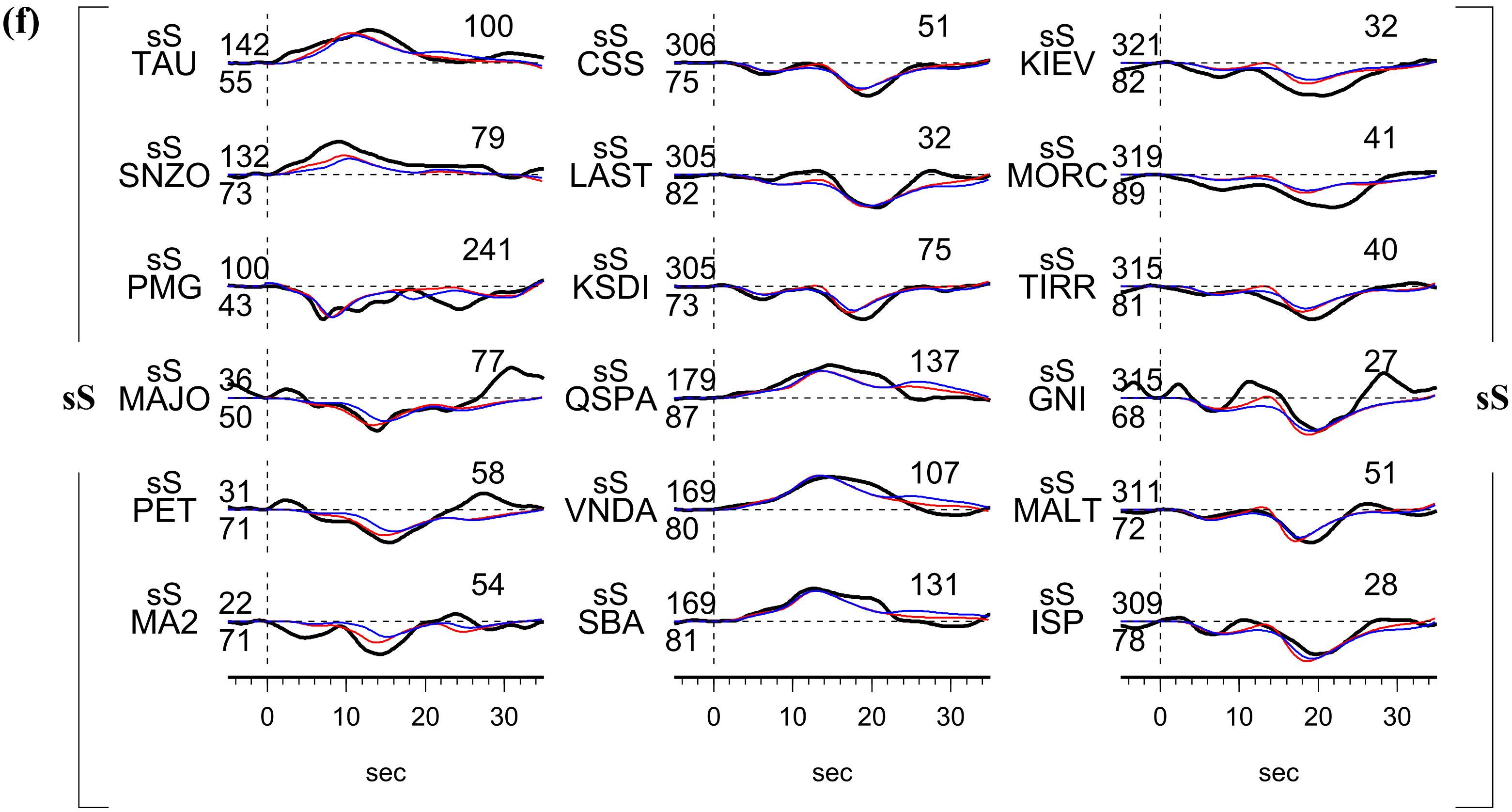
(f)
sS
sS
sS TAU 142 55 100
sS CSS 306 75 51
sS KIEV 321 82 32
sS SNZO 132 73 79
sS LAST 305 82 32
sS MORC 319 89 41
sS PMG 100 43 241
sS KSDI 305 73 75
sS TIRR 315 81 40
sS MAJO 36 50 77
sS QSPA 179 87 137
sS GNI 315 68 27
sS PET 31 71 58
sS VNDA 169 80 107
sS MALT 311 72 51
sS MA2 22 71 54
sS SBA 169 81 131
sS ISP 309 78 28
0
10
20
30
sec
0
10
20
30
sec
0
10
20
30
sec

E18. The 05 Feb 2005 Mw 7.1 earthquake

Earthquake E18 occurred 536 km beneath Philippine region (Table S4-0). The seismograms constitute good azimuth coverage with 31 P, 17 pP, 31 S and 18 sS wave data (Fig. S4-18a). The seismic energy can be modeled by three sub-events with a horizontal extension of 15 km (Fig. S4-18b). The strongest first sub-event is to the southeast, the second and third sub-event propagated to the northeast. Since the sub-events are quite close to each other, they overlap each other and seem to be one pulse in S and sS data (Figs. S4-18c – S4-18f). The GCMT sub-horizontal plane models the seismic data as well as the best-fitting sub-event model.

Table S4-18. Source parameters of inferred sub-events of E18

Sub-event	dt (s)	dn (km)	de (km)	dz (km)	duration (s)	Mw	strike (°)	dip (°)	slip (°)
1	4.2	-6.6	6.1	-1.7	3.8	6.9	163.2	14.8	252.3
2	7.2	1.9	6.3	-0.2	3.8	6.7	159.1	13.8	245.4
3	10.1	8.2	12.4	-3.4	3.0	6.5	162.1	14.3	247.9

(Fig. S4-18)

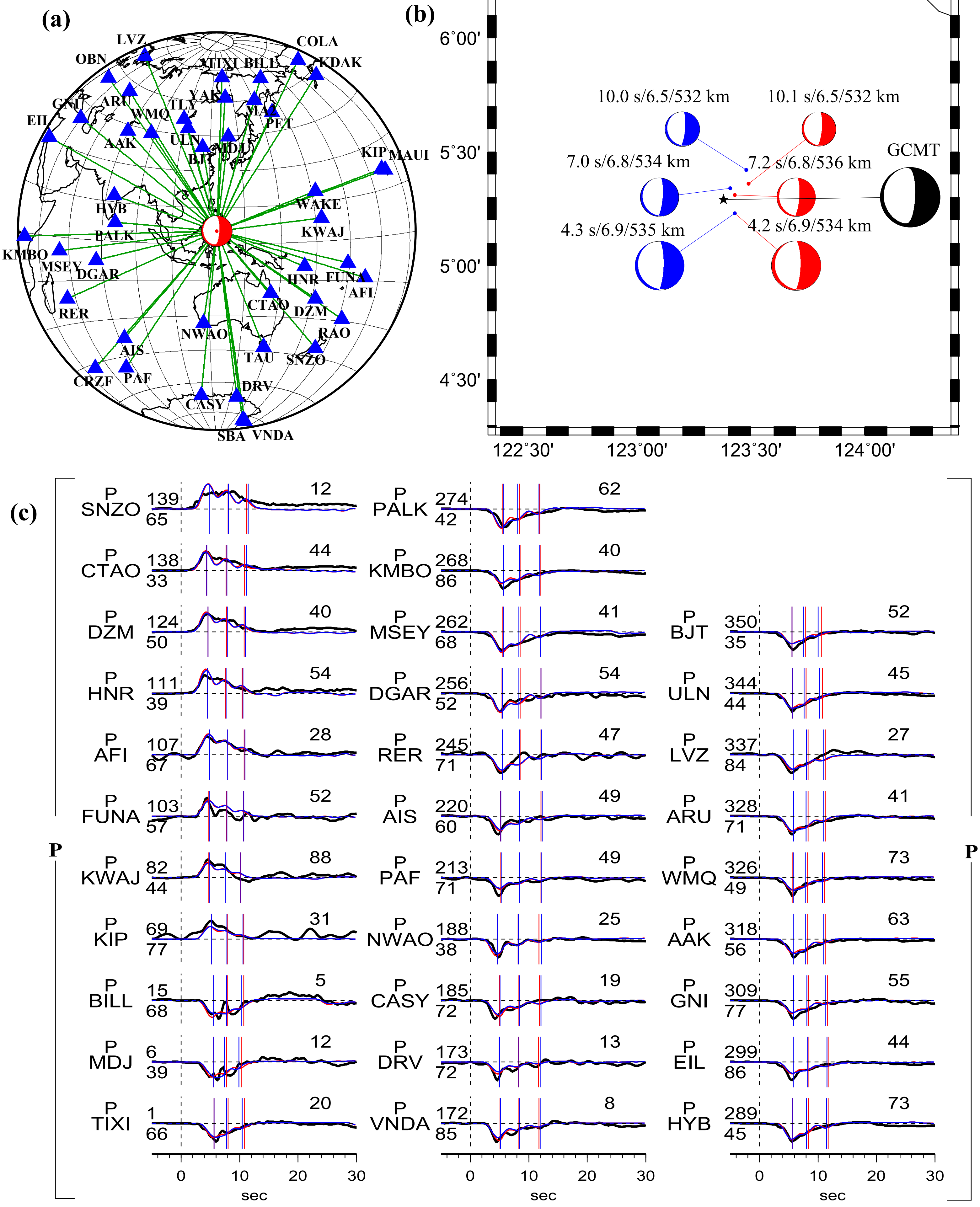
(a)
LVZ
COLA
OBN
TIXI
BILL
KDAK
GNI
ARU
YAK
TLY
MA2
PET
EIL
WMQ
AAK
ULN
MDJ
BJT
KIP
MAUI
HYB
WAKE
PALK
KWAJ
KMBO
MSEY
DGAR
HNR
FUNA
AFI
RER
CTAO
DZM
NWAO
RAO
AIS
TAU
SNZO
CRZF
PAF
DRV
CASY
SBA
VNDA
(b)
6˚00'
5˚30'
5˚00'
4˚30'
122˚30'
123˚00'
123˚30'
124˚00'
10.0 s/6.5/532 km
10.1 s/6.5/532 km
7.0 s/6.8/534 km
7.2 s/6.8/536 km
GCMT
4.3 s/6.9/535 km
4.2 s/6.9/534 km
(c)
P SNZO 139 65 12
P CTAO 138 33 44
P DZM 124 50 40
P HNR 111 39 54
P AFI 107 67 28
P FUNA 103 57 52
P KWAJ 82 44 88
P KIP 69 77 31
P BILL 15 68 5
P MDJ 6 39 12
P TIXI 1 66 20
P PALK 274 42 62
P KMBO 268 86 40
P MSEY 262 68 41
P DGAR 256 52 54
P RER 245 71 47
P AIS 220 60 49
P PAF 213 71 49
P NWAO 188 38 25
P CASY 185 72 19
P DRV 173 72 13
P VNDA 172 85 8
P BJT 350 35 52
P ULN 344 44 45
P LVZ 337 84 27
P ARU 328 71 41
P WMQ 326 49 73
P AAK 318 56 63
P GNI 309 77 55
P EIL 299 86 44
P HYB 289 45 73
P
P
0
10
20
30
sec

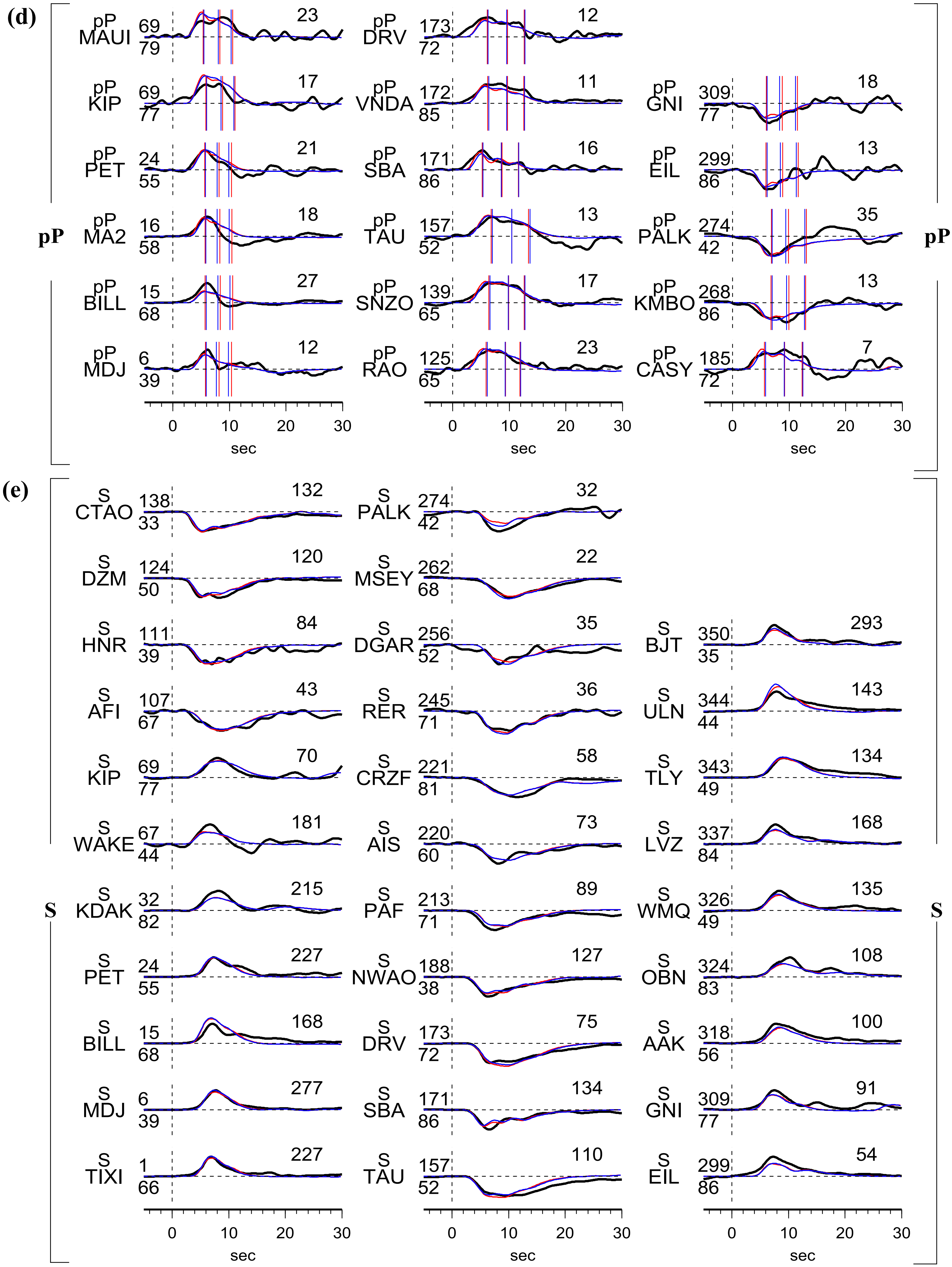
(d)
pP
pP MAUI 69 79 23
pP KIP 69 77 17
pP PET 24 55 21
pP MA2 16 58 18
pP BILL 15 68 27
pP MDJ 6 39 12
pP DRV 173 72 12
pP VNDA 172 85 11
pP SBA 171 86 16
pP TAU 157 52 13
pP SNZO 139 65 17
pP RAO 125 65 23
pP GNI 309 77 18
pP EIL 299 86 13
pP PALK 274 42 35
pP KMBO 268 86 13
pP CASY 185 72 7
0
10
20
30
sec
(e)
S
S CTAO 138 33 132
S DZM 124 50 120
S HNR 111 39 84
S AFI 107 67 43
S KIP 69 77 70
S WAKE 67 44 181
S KDAK 32 82 215
S PET 24 55 227
S BILL 15 68 168
S MDJ 6 39 277
S TIXI 1 66 227
S PALK 274 42 32
S MSEY 262 68 22
S DGAR 256 52 35
S RER 245 71 36
S CRZF 221 81 58
S AIS 220 60 73
S PAF 213 71 89
S NWAO 188 38 127
S DRV 173 72 75
S SBA 171 86 134
S TAU 157 52 110
S BJT 350 35 293
S ULN 344 44 143
S TLY 343 49 134
S LVZ 337 84 168
S WMQ 326 49 135
S OBN 324 83 108
S AAK 318 56 100
S GNI 309 77 91
S EIL 299 86 54
0
10
20
30
sec

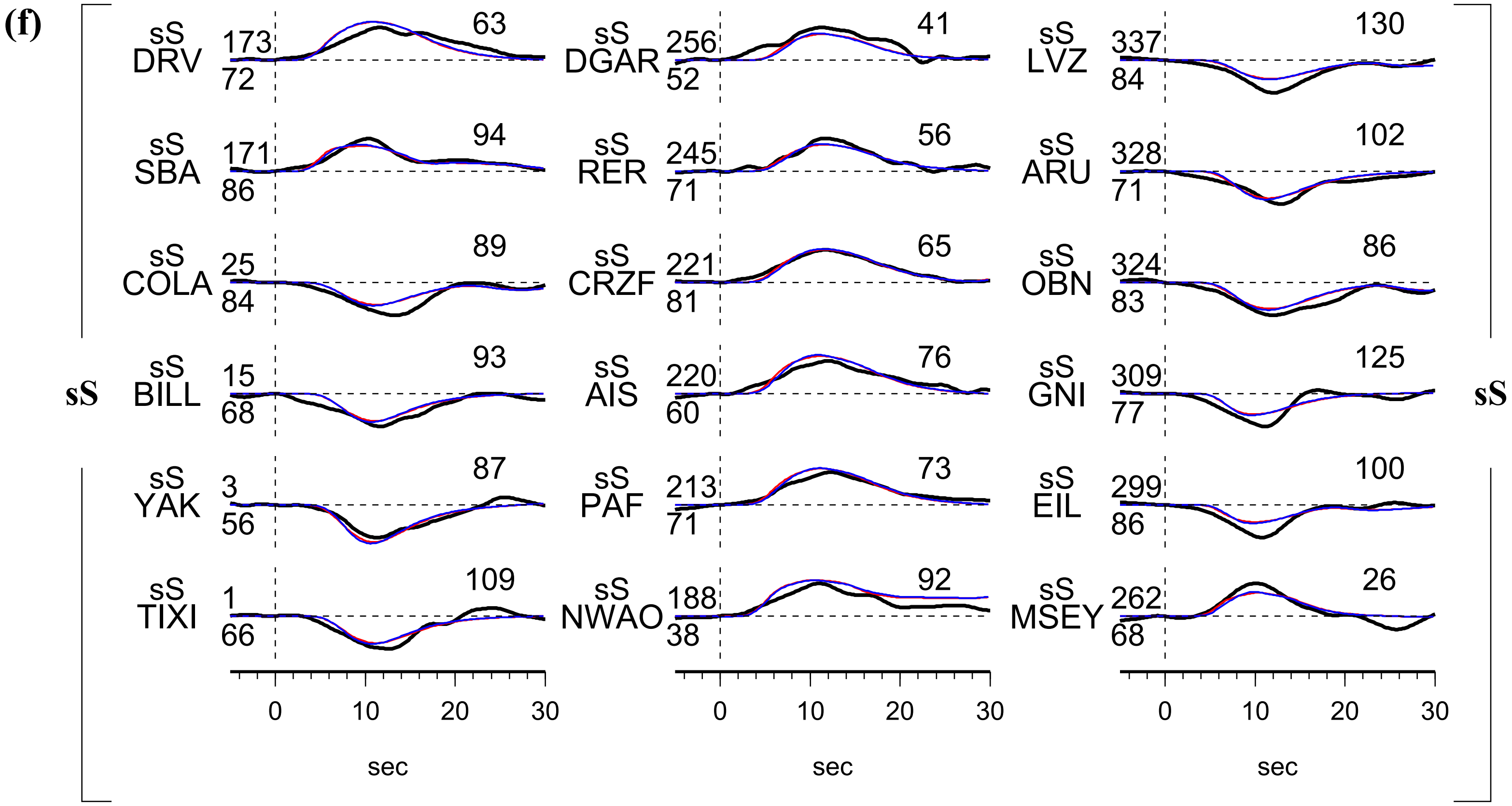
(f)
sS
sS
sS DRV 173 72 63
sS DGAR 256 52 41
sS LVZ 337 84 130
sS SBA 171 86 94
sS RER 245 71 56
sS ARU 328 71 102
sS COLA 25 84 89
sS CRZF 221 81 65
sS OBN 324 83 86
sS BILL 15 68 93
sS AIS 220 60 76
sS GNI 309 77 125
sS YAK 3 56 87
sS PAF 213 71 73
sS EIL 299 86 100
sS TIXI 1 66 109
sS NWAO 188 38 92
sS MSEY 262 68 26
0
10
20
30
sec
0
10
20
30
sec
0
10
20
30
sec

E19. The 02 Jan 2006 Mw 7.2 earthquake

Earthquake E19 occurred 593 km beneath Tonga region (Table S4-0). We infer the source process using 32 P, 15 pP, 24 S and 15 sS (Fig. S4-19a). The best-fitting source model is presented in Table S4-19 and Fig. S4-19b, and the synthetics fitting comparison is in Figs. S4-19c – S4-19f. The analysis is presented in the main text.

Table S4-19. Source parameters of inferred sub-events of E19

Sub-event	dt (s)	dn (km)	de (km)	dz (km)	duration (s)	Mw	strike (°)	dip (°)	slip (°)
1	2.9	2.9	9.8	-2.8	3.4	7.0	46.1	71.6	261.9
2	6.0	12.1	12.8	-5.0	3.6	6.8	50.7	78.8	257.8
3	7.6	19.9	20.7	-28.8	5.8	6.9	78.1	59.9	200.4

(Fig. S4-19)

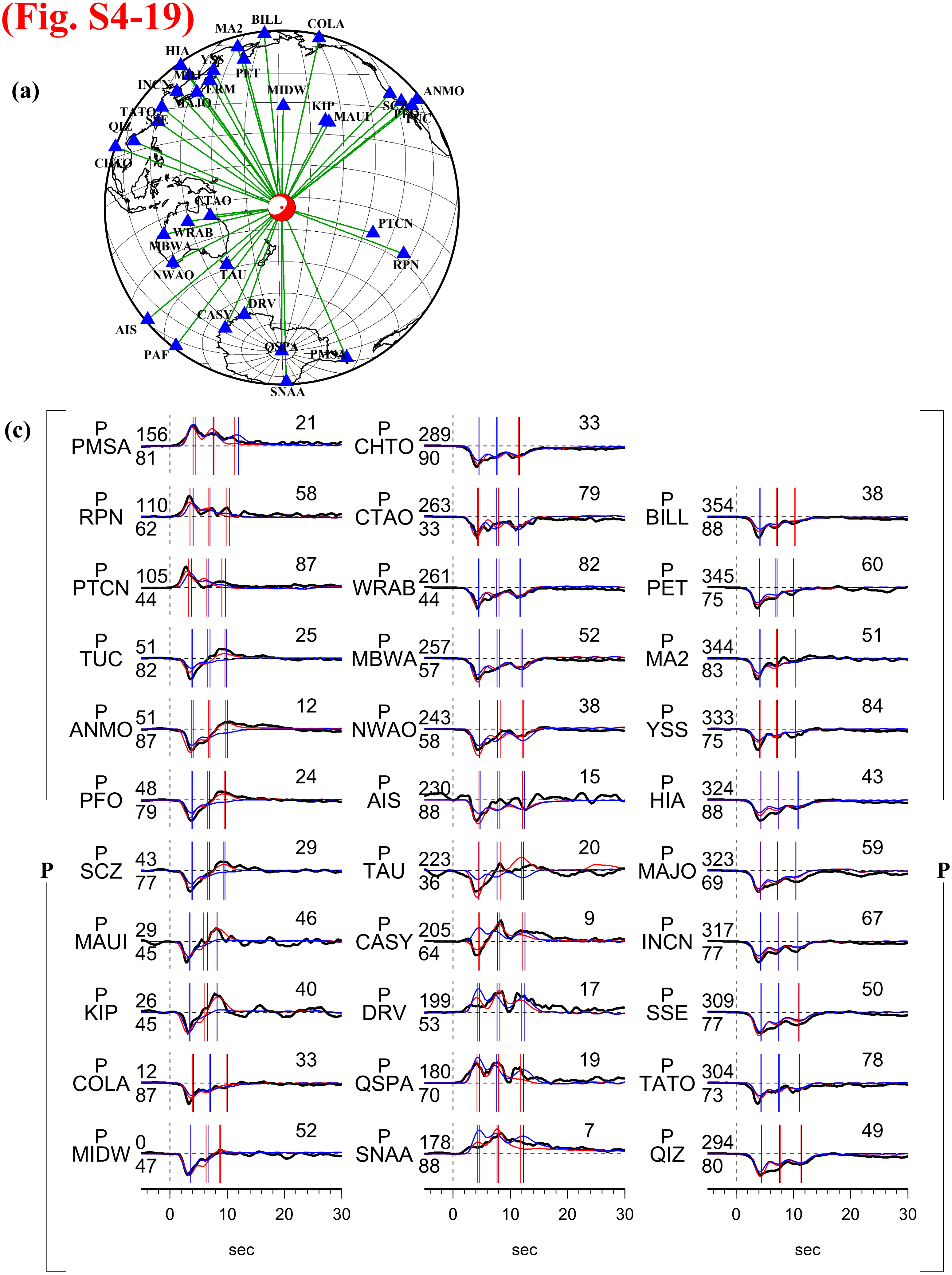
(a)
MA2
BILL
COLA
HIA
YSS
MDJ
PET
INCN
ERM
MAJO
MIDW
KIP
MAUI
SCZ
ANMO
PFO
TUC
TATO
SSE
QIZ
CHTO
CTAO
WRAB
MBWA
NWAO
TAU
PTCN
RPN
DRV
CASY
AIS
PAF
QSPA
PMSA
SNAA
(c)
P PMSA 156 81 21
P RPN 110 62 58
P PTCN 105 44 87
P TUC 51 82 25
P ANMO 51 87 12
P PFO 48 79 24
P SCZ 43 77 29
P MAUI 29 45 46
P KIP 26 45 40
P COLA 12 87 33
P MIDW 0 47 52
P CHTO 289 90 33
P CTAO 263 33 79
P WRAB 261 44 82
P MBWA 257 57 52
P NWAO 243 58 38
P AIS 230 88 15
P TAU 223 36 20
P CASY 205 64 9
P DRV 199 53 17
P QSPA 180 70 19
P SNAA 178 88 7
P BILL 354 88 38
P PET 345 75 60
P MA2 344 83 51
P YSS 333 75 84
P HIA 324 88 43
P MAJO 323 69 59
P INCN 317 77 67
P SSE 309 77 50
P TATO 304 73 78
P QIZ 294 80 49
0
10
20
30
sec
P
P

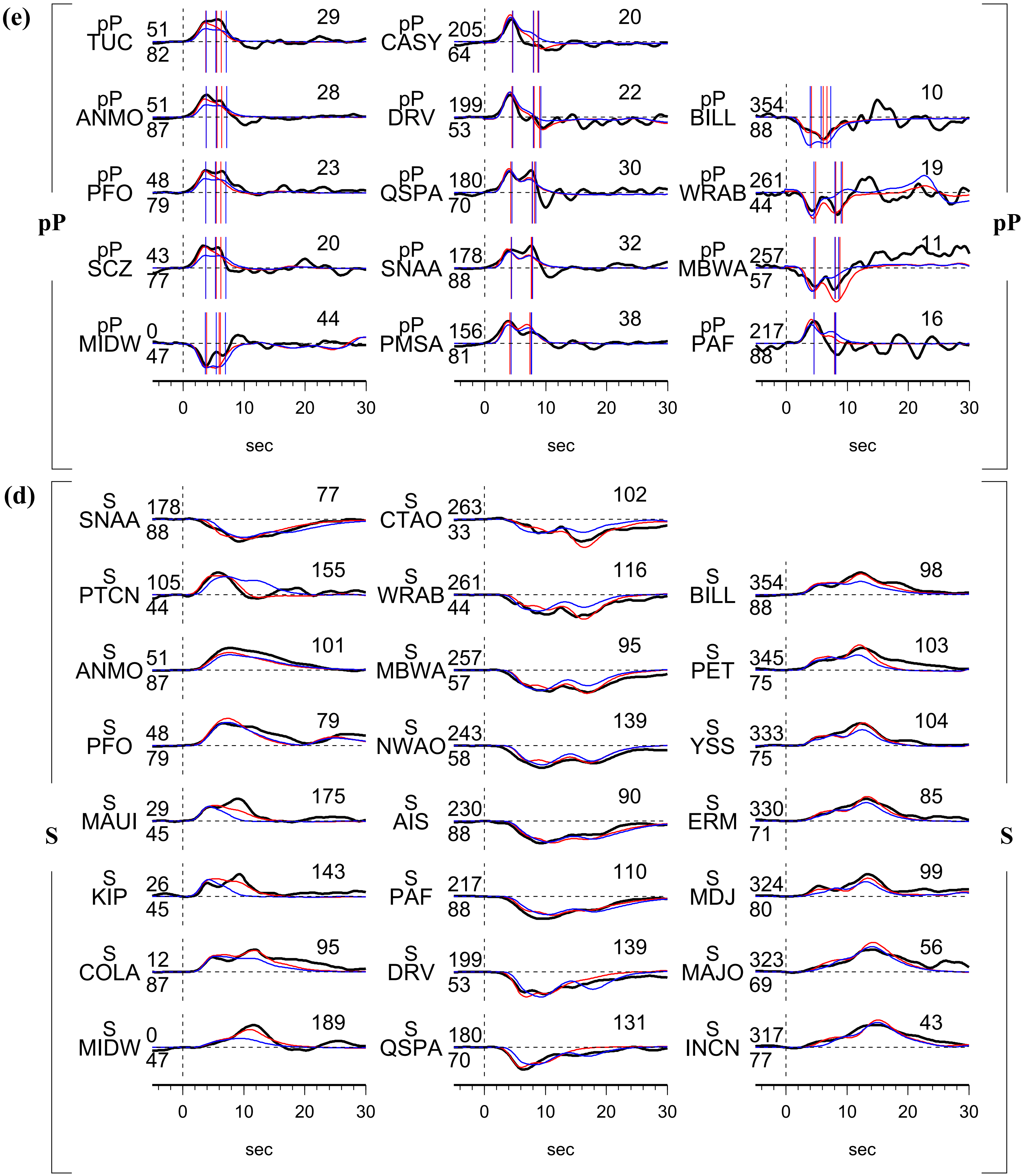
(e)
pP
pP TUC 51 82 29
pP CASY 205 64 20
pP ANMO 51 87 28
pP DRV 199 53 22
pP BILL 354 88 10
pP PFO 48 79 23
pP QSPA 180 70 30
pP WRAB 261 44 19
pP SCZ 43 77 20
pP SNAA 178 88 32
pP MBWA 257 57 11
pP MIDW 0 47 44
pP PMSA 156 81 38
pP PAF 217 88 16
0 10 20 30
sec
(d)
S
S SNAA 178 88 77
S CTAO 263 33 102
S PTCN 105 44 155
S WRAB 261 44 116
S BILL 354 88 98
S ANMO 51 87 101
S MBWA 257 57 95
S PET 345 75 103
S PFO 48 79 79
S NWAO 243 58 139
S YSS 333 75 104
S MAUI 29 45 175
S AIS 230 88 90
S ERM 330 71 85
S KIP 26 45 143
S PAF 217 88 110
S MDJ 324 80 99
S COLA 12 87 95
S DRV 199 53 139
S MAJO 323 69 56
S MIDW 0 47 189
S QSPA 180 70 131
S INCN 317 77 43
0 10 20 30
sec

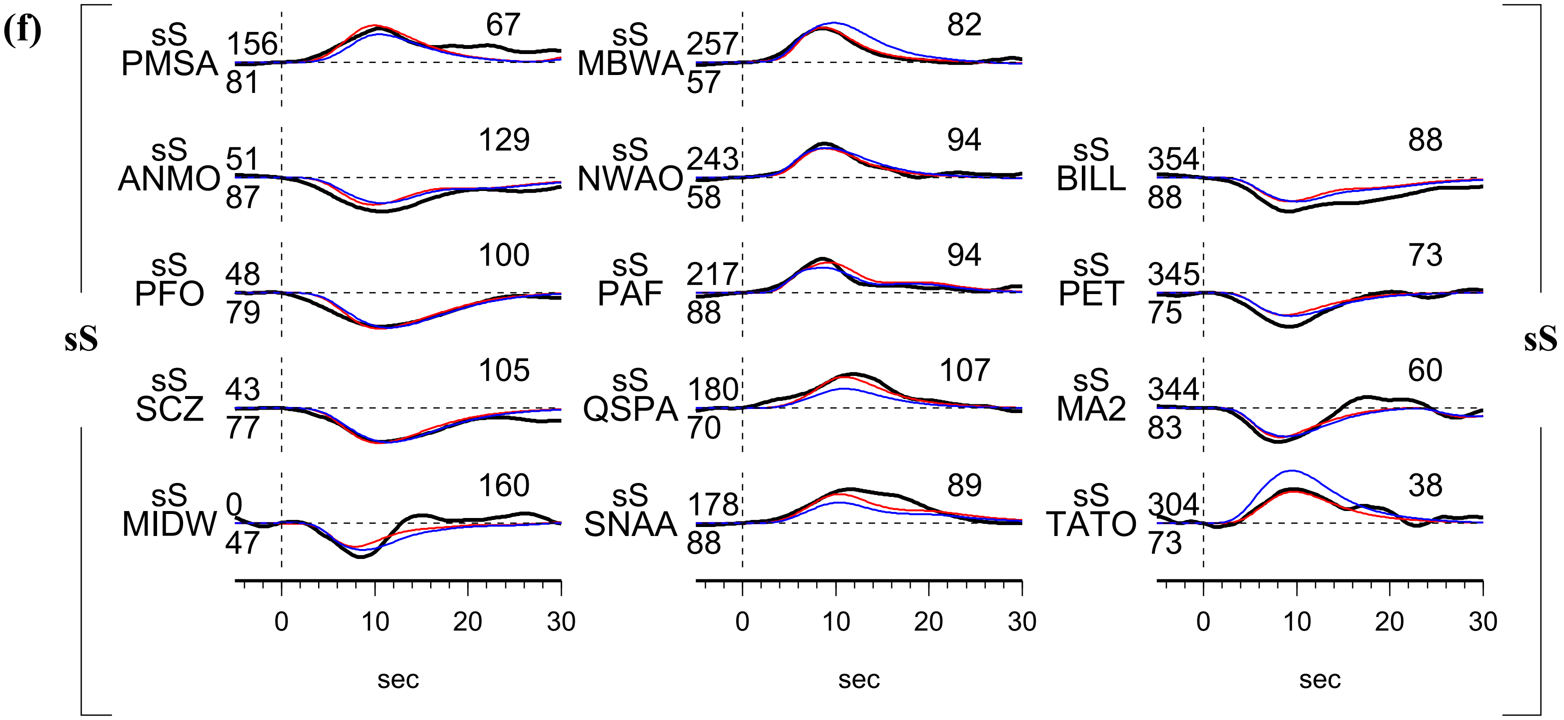
(f)
sS
sS
sS PMSA 156 81 67
sS MBWA 257 57 82
sS ANMO 51 87 129
sS NWAO 243 58 94
sS BILL 354 88 88
sS PFO 48 79 100
sS PAF 217 88 94
sS PET 345 75 73
sS SCZ 43 77 105
sS QSPA 180 70 107
sS MA2 344 83 60
sS MIDW 0 47 160
sS SNAA 178 88 89
sS TATO 304 73 38
0
10
20
30
sec

E20. The 05 Jul 2008 Mw 7.7 earthquake

Earthquake E20 occurred 632 km beneath Sea of Okhotsk (Table S4-0). The seismograms constitute good azimuth coverage with 36 P, 18 pP, 21 S and 19 sS wave data (Fig. S4-20a). The earthquake energy can be divided into two portions. The portion of the first ten seconds can be modeled by four sub-events, which can be modeled reasonably well, while the second portion with smaller amplitude is not perfectly modeled (Figs. S4-20c – S4-20f). The second portion is ignored by the GCMT solution. The first four sub-events occurred in a small extension of ~ 12 km. The first three sub-events propagated to the north, and the fourth sub-event is to the south. The fifth sub-event is 3.6 km to the east of and 7.8 km below the initiation point and the latter three sub-events propagate to further northeast at the depth range between 10 and 20 km (Table S4-20, Fig. S4-20b). Therefore, the first and second portion of data may occur in different depths. Moreover, the focal mechanisms do not prefer the planar model. It is also interesting to note that the ending sub-event is very close to the last sub-event of the 2013 Mw 8.3 Okhotsk deep earthquake, with totally different focal mechanisms (Chen et al, 2014).

Table S4-20. Source parameters of inferred sub-events of E20

Sub-event	dt (s)	dn (km)	de (km)	dz (km)	duration (s)	Mw	strike (°)	dip (°)	slip (°)
1	1.8	1.6	1.5	0.0	3.0	6.9	145.8	53.8	230.0
2	4.8	3.9	2.9	-3.0	3.0	7.2	147.7	50.7	236.6
3	7.2	8.1	8.0	-4.0	4.0	7.3	145.4	50.0	227.9
4	9.4	-9.9	-2.7	-3.2	4.0	7.2	163.7	40.1	236.6
5	12.8	3.6	0.0	-7.8	4.0	7.0	135.5	53.5	200.2
6	15.5	8.6	5.0	-10.8	4.0	6.9	155.0	31.7	198.1
7	18.8	30.4	17.8	-14.0	6.0	7.0	115.7	57.1	208.0
8	22.1	37.4	20.8	-16.0	6.0	7.0	140.5	41.7	197.2

(Fig. S4-20)

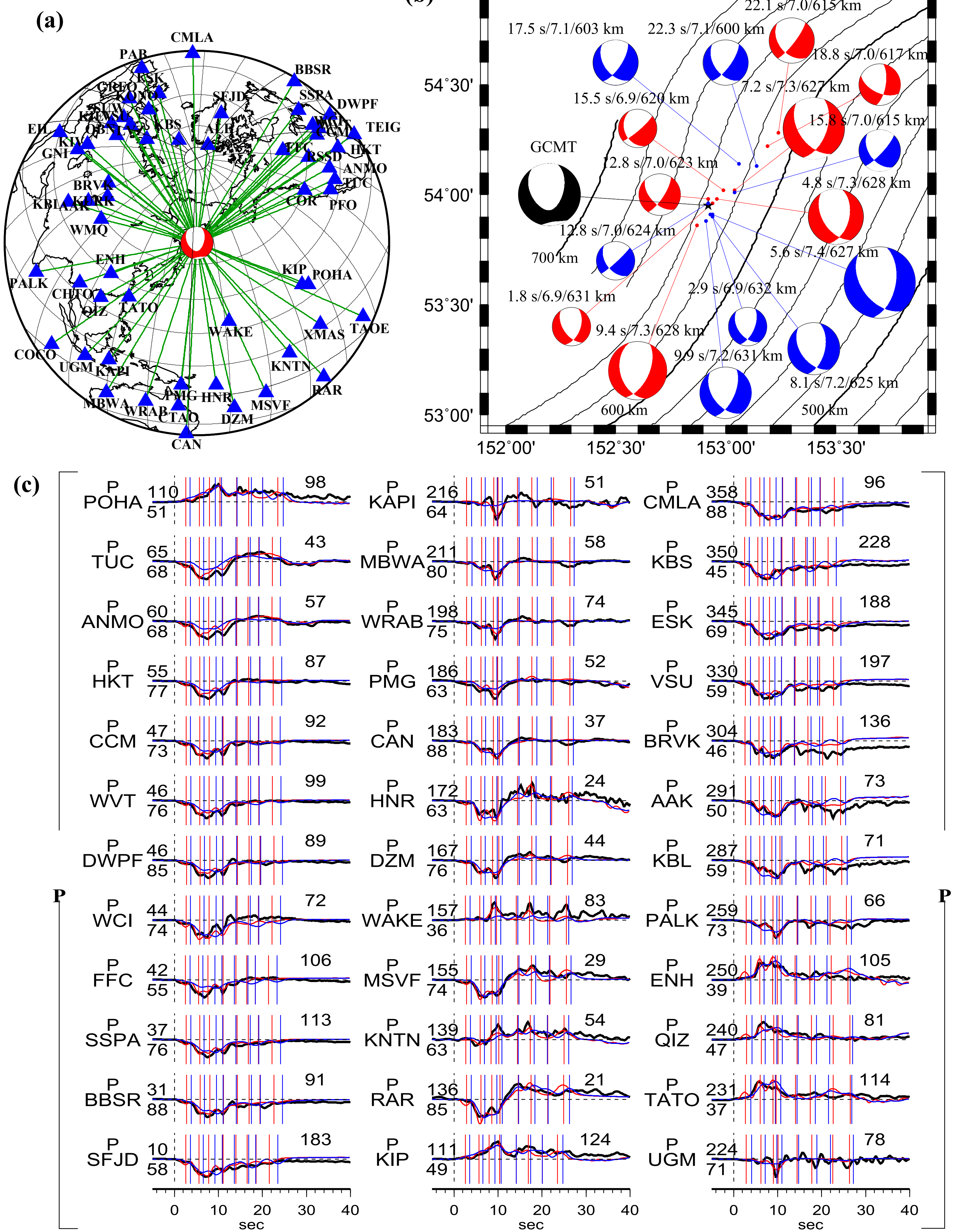
(a)
CMLA
PAB
ESK
GRFO
KONO
BBSR
SFJD
SSPA
DWPF
VSU
KIEV
OBN
KBS
ALE
WCI
TEIG
EIL
CCM
KIV
GNI
FFC
HKT
RSSD
ANMO
TUC
BRVK
KBL
AAK
COR
PFO
WMQ
ENH
KIP
POHA
PALK
CHTO
QIZ
TATO
TAOE
XMAS
WAKE
COCO
UGM
KAPI
KNTN
RAR
MBWA
PMG
HNR
MSVF
WRAB
CTAO
DZM
CAN
(b)
22.1 s/7.0/615 km
17.5 s/7.1/603 km
22.3 s/7.1/600 km
18.8 s/7.0/617 km
15.5 s/6.9/620 km
7.2 s/7.3/627 km
15.8 s/7.0/615 km
GCMT
12.8 s/7.0/623 km
4.8 s/7.3/628 km
12.8 s/7.0/624 km
700 km
5.6 s/7.4/627 km
1.8 s/6.9/631 km
2.9 s/6.9/632 km
9.4 s/7.3/628 km
9.9 s/7.2/631 km
8.1 s/7.2/625 km
600 km
500 km
54°30'
54°00'
53°30'
53°00'
152°00'
152°30'
153°00'
153°30'
(c)
P POHA 110 51 98
P TUC 65 68 43
P ANMO 60 68 57
P HKT 55 77 87
P CCM 47 73 92
P WVT 46 76 99
P DWPF 46 85 89
P WCI 44 74 72
P FFC 42 55 106
P SSPA 37 76 113
P BBSR 31 88 91
P SFJD 10 58 183
P KAPI 216 64 51
P MBWA 211 80 58
P WRAB 198 75 74
P PMG 186 63 52
P CAN 183 88 37
P HNR 172 63 24
P DZM 167 76 44
P WAKE 157 36 83
P MSVF 155 74 29
P KNTN 139 63 54
P RAR 136 85 21
P KIP 111 49 124
P CMLA 358 88 96
P KBS 350 45 228
P ESK 345 69 188
P VSU 330 59 197
P BRVK 304 46 136
P AAK 291 50 73
P KBL 287 59 71
P PALK 259 73 66
P ENH 250 39 105
P QIZ 240 47 81
P TATO 231 37 114
P UGM 224 71 78
P
P
0
10
20
30
40
sec

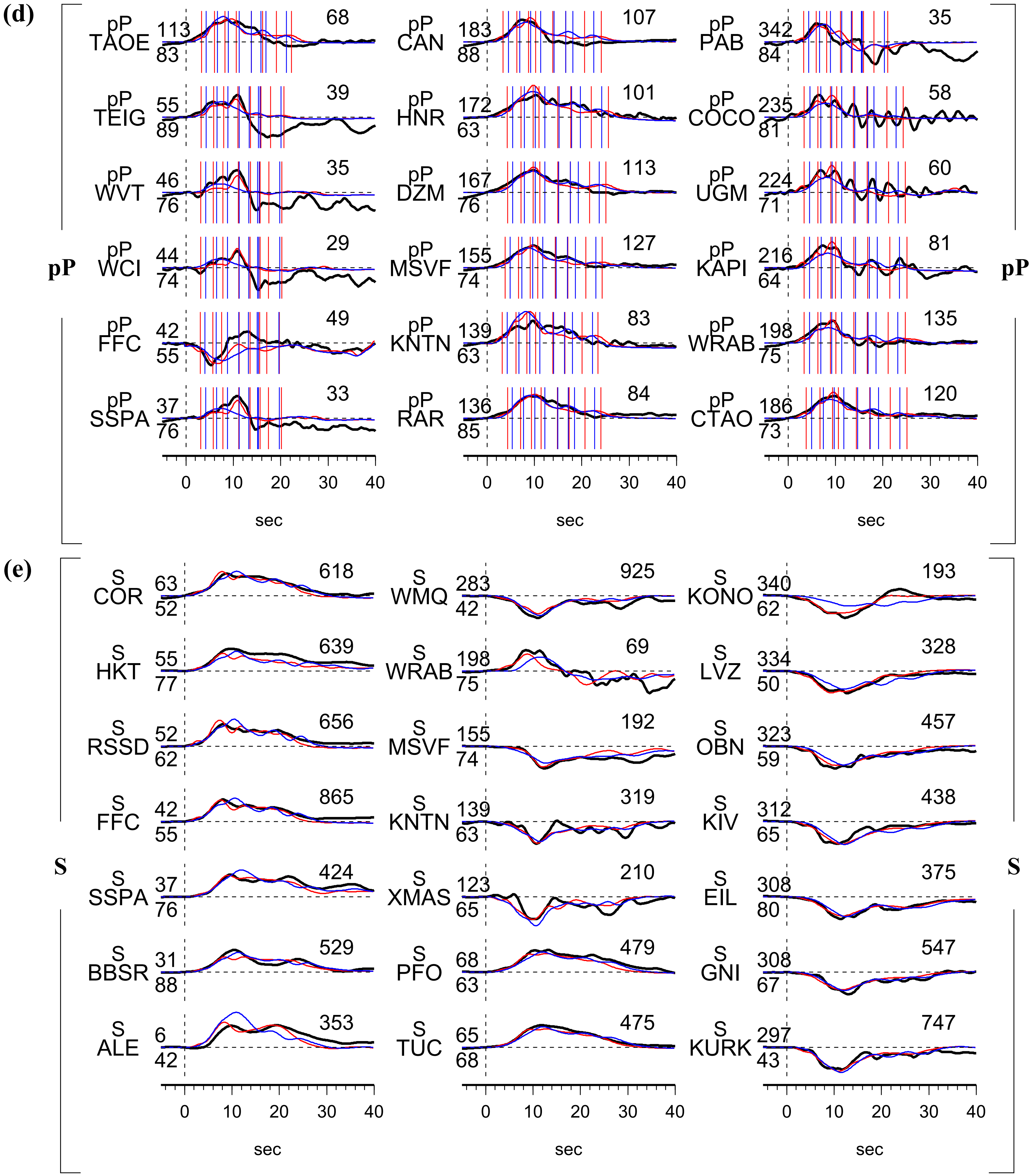
(d)
pP
pP TAOE 113 83 68
pP CAN 183 88 107
pP PAB 342 84 35
pP TEIG 55 89 39
pP HNR 172 63 101
pP COCO 235 81 58
pP WVT 46 76 35
pP DZM 167 76 113
pP UGM 224 71 60
pP WCI 44 74 29
pP MSVF 155 74 127
pP KAPI 216 64 81
pP FFC 42 55 49
pP KNTN 139 63 83
pP WRAB 198 75 135
pP SSPA 37 76 33
pP RAR 136 85 84
pP CTAO 186 73 120
0 10 20 30 40
sec
(e)
S
S COR 63 52 618
S WMQ 283 42 925
S KONO 340 62 193
S HKT 55 77 639
S WRAB 198 75 69
S LVZ 334 50 328
S RSSD 52 62 656
S MSVF 155 74 192
S OBN 323 59 457
S FFC 42 55 865
S KNTN 139 63 319
S KIV 312 65 438
S SSPA 37 76 424
S XMAS 123 65 210
S EIL 308 80 375
S BBSR 31 88 529
S PFO 68 63 479
S GNI 308 67 547
S ALE 6 42 353
S TUC 65 68 475
S KURK 297 43 747
0 10 20 30 40
sec

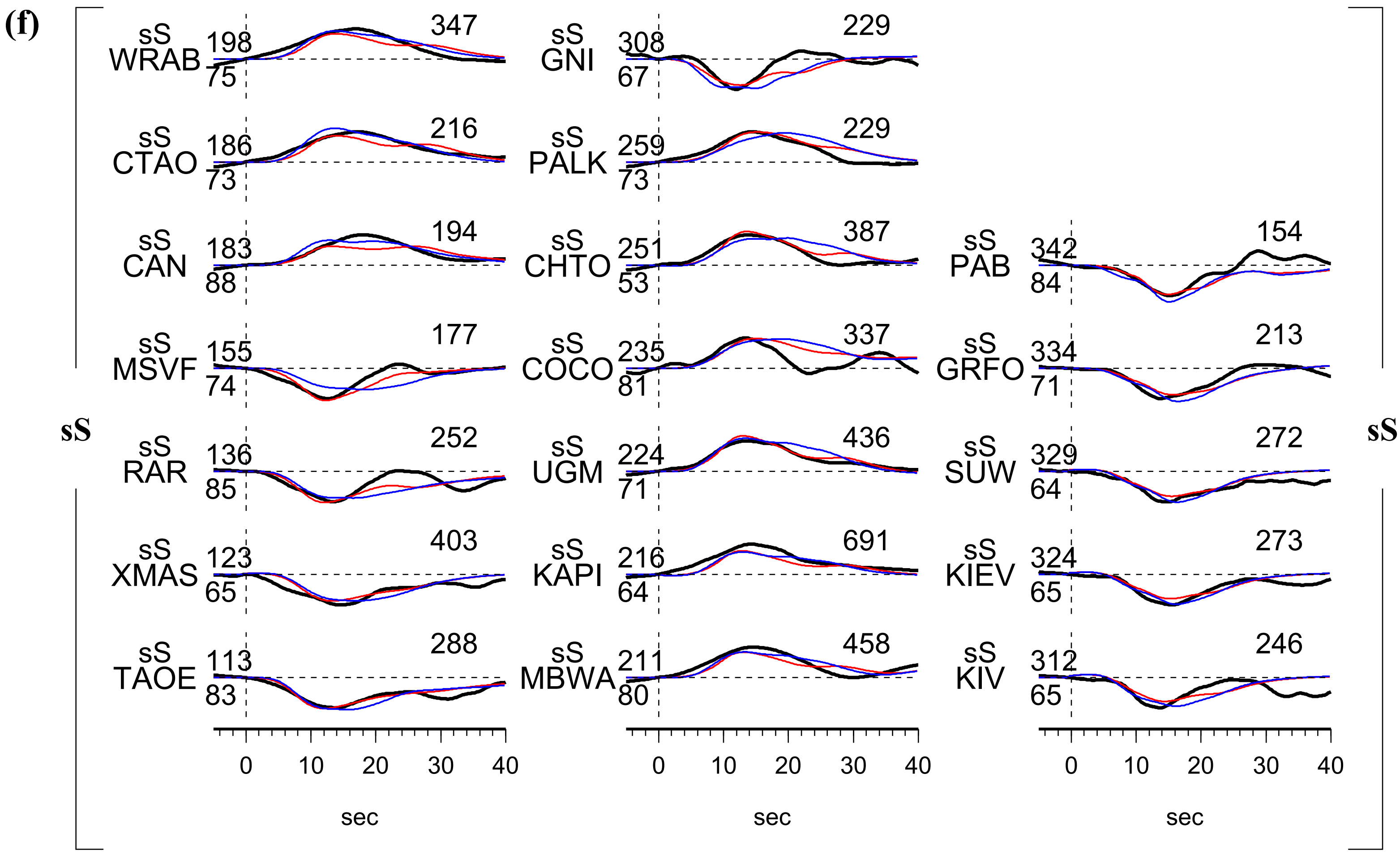
(f)
sS
sS
sS WRAB 198 75 347
sS GNI 308 67 229
sS CTAO 186 73 216
sS PALK 259 73 229
sS CAN 183 88 194
sS CHTO 251 53 387
sS PAB 342 84 154
sS MSVF 155 74 177
sS COCO 235 81 337
sS GRFO 334 71 213
sS RAR 136 85 252
sS UGM 224 71 436
sS SUW 329 64 272
sS XMAS 123 65 403
sS KAPI 216 64 691
sS KIEV 324 65 273
sS TAOE 113 83 288
sS MBWA 211 80 458
sS KIV 312 65 246
0
10
20
30
40
sec

E21. The 24 Nov 2008 Mw 7.3 earthquake

Earthquake E21 occurred 490 km beneath Sea of Okhotsk (Table S4-0). The seismograms constitute good azimuth coverage with 42 P, 30 pP, 32 S and 22 sS waveforms (Fig. S4-21a). The seismic energy can be modeled by four sub-events (Table S4-21, Fig. S4-21b). The first sub-event is 5 km to the southeast of the initiation point, the second and third sub-events propagated to the northeast and the fourth sub-event is to the south. The first three sub-events propagate around the sub-horizontal plane; and the fourth is 5 km from both the GCMT planes. Focal mechanisms of the sub-events cannot be model on a fault plane. (Figs. S4-21c – S4-21f).

Table S4-21. Source parameters of inferred sub-events of E21

Sub-event	dt (s)	dn (km)	de (km)	dz (km)	duration (s)	Mw	strike (°)	dip (°)	slip (°)
1	1.8	-2.0	4.5	0.0	3.0	6.7	259.3	14.7	313.4
2	9.6	15.2	1.5	3.5	7.0	7.1	270.5	22.7	323.3
3	13.2	27.0	-6.3	-4.5	3.0	6.7	295.7	12.9	352.3
4	13.3	-6.9	-4.9	-4.9	3.0	6.8	260.0	10.3	333.9

(Fig. S4-21)

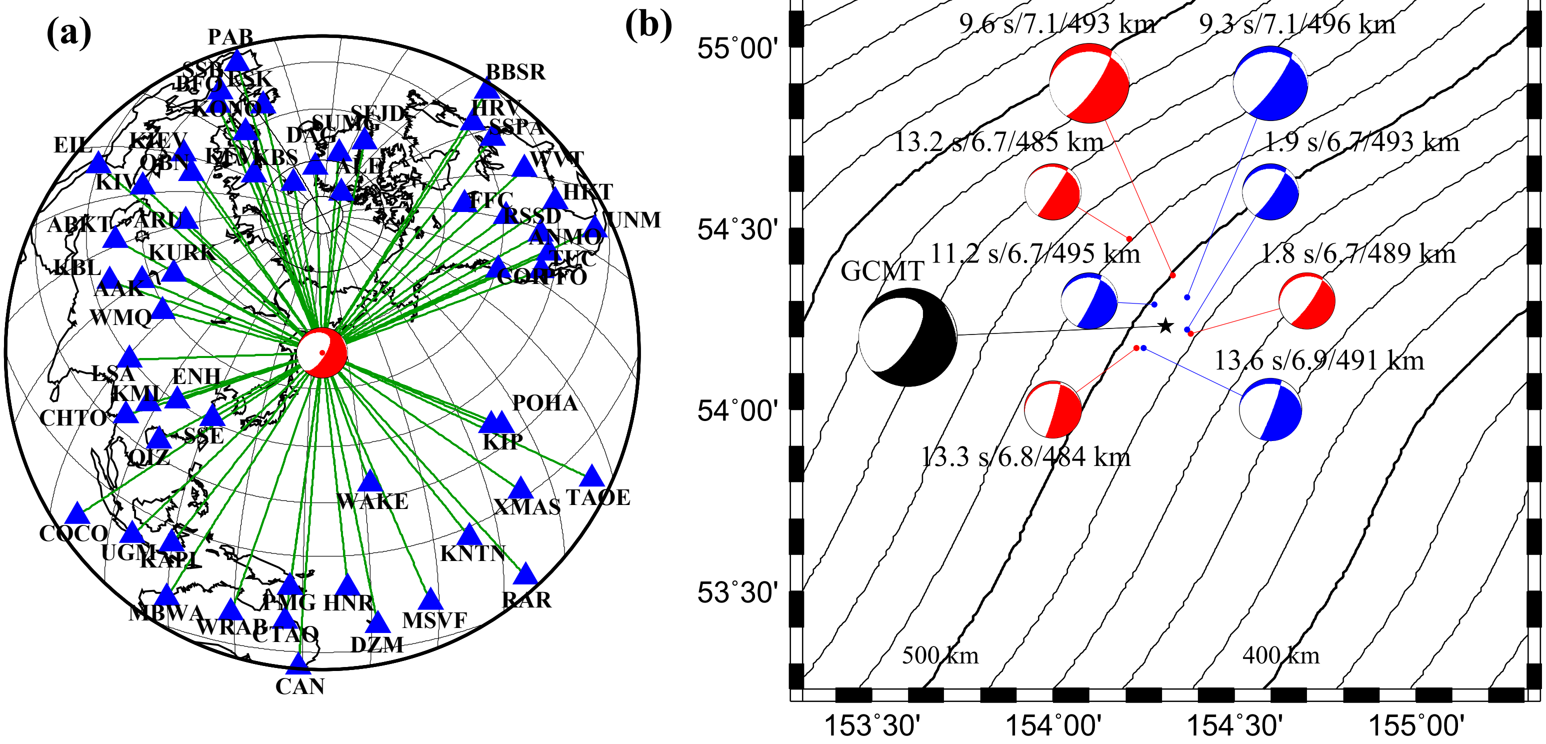
(a)
PAB
SSB
BFO
ESK
KONO
BBSR
HRV
SSPA
SFJD
SUMG
DAG
EIL
KIEV
OBN
KEV
KBS
ALE
WVT
HKT
TUC
UNM
ANMO
RSSD
FFC
CORFO
KIV
ABKT
ARU
KURK
KBL
AAK
WMQ
LSA
KMI
ENH
CHTO
SSE
QIZ
POHA
KIP
WAKE
XMAS
TAOE
COCO
UGM
KAPI
KNTN
RAR
MBWA
WRAB
PMG
HNR
CTAO
MSVF
DZM
CAN
(b)
9.6 s/7.1/493 km
9.3 s/7.1/496 km
13.2 s/6.7/485 km
1.9 s/6.7/493 km
11.2 s/6.7/495 km
1.8 s/6.7/489 km
GCMT
13.6 s/6.9/491 km
13.3 s/6.8/484 km
500 km
400 km
55˚00'
54˚30'
54˚00'
53˚30'
153˚30'
154˚00'
154˚30'
155˚00'

(c)

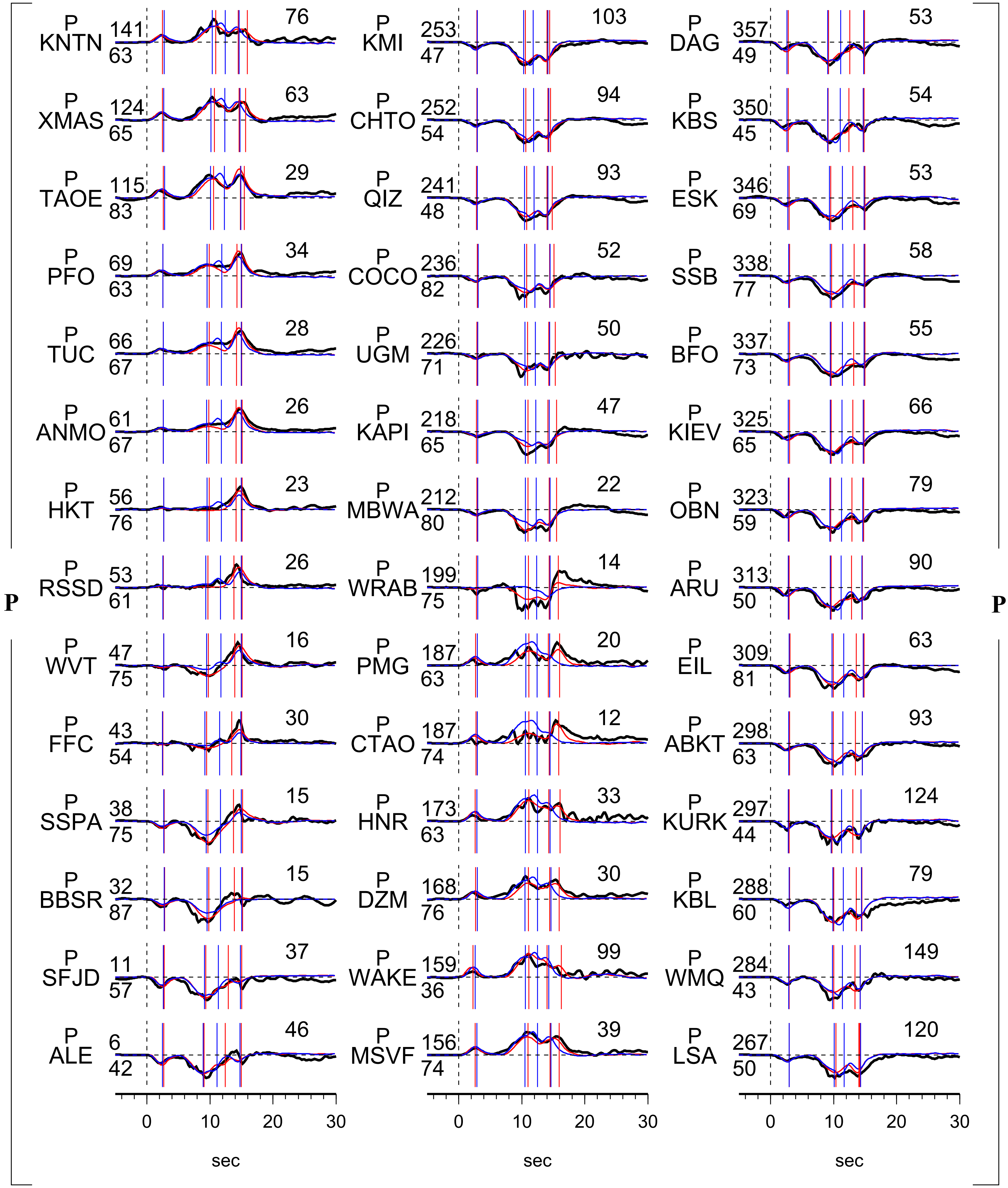

P
P
P KNTN 141 63 76
P XMAS 124 65 63
P TAOE 115 83 29
P PFO 69 63 34
P TUC 66 67 28
P ANMO 61 67 26
P HKT 56 76 23
P RSSD 53 61 26
P WVT 47 75 16
P FFC 43 54 30
P SSPA 38 75 15
P BBSR 32 87 15
P SFJD 11 57 37
P ALE 6 42 46
P KMI 253 47 103
P CHTO 252 54 94
P QIZ 241 48 93
P COCO 236 82 52
P UGM 226 71 50
P KAPI 218 65 47
P MBWA 212 80 22
P WRAB 199 75 14
P PMG 187 63 20
P CTAO 187 74 12
P HNR 173 63 33
P DZM 168 76 30
P WAKE 159 36 99
P MSVF 156 74 39
P DAG 357 49 53
P KBS 350 45 54
P ESK 346 69 53
P SSB 338 77 58
P BFO 337 73 55
P KIEV 325 65 66
P OBN 323 59 79
P ARU 313 50 90
P EIL 309 81 63
P ABKT 298 63 93
P KURK 297 44 124
P KBL 288 60 79
P WMQ 284 43 149
P LSA 267 50 120
0
10
20
30
sec
0
10
20
30
sec
0
10
20
30
sec

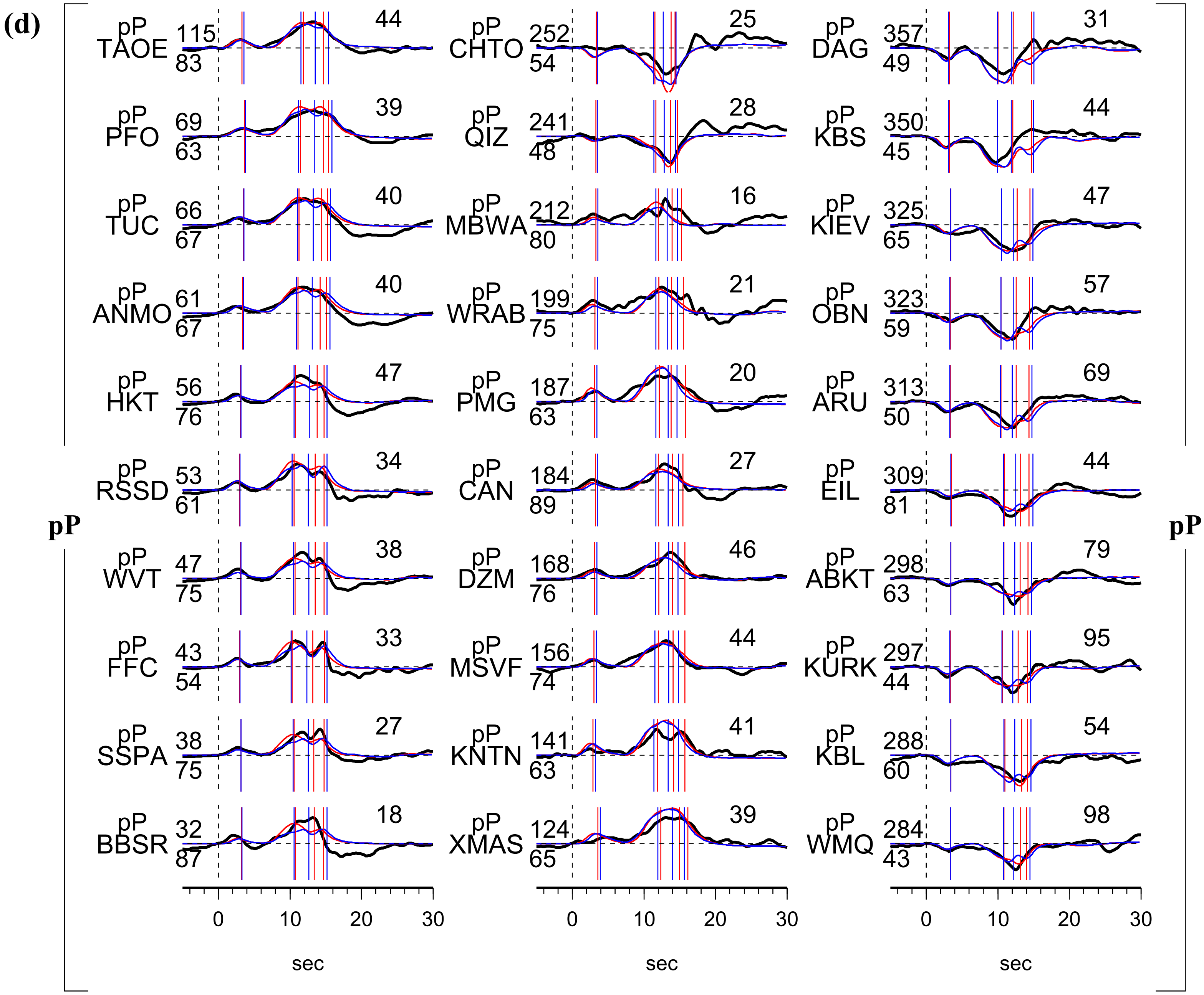(d)
pP
pP
pP TAOE 115 83 44
pP PFO 69 63 39
pP TUC 66 67 40
pP ANMO 61 67 40
pP HKT 56 76 47
pP RSSD 53 61 34
pP WVT 47 75 38
pP FFC 43 54 33
pP SSPA 38 75 27
pP BBSR 32 87 18
pP CHTO 252 54 25
pP QIZ 241 48 28
pP MBWA 212 80 16
pP WRAB 199 75 21
pP PMG 187 63 20
pP CAN 184 89 27
pP DZM 168 76 46
pP MSVF 156 74 44
pP KNTN 141 63 41
pP XMAS 124 65 39
pP DAG 357 49 31
pP KBS 350 45 44
pP KIEV 325 65 47
pP OBN 323 59 57
pP ARU 313 50 69
pP EIL 309 81 44
pP ABKT 298 63 79
pP KURK 297 44 95
pP KBL 288 60 54
pP WMQ 284 43 98
0
10
20
30
sec
0
10
20
30
sec
0
10
20
30
sec

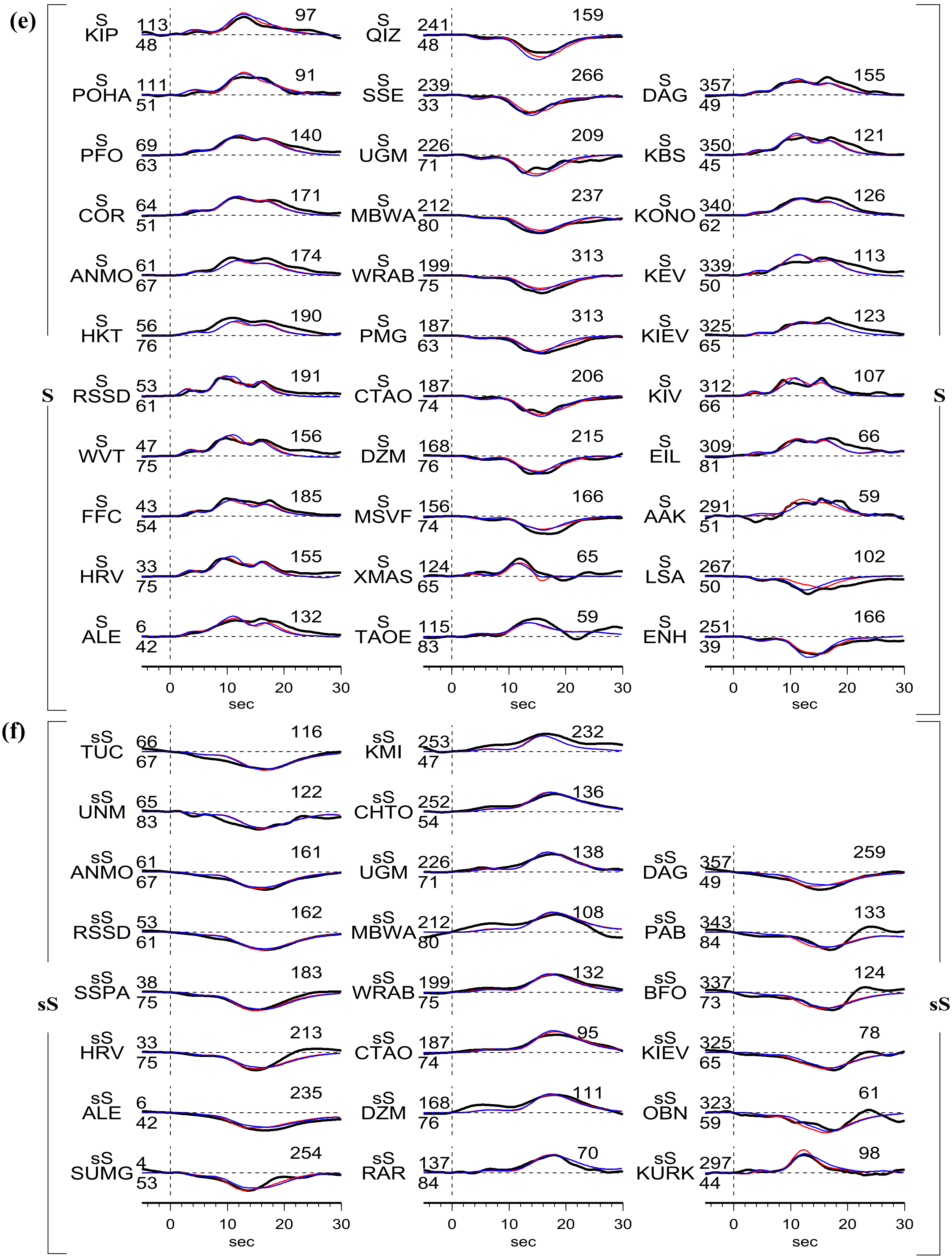
(e)
S
S KIP 113 48 97
S QIZ 241 48 159
S POHA 111 51 91
S SSE 239 33 266
S DAG 357 49 155
S PFO 69 63 140
S UGM 226 71 209
S KBS 350 45 121
S COR 64 51 171
S MBWA 212 80 237
S KONO 340 62 126
S ANMO 61 67 174
S WRAB 199 75 313
S KEV 339 50 113
S HKT 56 76 190
S PMG 187 63 313
S KIEV 325 65 123
S RSSD 53 61 191
S CTAO 187 74 206
S KIV 312 66 107
S WVT 47 75 156
S DZM 168 76 215
S EIL 309 81 66
S FFC 43 54 185
S MSVF 156 74 166
S AAK 291 51 59
S HRV 33 75 155
S XMAS 124 65 65
S LSA 267 50 102
S ALE 6 42 132
S TAOE 115 83 59
S ENH 251 39 166
0
10
20
30
sec
(f)
sS
sS TUC 66 67 116
sS KMI 253 47 232
sS UNM 65 83 122
sS CHTO 252 54 136
sS ANMO 61 67 161
sS UGM 226 71 138
sS DAG 357 49 259
sS RSSD 53 61 162
sS MBWA 212 80 108
sS PAB 343 84 133
sS SSPA 38 75 183
sS WRAB 199 75 132
sS BFO 337 73 124
sS HRV 33 75 213
sS CTAO 187 74 95
sS KIEV 325 65 78
sS ALE 6 42 235
sS DZM 168 76 111
sS OBN 323 59 61
sS SUMG 4 53 254
sS RAR 137 84 70
sS KURK 297 44 98
0
10
20
30
sec

E22. The 23 Jul 2010 Mw 7.3 earthquake

Earthquake E22 occurred 607 km beneath Philippine region (Table S4-0). The seismograms constitute good azimuth coverage with 38 P, 27 pP, 30 S and 23 sS wave data (Fig. S4-22a). The Mw 7.3 earthquake has a long duration of 20 s and a large source extension of ~45 km (Table S4-22, Fig. S4-22b). The horizontal extension is generally consistent with the back-projection result (Zhang and Xu, 2012). The earthquake has two portions of energy. The first portion can be modeled by three sub-events aligning along the nodal axis (intersection of the GCMT fault planes), with similar focal mechanisms consistent with the GCMT sub-horizontal plane. The second portion can be model by two sub-events still close to the nodal axis, but with focal mechanisms inconsistent with the plane (Figs. S4-22c – S4-22f).

Table S4-22. Source parameters of inferred sub-events of E22

Sub-event	dt (s)	dn (km)	de (km)	dz (km)	duration (s)	Mw	strike (°)	dip (°)	slip (°)
1	2.7	-1.2	4.2	1.7	3.4	6.8	246.8	14.9	305.1
2	5.7	-11.4	2.3	-0.3	5.2	6.8	258.1	11.2	319.7
3	8.6	-18.8	1.2	-3.4	4.8	6.8	258.5	20.1	324.3
4	12.6	-31.8	-3.3	-17.0	6.0	6.9	242.9	21.8	317.1
5	16.4	-41.5	-11.7	-18.0	7.4	6.8	243.8	16.6	316.0

(Fig. S4-22)

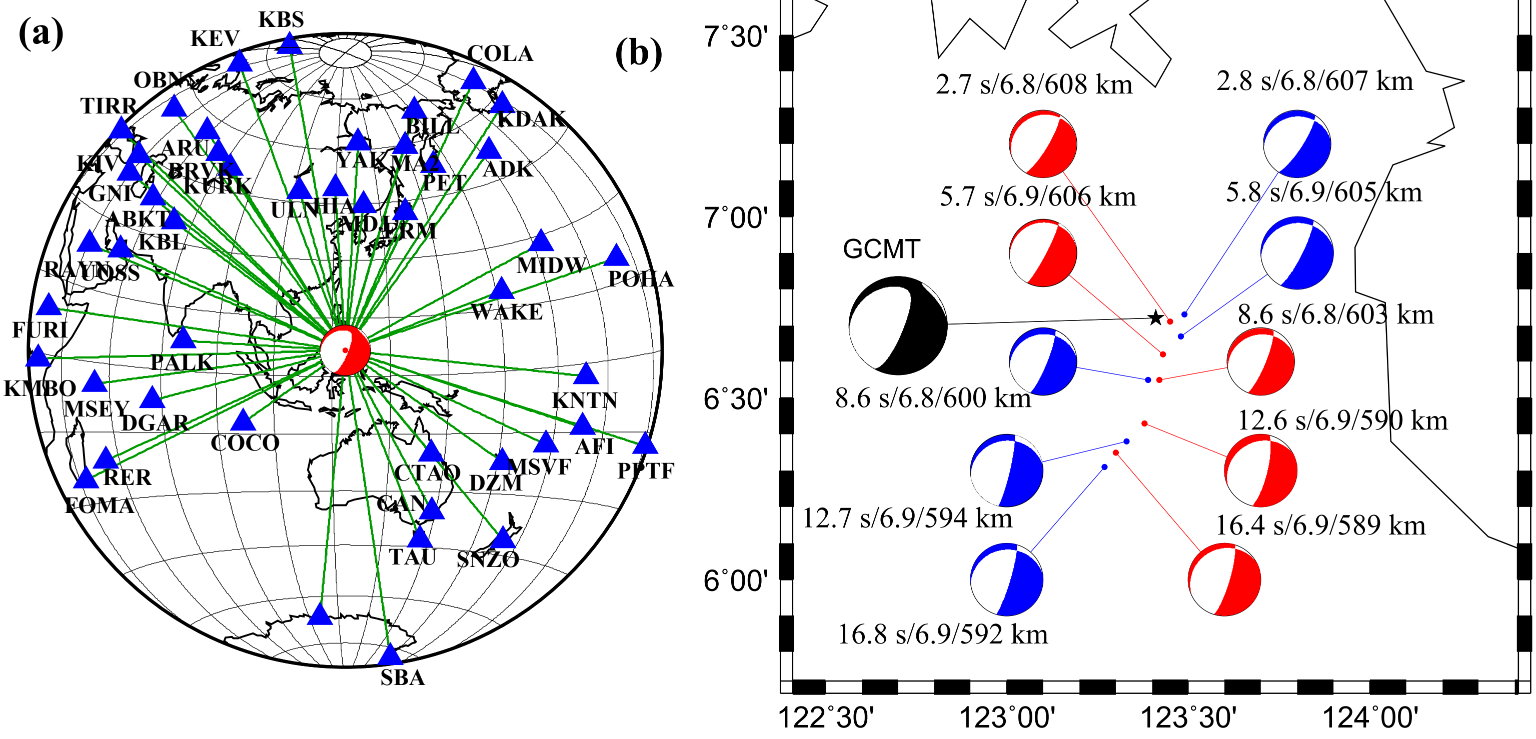
(a)
KBS
KEV
COLA
OBN
TIRR
KDAK
BILL
ARU
YAK
MA2
KIV
BRVK
PET
ADK
GNI
KURK
ULN
HIA
MDJ
ERM
ABKT
KBL
RAYN
UOSS
MIDW
POHA
WAKE
FURI
PALK
KMBO
KNTN
MSEY
DGAR
COCO
AFI
PPTF
RER
CTAO
DZM
MSVF
FOMA
CAN
TAU
SNZO
SBA
(b)
7˚30'
7˚00'
6˚30'
6˚00'
122˚30'
123˚00'
123˚30'
124˚00'
GCMT
2.7 s/6.8/608 km
2.8 s/6.8/607 km
5.7 s/6.9/606 km
5.8 s/6.9/605 km
8.6 s/6.8/603 km
8.6 s/6.8/600 km
12.6 s/6.9/590 km
12.7 s/6.9/594 km
16.4 s/6.9/589 km
16.8 s/6.9/592 km

(c)

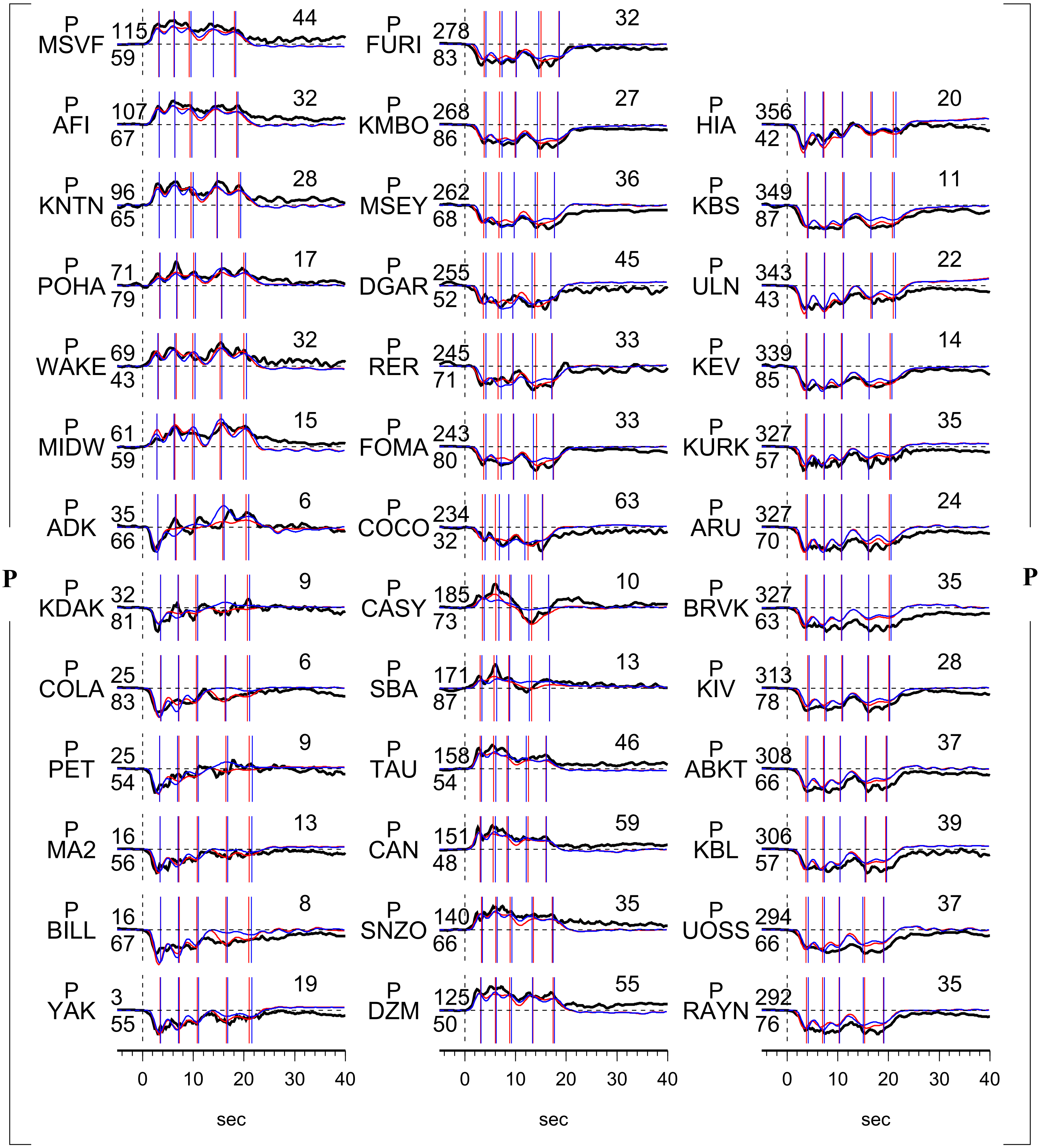
P
P
P MSVF 115 59 44
P AFI 107 67 32
P KNTN 96 65 28
P POHA 71 79 17
P WAKE 69 43 32
P MIDW 61 59 15
P ADK 35 66 6
P KDAK 32 81 9
P COLA 25 83 6
P PET 25 54 9
P MA2 16 56 13
P BILL 16 67 8
P YAK 3 55 19
P FURI 278 83 32
P KMBO 268 86 27
P MSEY 262 68 36
P DGAR 255 52 45
P RER 245 71 33
P FOMA 243 80 33
P COCO 234 32 63
P CASY 185 73 10
P SBA 171 87 13
P TAU 158 54 46
P CAN 151 48 59
P SNZO 140 66 35
P DZM 125 50 55
P HIA 356 42 20
P KBS 349 87 11
P ULN 343 43 22
P KEV 339 85 14
P KURK 327 57 35
P ARU 327 70 24
P BRVK 327 63 35
P KIV 313 78 28
P ABKT 308 66 37
P KBL 306 57 39
P UOSS 294 66 37
P RAYN 292 76 35
0 10 20 30 40
sec
0 10 20 30 40
sec
0 10 20 30 40
sec

(d)

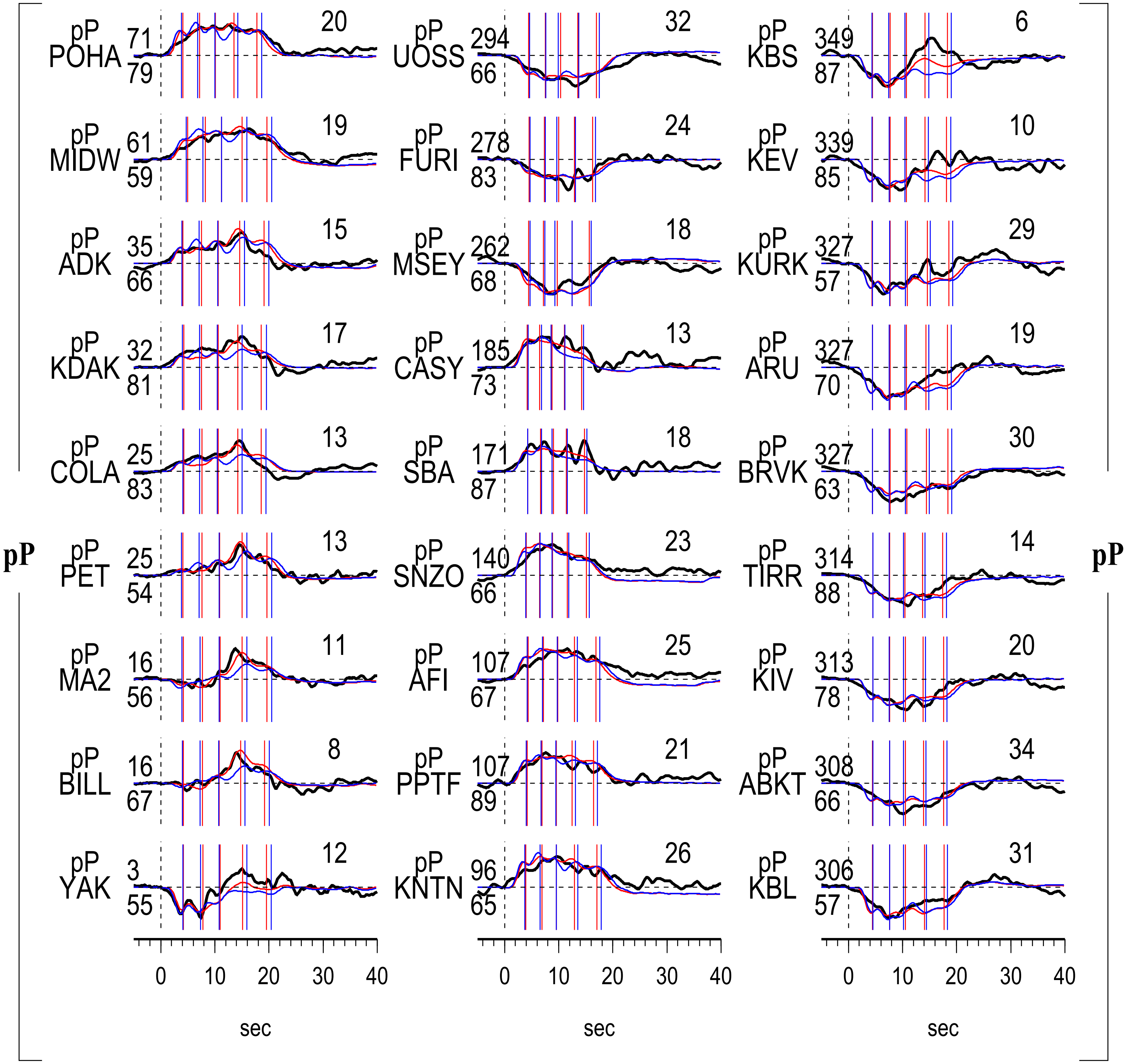
pP
pP
pP POHA 71 79 20
pP MIDW 61 59 19
pP ADK 35 66 15
pP KDAK 32 81 17
pP COLA 25 83 13
pP PET 25 54 13
pP MA2 16 56 11
pP BILL 16 67 8
pP YAK 3 55 12
pP UOSS 294 66 32
pP FURI 278 83 24
pP MSEY 262 68 18
pP CASY 185 73 13
pP SBA 171 87 18
pP SNZO 140 66 23
pP AFI 107 67 25
pP PPTF 107 89 21
pP KNTN 96 65 26
pP KBS 349 87 6
pP KEV 339 85 10
pP KURK 327 57 29
pP ARU 327 70 19
pP BRVK 327 63 30
pP TIRR 314 88 14
pP KIV 313 78 20
pP ABKT 308 66 34
pP KBL 306 57 31
0
10
20
30
40
sec
0
10
20
30
40
sec
0
10
20
30
40
sec

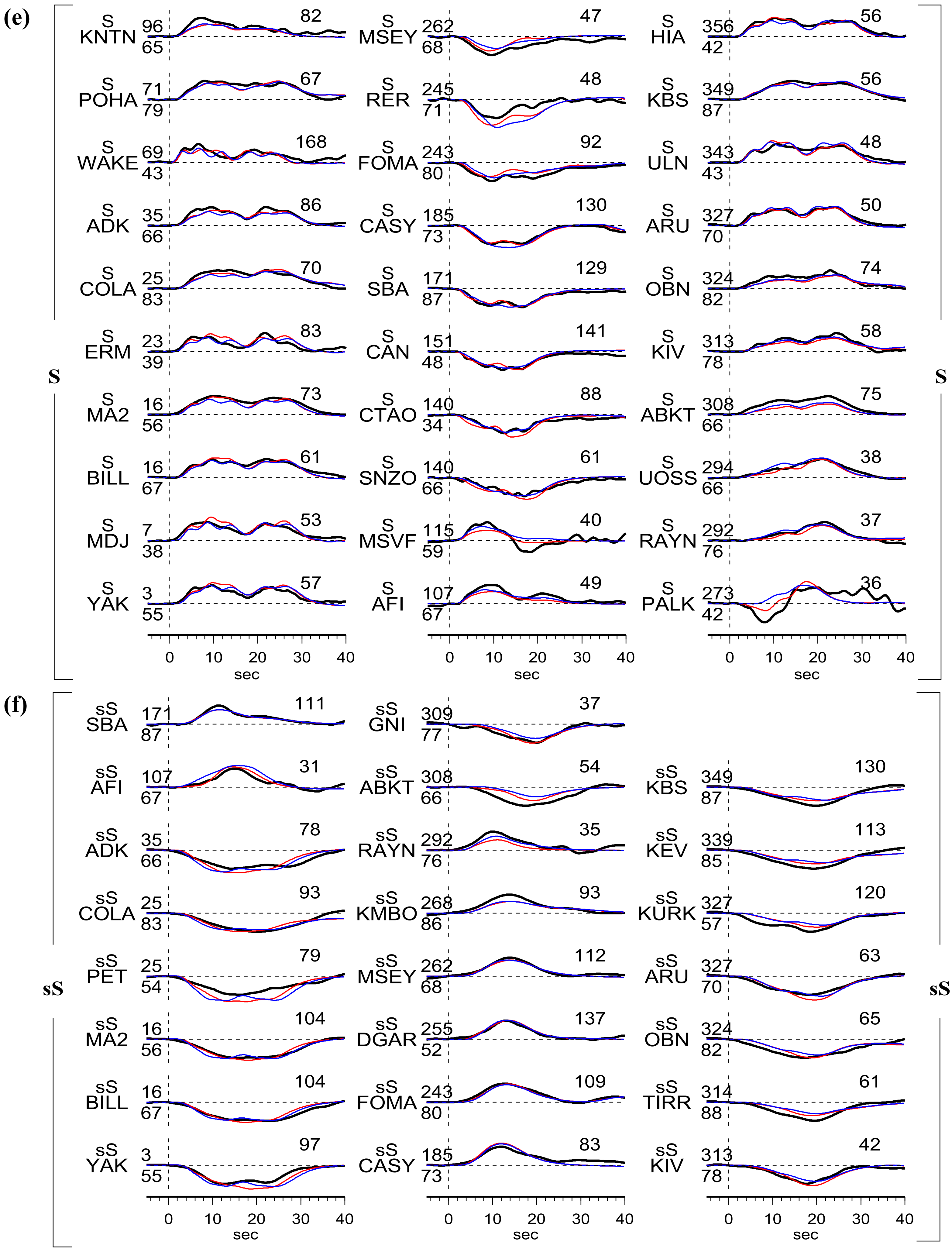
(e)
S KNTN 96 65 82
S MSEY 262 68 47
S HIA 356 42 56
S POHA 71 79 67
S RER 245 71 48
S KBS 349 87 56
S WAKE 69 43 168
S FOMA 243 80 92
S ULN 343 43 48
S ADK 35 66 86
S CASY 185 73 130
S ARU 327 70 50
S COLA 25 83 70
S SBA 171 87 129
S OBN 324 82 74
S ERM 23 39 83
S CAN 151 48 141
S KIV 313 78 58
S MA2 16 56 73
S CTAO 140 34 88
S ABKT 308 66 75
S BILL 16 67 61
S SNZO 140 66 61
S UOSS 294 66 38
S MDJ 7 38 53
S MSVF 115 59 40
S RAYN 292 76 37
S YAK 3 55 57
S AFI 107 67 49
S PALK 273 42 36
S
0 10 20 30 40
sec
(f)
sS SBA 171 87 111
sS GNI 309 77 37
sS AFI 107 67 31
sS ABKT 308 66 54
sS KBS 349 87 130
sS ADK 35 66 78
sS RAYN 292 76 35
sS KEV 339 85 113
sS COLA 25 83 93
sS KMBO 268 86 93
sS KURK 327 57 120
sS PET 25 54 79
sS MSEY 262 68 112
sS ARU 327 70 63
sS MA2 16 56 104
sS DGAR 255 52 137
sS OBN 324 82 65
sS BILL 16 67 104
sS FOMA 243 80 109
sS TIRR 314 88 61
sS YAK 3 55 97
sS CASY 185 73 83
sS KIV 313 78 42
sS
0 10 20 30 40
sec

E23. The 23 Jul 2010 Mw 7.6 earthquake

Earthquake E23 occurred 587 km beneath Philippine region (Table S4-0). The seismograms constitute good azimuth coverage with 38 P, 25 pP, 29 S and 18 sS wave data (Fig. S4-23a). The seismic energy can be modeled by four sub-events (Fig. S4-23b). The first two weak sub-events propagate to the southeast, and the latter two sub-events propagated to the northeast (Table S4-23). Overall, the earthquake possesses a small extension of ~ 20 km, comparing to most of the events with Mw > 7.5. The earthquake can be modeled on the GCMT sub-horizontal plane as well as the best-fitting model (Figs. S4-23c – S4-23f).

Table S4-23. Source parameters of inferred sub-events of E23

Sub-event	dt (s)	dn (km)	de (km)	dz (km)	duration (s)	Mw	strike (°)	dip (°)	slip (°)
1	6.1	-7.3	7.4	-2.6	2.8	7.0	234.7	17.3	316.0
2	8.6	-5.2	11.4	-2.8	2.4	6.9	251.0	22.1	342.2
3	10.9	3.1	21.9	-8.6	5.0	7.3	241.1	23.6	325.2
4	14.4	9.7	16.1	-0.1	7.0	7.3	204.5	7.4	311.2

(Fig. S4-23)

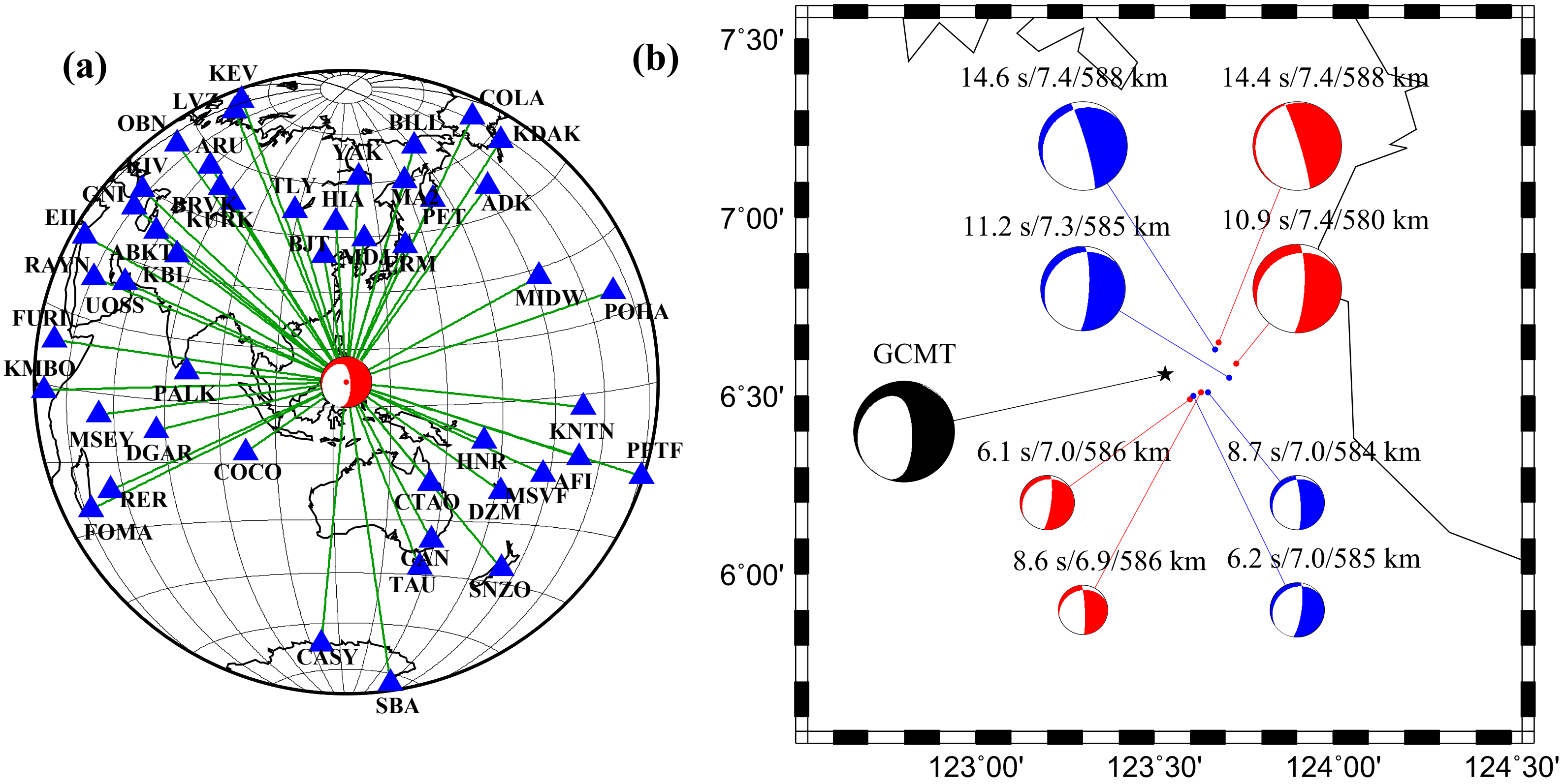
(a)
KEV
LVZ
OBN
COLA
BILL
KDAK
ARU
KIV
YAK
GNI
TLY
HIA
MA2
ADK
BRVK
PET
KURK
EIL
BJT
MDJ
ERM
ABKT
RAYN
KBL
MIDW
UOSS
POHA
FURI
KMBO
PALK
KNTN
MSEY
DGAR
PPTF
COCO
HNR
AFI
RER
MSVF
CTAO
DZM
FOMA
CAN
TAU
SNZO
CASY
SBA
(b)
7˚30'
7˚00'
6˚30'
6˚00'
123˚00'
123˚30'
124˚00'
124˚30'
14.6 s/7.4/588 km
14.4 s/7.4/588 km
11.2 s/7.3/585 km
10.9 s/7.4/580 km
GCMT
6.1 s/7.0/586 km
8.7 s/7.0/584 km
8.6 s/6.9/586 km
6.2 s/7.0/585 km

(c)

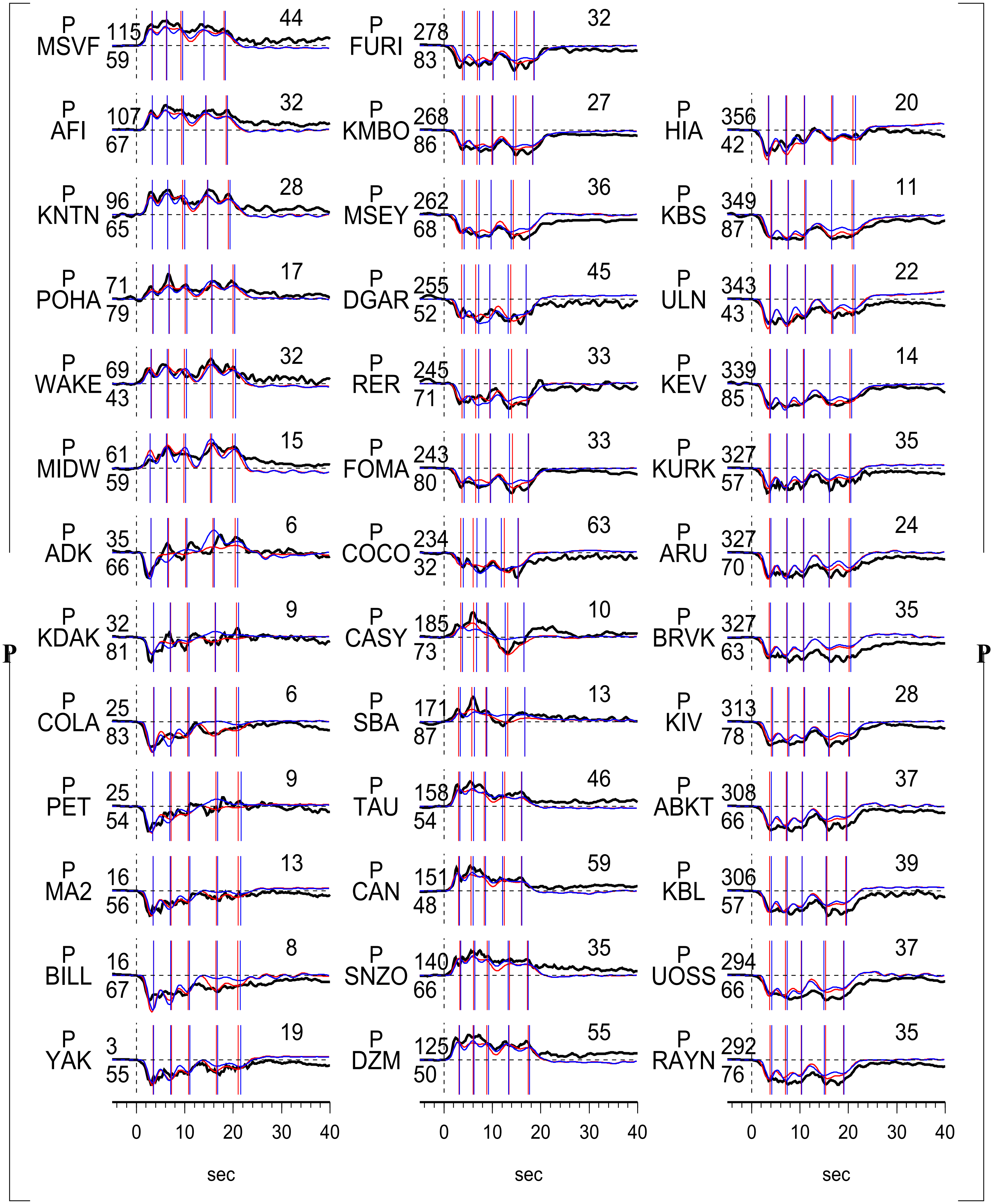
P
MSVF 115 59 44
P
AFI 107 67 32
P
KNTN 96 65 28
P
POHA 71 79 17
P
WAKE 69 43 32
P
MIDW 61 59 15
P
ADK 35 66 6
P
KDAK 32 81 9
P
COLA 25 83 6
P
PET 25 54 9
P
MA2 16 56 13
P
BILL 16 67 8
P
YAK 3 55 19
P
FURI 278 83 32
P
KMBO 268 86 27
P
MSEY 262 68 36
P
DGAR 255 52 45
P
RER 245 71 33
P
FOMA 243 80 33
P
COCO 234 32 63
P
CASY 185 73 10
P
SBA 171 87 13
P
TAU 158 54 46
P
CAN 151 48 59
P
SNZO 140 66 35
P
DZM 125 50 55
P
HIA 356 42 20
P
KBS 349 87 11
P
ULN 343 43 22
P
KEV 339 85 14
P
KURK 327 57 35
P
ARU 327 70 24
P
BRVK 327 63 35
P
KIV 313 78 28
P
ABKT 308 66 37
P
KBL 306 57 39
P
UOSS 294 66 37
P
RAYN 292 76 35
0
10
20
30
40
sec
0
10
20
30
40
sec
0
10
20
30
40
sec
P
P

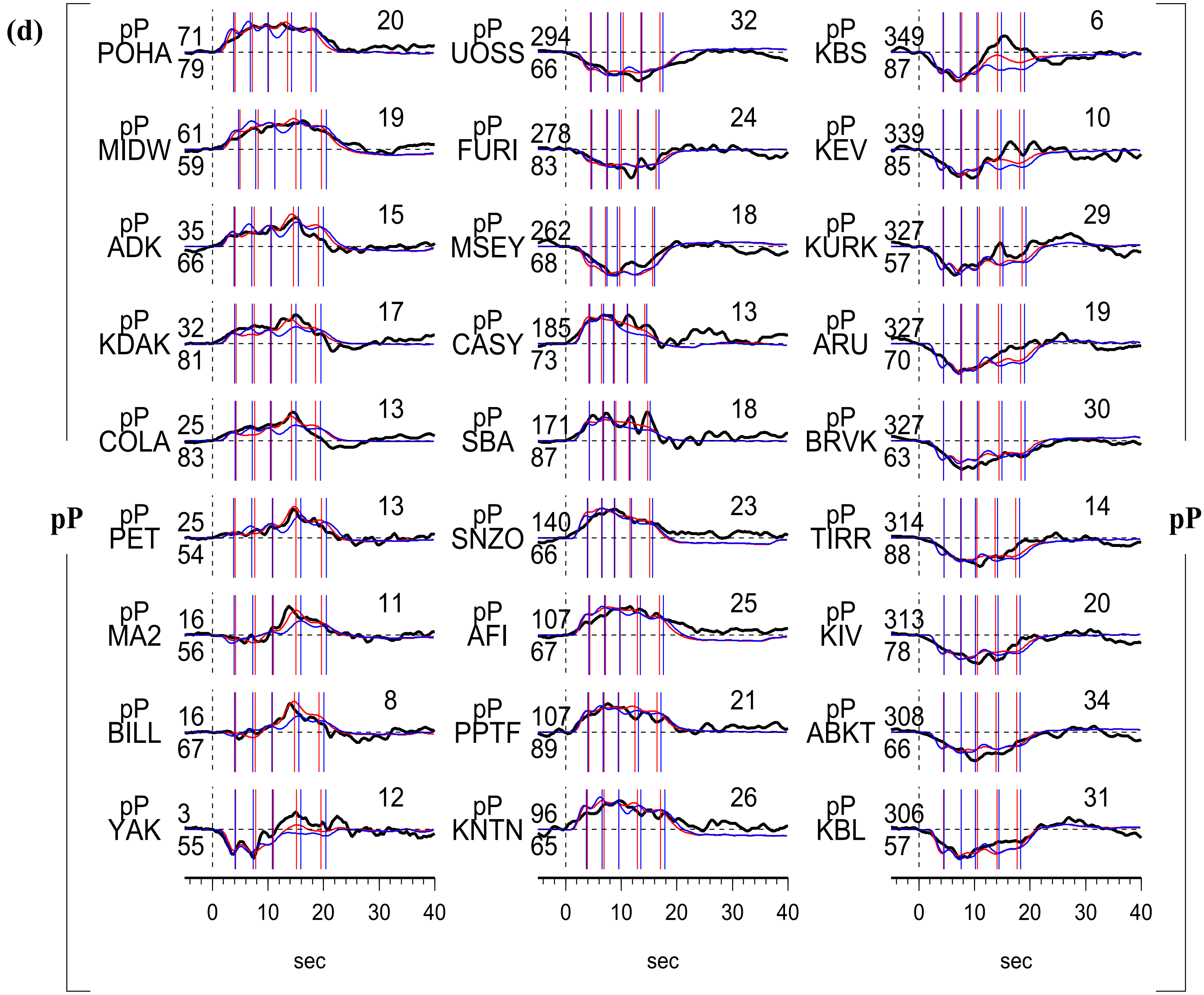
(d)
pP
pP
pP POHA 71 79 20
pP MIDW 61 59 19
pP ADK 35 66 15
pP KDAK 32 81 17
pP COLA 25 83 13
pP PET 25 54 13
pP MA2 16 56 11
pP BILL 16 67 8
pP YAK 3 55 12
pP UOSS 294 66 32
pP FURI 278 83 24
pP MSEY 262 68 18
pP CASY 185 73 13
pP SBA 171 87 18
pP SNZO 140 66 23
pP AFI 107 67 25
pP PPTF 107 89 21
pP KNTN 96 65 26
pP KBS 349 87 6
pP KEV 339 85 10
pP KURK 327 57 29
pP ARU 327 70 19
pP BRVK 327 63 30
pP TIRR 314 88 14
pP KIV 313 78 20
pP ABKT 308 66 34
pP KBL 306 57 31
0
10
20
30
40
sec
0
10
20
30
40
sec
0
10
20
30
40
sec

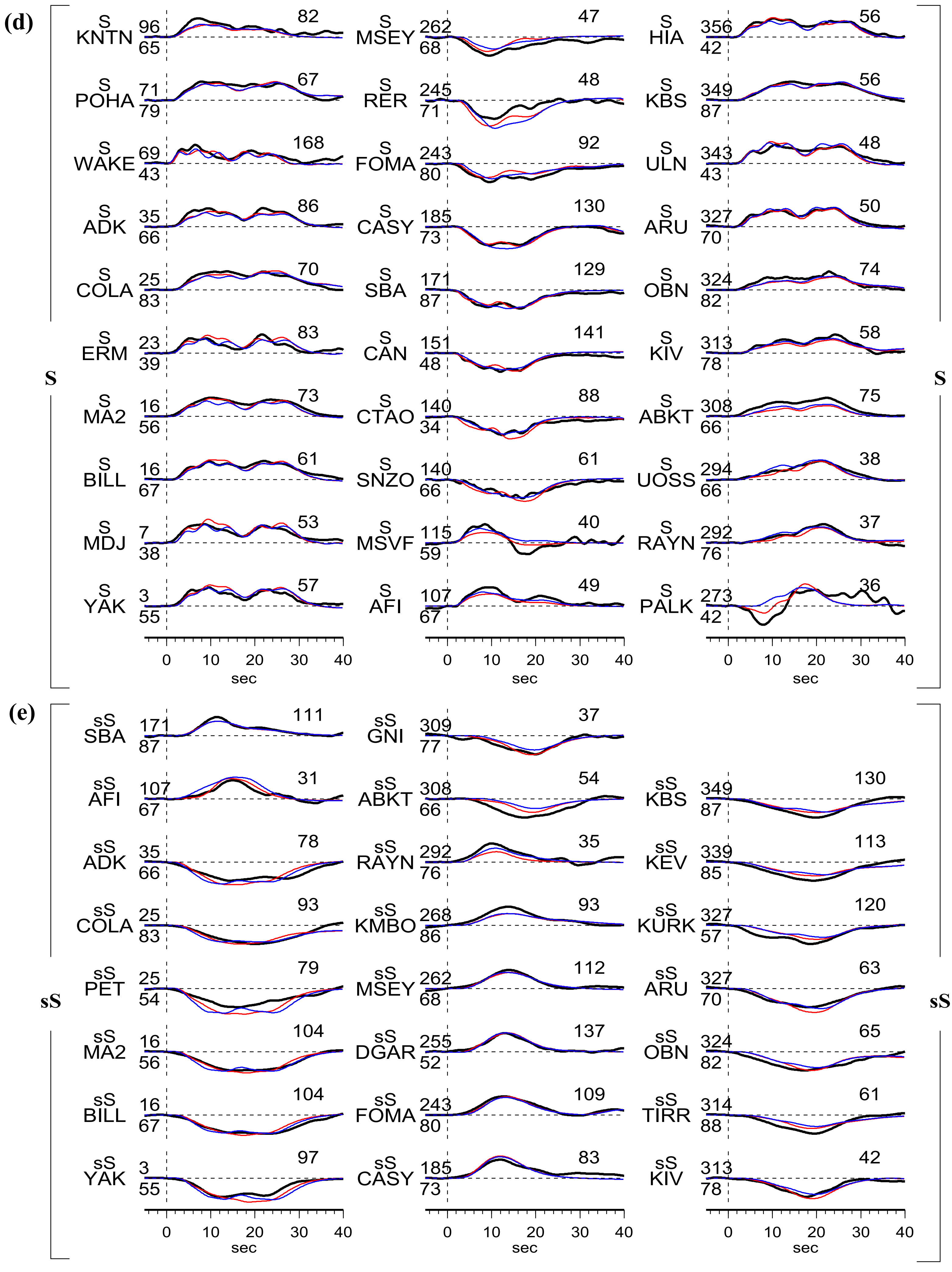
(d)
S
S KNTN 96 65 82
S MSEY 262 68 47
S HIA 356 42 56
S POHA 71 79 67
S RER 245 71 48
S KBS 349 87 56
S WAKE 69 43 168
S FOMA 243 80 92
S ULN 343 43 48
S ADK 35 66 86
S CASY 185 73 130
S ARU 327 70 50
S COLA 25 83 70
S SBA 171 87 129
S OBN 324 82 74
S ERM 23 39 83
S CAN 151 48 141
S KIV 313 78 58
S MA2 16 56 73
S CTAO 140 34 88
S ABKT 308 66 75
S BILL 16 67 61
S SNZO 140 66 61
S UOSS 294 66 38
S MDJ 7 38 53
S MSVF 115 59 40
S RAYN 292 76 37
S YAK 3 55 57
S AFI 107 67 49
S PALK 273 42 36
0
10
20
30
40
sec
(e)
sS
sS SBA 171 87 111
sS GNI 309 77 37
sS AFI 107 67 31
sS ABKT 308 66 54
sS KBS 349 87 130
sS ADK 35 66 78
sS RAYN 292 76 35
sS KEV 339 85 113
sS COLA 25 83 93
sS KMBO 268 86 93
sS KURK 327 57 120
sS PET 25 54 79
sS MSEY 262 68 112
sS ARU 327 70 63
sS MA2 16 56 104
sS DGAR 255 52 137
sS OBN 324 82 65
sS BILL 16 67 104
sS FOMA 243 80 109
sS TIRR 314 88 61
sS YAK 3 55 97
sS CASY 185 73 83
sS KIV 313 78 42

E24. The 01 Jan 2011 Mw 7.0 earthquake

Earthquake E24 occurred 577 km beneath South America (Table S4-0). The seismograms constitute good azimuth coverage with 35 P, 23 pP, 28 S and 17 sS wave data (Fig. S4-24a). The seismic energy can be modeled by three sub-events (Table S4-24, Fig. S4-24b). The first and second sub-events are located very close to the initiation point. It is interesting to note that, they have slightly different radiation patterns, although in so a close distance. The third sub-event is ~30 km to the south, with a peak time of 7.7 s. The sub-events propagated around the GCMT sub-horizontal plane, but the planar model cannot fit the radiation pattern of the seismic data (Figs. S4-24c – S4-24f).

Table S4-24. Source parameters of inferred sub-events of E24

Sub-event	dt (s)	dn (km)	de (km)	dz (km)	duration (s)	Mw	strike (°)	dip (°)	slip (°)
1	1.2	1.4	0.8	-0.6	2.0	6.6	368.9	24.9	299.6
2	3.0	-1.4	0.0	0.4	2.4	6.8	371.4	30.1	315.4
3	7.7	-26.4	-3.3	0.2	4.0	6.7	344.4	19.9	270.5

(Fig. S4-24)

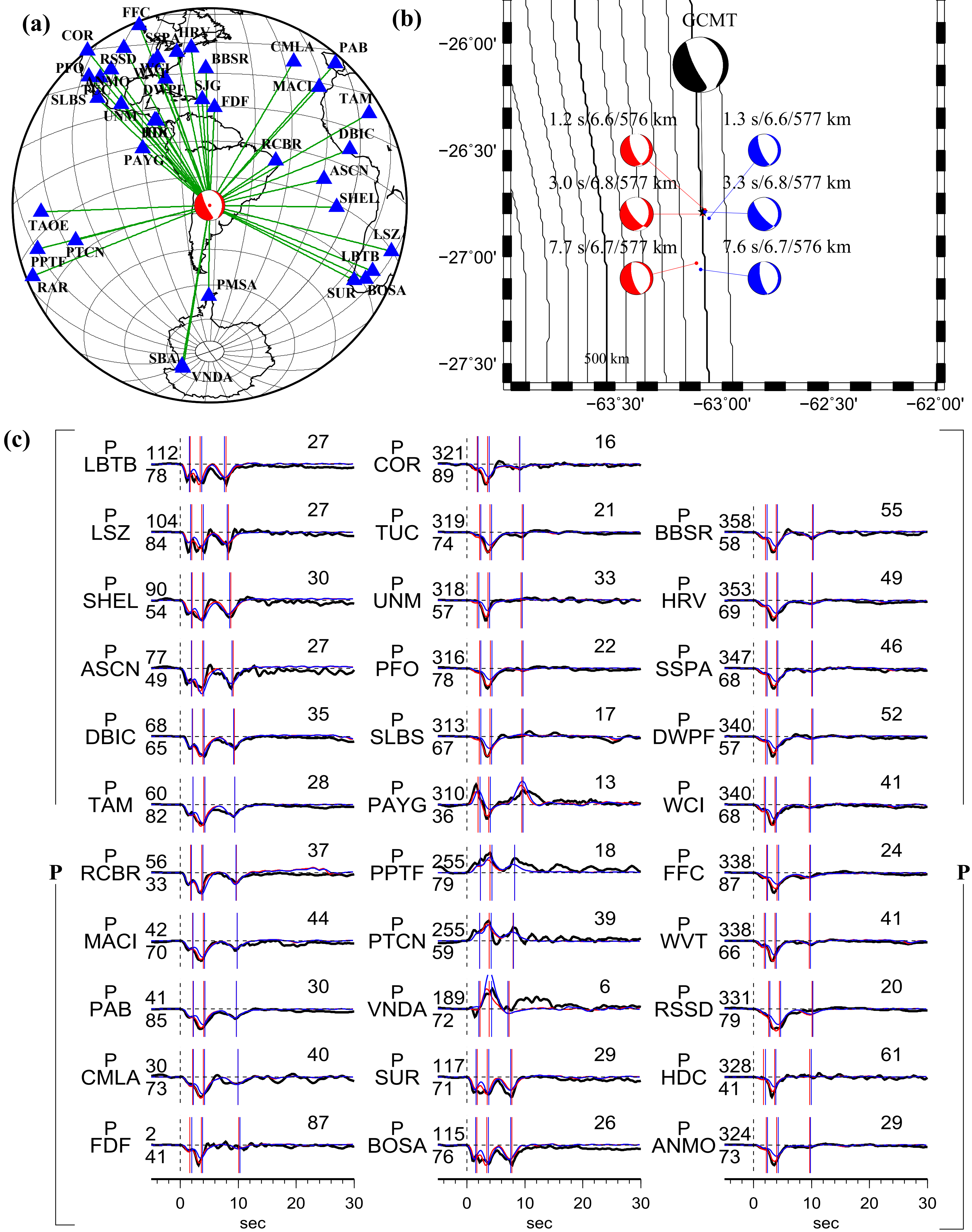
(a)
FFC
COR
SSPA
HRV
CMLA
PAB
RSSD
PFO
WCI
WVT
BBSR
ANMO
TUC
DWPF
SJG
MACI
SLBS
FDF
TAM
UNM
HDC
DBIC
PAYG
RCBR
ASCN
SHEL
TAOE
PTCN
PPTF
RAR
LSZ
LBTB
PMSA
SUR
BOSA
SBA
VNDA
(b)
GCMT
−26˚00'
−26˚30'
−27˚00'
−27˚30'
−63˚30'
−63˚00'
−62˚30'
−62˚00'
1.2 s/6.6/576 km
1.3 s/6.6/577 km
3.0 s/6.8/577 km
3.3 s/6.8/577 km
7.7 s/6.7/577 km
7.6 s/6.7/576 km
500 km
(c)
P LBTB 112 78 27
P LSZ 104 84 27
P SHEL 90 54 30
P ASCN 77 49 27
P DBIC 68 65 35
P TAM 60 82 28
P RCBR 56 33 37
P MACI 42 70 44
P PAB 41 85 30
P CMLA 30 73 40
P FDF 2 41 87
P COR 321 89 16
P TUC 319 74 21
P UNM 318 57 33
P PFO 316 78 22
P SLBS 313 67 17
P PAYG 310 36 13
P PPTF 255 79 18
P PTCN 255 59 39
P VNDA 189 72 6
P SUR 117 71 29
P BOSA 115 76 26
P BBSR 358 58 55
P HRV 353 69 49
P SSPA 347 68 46
P DWPF 340 57 52
P WCI 340 68 41
P FFC 338 87 24
P WVT 338 66 41
P RSSD 331 79 20
P HDC 328 41 61
P ANMO 324 73 29
P
P
0
10
20
30
sec

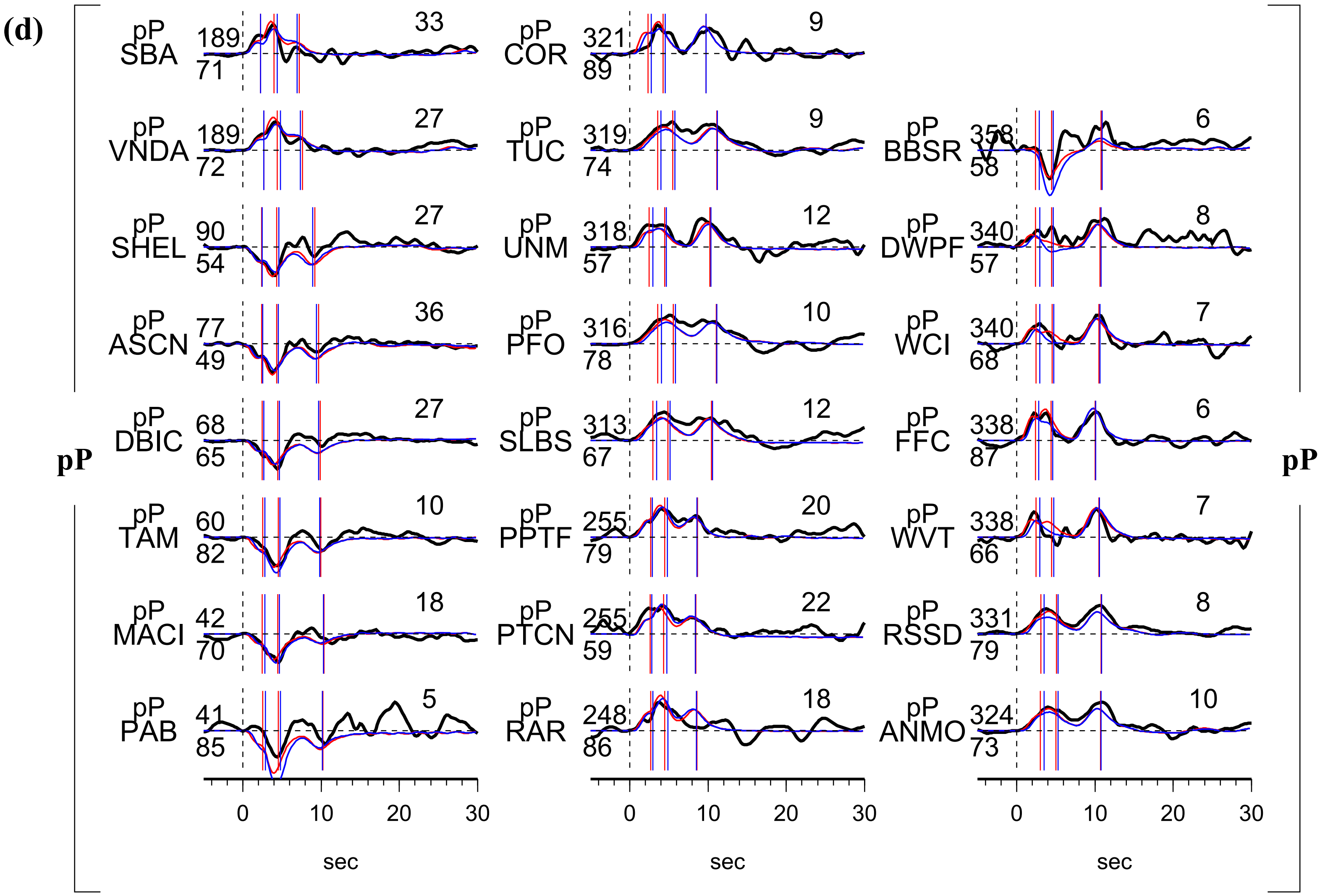
(d)
pP
pP
pP SBA 189 71 33
pP COR 321 89 9
pP VNDA 189 72 27
pP TUC 319 74 9
pP BBSR 358 58 6
pP SHEL 90 54 27
pP UNM 318 57 12
pP DWPF 340 57 8
pP ASCN 77 49 36
pP PFO 316 78 10
pP WCI 340 68 7
pP DBIC 68 65 27
pP SLBS 313 67 12
pP FFC 338 87 6
pP TAM 60 82 10
pP PPTF 255 79 20
pP WVT 338 66 7
pP MACI 42 70 18
pP PTCN 255 59 22
pP RSSD 331 79 8
pP PAB 41 85 5
pP RAR 248 86 18
pP ANMO 324 73 10
0
10
20
30
sec
0
10
20
30
sec
0
10
20
30
sec

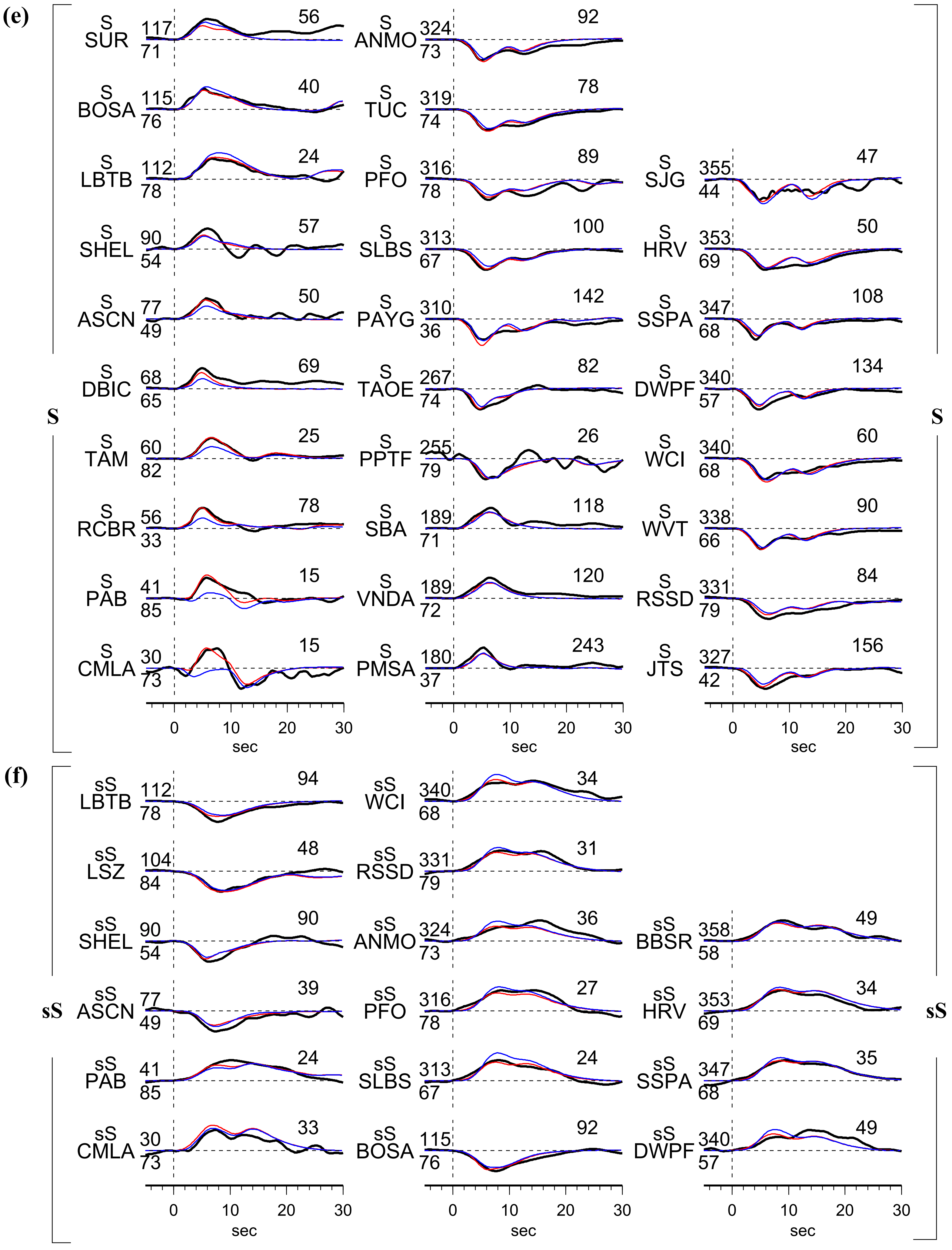
(e)
S
S SUR 117 71 56
S ANMO 324 73 92
S BOSA 115 76 40
S TUC 319 74 78
S LBTB 112 78 24
S PFO 316 78 89
S SJG 355 44 47
S SHEL 90 54 57
S SLBS 313 67 100
S HRV 353 69 50
S ASCN 77 49 50
S PAYG 310 36 142
S SSPA 347 68 108
S DBIC 68 65 69
S TAOE 267 74 82
S DWPF 340 57 134
S TAM 60 82 25
S PPTF 255 79 26
S WCI 340 68 60
S RCBR 56 33 78
S SBA 189 71 118
S WVT 338 66 90
S PAB 41 85 15
S VNDA 189 72 120
S RSSD 331 79 84
S CMLA 30 73 15
S PMSA 180 37 243
S JTS 327 42 156
0 10 20 30
sec
(f)
sS
sS LBTB 112 78 94
sS WCI 340 68 34
sS LSZ 104 84 48
sS RSSD 331 79 31
sS SHEL 90 54 90
sS ANMO 324 73 36
sS BBSR 358 58 49
sS ASCN 77 49 39
sS PFO 316 78 27
sS HRV 353 69 34
sS PAB 41 85 24
sS SLBS 313 67 24
sS SSPA 347 68 35
sS CMLA 30 73 33
sS BOSA 115 76 92
sS DWPF 340 57 49
0 10 20 30
sec

E25. The 15 Sep 2011 Mw 7.3 earthquake

Earthquake E25 occurred 604 km beneath Tonga region (Table S4-0). The seismograms constitute good azimuth coverage with 28 P, 22 pP, 30 S and 14 sS wave data (Fig. S4-25a). The seismic energy can be modeled by four sub-events (Table S4-25, Fig. S4-25b). The first sub-event is 2.5 km to the northeast of the initiation point, the latter sub-events propagated to the southwest. Arrival times of the first three sub-events are consistent with the sub-horizontal plane, while the fourth has a little depth difference (Fig. S4-25c). The planar model cannot model the radiation patterns of pP and SH waves (Figs. S4-25d, S4-25e).

Table S4-25. Source parameters of inferred sub-events of E25

Sub-event	dt (s)	dn (km)	de (km)	dz (km)	duration (s)	Mw	strike (°)	dip (°)	slip (°)
1	3.0	1.8	1.9	0.0	3.2	6.8	39.9	89.6	230.9
2	6.9	-4.4	-6.3	2.2	5.0	7.0	41.0	88.2	242.5
3	9.9	-8.0	-9.6	-4.8	5.0	7.1	52.5	77.6	228.1
4	12.7	-3.5	-25.5	-2.6	3.0	6.8	61.6	79.3	222.5

(Fig. S4-25)

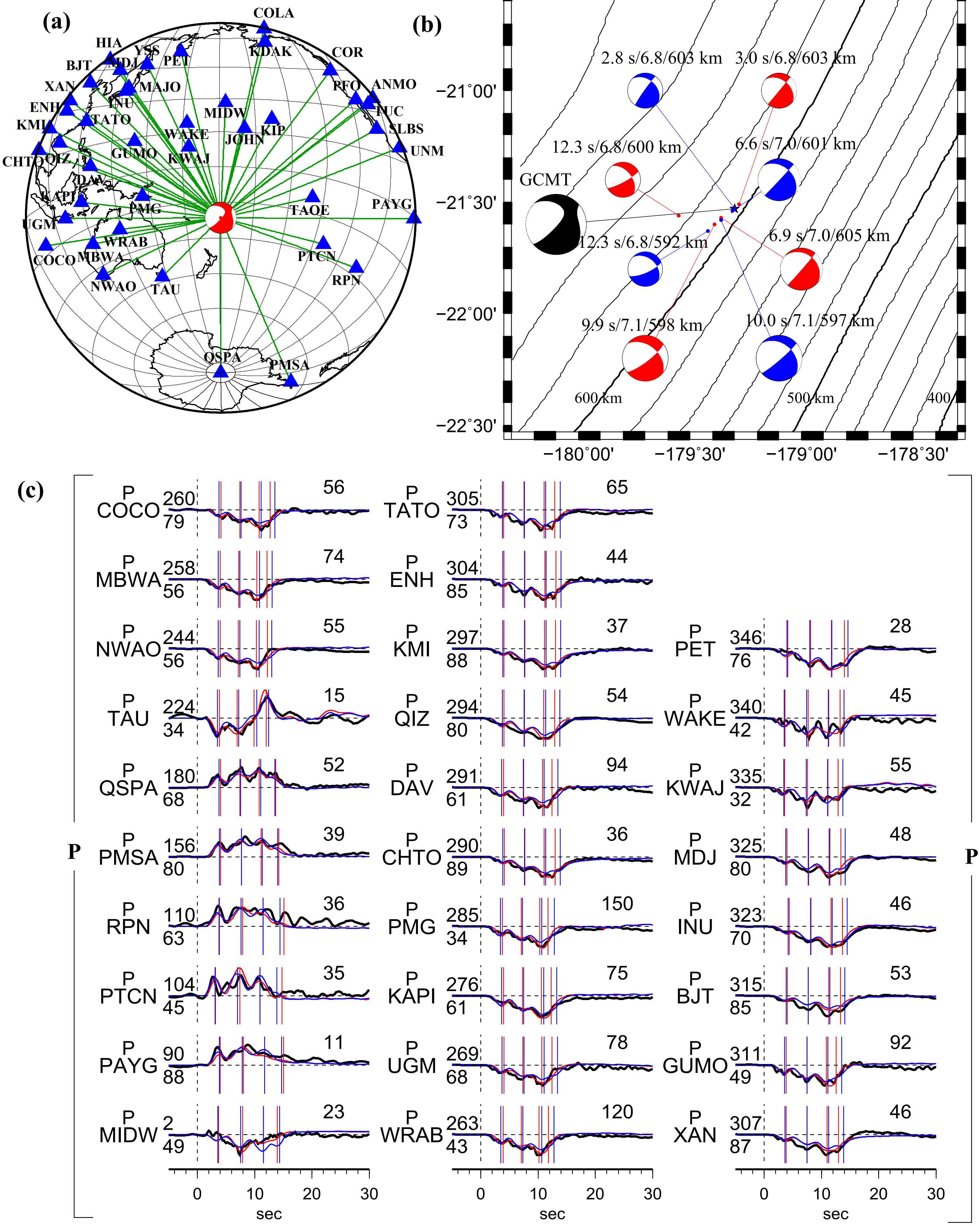
(a)
COLA
KDAK
COR
HIA
YSS
PET
BJT
MDJ
XAN
MAJO
PFO
ANMO
INU
TUC
ENH
TATO
MIDW
KIP
KMI
WAKE
SLBS
JOHN
CHTO
QIZ
GUMO
KWAJ
UNM
DAV
KAPI
TAOE
PAYG
PMG
UGM
WRAB
COCO
MBWA
PTCN
NWAO
TAU
RPN
QSPA
PMSA
(b)
2.8 s/6.8/603 km
3.0 s/6.8/603 km
12.3 s/6.8/600 km
6.6 s/7.0/601 km
GCMT
12.3 s/6.8/592 km
6.9 s/7.0/605 km
9.9 s/7.1/598 km
10.0 s/7.1/597 km
600 km
500 km
400
−21˚00'
−21˚30'
−22˚00'
−22˚30'
−180˚00'
−179˚30'
−179˚00'
−178˚30'
(c)
P COCO 260 79 56
P TATO 305 73 65
P MBWA 258 56 74
P ENH 304 85 44
P NWAO 244 56 55
P KMI 297 88 37
P PET 346 76 28
P TAU 224 34 15
P QIZ 294 80 54
P WAKE 340 42 45
P QSPA 180 68 52
P DAV 291 61 94
P KWAJ 335 32 55
P PMSA 156 80 39
P CHTO 290 89 36
P MDJ 325 80 48
P RPN 110 63 36
P PMG 285 34 150
P INU 323 70 46
P PTCN 104 45 35
P KAPI 276 61 75
P BJT 315 85 53
P PAYG 90 88 11
P UGM 269 68 78
P GUMO 311 49 92
P MIDW 2 49 23
P WRAB 263 43 120
P XAN 307 87 46
P
P
0
10
20
30
sec

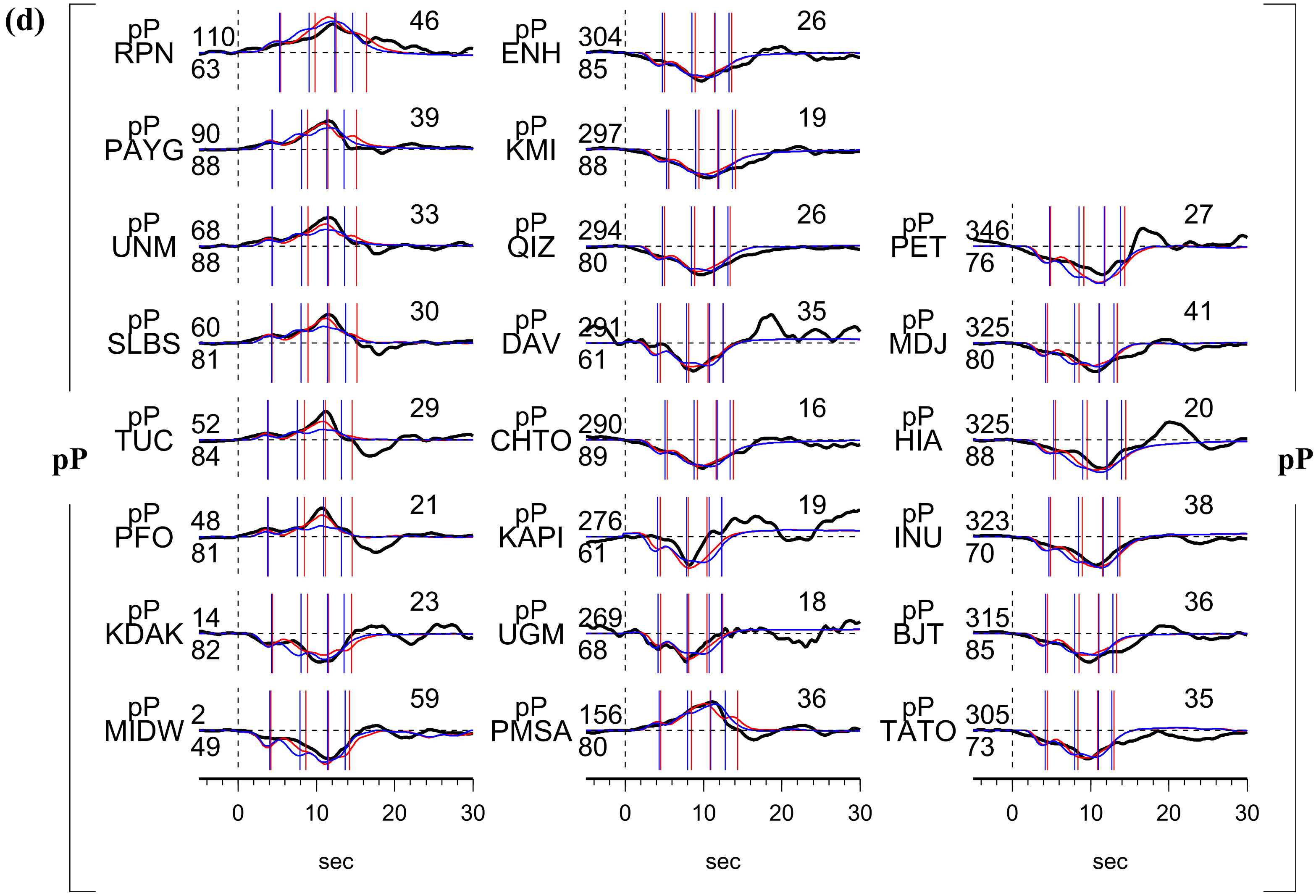
(d)
pP
pP
pP RPN 110 63 46
pP PAYG 90 88 39
pP UNM 68 88 33
pP SLBS 60 81 30
pP TUC 52 84 29
pP PFO 48 81 21
pP KDAK 14 82 23
pP MIDW 2 49 59
pP ENH 304 85 26
pP KMI 297 88 19
pP QIZ 294 80 26
pP DAV 291 61 35
pP CHTO 290 89 16
pP KAPI 276 61 19
pP UGM 269 68 18
pP PMSA 156 80 36
pP PET 346 76 27
pP MDJ 325 80 41
pP HIA 325 88 20
pP INU 323 70 38
pP BJT 315 85 36
pP TATO 305 73 35
0
10
20
30
sec
0
10
20
30
sec
0
10
20
30
sec

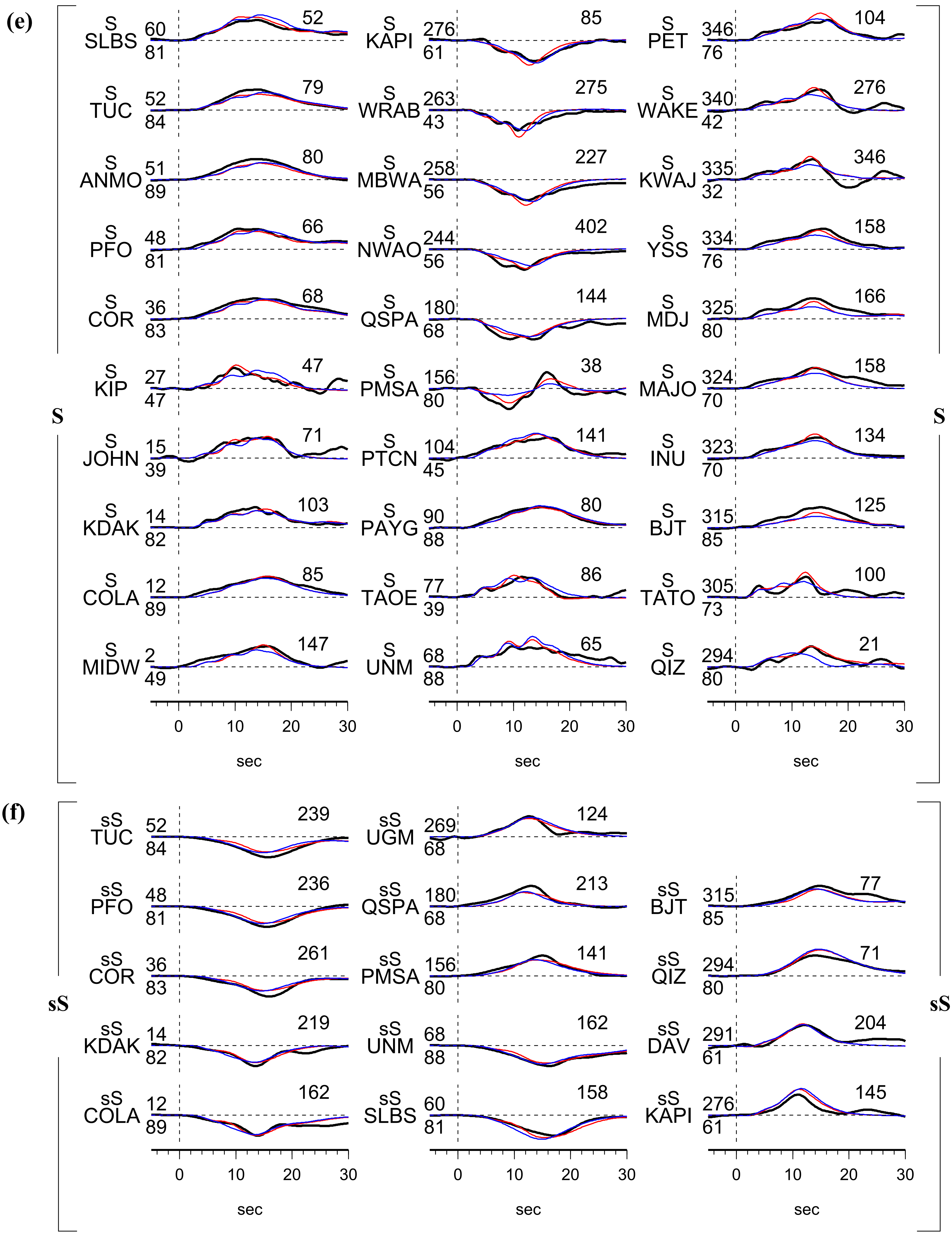
(e)
S
S SLBS 60 81 52
S KAPI 276 61 85
S PET 346 76 104
S TUC 52 84 79
S WRAB 263 43 275
S WAKE 340 42 276
S ANMO 51 89 80
S MBWA 258 56 227
S KWAJ 335 32 346
S PFO 48 81 66
S NWAO 244 56 402
S YSS 334 76 158
S COR 36 83 68
S QSPA 180 68 144
S MDJ 325 80 166
S KIP 27 47 47
S PMSA 156 80 38
S MAJO 324 70 158
S JOHN 15 39 71
S PTCN 104 45 141
S INU 323 70 134
S KDAK 14 82 103
S PAYG 90 88 80
S BJT 315 85 125
S COLA 12 89 85
S TAOE 77 39 86
S TATO 305 73 100
S MIDW 2 49 147
S UNM 68 88 65
S QIZ 294 80 21
0
10
20
30
sec
(f)
sS
sS TUC 52 84 239
sS UGM 269 68 124
sS PFO 48 81 236
sS QSPA 180 68 213
sS BJT 315 85 77
sS COR 36 83 261
sS PMSA 156 80 141
sS QIZ 294 80 71
sS KDAK 14 82 219
sS UNM 68 88 162
sS DAV 291 61 204
sS COLA 12 89 162
sS SLBS 60 81 158
sS KAPI 276 61 145
0
10
20
30
sec

E26. The 24 May 2013 Mw 8.3 Okhotsk earthquake

The earthquake occurred beneath Sea of Okhotsk, with moment magnitude of Mw 8.3 in the GCMT solution and a hypocenter depth of 598 km reported by the USGS (United States Geological Survey). The seismic source directivity analyses showed that the source front generally propagates along ~N160°E and ~35 km downward. The multiple source inversion results suggested that the earthquake could be modeled by six sub-events (Table S4-26). Sub-events 1a and 1b exhibit bilateral propagation to northeast and southeast. Sub-events 2 and 4 propagate downward along an azimuth of 155°-165°, while sub-event 3 occurs southeast to the initiation point but northwest to subevent 2 (Fig. S4-26a). The inverted source region has a horizontal extension of 64 km and a depth extension of 35 km (Fig. S4-26b). The best planar (sub-vertical plane) model cannot fit the seismic waveform as the best fitting sub-event model does. The most obvious misfits of the best planar model are present at stations around 90˚ and 270˚. The sub-events arrive earlier in the observed P waveforms than in the synthetics at stations POHA, KIP, JOHN and RAR, and later at stations ENH, CHTO, LSA, KBL, MAKZ, AAK and BRVK. The mismatch of arrival times is also evident in the S waveforms at stations PFO, COR and WAKE, and the sS waveforms at stations EIL, KIEV, and GRFO. The misfits of radiation pattern are evident in P waveform at station PMG and in sS waveforms at stations ANMO and TUC (Figs. 4-26c – 4-26f) (Chen et al., 2014).

Table S4-26. Source parameters of inverted six subevents of 24 May 2013 Okhotsk Earthquake

Sub-event	dt (s)	dn (km)	de (km)	dz (km)	duration (s)	Mw	strike (°)	dip (°)	slip (°)
0	0	0	0	0	3	7.0	8.9	87.7	278.0
1a	1.7	4.3	4.6	1.1	12.0	7.9	13.7	85.2	278.1
1b	7.8	-6.2	8.5	0.1	12.0	7.9	23.3	86.6	263.6
2	12.0	-44.9	15.7	16.7	9.0	7.9	4.0	76.3	282.3
3	16.2	-21.8	10.1	4.2	11.8	7.9	17.6	85.4	256.4
4	22.5	-57.8	15.4	35.4	12.0	7.9	-5.7	69.5	272.4

(Fig. S4-26)

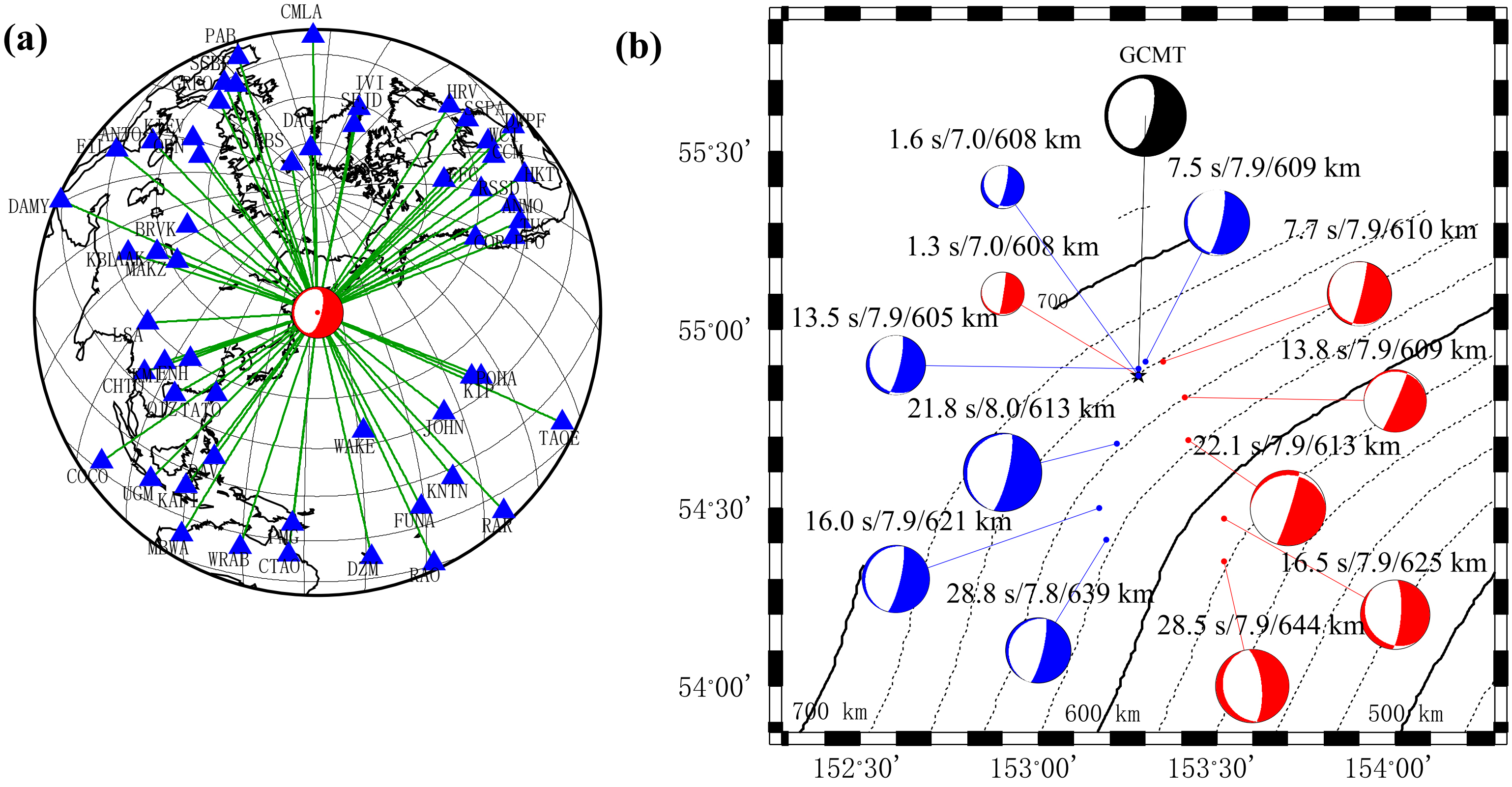
(a)
CMLA
PAR
SSB
IVI
SFJD
HRV
SSPA
DAG
KBS
ANTO
KIEV
OBN
ESK
DAMY
BRVK
KBL
MAKZ
LSA
CHTO
ENH
QIZ
TATO
POHA
KIP
TAOE
JOHN
WAKE
COCO
UGM
KAPI
DAV
KNTN
FUNA
RAR
MBWA
WRAB
CTAO
PMG
DZM
RAO
CCM
CCO
TUC
ANMO
PFO
YKT
FFC
(b)
GCMT
1.6 s/7.0/608 km
7.5 s/7.9/609 km
1.3 s/7.0/608 km
7.7 s/7.9/610 km
700
13.5 s/7.9/605 km
13.8 s/7.9/609 km
21.8 s/8.0/613 km
22.1 s/7.9/613 km
16.0 s/7.9/621 km
16.5 s/7.9/625 km
28.8 s/7.8/639 km
28.5 s/7.9/644 km
700 km
600 km
500 km
55°30'
55°00'
54°30'
54°00'
152°30'
153°00'
153°30'
154°00'

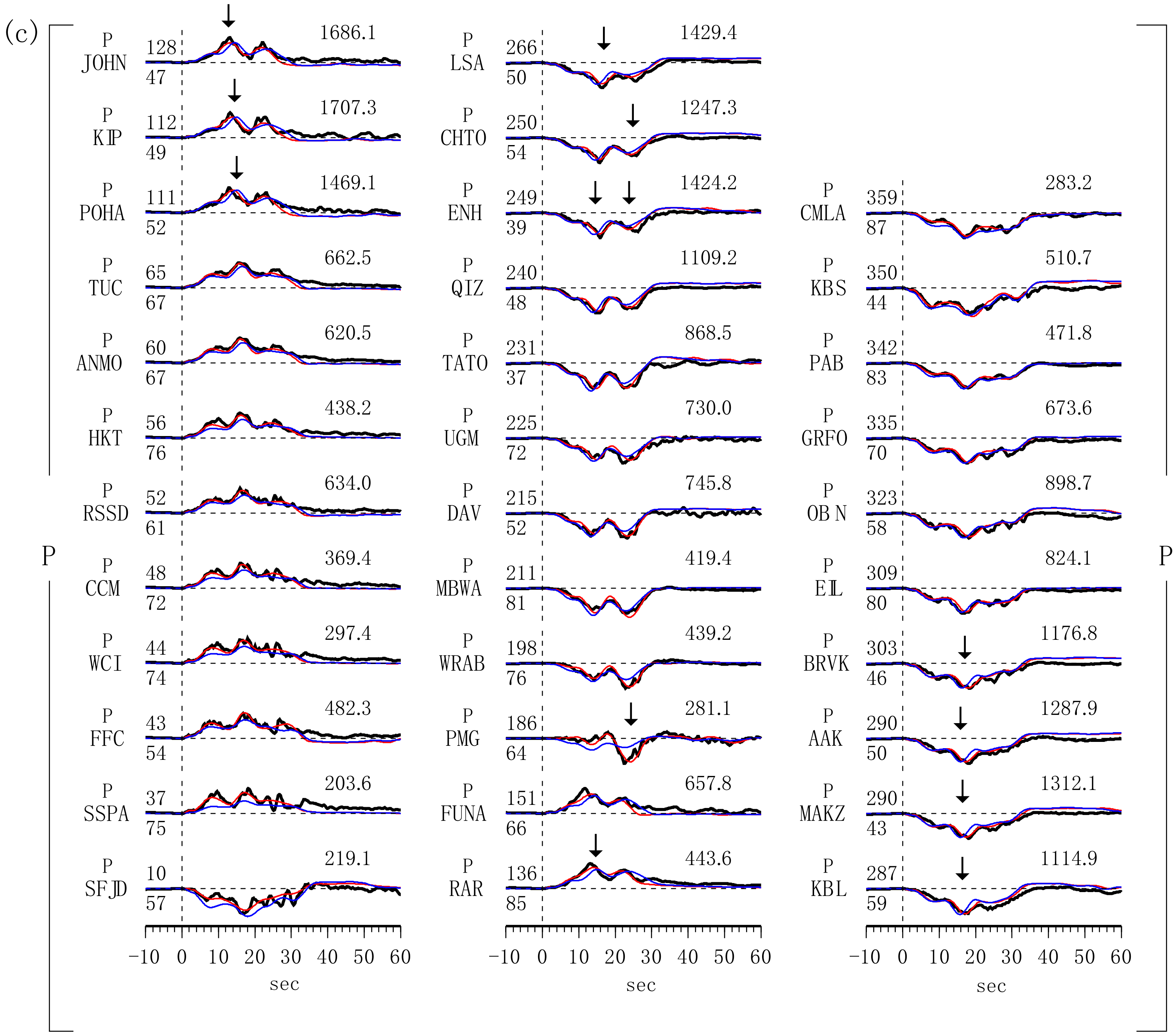
(c)
P
P JOHN 128 47 1686.1
P KIP 112 49 1707.3
P POHA 111 52 1469.1
P TUC 65 67 662.5
P ANMO 60 67 620.5
P HKT 56 76 438.2
P RSSD 52 61 634.0
P CCM 48 72 369.4
P WCI 44 74 297.4
P FFC 43 54 482.3
P SSPA 37 75 203.6
P SFJD 10 57 219.1
P LSA 266 50 1429.4
P CHTO 250 54 1247.3
P ENH 249 39 1424.2
P QIZ 240 48 1109.2
P TATO 231 37 868.5
P UGM 225 72 730.0
P DAV 215 52 745.8
P MBWA 211 81 419.4
P WRAB 198 76 439.2
P PMG 186 64 281.1
P FUNA 151 66 657.8
P RAR 136 85 443.6
P CMLA 359 87 283.2
P KBS 350 44 510.7
P PAB 342 83 471.8
P GRFO 335 70 673.6
P OBN 323 58 898.7
P EIL 309 80 824.1
P BRVK 303 46 1176.8
P AAK 290 50 1287.9
P MAKZ 290 43 1312.1
P KBL 287 59 1114.9
−10 0 10 20 30 40 50 60
sec

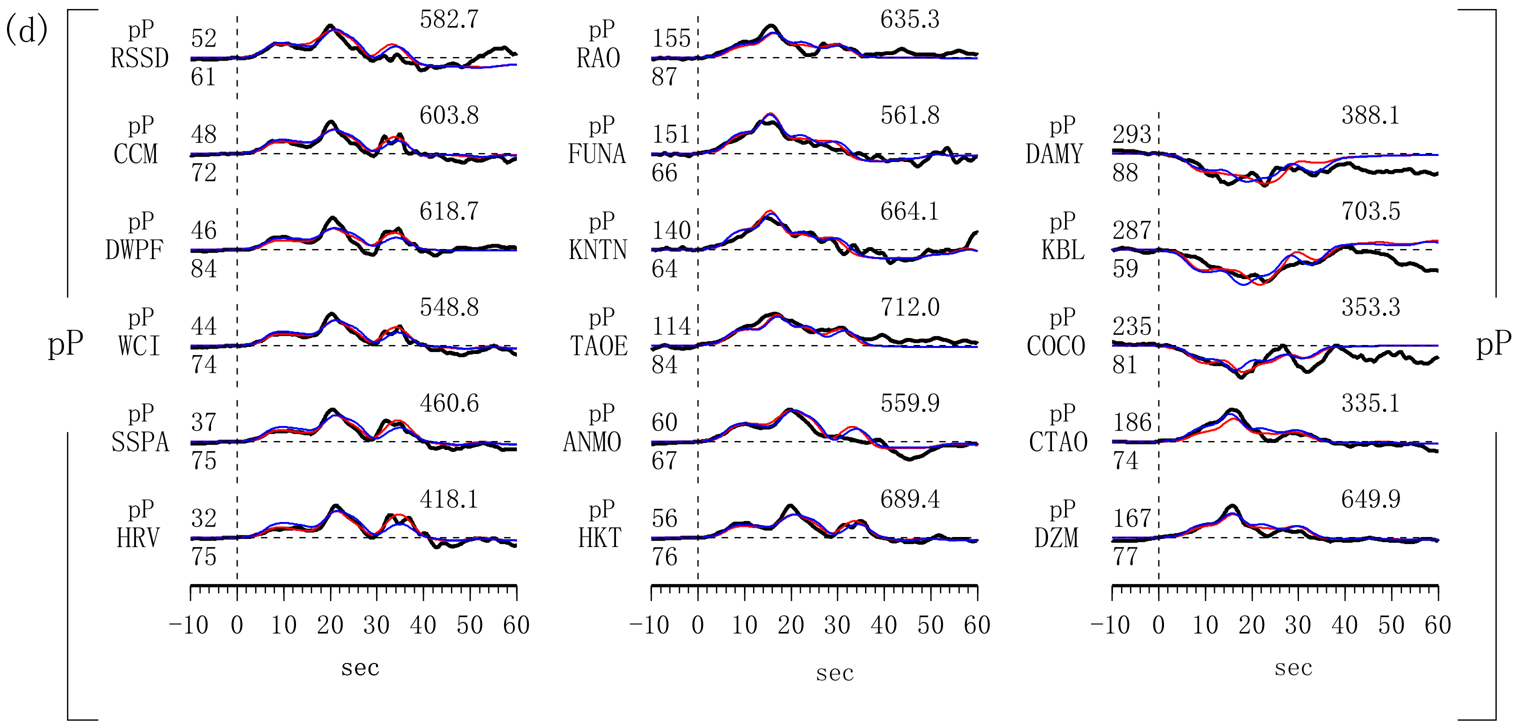
(d)
pP
pP RSSD 52 61 582.7
pP CCM 48 72 603.8
pP DWPF 46 84 618.7
pP WCI 44 74 548.8
pP SSPA 37 75 460.6
pP HRV 32 75 418.1
pP RAO 155 87 635.3
pP FUNA 151 66 561.8
pP KNTN 140 64 664.1
pP TAOE 114 84 712.0
pP ANMO 60 67 559.9
pP HKT 56 76 689.4
pP DAMY 293 88 388.1
pP KBL 287 59 703.5
pP COCO 235 81 353.3
pP CTAO 186 74 335.1
pP DZM 167 77 649.9
−10 0 10 20 30 40 50 60
sec

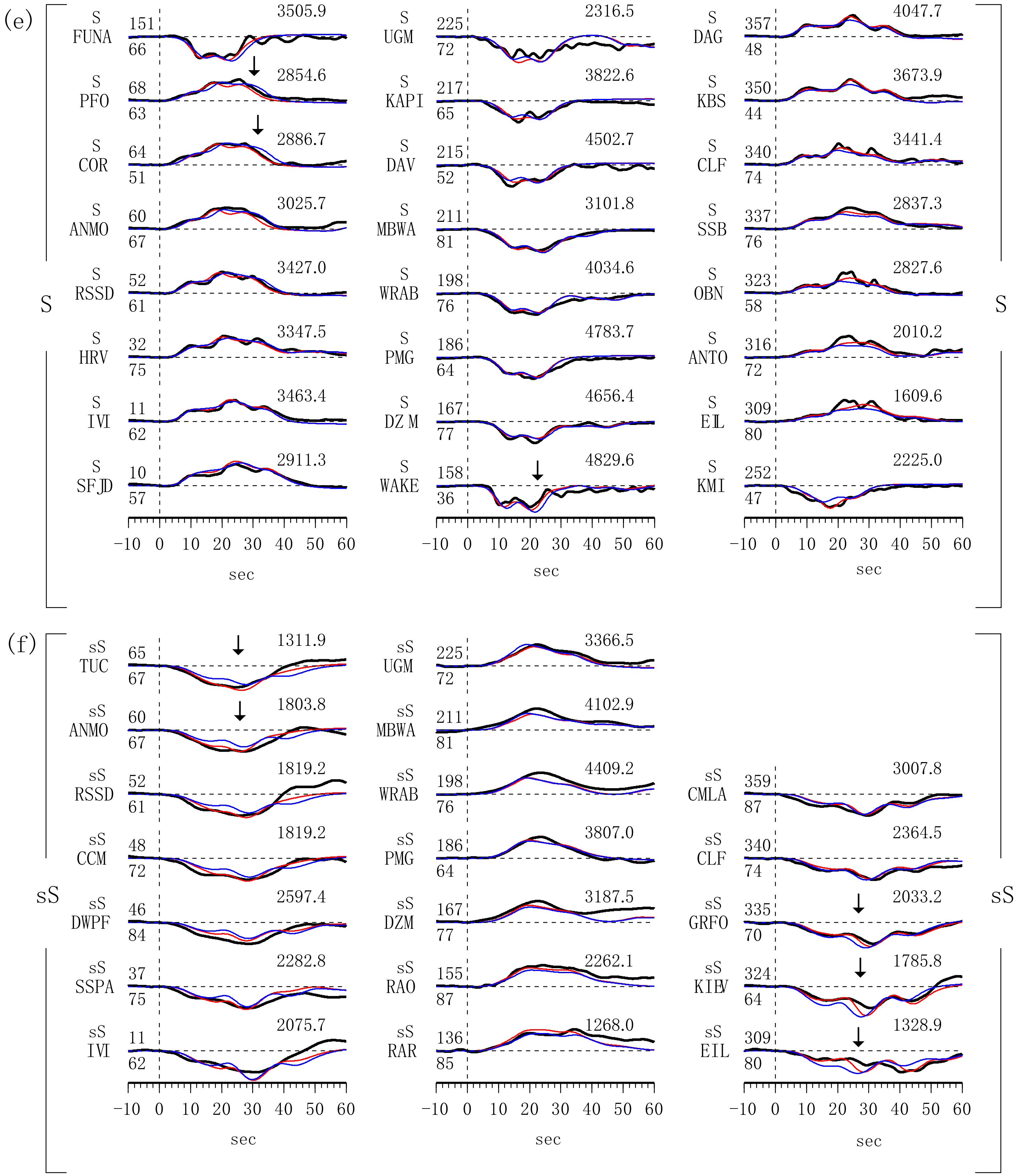
(e)
S
S FUNA 151 66 3505.9
S PFO 68 63 2854.6
S COR 64 51 2886.7
S ANMO 60 67 3025.7
S RSSD 52 61 3427.0
S HRV 32 75 3347.5
S IVI 11 62 3463.4
S SFJD 10 57 2911.3
S UGM 225 72 2316.5
S KAPI 217 65 3822.6
S DAV 215 52 4502.7
S MBWA 211 81 3101.8
S WRAB 198 76 4034.6
S PMG 186 64 4783.7
S DZM 167 77 4656.4
S WAKE 158 36 4829.6
S DAG 357 48 4047.7
S KBS 350 44 3673.9
S CLF 340 74 3441.4
S SSB 337 76 2837.3
S OBN 323 58 2827.6
S ANTO 316 72 2010.2
S EIL 309 80 1609.6
S KMI 252 47 2225.0
−10 0 10 20 30 40 50 60
sec
(f)
sS
sS TUC 65 67 1311.9
sS ANMO 60 67 1803.8
sS RSSD 52 61 1819.2
sS CCM 48 72 1819.2
sS DWPF 46 84 2597.4
sS SSPA 37 75 2282.8
sS IVI 11 62 2075.7
sS UGM 225 72 3366.5
sS MBWA 211 81 4102.9
sS WRAB 198 76 4409.2
sS PMG 186 64 3807.0
sS DZM 167 77 3187.5
sS RAO 155 87 2262.1
sS RAR 136 85 1268.0
sS CMLA 359 87 3007.8
sS CLF 340 74 2364.5
sS GRFO 335 70 2033.2
sS KIEV 324 64 1785.8
sS EIL 309 80 1328.9
−10 0 10 20 30 40 50 60
sec

Reference

Antolik, M., Dreger, D., Romanowicz, B., 1999. Rupture processes of large deep-focus earthquakes from inversion of moment rate functions. Journal of Geophysical Research-Solid Earth 104, 863-894.

Chen, Y., Wen, L., Ji, C., 2014. A cascading failure during the 24 May 2013 great Okhotsk deep earthquake. Journal of Geophysical Research-Solid Earth 119, 3035-3049.

Myhill, R., Warren, L.M., 2012. Fault plane orientations of deep earthquakes in the Izu-Bonin-Marianas subduction zone. Journal of Geophysical Research-Solid Earth 117.

Warren, L.M., Hughes, A.N., Silver, P.G., 2007. Earthquake mechanics and deformation in the Tonga-Kermadec subduction zone from fault plane orientations of intermediate- and deep-focus earthquakes. Journal of Geophysical Research-Solid Earth 112.

Warren, L.M., Silver, P.G., 2006. Measurement of differential rupture durations as constraints on the source finiteness of deep-focus earthquakes. Journal of Geophysical Research-Solid Earth 111.

Wiens, D.A., McGuire, J.J., Shore, P.J., Bevis, M.G., Draunidalo, K., Prasad, G., Helu, S.P., 1994. A deep earthquake aftershock sequence and implications for the rupture mechanism of deep earthuqakes. Nature 372, 540-543.

Zhan, Z., Kanamori, H., Tsai, V.C., Helmberger, D.V., Wei, S., 2014. Rupture complexity of the 1994 Bolivia and 2013 Sea of Okhotsk deep earthquakes. Earth and Planetary Science Letters 385, 89-96.

Zhang, J.W., Xu, Y., 2012. Source characteristics of the deep Philippine earthquake cluster, 23 and 24 July 2010. J. Seismol. 16, 275-289.

Supplementary Tables and Figures for Chapter 5

Table S5-1. Source parameters of inferred sub-events of E2

Sub-event	dt (s)	dn (km)	de (km)	dz (km)	duration (s)	Mw	strike (°)	dip (°)	slip (°)
I1	3.0	0.5	1.7	0.0	3.0	6.9	299.3	16.8	286.5
I2	6.1	0.9	13.2	-0.7	5.0	7.1	294.9	5.0	282.2
I3	8.9	-1.1	15.3	-1.4	4.8	7.2	308.3	8.2	306.9
I4	11.5	5.2	22.9	-2.1	4.0	7.1	299.3	5.1	291.4
S1	15.4	2.6	20.4	8.9	7.6	7.7	297.1	14.5	288.3
S2	19.2	5.6	25.5	5.0	8.0	7.8	293.4	7.3	286.1
S3	24.6	15.4	14.5	5.1	10.0	7.8	312.2	11.2	308.7
S4	30.8	21.7	22.6	18.0	12.0	7.9	313.4	8.4	311.0
S5	38.4	20.2	41.2	39.0	10.0	7.8	311.6	10.0	305.9

Note: the sub-events begin with ‘I’ are the initial sub-events inferred in this study, while those begin with ‘S’ are the major sub-events inferred in our previous studies.

Table S5-2. Source parameters of inferred sub-events of E8

Sub-event	dt (s)	dn (km)	de (km)	dz (km)	duration (s)	Mw	strike (°)	dip (°)	slip (°)
I1	0.7	1.6	0.2	0.0	1.2	5.8	86.0	22.5	172.5
I2	2.2	3.9	2.4	2.0	1.2	6.0	73.7	40.1	216.1
I3	3.9	2.0	5.6	4.2	1.2	6.0	91.9	22.9	199.1
I4	5.8	-0.1	5.4	1.5	1.2	5.9	86.8	22.0	200.2
I5	7.2	-0.3	0.0	-1.9	1.2	6.1	76.3	34.9	216.5
S1	9.9	-7.3	6.3	-2.5	4.0	6.6	94.5	20.3	198.6
S2	14.1	8.7	12.7	-4.4	4.0	6.8	89.9	29.1	201.0
S3	17.2	27.0	12.4	-4.0	4.6	6.7	90.5	33.1	206.8
S4	23.8	24.5	-14.7	-8.1	5.0	6.5	56.4	14.0	158.9

Table S5-3. Source parameters of inferred sub-events of E14

Sub-event	dt (s)	dn (km)	de (km)	dz (km)	duration (s)	Mw	strike (°)	dip (°)	slip (°)
I1	1.4	0.0	0.0	0.0	2.4	6.1	306.7	38.8	12.8
I2	3.3	4.0	3.0	0.0	1.6	6.1	293.6	38.8	9.1
I3	5.6	-2.8	-13.2	0.0	1.6	6.3	311.1	28.6	3.3
S1	7.9	-15.9	1.6	-0.6	3.0	7.0	314.2	6.5	27.7
S2	10.1	-8.5	5.3	3.1	3.0	7.0	326.0	9.6	40.8

Table S5-4. Source parameters of inferred sub-events of E16

Sub-event	dt (s)	dn (km)	de (km)	dz (km)	duration (s)	Mw	strike (°)	dip (°)	slip (°)
I1	0.9	1.6	-2.0	0.0	1.4	5.7	254.7	30.0	12.4
I2	3.5	-2.0	-2.8	0.0	1.6	6.1	375.0	44.6	146.2
S1	7.3	6.5	-4.6	4.8	2.2	6.9	342.9	33.9	126.1
S2	9.3	13.2	-10.8	1.3	2.4	6.8	345.2	50.7	138.2
S3	12.0	16.9	-25.3	5.8	2.4	6.5	329.4	66.0	125.7

Table S5-5. Source parameters of inferred sub-events of E20

Sub-event	dt (s)	dn (km)	de (km)	dz (km)	duration (s)	Mw	strike (°)	dip (°)	slip (°)
I1	1.1	0.0	1.0	0.0	1.8	6.7	150.0	49.7	232.7
I2	2.5	1.2	2.8	0.0	1.6	6.7	159.3	48.1	235.0
S1	4.8	3.9	2.9	-3.0	3.0	7.2	147.7	50.7	236.6
S2	7.2	8.1	8.0	-4.0	4.0	7.3	145.4	50.0	227.9
S3	9.4	-9.9	-2.7	-3.2	4.0	7.2	163.7	40.1	236.6
S4	12.8	3.6	0.0	-7.8	4.0	7.0	135.5	53.5	200.2
S5	15.5	8.6	5.0	-10.8	4.0	6.9	155.0	31.7	198.1
S6	18.8	30.4	17.8	-14.0	6.0	7.0	115.7	57.1	208.0
S7	22.1	37.4	20.8	-16.0	6.0	7.0	140.5	41.7	197.2

Table S5-6. Source parameters of inferred sub-events of E23

Sub-event	dt (s)	dn (km)	de (km)	dz (km)	duration (s)	Mw	strike (°)	dip (°)	slip (°)
I1	1.9	0.7	-0.9	0.0	2.2	6.6	241.4	28.1	327.2
I2	3.7	-3.0	6.0	0.0	2.8	6.6	236.9	19.8	322.8
S1	6.1	-7.3	7.4	-2.6	2.8	7.0	234.7	17.3	316.0
S2	8.6	-5.2	11.4	-2.8	2.4	6.9	251.0	22.1	342.2
S3	10.9	3.1	21.9	-8.6	5.0	7.3	241.1	23.6	325.2
S4	14.4	9.7	16.1	-0.1	7.0	7.3	204.5	7.4	311.2

Supplementary Figures

Because Figs. S5-1 –S5-6 have similar figure captions, we present an example figure caption for all the events. Figs. S5-1b and S5-2b are presented as Figs. 5-2b and 5-3b, respectively, in the main text.

Figs. S5-1 –S5-6 (a) Location and the GCMT focal mechanism of the earthquake (red beach ball) and used seismic stations (blue triangles), labeled with station names. The green traces are the ray paths from the earthquake and seismic stations. (b) Locations of the best-fitting models of the major sub-events (red points) and the weak initiation sub-events (green points), and the initiated location (black star) of the earthquakes, along with slab depth contours (black traces, labelled with slab depths). Black beach ball describes GCMT focal mechanism of the event. Red and green beach balls represent inferred focal mechanisms of the major sub-events and the weak initiation sub-events of the best-fitting model, labeled with the sub-event peak times, moment magnitudes and depths. (c) –(e) Observed seismograms normalized by maximum amplitudes of the whole seismograms (black traces) and the initiation phases (dash traces) comparing with synthetics predicted by the best-fitting model of the major sub-events (red traces) and the initiation sub-events (green traces), for (c) P waves, (d) pP waves and (e) SH waves. The red and green lines label the peak times of the major sub-events and the initiation sub-events.

Fig. S5-1

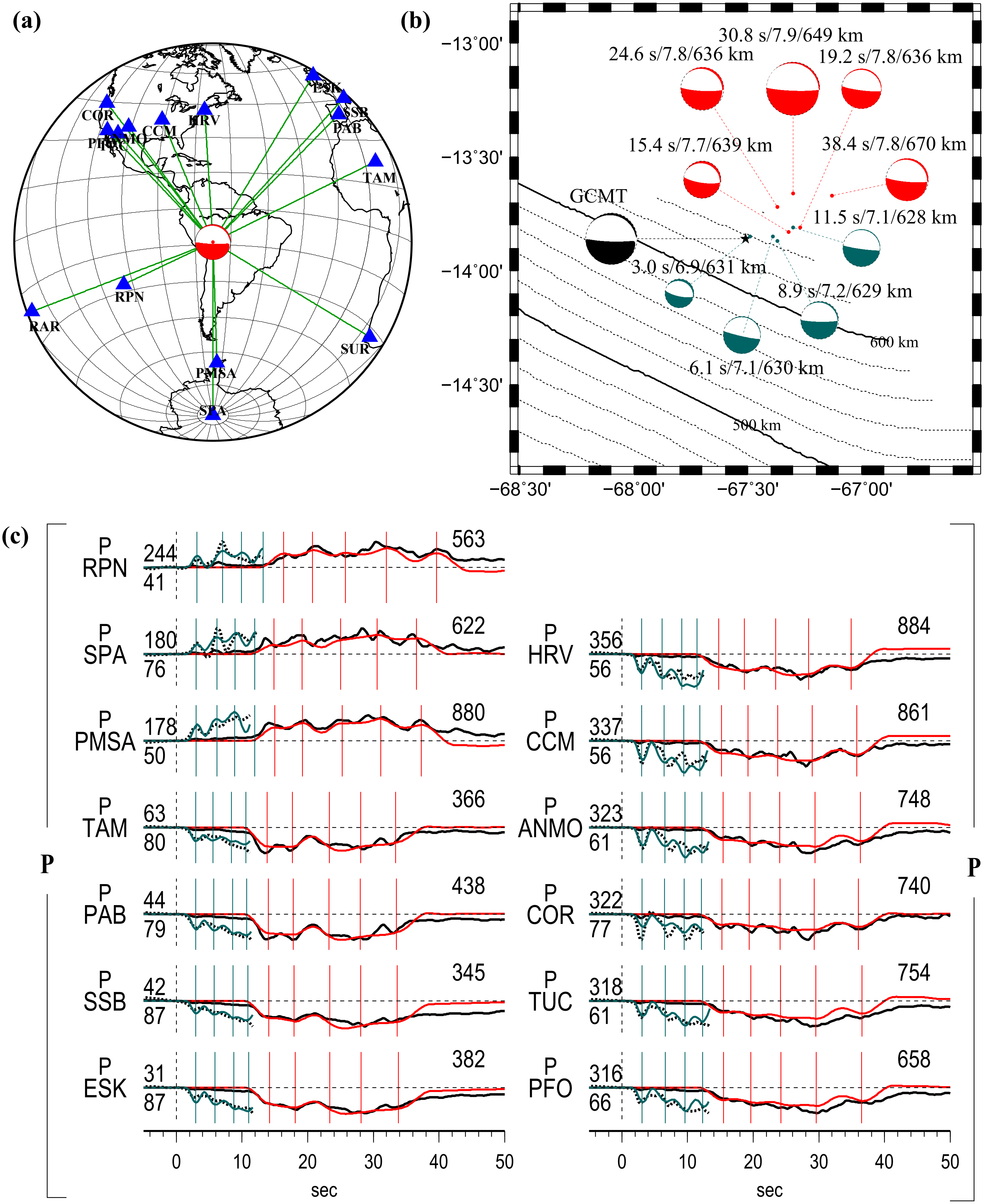
(a)
COR
PFO
TUC
ANMO
CCM
HRV
ESK
SSB
PAB
TAM
RPN
RAR
SUR
PMSA
SPA
(b)
−13˚00'
−13˚30'
−14˚00'
−14˚30'
−68˚30'
−68˚00'
−67˚30'
−67˚00'
30.8 s/7.9/649 km
24.6 s/7.8/636 km
19.2 s/7.8/636 km
15.4 s/7.7/639 km
38.4 s/7.8/670 km
GCMT
11.5 s/7.1/628 km
3.0 s/6.9/631 km
8.9 s/7.2/629 km
6.1 s/7.1/630 km
600 km
500 km
(c)
P
RPN
244
41
563
P
SPA
180
76
622
P
PMSA
178
50
880
P
TAM
63
80
366
P
PAB
44
79
438
P
SSB
42
87
345
P
ESK
31
87
382
P
HRV
356
56
884
P
CCM
337
56
861
P
ANMO
323
61
748
P
COR
322
77
740
P
TUC
318
61
754
P
PFO
316
66
658
0
10
20
30
40
50
sec
0
10
20
30
40
50
sec
P
P

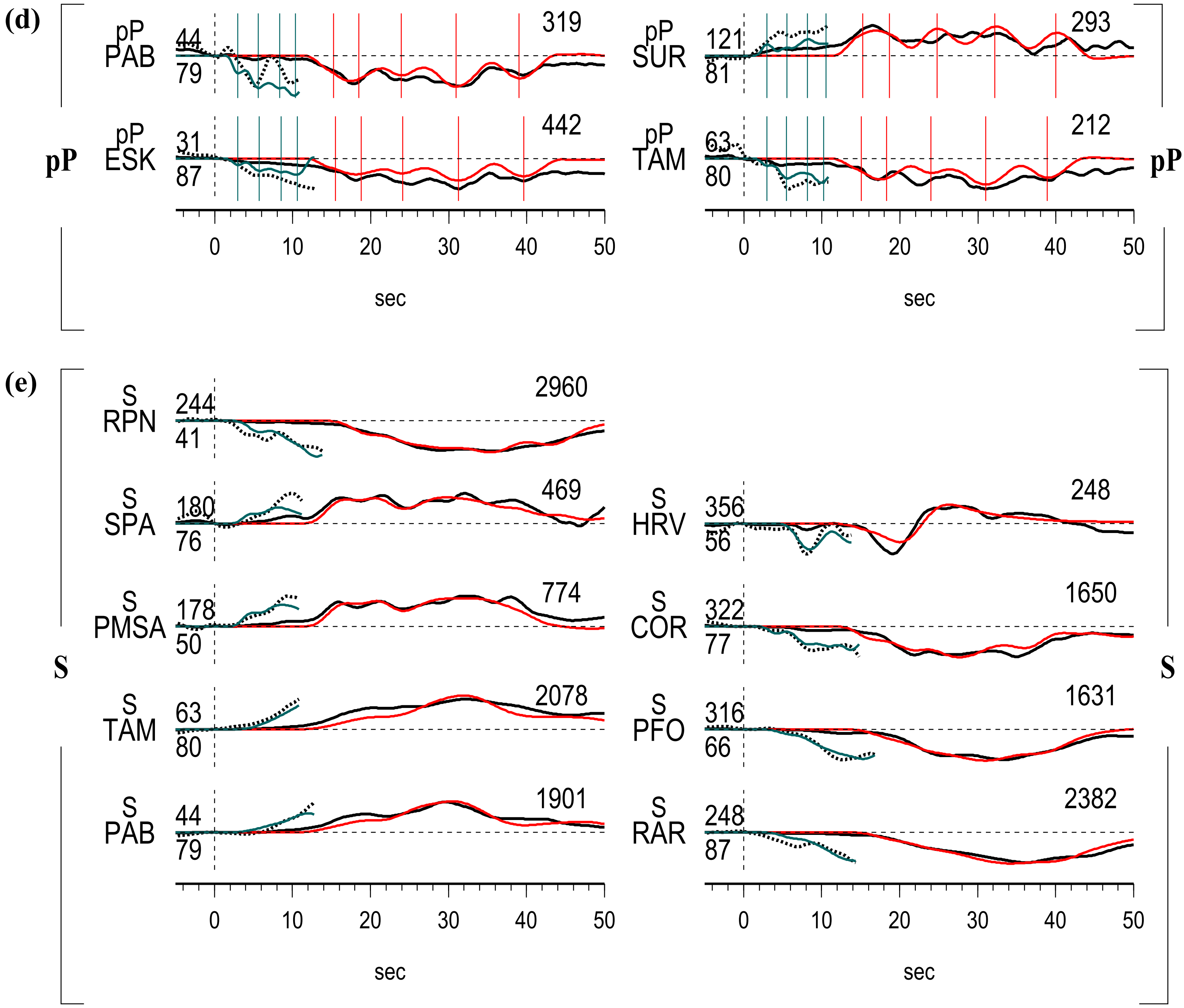
(d)
pP
pP PAB 44 79 319
pP SUR 121 81 293
pP ESK 31 87 442
pP TAM 63 80 212
pP
0 10 20 30 40 50
sec
0 10 20 30 40 50
sec
(e)
S
S RPN 244 41 2960
S SPA 180 76 469
S HRV 356 56 248
S PMSA 178 50 774
S COR 322 77 1650
S TAM 63 80 2078
S PFO 316 66 1631
S PAB 44 79 1901
S RAR 248 87 2382
S
0 10 20 30 40 50
sec
0 10 20 30 40 50
sec

Fig. S5-2

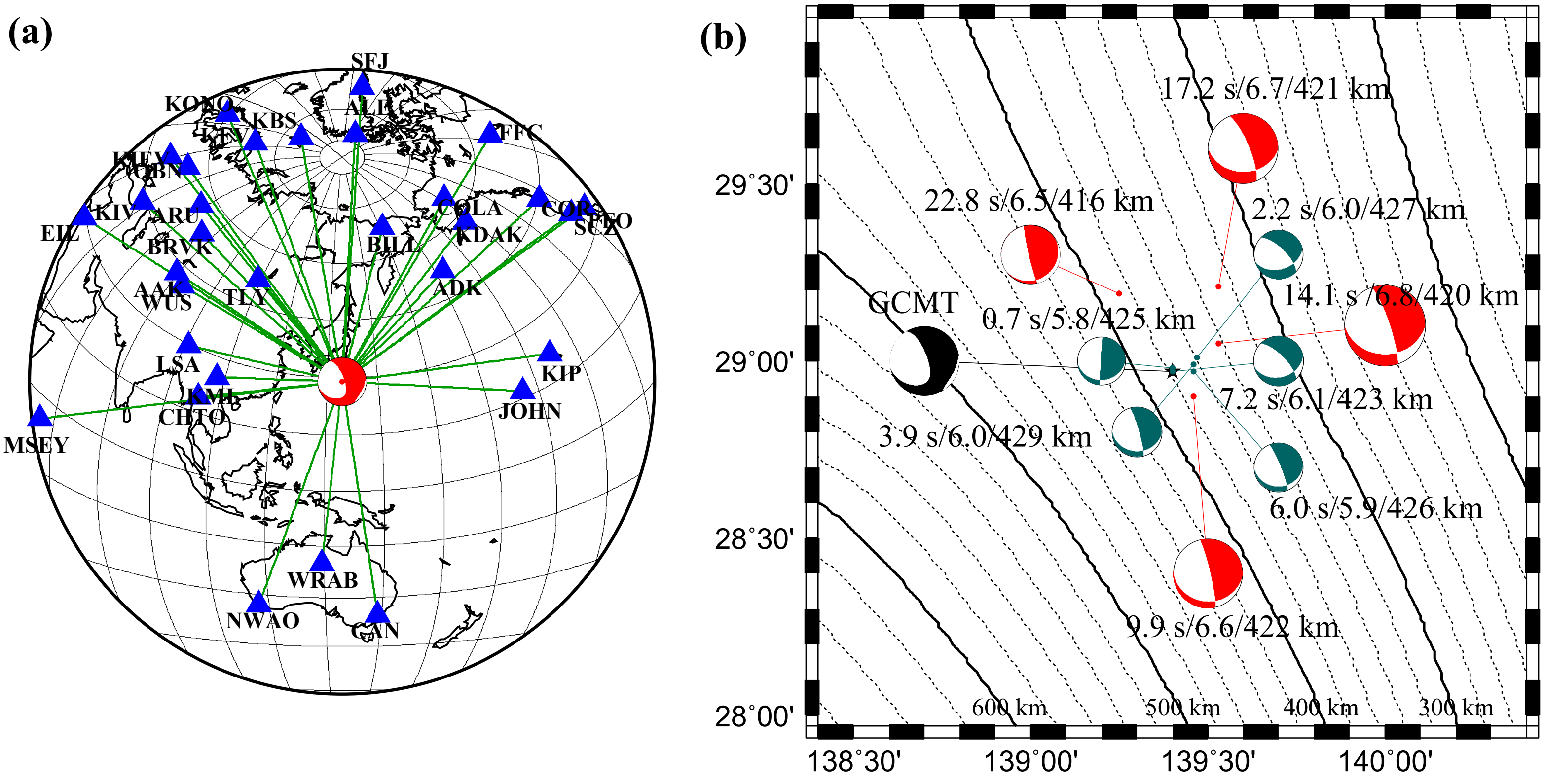
(a)
SFJ
KONO
ALE
KBS
KEV
FFC
KIEV
OBN
KIV
ARU
COLA
COR
PFO
SCZ
EIL
KDAK
BRVK
BILL
AAK
WUS
TLY
ADK
LSA
KIP
KMI
CHTO
JOHN
MSEY
WRAB
NWAO
CAN
(b)
17.2 s/6.7/421 km
22.8 s/6.5/416 km
2.2 s/6.0/427 km
14.1 s /6.8/420 km
GCMT
0.7 s/5.8/425 km
7.2 s/6.1/423 km
3.9 s/6.0/429 km
6.0 s/5.9/426 km
9.9 s/6.6/422 km
600 km
500 km
400 km
300 km
29˚30'
29˚00'
28˚30'
28˚00'
138˚30'
139˚00'
139˚30'
140˚00'

(c)

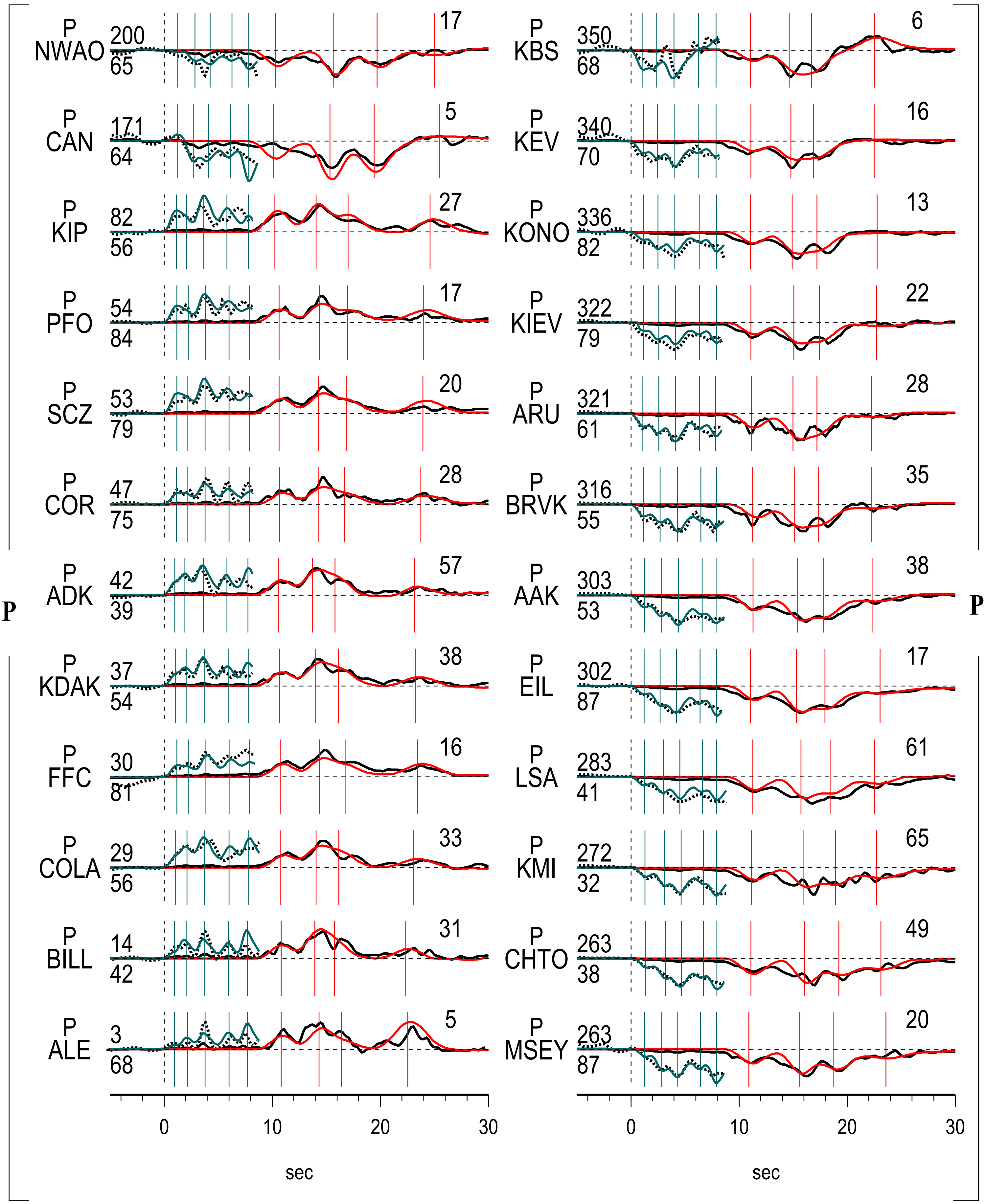

P
NWAO
200
65
17
P
KBS
350
68
6
P
CAN
171
64
5
P
KEV
340
70
16
P
KIP
82
56
27
P
KONO
336
82
13
P
PFO
54
84
17
P
KIEV
322
79
22
P
SCZ
53
79
20
P
ARU
321
61
28
P
COR
47
75
28
P
BRVK
316
55
35
P
P
ADK
42
39
57
P
AAK
303
53
38
P
P
KDAK
37
54
38
P
EIL
302
87
17
P
FFC
30
81
16
P
LSA
283
41
61
P
COLA
29
56
33
P
KMI
272
32
65
P
BILL
14
42
31
P
CHTO
263
38
49
P
ALE
3
68
5
P
MSEY
263
87
20
0
10
20
30
sec
0
10
20
30
sec

(d)

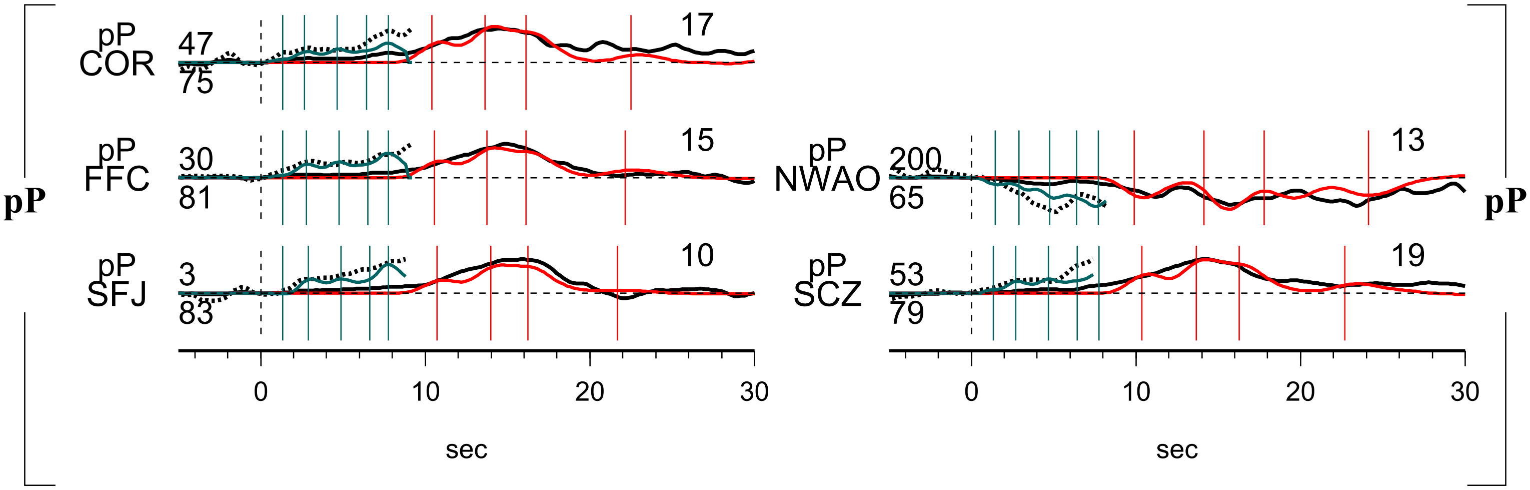
pP
pP
COR 47 75 17
FFC 30 81 15
SFJ 3 83 10
NWAO 200 65 13
SCZ 53 79 19
pP
0
10
20
30
sec
0
10
20
30
sec

(e)

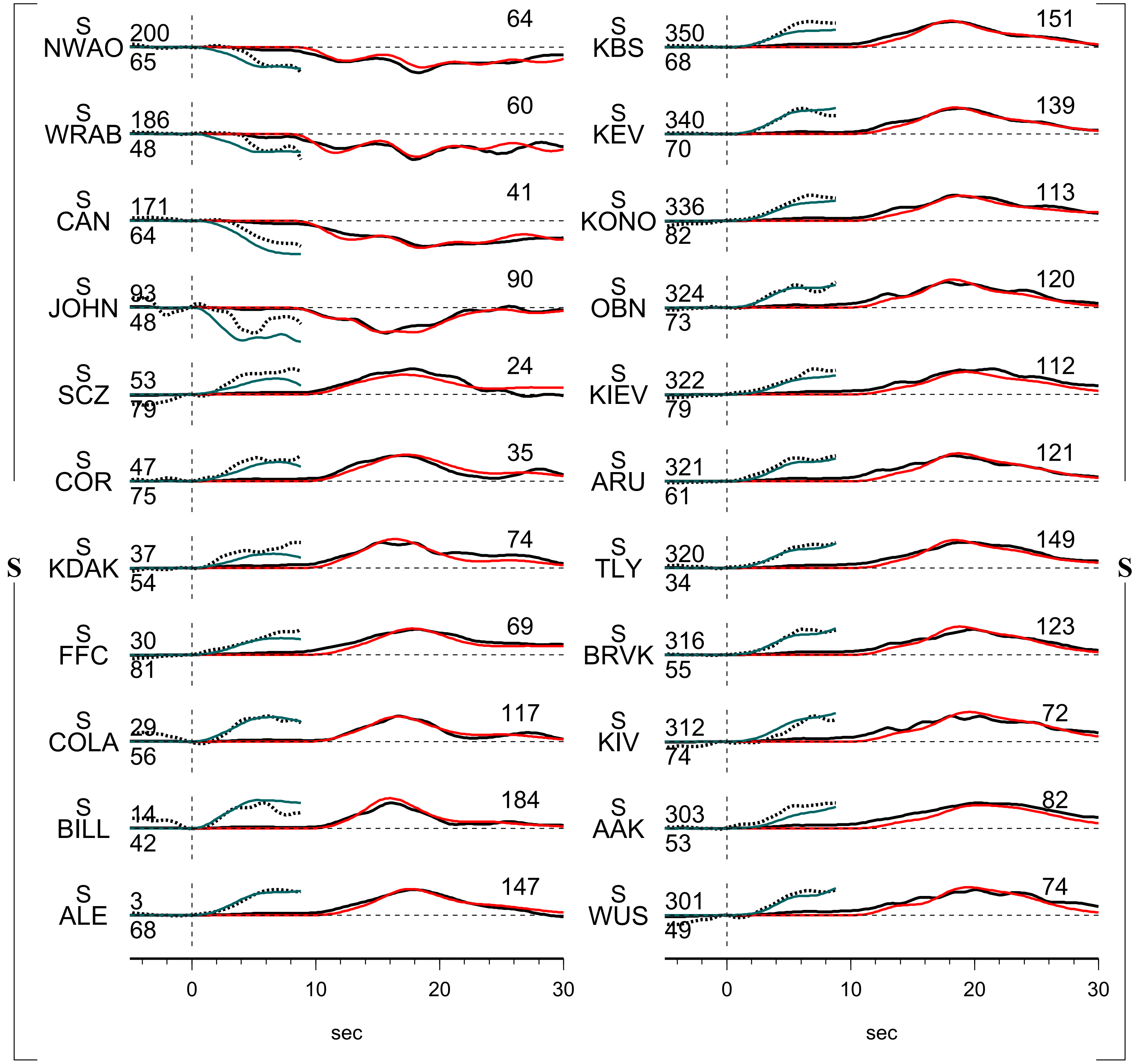
S
S
NWAO 200 65 64
WRAB 186 48 60
CAN 171 64 41
JOHN 93 48 90
SCZ 53 79 24
COR 47 75 35
KDAK 37 54 74
FFC 30 81 69
COLA 29 56 117
BILL 14 42 184
ALE 3 68 147
KBS 350 68 151
KEV 340 70 139
KONO 336 82 113
OBN 324 73 120
KIEV 322 79 112
ARU 321 61 121
TLY 320 34 149
BRVK 316 55 123
KIV 312 74 72
AAK 303 53 82
WUS 301 49 74
0
10
20
30
sec
0
10
20
30
sec

Fig. S5-3

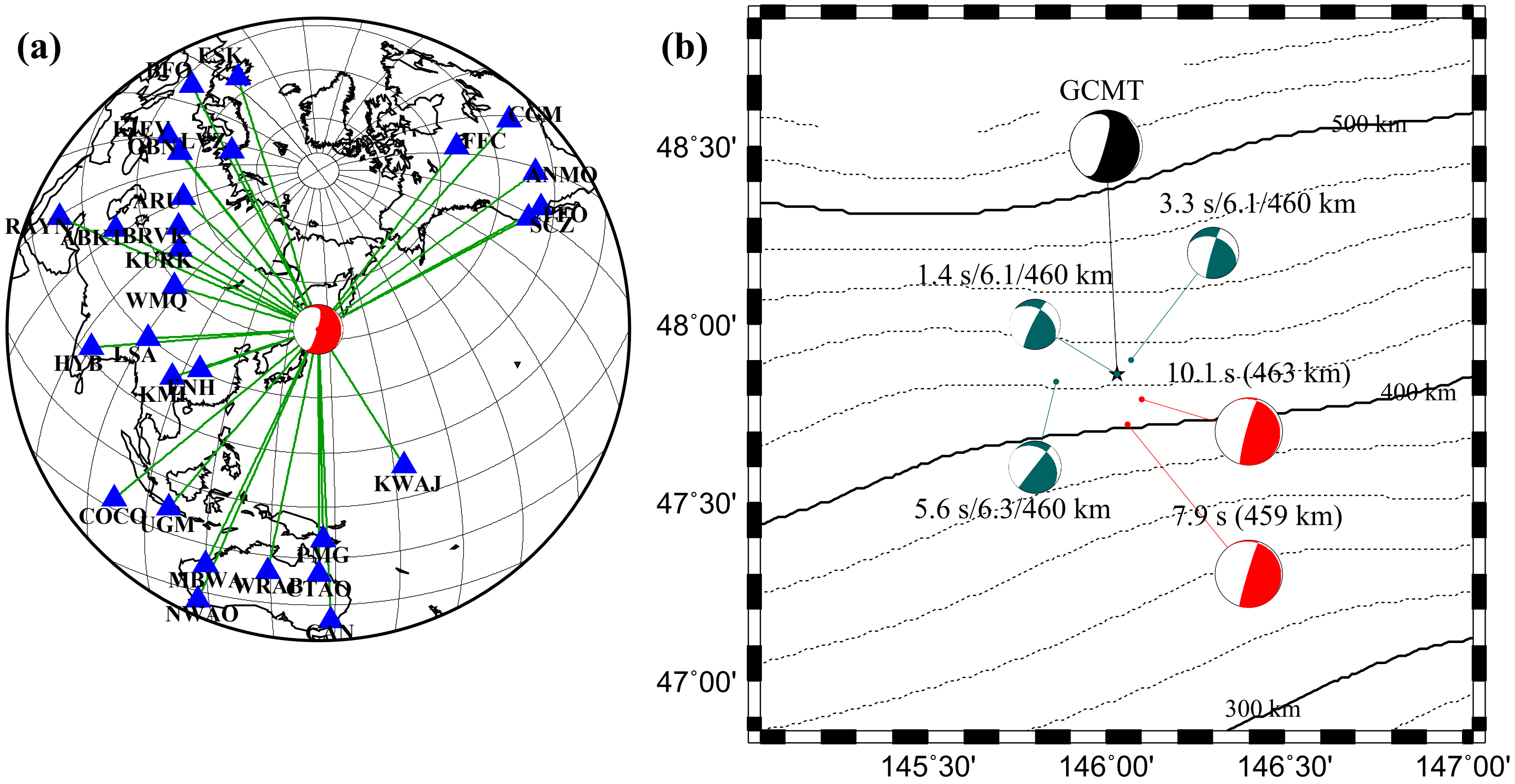

(a)
BFO
ESK
KIEV
OBN
LVZ
ARU
RAYN
ABKT
BRVK
KURK
WMQ
HYB
LSA
KMI
ENH
COCO
UGM
MBWA
NWAO
WRAB
CTAO
PMG
CAN
KWAJ
FFC
CCM
ANMO
PFO
SCZ
(b)
GCMT
500 km
3.3 s/6.1/460 km
1.4 s/6.1/460 km
10.1 s (463 km)
400 km
5.6 s/6.3/460 km
7.9 s (459 km)
300 km
48˚30'
48˚00'
47˚30'
47˚00'
145˚30'
146˚00'
146˚30'
147˚00'

(c)

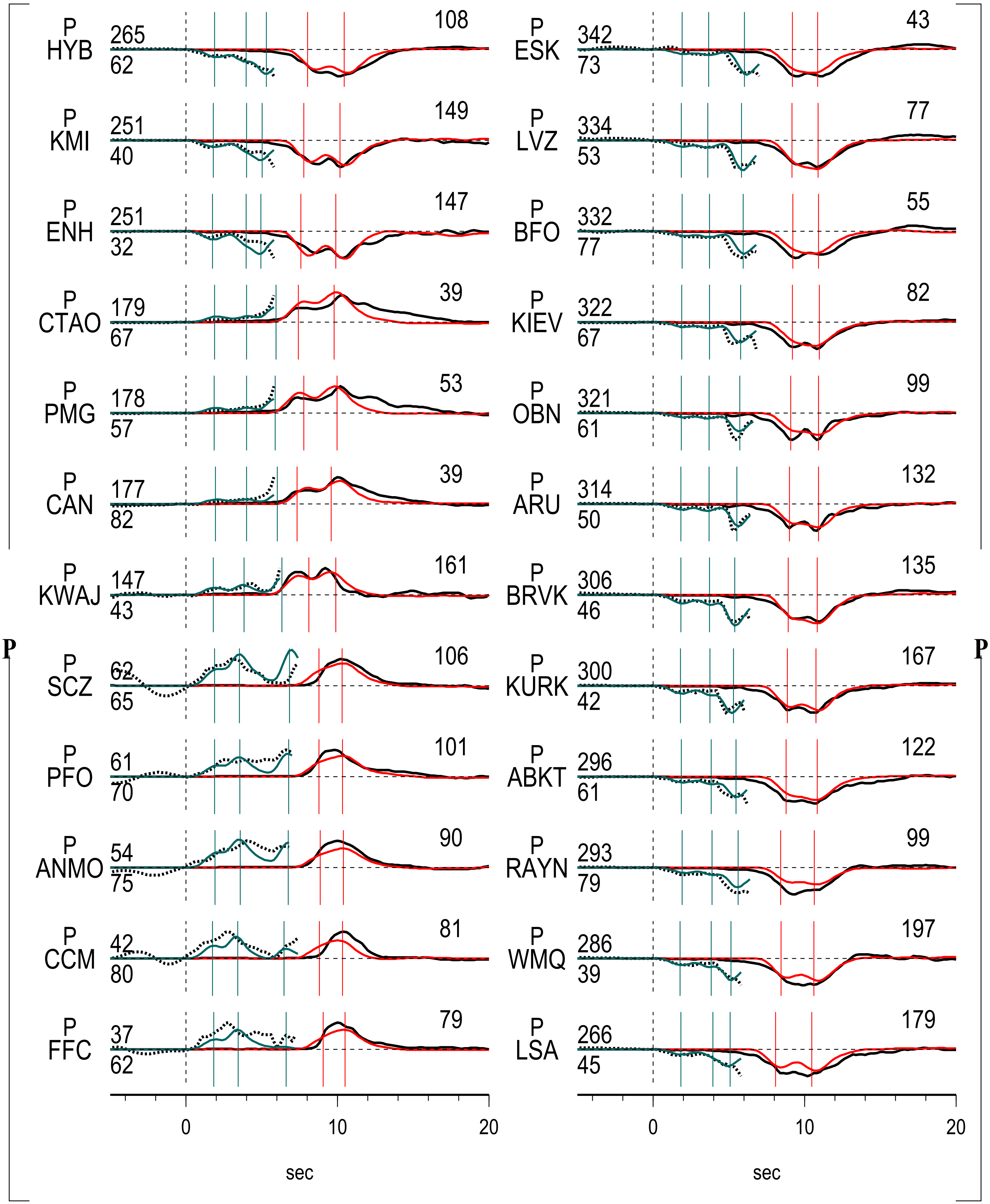
P
HYB
265
62
108
P
ESK
342
73
43
P
KMI
251
40
149
P
LVZ
334
53
77
P
ENH
251
32
147
P
BFO
332
77
55
P
CTAO
179
67
39
P
KIEV
322
67
82
P
PMG
178
57
53
P
OBN
321
61
99
P
CAN
177
82
39
P
ARU
314
50
132
P
KWAJ
147
43
161
P
BRVK
306
46
135
P
P
SCZ
62
65
106
P
KURK
300
42
167
P
PFO
61
70
101
P
ABKT
296
61
122
P
ANMO
54
75
90
P
RAYN
293
79
99
P
CCM
42
80
81
P
WMQ
286
39
197
P
FFC
37
62
79
P
LSA
266
45
179
0
10
20
sec
0
10
20
sec

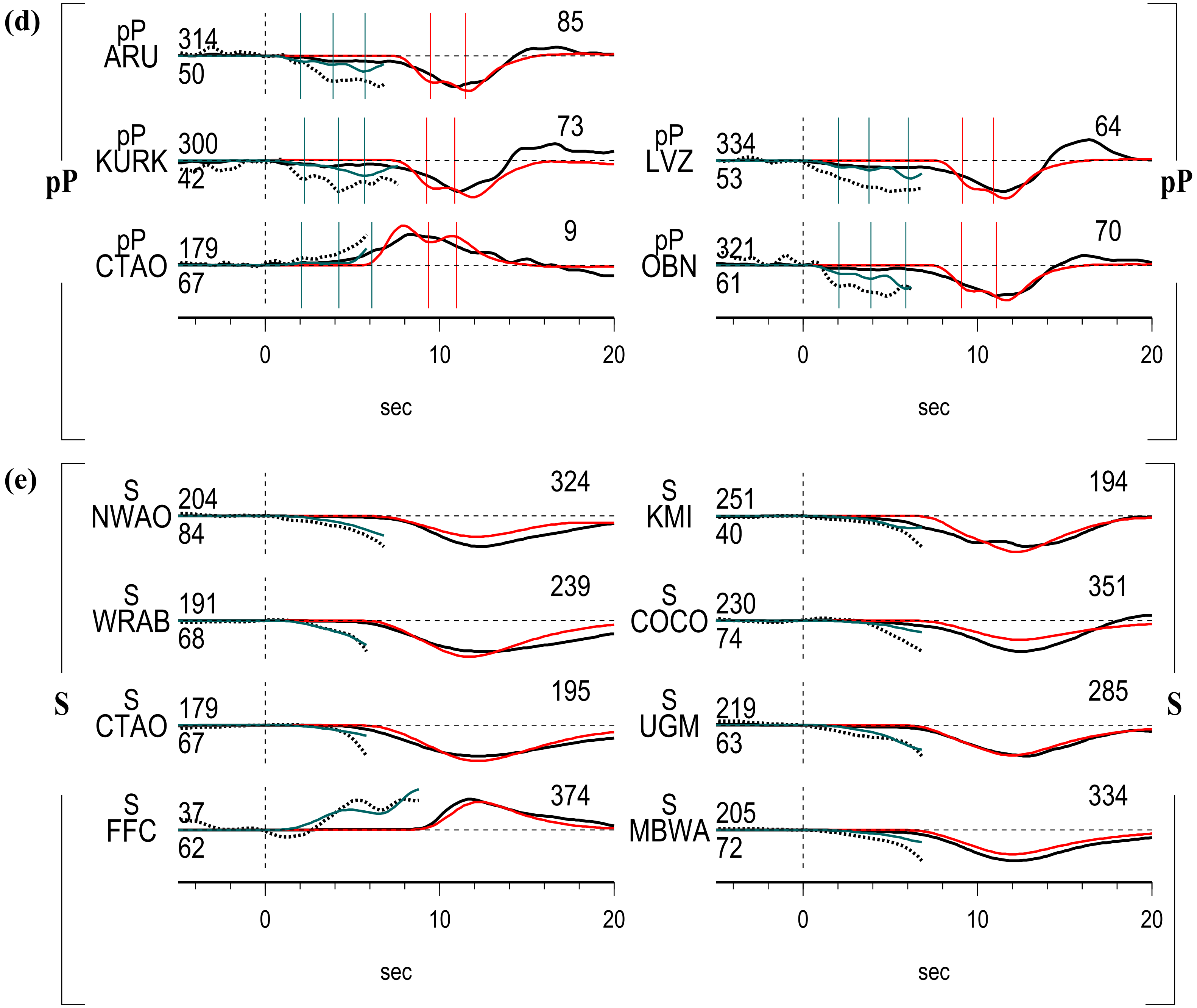
(d)
pP
pP
ARU 314 50 85
KURK 300 42 73
LVZ 334 53 64
CTAO 179 67 9
OBN 321 61 70
0
10
20
sec
(e)
S
S
NWAO 204 84 324
KMI 251 40 194
WRAB 191 68 239
COCO 230 74 351
CTAO 179 67 195
UGM 219 63 285
FFC 37 62 374
MBWA 205 72 334
0
10
20
sec

Fig. S5-4

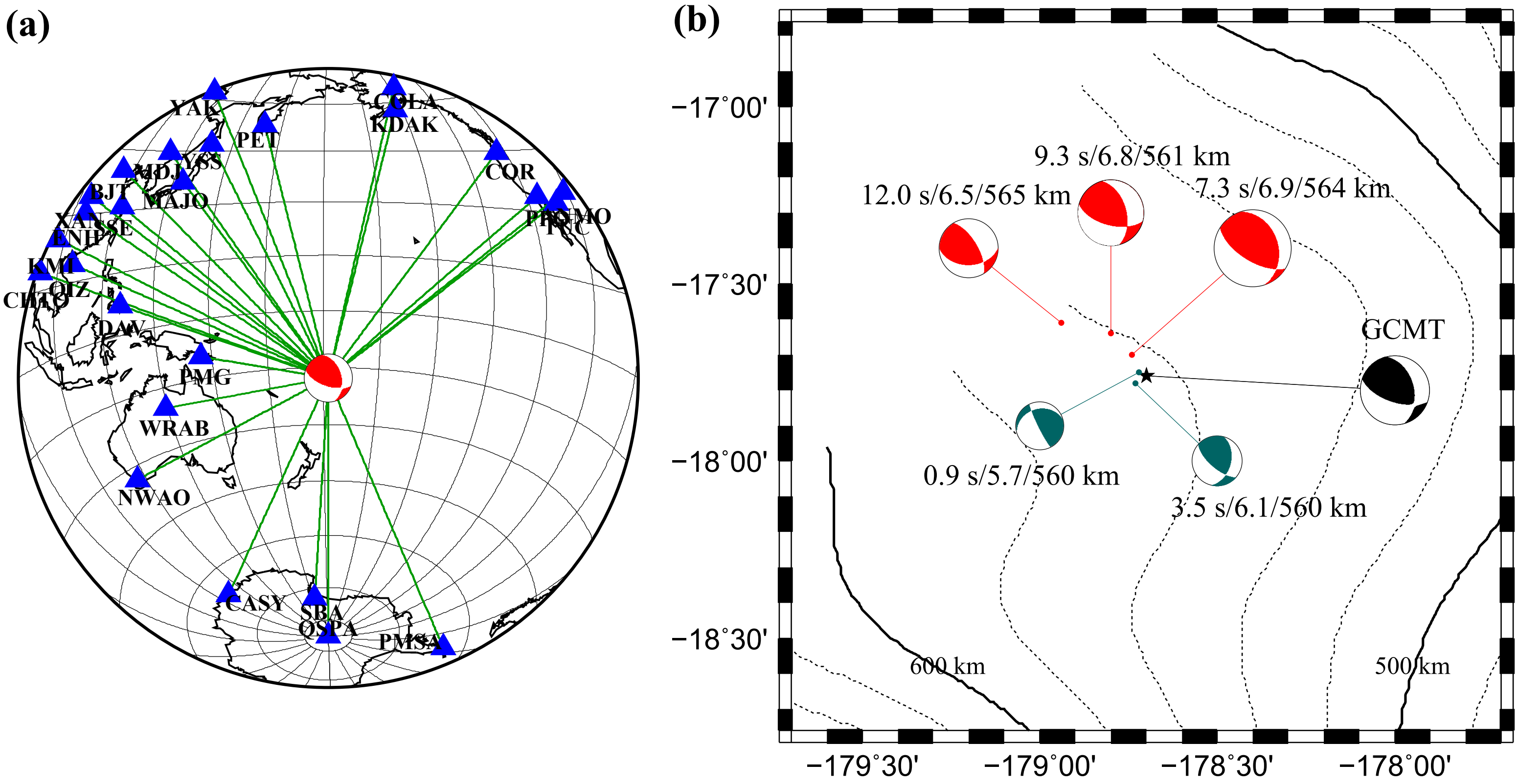
(a)
YAK
COLA
KDAK
PET
YSS
MDJ
MAJO
COR
BJT
XAN
SSE
ENH
PFO
TUC
KMI
QIZ
CHTO
DAV
PMG
WRAB
NWAO
CASY
SBA
QSPA
PMSA
(b)
−17˚00'
−17˚30'
−18˚00'
−18˚30'
−179˚30'
−179˚00'
−178˚30'
−178˚00'
9.3 s/6.8/561 km
12.0 s/6.5/565 km
7.3 s/6.9/564 km
GCMT
0.9 s/5.7/560 km
3.5 s/6.1/560 km
600 km
500 km

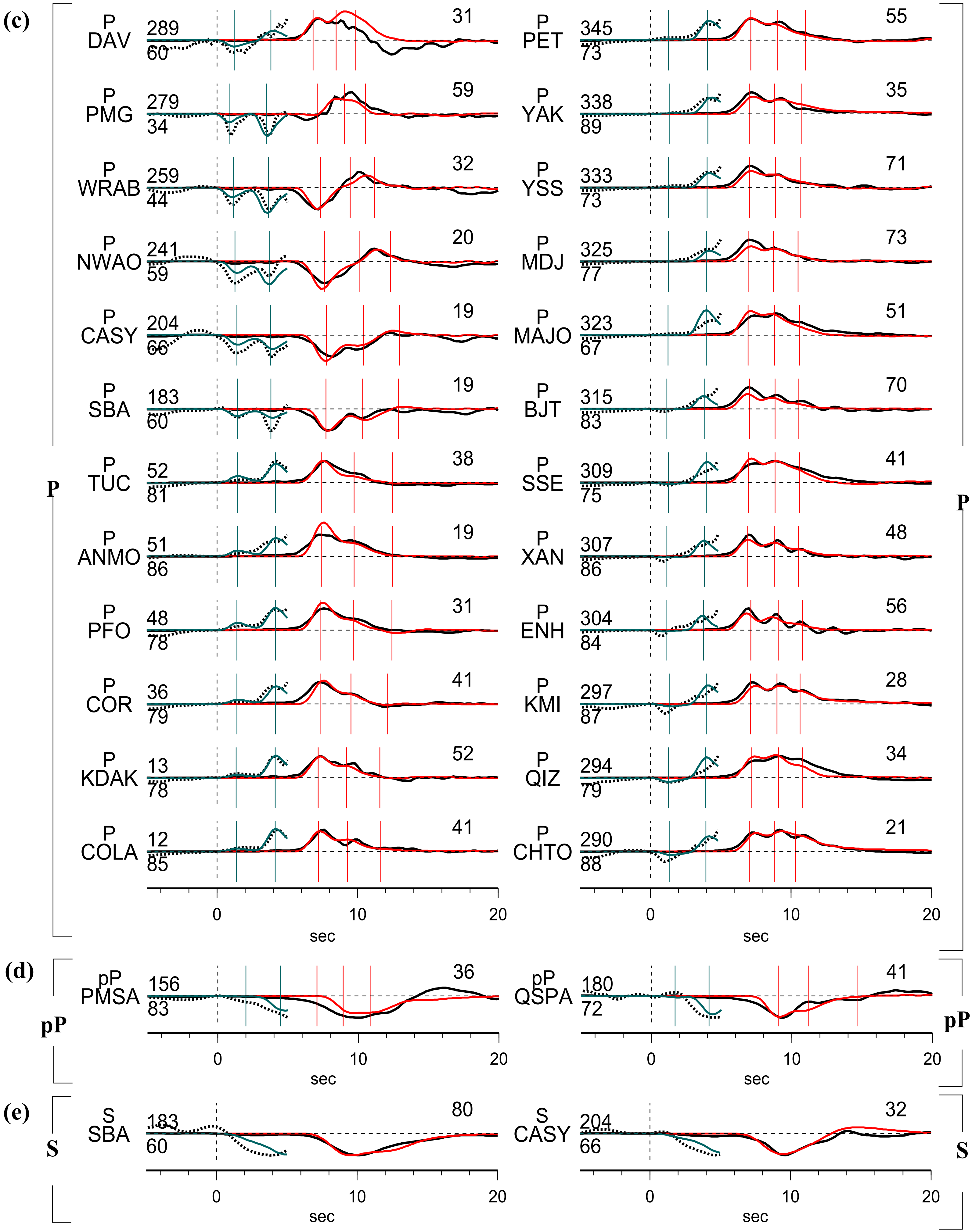
(c)
P DAV 289 60 31
P PET 345 73 55
P PMG 279 34 59
P YAK 338 89 35
P WRAB 259 44 32
P YSS 333 73 71
P NWAO 241 59 20
P MDJ 325 77 73
P CASY 204 66 19
P MAJO 323 67 51
P SBA 183 60 19
P BJT 315 83 70
P TUC 52 81 38
P SSE 309 75 41
P ANMO 51 86 19
P XAN 307 86 48
P PFO 48 78 31
P ENH 304 84 56
P COR 36 79 41
P KMI 297 87 28
P KDAK 13 78 52
P QIZ 294 79 34
P COLA 12 85 41
P CHTO 290 88 21
P
P
0
10
20
sec
0
10
20
sec
(d)
pP PMSA 156 83 36
pP QSPA 180 72 41
pP
pP
0
10
20
sec
0
10
20
sec
(e)
S SBA 183 60 80
S CASY 204 66 32
S
S
0
10
20
sec
0
10
20
sec

Fig. S5-5

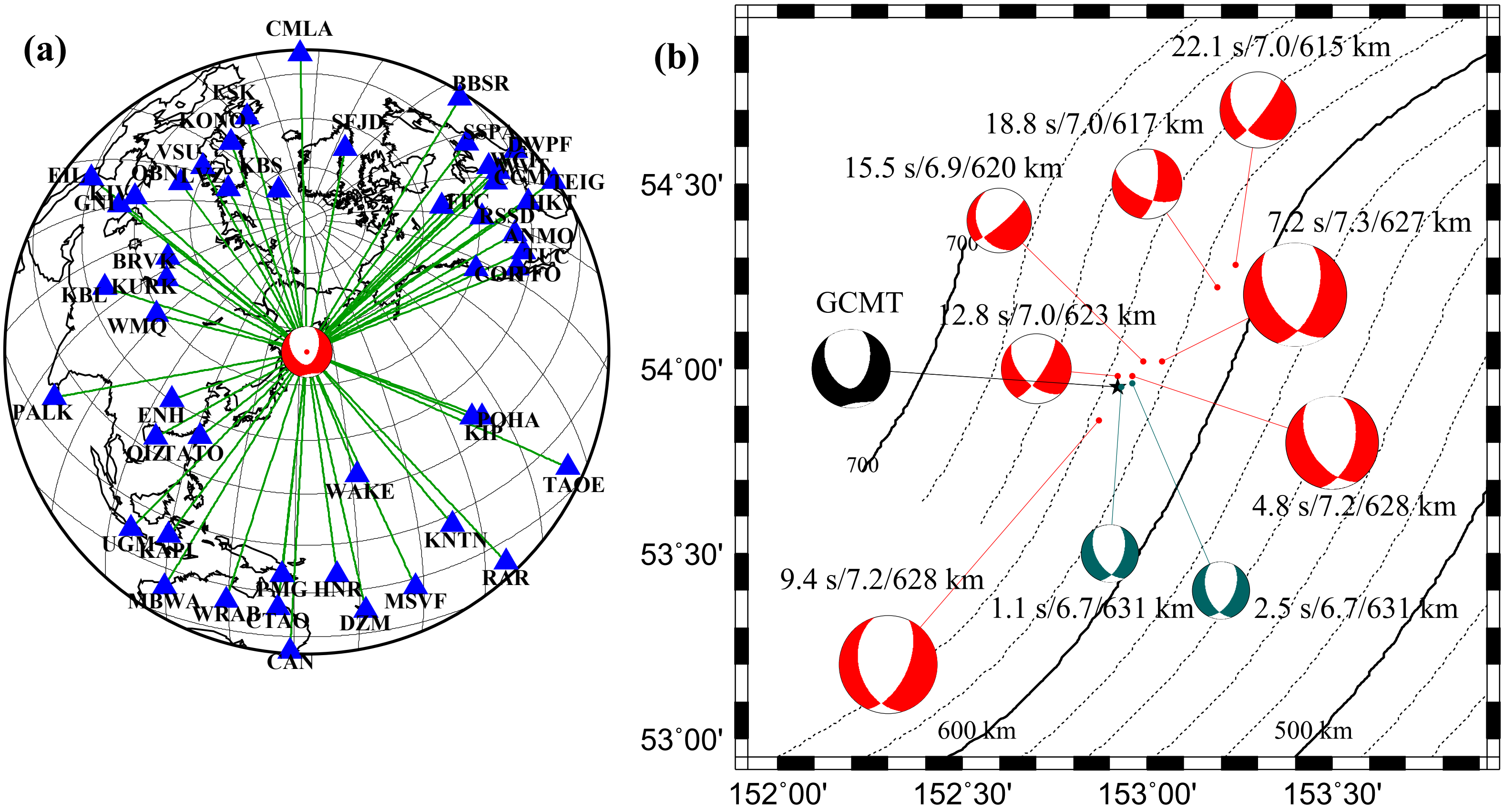
(a)
CMLA
BBSR
ESK
KONO
SFJD
SSPA
DWPF
VSU
OBN
LVZ
KBS
EIL
KIV
GNI
WVT
CCM
TEIG
TFC
HKT
RSSD
ANMO
TUC
COR
PFO
BRVK
KURK
KBL
WMQ
PALK
ENH
QIZ
TATO
POHA
KIP
TAOE
WAKE
KNTN
UGM
KAPI
RAR
PMG
HNR
MSVF
MBWA
WRAB
CTAO
DZM
CAN
(b)
22.1 s/7.0/615 km
18.8 s/7.0/617 km
15.5 s/6.9/620 km
7.2 s/7.3/627 km
GCMT
12.8 s/7.0/623 km
4.8 s/7.2/628 km
9.4 s/7.2/628 km
1.1 s/6.7/631 km
2.5 s/6.7/631 km
700
700
600 km
500 km
54°30'
54°00'
53°30'
53°00'
152°00'
152°30'
153°00'
153°30'

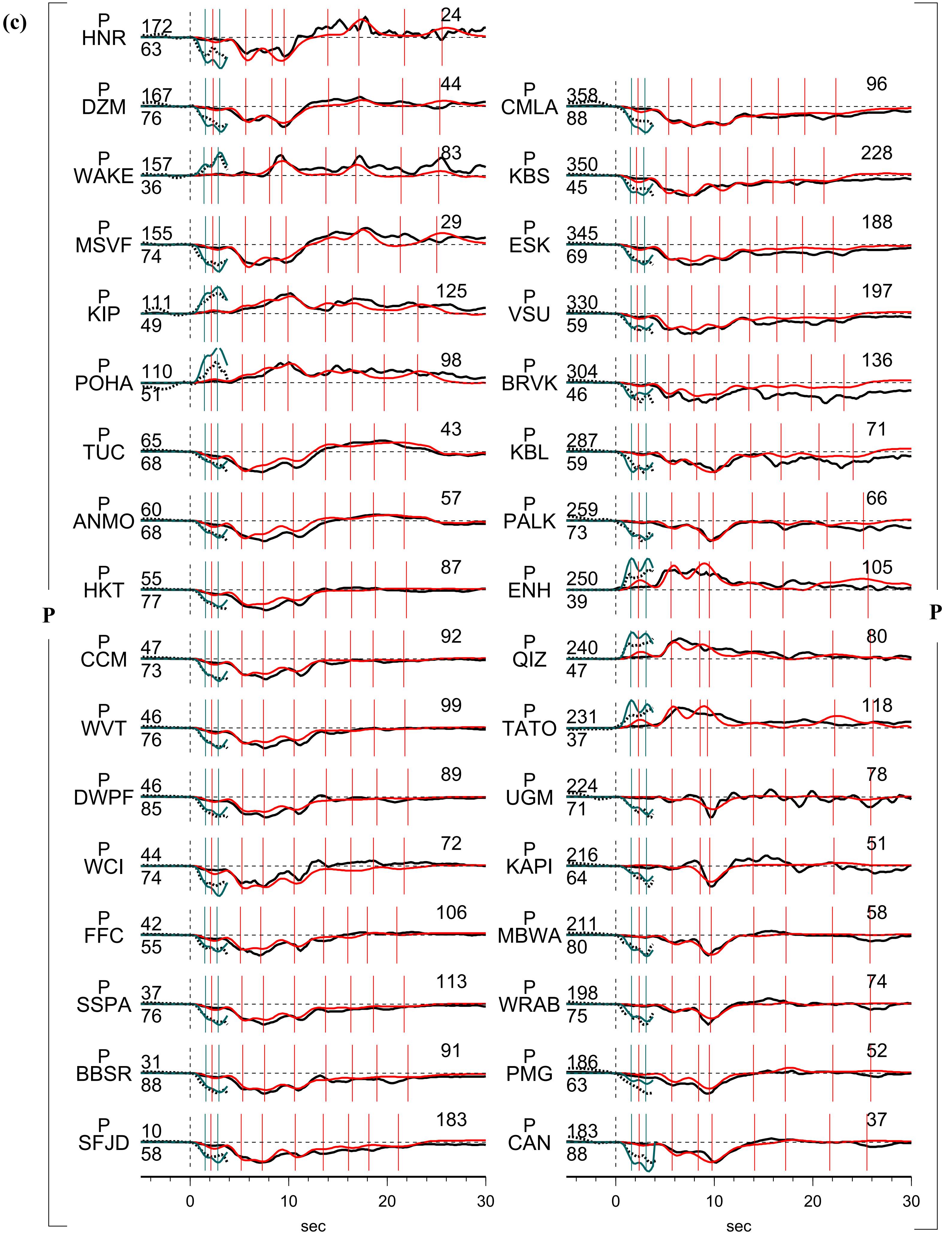
(c)
P
P
P HNR 172 63 24
P DZM 167 76 44
P WAKE 157 36 83
P MSVF 155 74 29
P KIP 111 49 125
P POHA 110 51 98
P TUC 65 68 43
P ANMO 60 68 57
P HKT 55 77 87
P CCM 47 73 92
P WVT 46 76 99
P DWPF 46 85 89
P WCI 44 74 72
P FFC 42 55 106
P SSPA 37 76 113
P BBSR 31 88 91
P SFJD 10 58 183
P CMLA 358 88 96
P KBS 350 45 228
P ESK 345 69 188
P VSU 330 59 197
P BRVK 304 46 136
P KBL 287 59 71
P PALK 259 73 66
P ENH 250 39 105
P QIZ 240 47 80
P TATO 231 37 118
P UGM 224 71 78
P KAPI 216 64 51
P MBWA 211 80 58
P WRAB 198 75 74
P PMG 186 63 52
P CAN 183 88 37
0
10
20
30
sec
0
10
20
30
sec

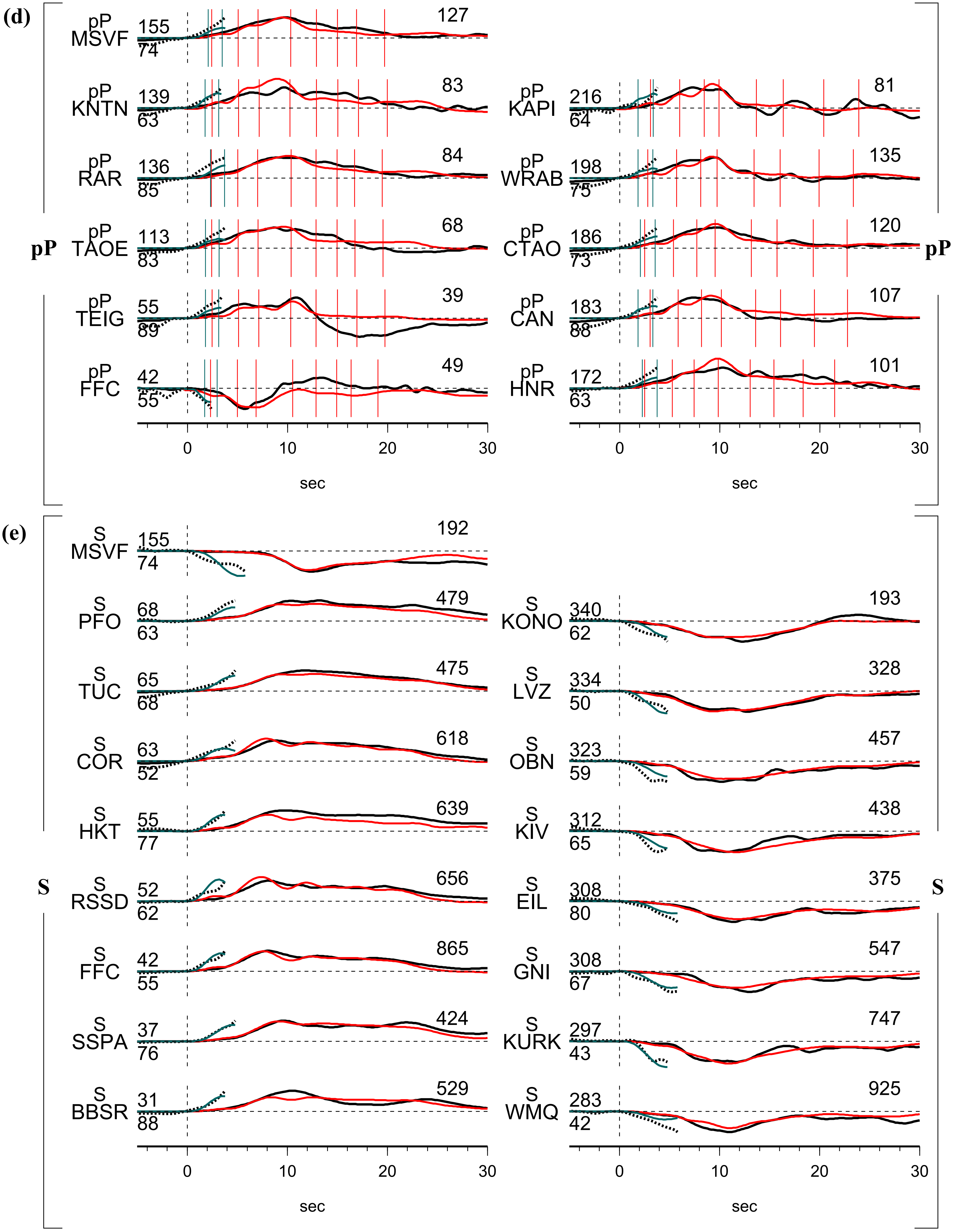

(d)
pP
pP
pP MSVF 155 74 127
pP KNTN 139 63 83
pP RAR 136 85 84
pP TAOE 113 83 68
pP TEIG 55 89 39
pP FFC 42 55 49
pP KAPI 216 64 81
pP WRAB 198 75 135
pP CTAO 186 73 120
pP CAN 183 88 107
pP HNR 172 63 101
0
10
20
30
sec
0
10
20
30
sec
(e)
S
S
S MSVF 155 74 192
S PFO 68 63 479
S TUC 65 68 475
S COR 63 52 618
S HKT 55 77 639
S RSSD 52 62 656
S FFC 42 55 865
S SSPA 37 76 424
S BBSR 31 88 529
S KONO 340 62 193
S LVZ 334 50 328
S OBN 323 59 457
S KIV 312 65 438
S EIL 308 80 375
S GNI 308 67 547
S KURK 297 43 747
S WMQ 283 42 925
0
10
20
30
sec
0
10
20
30
sec

Fig. S5-6

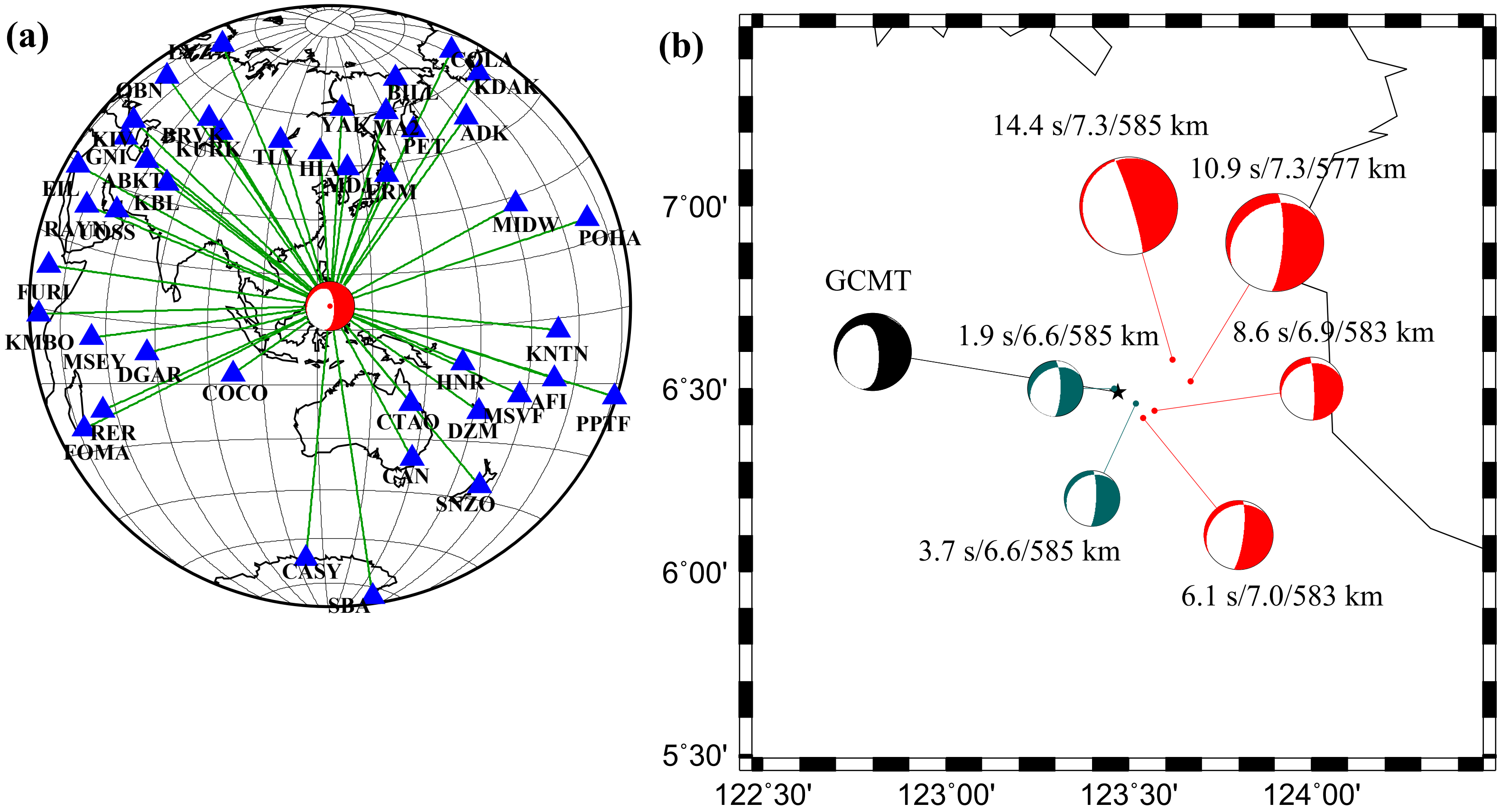
(a)
LVZ
OBN
KIV
GNI
EIL
ABKT
KBL
RAYN
UOSS
FURI
KMBO
MSEY
DGAR
COCO
BRVK
KURK
TLY
HIA
YAK
MA2
BILL
COLA
KDAK
PET
ADK
MDJ
ERM
MIDW
POHA
KNTN
HNR
AFI
PPTF
MSVF
DZM
CTAO
CAN
SNZO
RER
FOMA
CASY
SBA
(b)
14.4 s/7.3/585 km
10.9 s/7.3/577 km
GCMT
1.9 s/6.6/585 km
8.6 s/6.9/583 km
3.7 s/6.6/585 km
6.1 s/7.0/583 km
7˚00'
6˚30'
6˚00'
5˚30'
122˚30'
123˚00'
123˚30'
124˚00'

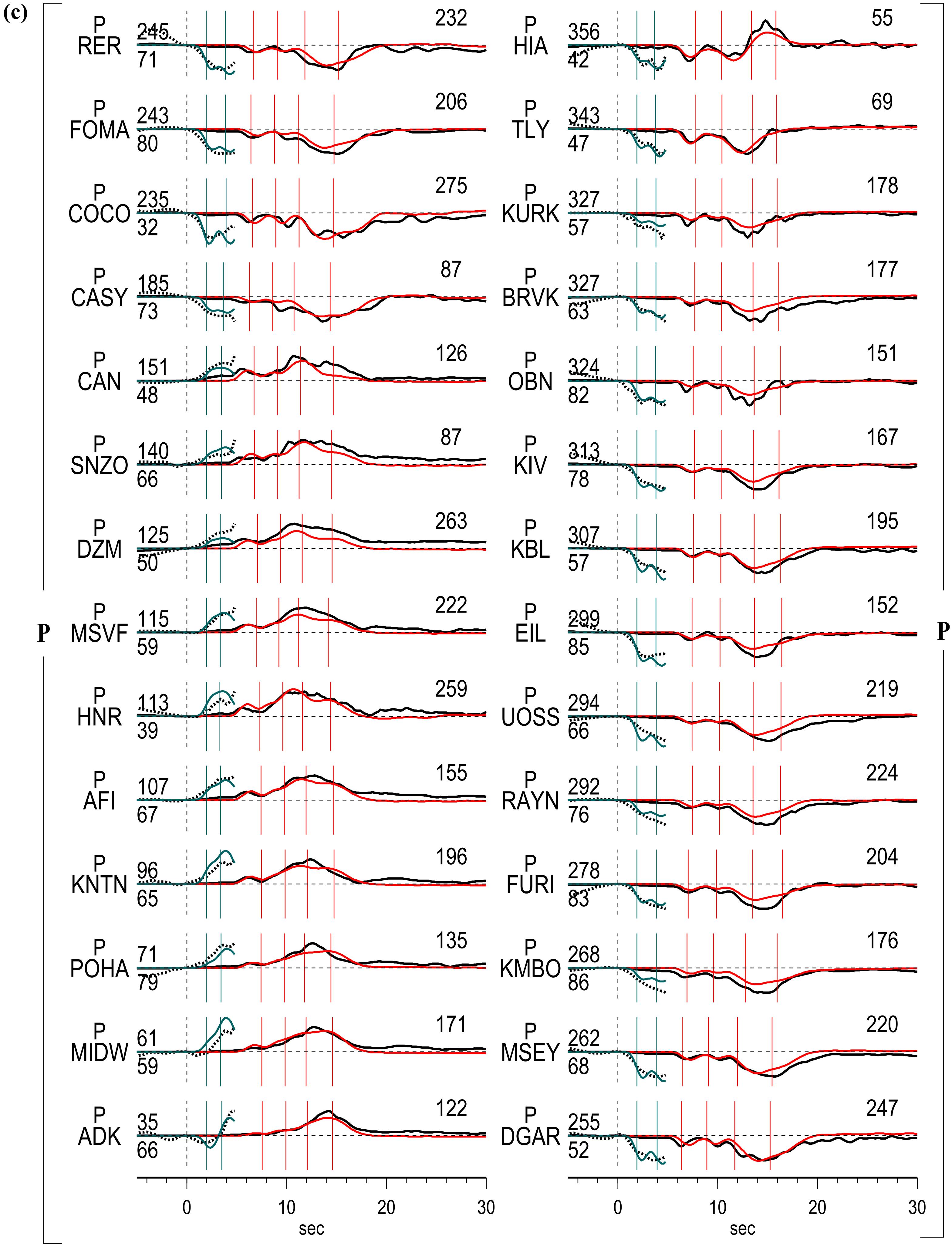(c)
P
P
P RER 245 71 232
P FOMA 243 80 206
P COCO 235 32 275
P CASY 185 73 87
P CAN 151 48 126
P SNZO 140 66 87
P DZM 125 50 263
P MSVF 115 59 222
P HNR 113 39 259
P AFI 107 67 155
P KNTN 96 65 196
P POHA 71 79 135
P MIDW 61 59 171
P ADK 35 66 122
P HIA 356 42 55
P TLY 343 47 69
P KURK 327 57 178
P BRVK 327 63 177
P OBN 324 82 151
P KIV 313 78 167
P KBL 307 57 195
P EIL 299 85 152
P UOSS 294 66 219
P RAYN 292 76 224
P FURI 278 83 204
P KMBO 268 86 176
P MSEY 262 68 220
P DGAR 255 52 247
0
10
20
30
sec
0
10
20
30
sec

(d)

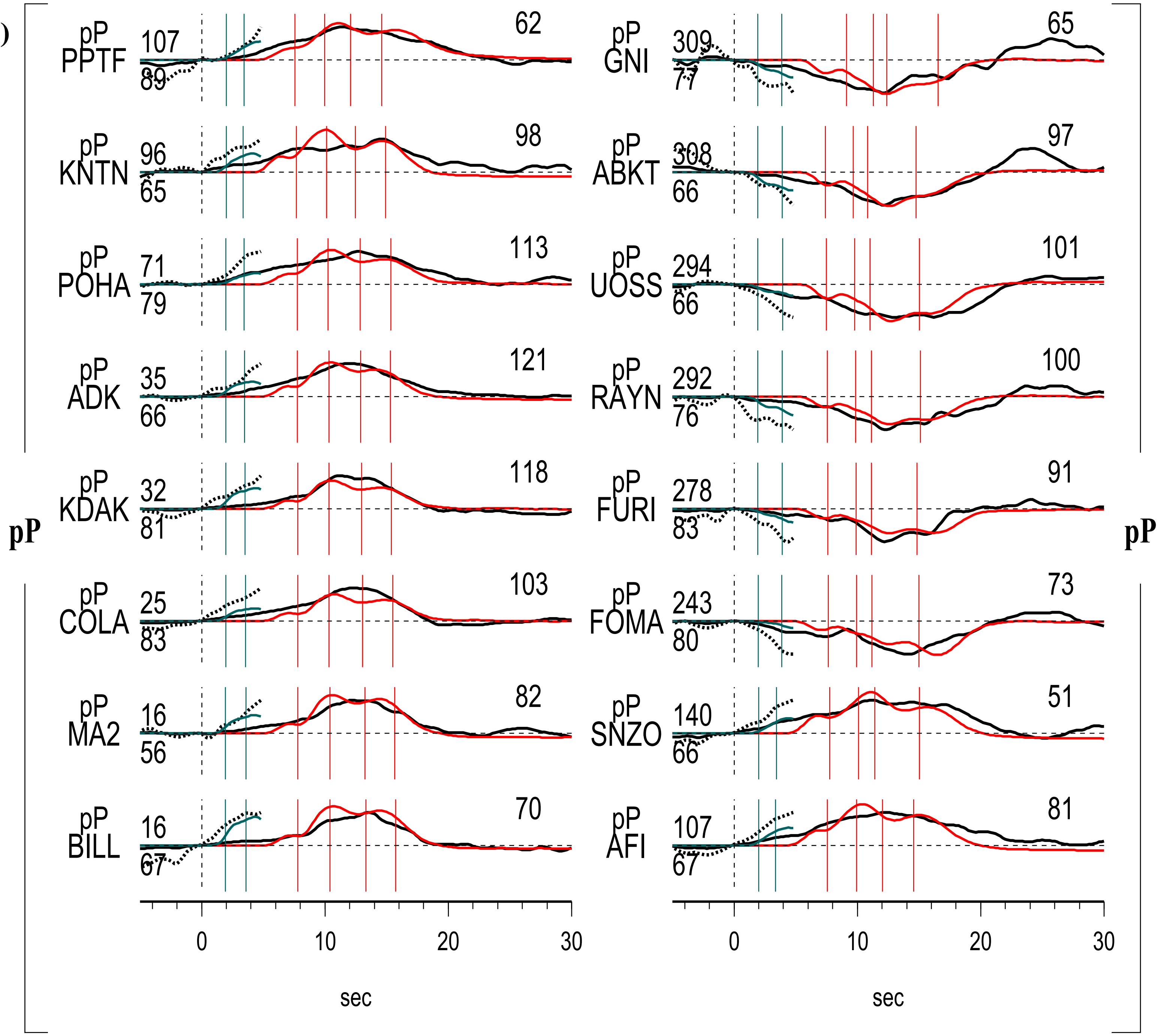
pP
pP
pP PPTF 107 89 62
pP KNTN 96 65 98
pP POHA 71 79 113
pP ADK 35 66 121
pP KDAK 32 81 118
pP COLA 25 83 103
pP MA2 16 56 82
pP BILL 16 67 70
pP GNI 309 77 65
pP ABKT 308 66 97
pP UOSS 294 66 101
pP RAYN 292 76 100
pP FURI 278 83 91
pP FOMA 243 80 73
pP SNZO 140 66 51
pP AFI 107 67 81
0
10
20
30
sec
0
10
20
30
sec

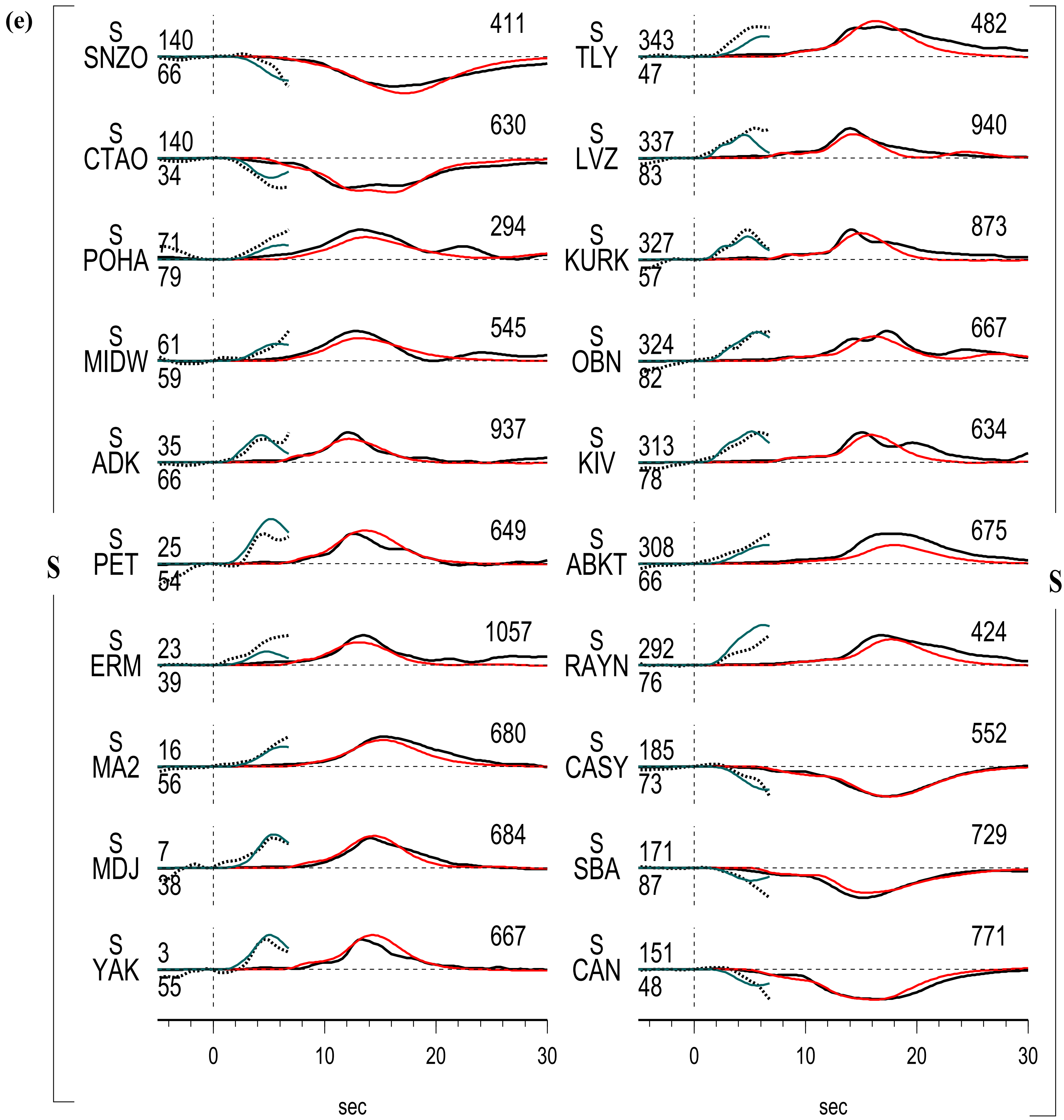
(e)
S
S
S SNZO 140 66 411
S CTAO 140 34 630
S POHA 71 79 294
S MIDW 61 59 545
S ADK 35 66 937
S PET 25 54 649
S ERM 23 39 1057
S MA2 16 56 680
S MDJ 7 38 684
S YAK 3 55 667
S TLY 343 47 482
S LVZ 337 83 940
S KURK 327 57 873
S OBN 324 82 667
S KIV 313 78 634
S ABKT 308 66 675
S RAYN 292 76 424
S CASY 185 73 552
S SBA 171 87 729
S CAN 151 48 771
0
10
20
30
sec
0
10
20
30
sec